Transactions of the ASME, Journal of Heat Transfer
(ISSN 0022-1481) is published monthly by The American Society of Mechanical Engineers, Three Park Avenue, New York, NY 10016. Periodicals postage paid at New York, NY and additional mailing offices.
POSTMASTER: Send address changes to Transactions of the ASME, Journal of Heat Transfer, c/o THE AMERICAN SOCIETY OF MECHANICAL ENGINEERS, 22 Law Drive, Box 2300, Fairfield, NJ 07007-2300.
CHANGES OF ADDRESS must be received at Society headquarters seven weeks before they are to be effective. Please send old label and new address.

Journal of Heat Transfer

Published Monthly by ASME

VOLUME 131 • NUMBER 4 • APRIL 2009

GUEST EDITORIAL

040301 **Special Issue on Micro/Nanoscale Heat Transfer—Part II**
Ping Cheng, Steve Choi, Yogesh Jaluria, Dongqing Li, Pamela Norris, and "Robert" D. Y. Tzou

MICRO/NANOSCALE HEAT TRANSFER—PART II

043201 **Thermal Conductivity Measurements on Polycrystalline Silicon Microbridges Using the 3ω Technique**
Patrick E. Hopkins and Leslie M. Phinney

043202 **Molecular Dynamics Based Analysis of Nucleation and Surface Energy of Droplets in Supersaturated Vapors of Methane and Ethane**
Jadran Vrabec, Martin Horsch, and Hans Hasse

043203 **Heat Transfer Augmentation of Aqueous Suspensions of Nanodiamonds in Turbulent Pipe Flow**
Shuichi Torii and Wen-Jei Yang

043204 **Experimental Study of Flow Critical Heat Flux in Alumina-Water, Zinc-Oxide-Water, and Diamond-Water Nanofluids**
Sung Joong Kim, Tom McKrell, Jacopo Buongiorno, and Lin-Wen Hu

043205 **Effect of CuO Nanoparticle Concentration on R134a/Lubricant Pool-Boiling Heat Transfer**
M. A. Kedzierski

043206 **Atomic-Scale Three-Dimensional Phononic Crystals With a Very Low Thermal Conductivity to Design Crystalline Thermoelectric Devices**
Jean-Numa Gillet, Yann Chalopin, and Sebastian Volz

043207 **Examining Interfacial Diffuse Phonon Scattering Through Transient Thermoreflectance Measurements of Thermal Boundary Conductance**
Pamela M. Norris and Patrick E. Hopkins

043208 **Contribution of Ballistic Electron Transport to Energy Transfer During Electron-Phonon Nonequilibrium in Thin Metal Films**
Patrick E. Hopkins and Pamela M. Norris

043209 **Numerical Study of Thermally Targeted Liposomal Drug Delivery in Tumor**
Aili Zhang, Xipeng Mi, Geer Yang, and Lisa X. Xu

043210 **Experimental Investigation of Miniature Three-Dimensional Flat-Plate Oscillating Heat Pipe**
S. M. Thompson, H. B. Ma, R. A. Winholtz, and C. Wilson

043211 **Recent Work on Boiling and Condensation in Microchannels**
Ping Cheng, Guodong Wang, and Xiaojun Quan

(Contents continued on inside back cover)

This journal is printed on acid-free paper, which exceeds the ANSI Z39.48-1992 specification for permanence of paper and library materials. ♾™
♻ 85% recycled content, including 10% post-consumer fibers.

(**Contents continued**)

Journal of Heat Transfer **Volume 131, Number 4** **APRIL 2009**

TECHNICAL BRIEFS

044501 Solution of Thermally Developing Zone in Short Micro-/Nanoscale Channels
Masoud Darbandi and Shidvash Vakilipour

The ASME Journal of Heat Transfer is abstracted and indexed in the following:

Applied Science and Technology Index, Chemical Abstracts, Chemical Engineering and Biotechnology Abstracts (Electronic equivalent of Process and Chemical Engineering), Civil Engineering Abstracts, Compendex (The electronic equivalent of Engineering Index), Corrosion Abstracts, Current Contents, E & P Health, Safety, and Environment, Ei EncompassLit, Engineered Materials Abstracts, Engineering Index, Enviroline (The electronic equivalent of Environment Abstracts), Environment Abstracts, Environmental Engineering Abstracts, Environmental Science and Pollution Management, Fluidex, Fuel and Energy Abstracts, Index to Scientific Reviews, INSPEC, International Building Services Abstracts, Mechanical & Transportation Engineering Abstracts, Mechanical Engineering Abstracts, METADEX (The electronic equivalent of Metals Abstracts and Alloys Index), Petroleum Abstracts, Process and Chemical Engineering, Referativnyi Zhurnal, Science Citation Index, SciSearch (The electronic equivalent of Science Citation Index), Theoretical Chemical Engineering

Journal of Heat Transfer

Guest Editorial

Special Issue on Micro/Nanoscale Heat Transfer—Part II

Research and education on micro/nanoscale heat transfer have advanced rapidly over the last decade through many dedicated individuals and teams, with direct impact now extending into other fields in both science and engineering. Continuing the synergistic efforts in 2002 and 2007,[1] ASME Micro/Nanoscale Heat Transfer International Conference (MNHT08) was held in National Cheng Kung University, Tainan, Taiwan, during January 6–9, 2008: http://www.asmeconferences.org/MNHT08/index.cfm. The conference is dedicated to Dr. Chang-Lin Tien (1935–2002), a world renowned scholar and a leader in higher education, whose intellect and unique visions have continued to inspire our most serious efforts in expanding the frontiers of micro/nanoscale heat transfer. We continue the selected papers from MNHT08 in this issue of the *ASME Journal of Heat Transfer*. Part I appeared in the March 2009 issue.

MNHT08 is composed of 18 technical tracks, with 5 keynote lecturers and over 300 participants from 18 countries. The 257 technical papers cover the full spectrum from microscopic thermophysical processes and properties, microfluidics and nanofluidics, heat transfer in small scale, ultrafast heat transport, interfacial heat transfer, nanofluids, microchannels, micro/nanoscale experimental heat transfer, micro/miniature two-phase systems, thermophysical and mechanical properties, ultrafast coupling in small scales, nano-systems and engineering, nano/microscale thermal radiation, computational micro/nanoscale heat and mass transfer, to micro/nanoscale heat and mass transfer in bio/medical systems. The papers included in this issue are representatives selected from these areas of research. There are a few papers in this issue that are review in nature, for the purpose of capturing the progress being made in a field as well as for presenting new challenges for the future. There are also research papers reporting innovative approaches and new findings, aiming toward advancing the state-of-the-art development in micro/nanoscale heat and mass transfer. Two salient features combined, we hope this issue will not only serve the community well, but also provide a valuable collection for inspiring new researchers to join this fascinating area of research.

Researchers in micro/nanoscale heat and mass transfer have enjoyed strong growth of the field over the past decade. Many sophisticated physical phenomena in small scales have been unveiled by dedicated individuals and research teams. The rapid evolution and continued explorations into even finer scales of space and time, however, may often generate more profound physics to be better understood. This is particularly the case when the thermal field is coupling with other fields in transporting mass, energy, momentum, and charges in micro/nanoscale. Combined approaches that integrate over analytical, experimental, and numerical phases have now become more important than ever in unveiling the interweaving physical phenomena in smaller scale. It is important to continue our endeavors in generating in-depth scientific understanding and enabling commercial technology for advancing micro/nanodevices, but it may be equally important to "wrap up" our knowledge by reviewing what we have tried to establish from time to time. This focus will remain as the ASME Micro/Nanoscale Heat Transfer International Conference continues into the future.

Special thanks are extended to the reviewers, the Editorial Assistant Shefali Patel, and publishing staff for the *ASME Journal of Heat Transfer*, who have made this special issue on *Micro/Nanoscale Heat Transfer* a reality. Enthusiastic supports from National Cheng Kung University, Chinese Society of Mechanical Engineers, and Industrial Technology and Research Institute (ITRI) in Taiwan are greatly appreciated. We wish to thank the Air Force Office of Scientific Research, Asian Office of Aerospace Research and Development (AOARD), and the Office of Naval Research Global (ONRG) for their contributions to the success of this conference.

Ping Cheng
Shanghai Jiaotong University, China

Steve Choi
University of Illinois at Chicago, USA

Yogesh Jaluria
Rutgers, The State University of New Jersey, USA

Dongqing Li
University of Waterloo, Canada

Pamela Norris
University of Virginia, USA

"Robert" D. Y. Tzou
University of Missouri, USA

[1]Special Issue: Micro/Nanoscale Heat Transfer, *ASME Journal of Heat Transfer*, Vol. 124, April 2002. Special Issue: Micro/Nanoscale Radiative Transfer, *ASME Journal of Heat Transfer*, Vol. 129, January 2007.

Thermal Conductivity Measurements on Polycrystalline Silicon Microbridges Using the 3ω Technique

Patrick E. Hopkins[1]
Department of Mechanical and Aerospace Engineering,
University of Virginia,
P.O. Box 400746,
Charlottesville, VA 22904-4746

Leslie M. Phinney[2]
Engineering Sciences Center,
Sandia National Laboratories,
P.O. Box 5800,
Albuquerque, NM 87185-0346
e-mail: lmphinn@sandia.gov

The thermal performance of microelectromechanical systems devices is governed by the structure and composition of the constituent materials as well as the geometrical design. With the continued reduction in the characteristic sizes of these devices, experimental determination of the thermal properties becomes more difficult. In this study, the thermal conductivity of polycrystalline silicon (polysilicon) microbridges are measured with the transient 3ω technique and compared with measurements on the same structures using a steady state Joule heating technique. The microbridges with lengths from 200 μm to 500 μm were designed and fabricated using the Sandia National Laboratories SUMMiT V™ surface micromachining process. The advantages and disadvantages of the two experimental methods are examined for suspended microbridge geometries. The differences between the two measurements, which arise from the geometry of the test structures and electrical contacts, are explained by bond pad heating and thermal resistance effects. [DOI: 10.1115/1.3072907]

Keywords: thermal conductivity, 3ω technique, polycrystalline silicon, suspended microbridge, thermal boundary resistance

1 Introduction

The characteristic lengths of material features contained in microelectronic devices are continually decreasing while the power generation needs and requirements continue to increase [1]. This is creating a huge incentive for efficient and effective thermal management, especially for materials with characteristic lengths on the order of the mean free paths of the carriers. Reduction in these mean free paths results from fabrication processes that produce more carrier scattering mechanisms in the materials [2]. For example, consider fabricating a semiconductor microcantilever, which involves the deposition of several materials as well as lithographic etching. The types of materials used to create the structure influences several characteristics of the final microcantilever, including surface roughness, sizes of geometric and grain boundaries, lattice dislocations, and impurities, which increase phonon scattering events and can significantly alter the thermal properties of the final structure [3]. However, the contribution of these individual phonon scattering processes on the thermal properties of the structure is very difficult to predict without experimental characterization and thermal testing [3]. Therefore, accurate experimental testing of thermal properties in low dimensional structures is becoming increasingly important to effective thermal management in current and future microelectronic materials [4].

Electrically based measurements have been successful in measuring thermal properties in low dimensional silicon structures, which are common in microelectromechanical systems (MEMS) and integrated circuits. Steady state resistance methods have successfully measured the thermal conductivity of various silicon structures, including undoped [5] and doped [3] polycrystalline silicon (polysilicon) films, doped single crystalline free standing films [6] and microcantilevers [7], doped polysilicon suspended films [8–10], and doped polysilicon suspended microbridges [11–13]. The advantages of these steady state techniques are the ease of measurement and analysis. However, processing constraints and measurement methods that are not optimized to minimize error due to experimental factors (i.e., convection and radiation losses) and test structure geometries (i.e., electrical probe contact resistance and heat flow to underlying structures or substrates) can lead to a complicated analysis to determine the true conductivity of the structure. For example, Phinney et al. [11] used a steady state technique to measure the temperature dependent thermal conductivity of polysilicon microbridges attached to bulk bond/electrical contact pads. Although the room temperature thermal conductivity values agreed with those from the room temperature studied by Tai et al. [12,13], the temperature dependent values and trends did not agree with previously reported values of thermal conductivity of polysilicon [3,5,8–10]. These differences could be due to complications from contact resistance and heat transfer to the substrate. By using a transient measurement technique, such as the 3ω technique, these effects could be reduced in comparison to a steady state method.

The 3ω technique was originally used by Cahill [14,15] to measure the thermal conductivity of bulk dielectric solids across a wide range of temperatures from 30 K to 750 K. Since then, this technique has been extended to measure the thermal conductivity of dielectric thin films [16], periodic superlattice structures [17], and nonperiodic multilayered structures [18,19]. In addition, this technique was extended to platinum and carbon nanotube suspended micro- and nanobridges [20,21]. The 3ω technique has several characteristics that make it an attractive alternative for thermal conductivity measurements on a wide range of materials and structures. The periodic nature of 3ω can make measurements inherently insensitive to radiative and convective losses, depending on the test section geometry. Second, a properly chosen ω input and range can eliminate problematic boundary conditions

[1]Present address: Engineering Sciences Center, Sandia National Laboratories, P.O. Box 5800, Albuquerque, NM 87185-0346.
[2]Corresponding author.
Contributed by the Heat Transfer Division of ASME for publication in the JOURNAL OF HEAT TRANSFER. Manuscript received March 27, 2008; final manuscript received December 9, 2008; published online February 11, 2009. Review conducted by Robert D. Tzou. Paper presented at the 2008 International Conference on Micro/Nanoscale Heat Transfer (MNHT2008), Tainan, Taiwan, January 6–9, 2008.

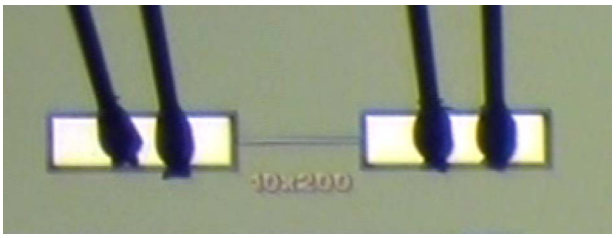

Fig. 1 Optical microscope image of a 10 μm wide×200 μm long test structure fabricated using the SUMMiT V™ process. The bond pads are 100 μm wide and 300 μm long. Two wires bonded to bond pad are visible in the image. The connections to the package are outside of the image.

that may exist between the sample and external test hardware [19]. Finally, since 3ω is a nondestructive technique, certain device geometries and material systems used in the high-powered microelectronic device systems of interest can be examined in their as-used conditions or with minimal post processing.

In this study, the thermal conductivity of polycrystalline silicon suspended bridge structures are measured with the 3ω technique. To the knowledge of the authors, this represents the first measurements of polysilicon bridges with the 3ω technique. The thermal conductivity of these same structures is also measured with a steady state resistance method, which allows for comparisons among the thermal conductivity measurement techniques. The suspended structures are fabricated using the Sandia Ultraplanar Multilevel MEMS Technology (SUMMiT V™) process [22,23]. In Sec. 2, the SUMMiT V™ process is described along with the test samples. The specific 3ω setup, analysis method, and assumptions are explained in Sec. 3. Section 4 presents the temperature dependent 3ω thermal conductivity results and compares them to the steady state measurements. The differences between the two measurements can be ascribed to contact and bond pad effects, for which steady state techniques must carefully account but which the 3ω technique is insensitive in the frequency domain. Therefore, these effects can be treated as an offset in 3ω analysis [16].

2 Suspended Test Structures

The SUMMiT V™ process [22] involves four structural *n*-type (phosphorous-doped) polysilicon layers with a fifth layer as a ground plane. The polysilicon layers are separated by sacrificial oxide layers that are etched away during the final release step. The two topmost layers, Poly3 and Poly4, are nominally 2.25 μm in thickness, while the bottom two, Poly1 and Poly2, are nominally 1.0 μm and 1.25 μm in thickness, respectively. The ground plane, Poly0, is 300 nm in thickness and lies above an 800 nm layer of silicon nitride and a 630 nm layer of silicon dioxide. The sacrificial oxide layers between the structural layers are each roughly 2.0 μm thick.

The thermal conductivity test structures are fabricated from the Poly4 layer and are nominally 2.25 μm thick. Test structures were designed with a width of 10 μm and four lengths: 200 μm, 300 μm, 400 μm, and 500 μm. The fixed-fixed bridge ends at bond pads, which are layered structures that mechanically anchor the beam to the substrate and provide a location for wire bonding to the package. The wires are bonded to a 700 nm layer of Al that is deposited on top of the bond pad. Figure 1 is an image of a 10 μm wide and 200 μm long suspended bridge test structure used in this study with the bond pads and bond wires visible.

3 3ω Experimental Considerations

As previously mentioned, the thermal conductivity of the Poly4 SUMMiT V™ bridge structures were measured with both steady state and 3ω techniques. Details of the steady state experimental setup, analysis, assumptions, and possible errors are described in

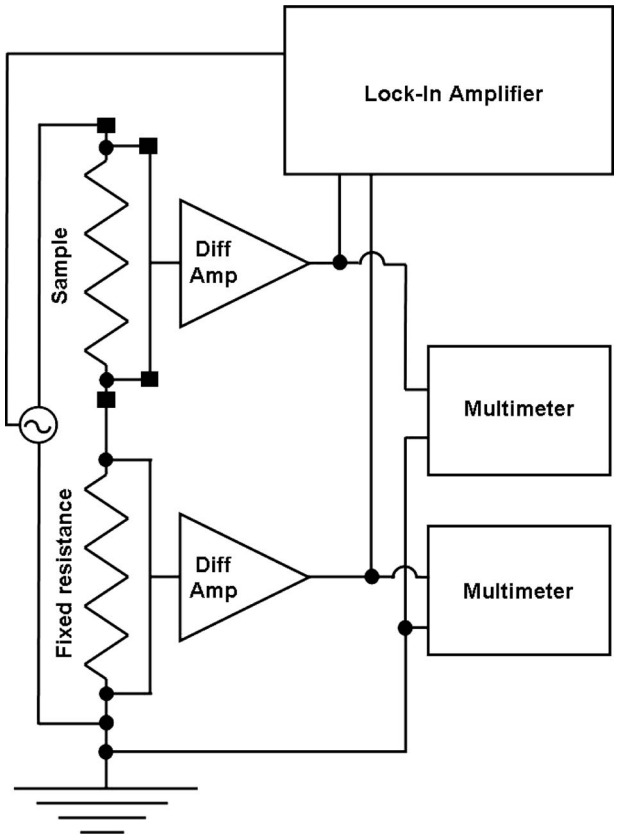

Fig. 2 Schematic representing circuit and data acquisition equipment in the 3ω measurements. The sample is the polysilicon microbridge structure, and the fixed resistance varied depending on the sample. The value of the fixed resistance was chosen to be slightly higher than the maximum resistance across the sample [14]. During testing, this value was set to be slightly higher than the room temperature resistance of the sample.

Refs. [11,24]. A description of the 3ω setup used for measurements on the Poly4 SUMMiT V™ bridge structure follows. Figure 2 shows a schematic of the electrical circuit with the data acquisition components of the experimental setup. This is essentially the same setup as Cahill's original experiment [14,15] only the use of a SR830 digital signal processing (DSP) lock-in amplifier with higher harmonic detection removes the need for a frequency tripling circuit. This lock-in greatly simplifies the circuit since it was used for the input current, reference signal, and measurement of the third harmonic (3ω) voltage. The ac sinusoidal input current, which was supplied by the lock-in amplifier, was passed through the sample and resistor of fixed resistance. Passing the resulting voltage drops through AD534 differential amplifiers reduces unwanted noise by producing a signal equal to the voltage drop across the sample and fixed resistor, respectively. The resulting signals were then differenced by the lock-in amplifier. Differencing the two resulting voltages across the sample and fixed resistor removed the majority of unwanted noise. The differenced voltage signal contains both ω and 3ω components. The lock-in amplifier was used to detect the small resulting 3ω component by comparing the differenced voltage signal with the input current (supplied by the lock-in amplifier).

The temperature dependent data were obtained while slowly heating and cooling the test structures in a liquid nitrogen cooled Henriksen cryostat that was pumped down to less than 1 mTorr. Only the sample is in the temperature controlled vacuum; the fixed resistor is wired in the circuit in ambient so that it experiences minimal temperature fluctuations. The voltage dissipated

across the sample and fixed resistor was determined with Agilent 34401A multimeters, and then the resistance across the test section was determined at each temperature. Since the majority of the resistance between the voltage probes on the bond pads lies in the bridge structure, the 3ω data were analyzed with the relationship between 3ω voltage and thermal conductivity derived by Lu et al. [21] for one-dimensional conduction along rodlike structures, given by

$$V_{3\omega} \approx \frac{4V^3L}{\pi^4 kAR^2\sqrt{1+(2\omega\gamma)^2}}\frac{dR}{dT} \tag{1}$$

where V and $V_{3\omega}$ are the voltage dissipated across the bridge structure and the third harmonic of the voltage detected across the bridge structure, respectively; L is the length of the bridge structure (the additional length from the bridge-bond pad connection was neglected since the lateral resistance in the bond pad is considered negligible compared with the resistance along the bridge structure); k is the thermal conductivity of the bridge structure; A is the cross-sectional area of the bridge structure; R is the electrical resistance measured across the bridge structure; ω is the angular frequency of the ac supplied to the circuit; and γ is the characteristic thermal time constant for the axial thermal process, which for this one-dimensional thermal process is defined as $\gamma = L^2C/\pi^2 k$ [21], where C is the heat capacity of the structure, and dR/dT is the change in the electrical resistance over the temperature range for the measurements. The electrical resistance as a function of temperature was determined from the voltage drop across the test section (ts) and fixed resistor (fr) and the resistance of the fixed resistor by $R_{ts}=R_{fr}V_{ts}/V_{fr}$. The measured dR/dT of the 200 μm, 300 μm, 400 μm, and 500 μm long bridges were 0.226 Ω/K, 0.328 Ω/K, 0.443 Ω/K, and 0.554 Ω/K, respectively. The temperature dependent resistance values measured using the steady state experimental technique were similar: 0.224 Ω/K, 0.334 Ω/K, 0.454 Ω/K, and 0.553 Ω/K, respectively. The electrical resistance of the test section exhibited a linear trend with temperature over the entire temperature range of interest; therefore dR/dT was constant. 3ω data were taken over a wide range of frequencies. At relatively low frequencies, where the thermal wavelength is much larger than the length of the structure, $\omega\gamma$ approaches zero and the resulting 3ω voltage is frequency independent. In this limit, Eq. (1) becomes

$$V_{3\omega} \approx \frac{4V^3L}{\pi^4 kAR^2}\frac{dR}{dT} \tag{2}$$

and the thermal conductivity can be easily determined from the in-phase portion of $V_{3\omega}$.

Figure 3 shows the $V_{3\omega}$ response on a 200 μm microbridge test structure at 294 K along with the best fit of Eq. (1) using k and γ as fitting parameters. The thermal conductivity is determined from the low frequency data, where the 3ω response is frequency independent. The time constant γ then determines the curvature of the 3ω response at higher frequencies. The best fit thermal conductivity of this structure is 66 W m^{-1} K^{-1}. The thermal time constant γ of this structure is 1.199 ms, as shown from the best fit of Eq. 1 in Fig. 3. Equation (1), solved with two other time constants of γ=0 s and γ=10 ms, is also shown in this figure.

During testing, the frequency range was swept from 5 rad s^{-1} to 10,000 rad s^{-1} during data collection at room temperature and low temperature (85 K). This identified the region of frequency independent $V_{3\omega}$ and also determined the maximum and minimum time constants of the structure over the temperature range. Data were taken at temperatures ranging from 85 K to 294 K. The temperature of the cryostat was ramped at 1.0 K/min and only a few selected frequencies in the frequency independent $V_{3\omega}$ range (low frequencies) were applied to the circuit so that the frequency range was swept approximately three times before the chamber changed 1 K.

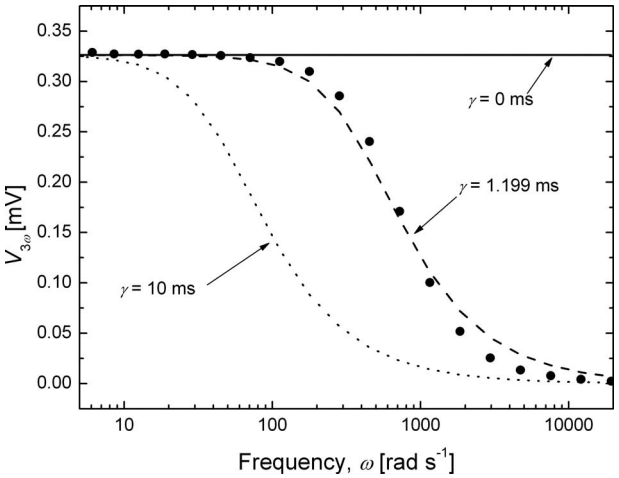

Fig. 3 Sensitivity of Eq. (1) to the thermal time constant γ. A best fit thermal conductivity k is 66 W m^{-1} K^{-1}. The thermal conductivity of the test structures is easily determined by identifying the region of frequency independent $V_{3\omega}$ and fitting Eq. (2) to the data.

4 Results

Figure 4 shows Eq. (1) fit to 3ω data on the different length bridge structures taken at 85 K and 294 K. The thermal conductivity k and time constant γ, determined from Eq. (1), are also shown in this figure. The data and Eq. (1) fit are normalized for clarity since the value of $V_{3\omega}$ is different for each bridge structure. As the bridge length decreases, the thermal time constant also decreases. This is expected since a shorter bridge structure will take less time to equilibrate. In addition, the time constant in each structure decreases as the temperature decreases. This causes the region of frequency independent $V_{3\omega}$ response to span a longer frequency range. Figure 5 summarizes the thermal time constant results from the data shown in Fig. 4. The time constant, which increases at higher temperatures, is related to the phonon mean free path and equilibration time. At lower temperatures, the phonon mean free path is longer than at higher temperatures, and the bridge structures take less time to equilibrate. The longer bridge structures also take more time to equilibrate than the shorter bridge structures since the longer bridge structures create more scattering events along the length of the bridge, which in turn leads to longer equilibration time.

Figure 6 compares the thermal conductivity of the four bridge structures taken with the 3ω technique to the thermal conductivity determined with the steady state method. The thermal conductivity 3ω data are reported in increments of 1.0 K. As previously motioned, there were approximately three frequency sweeps taken before the sample changed 1 K, so each data point in the 3ω represents the statistical average of three measurements. The standard deviation among the three measurements at each temperature increment is less than 2% for all temperatures; the sizes of the data points are greater than the uncertainty among the three measurements at each temperature.

Notice there is a length dependency in the thermal conductivity measurements, which could arise from the contact resistance at the bridge/bond pad junction [24]. This dependency is far less apparent in the 3ω data taken at lower temperatures, but at higher temperatures, the same dependency exists between the 3ω and the steady state measurements. Some of the length dependency error has been considered in the steady state analysis by examining bond pad heating [24]. Some length dependency error could also result from the geometry of the test structure; for example, the electrical connections are placed on the bond pads and not on the suspended test structure. This could add to the measured electrical

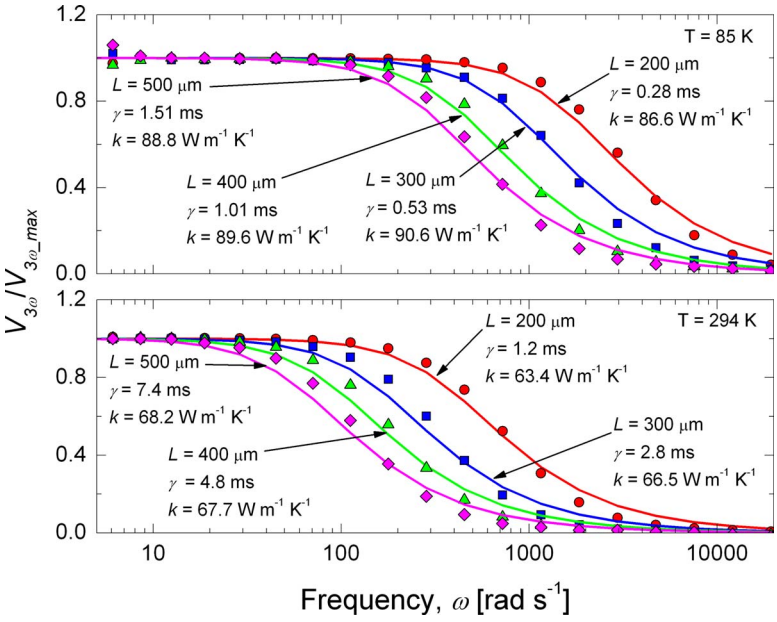

Fig. 4 3ω voltage on the different length bridge structures with the Eq. (1) fit to the data with best fit k and γ. The data and best fit are normalized for clarity. The frequency independent region of the 3ω voltage responses increases with a decrease in temperature.

resistance and subsequent thermal conductivity measurements. In addition, the locations of the electrical connections on the bond pads are not exact for each sample, which would also add to the error among the samples. The measured thermal conductivities of the bridge structures should not be length dependent (at these bridge lengths of several hundred microns), and the length dependencies are associated with measurement and instrumentation errors. The 3ω measurements appear to be less sensitive to these errors.

Figure 7 shows the 3ω measured thermal conductivity compared with the steady state data over the temperature range from 85 K to 294 K. The steady state thermal conductivity data on the bridge structures are larger than the thermal conductivity determined with the 3ω technique, especially at low temperature. The temperature trends and values of the 3ω data show much better agreement with literature values for polysilicon [3,5,8–10] than the steady state measurements.

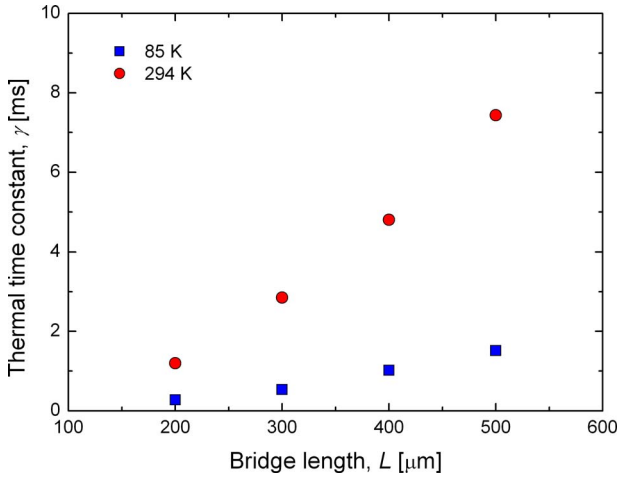

Fig. 5 Thermal time constant γ as a function of bridge length L determined at two different temperatures

In comparison of the 3ω polysilicon thermal conductivity to other reported values, potential for radiative heat losses must be considered; convective heat losses are considered negligible for microstructures under high vacuum [7,12,13,21]. These 3ω tests were conducted in a vacuum chamber with a maximum pressure of 1 mTorr and recent experimental and theoretical results have shown that convective losses can be neglected at pressures below 500 mTorr on samples with identical geometries subject to similar testing conditions [25].

Radiative heat loss per unit time per unit length W from a bridge with a rectangular cross section of area $A=d\times w$, where d is the thickness and w is the width of the bridge, to the environment of temperature T_0 is given by

$$W(x,t) = 2\varepsilon\sigma(d+w)[T^4(x,t) - T_0^4] \tag{3}$$

where ε is the emissivity of the polysilicon surface, σ is the Stefan–Boltzmann constant (5.67×10^{-8} W m^{-2} K^{-4}), x is the position along the polysilicon film, and t is the time. Defining an impulse function $\Delta(x,t)$, which represents the integral of the responses of the bridge to the instant "force" of current at each time interval [21], Eq. (3) can be approximated as

$$W \approx 8\varepsilon\sigma(d+w)T_0^3\Delta(x,t) \tag{4}$$

Following a similar analysis to the cylindrical rod radiation loss calculation by Lu et al. [21], the radiation heat loss coefficient g for a bridge with a rectangular cross section is given by

$$g = \frac{8\varepsilon\sigma(d+w)T_0^3}{Cdw} \tag{5}$$

Radiation heat loss can be neglected if $g\gamma \ll 1$. Taking the worst case scenario from the measured time constants in Fig. 5 for a 500 μm bridge at 294 K with γ=7.5 ms and assuming an emissivity of unity and bulk Si heat capacity of C=1.66 $\times10^6$ J m^{-3} K^{-1} [26] yields a criterion value of 2.8×10^{-2}, which is low enough to neglect radiation losses. However, to avoid inaccuracies from using bulk values for heat capacity, the mathematical definition of γ can be used with Eq. (5) to yield a crite-

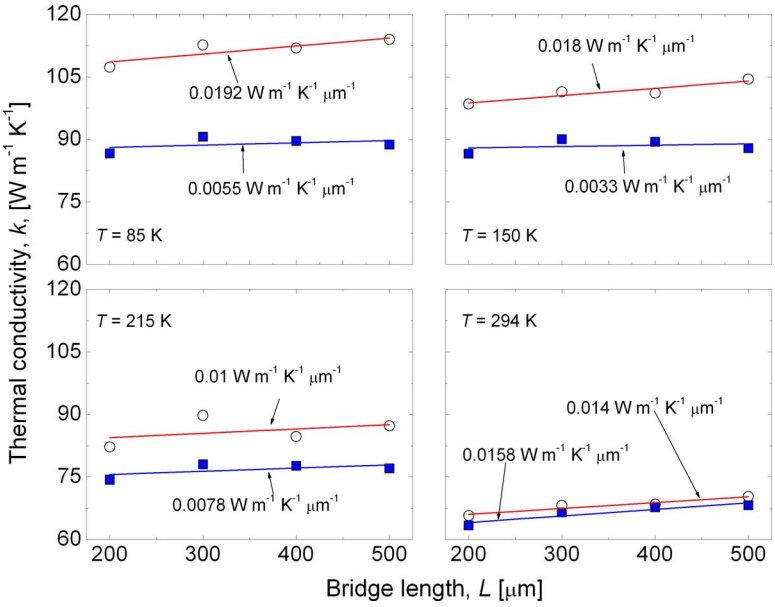

Fig. 6 Thermal conductivity measured with the 3ω (filled squares) and steady state (empty circles) [11] techniques as a function of bridge length at four different temperatures. The dependency of the data on bridge length is shown by the slope of the best fit line to the data. The bridge length dependency is essentially nonexistent in the lower temperature 3ω data, which is apparent by comparing the thermal conductivity trends with bridge length represented by the slopes of the best fit line to the data that are listed in the figures.

rion value based on the thermal conductivity measurements given by

$$\frac{8\varepsilon\sigma(d+w)T_0^3L^2}{\pi^2 dwk} \ll 1 \tag{6}$$

Taking the 500 μm bridge at 294 K with a measured k of 67 W m^{-1} K^{-1} yields a criterion value of 2.35×10^{-3}, using Eq. (6), which is certainly low enough to neglect radiation heat loss [7].

As previously mentioned, electrical and thermal resistances in the bond pads not associated with the test structure for which the 3ω measurements are insensitive in the frequency domain can be treated as an offset to the measured thermal conductivity [16]. Electrical resistance and bond pad offsets were neglected in the

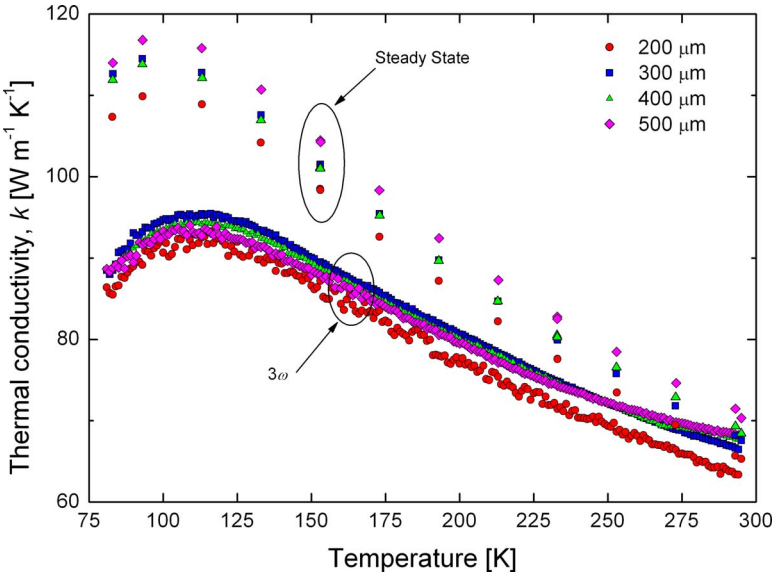

Fig. 7 Temperature dependent thermal conductivity data on the polysilicon bridge test structures. The 3ω and steady state measurements are both presented for comparison. The differences between the two sets of data determined from the different measurement techniques can be explained by the effects of bond pad heating and thermal boundary resistance between the Al wire bonded film and the bond pad.

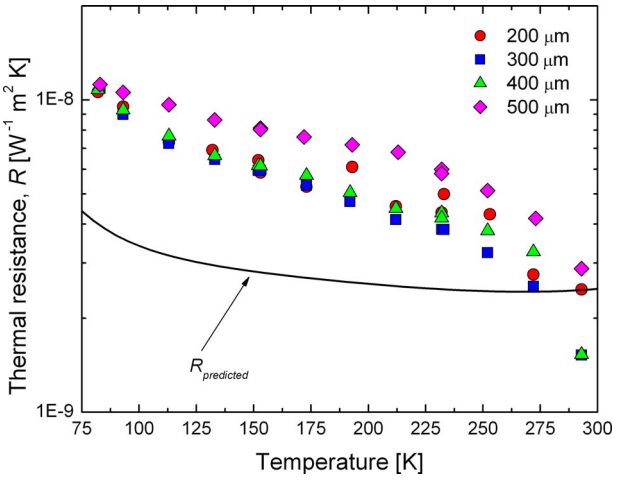

Fig. 8 Additional thermal resistances determined from the two data sets in Fig. 7 and Eq. (7) compared with the predicted thermal resistance $R_{predicted}$ of the 700 nm Al bond pad the Al/Si interface

analysis of the steady state data [11]. The lumped thermal resistance of the Al film to which the wires are bonded and the thermal boundary resistance [27] between the Al and the P4 polysilicon layer on the bond pad could play a significant role in thermal conductivity measurements, which may explain the difference between the 3ω and steady state measurements at the lower temperatures. To compare the steady state and 3ω measurements, these considerations are addressed in more detail by lumping these resistances into an interface resistance formulation. The thermal resistance not in the bridge test structure R is estimated by [16]

$$R = d\left(\frac{1}{k_{3\omega}} - \frac{1}{k_{ss}}\right) \tag{7}$$

where $k_{3\omega}$ is the thermal conductivity measured with the 3ω technique, k_{ss} is the thermal conductivity measured with the steady state technique, and d is the thickness of the P4 polysilicon layer. Since the 3ω technique is insensitive to the Al pad and interface resistances, the thermal conductivity determined with the 3ω technique represents the thermal conductivity of the polysilicon microbridge. The steady state measurements represent the thermal conductivity measured from voltage connection to voltage connection, which includes heat flow through the bond pads and is sensitive to the thermal resistances of the two Al bond pads and the thermal boundary resistances between the Al and the P4 structures. Using Eq. (7) the additional thermal resistance R is calculated from the difference between the two data sets shown in Fig. 7. Equation (7) calculations are shown in Fig. 8 along with calculations for an interface resistance assuming two parallel thermal resistors of a 700 nm Al film and an Al/Si interface. Using a lumped thermal resistance for the Al bond bad, and assuming a thermal conductivity of bulk Al, the Al film's thermal resistance is given by $R_{Al}=d_{Al}/k_{Al}$, where the temperature dependent thermal conductivity is taken from experimental data [28]. Using a bulk Al thermal conductivity for the 700 nm bond pad is valid since the electron mean free path in Al is approximately 50 nm [29]. The thermal resistance of an Al/Si interface is estimated from the diffuse mismatch model (DMM) [27]. The total resistance is then estimated as $R_{predicted}=(R_{Al}+R_{DMM})/2$.

To apply the DMM in its simplest form, the following assumptions are made [30]: (1) phonons are elastically scattered, (2) phonon scattering is completely diffused, and (3) the materials on either side of the interface are treated as Debye solids giving constant longitudinal and transverse acoustic velocities throughout the Brillouin zone. Using the DMM, the thermal boundary resistance R_{DMM} from side 1 (Al) to side 2 (Si) can be calculated by

$$\frac{1}{R_{DMM}} = \frac{1}{4}\sum_j u_{1,j}\int_0^{\nu_{1,j}^c} \alpha_1 h\nu D_{1,j}(\nu)\frac{\partial n(\nu,T)}{\partial T}d\nu \tag{8}$$

where the subscripts 1 and j refer to the side and the mode (with one longitudinal mode and two transverse modes, so Eq. (8) is summed over the three modes), respectively, ν is the phonon frequency, u is the phonon velocity, $\nu_{1,j}^c$ refers to the cutoff frequency of mode j on side 1, α is the phonon transmission coefficient, h is Planck's constant, D is the spectral phonon density of states per unit volume, and n is the Bose–Einstein distribution function. With assumption (3) discussed above, the Debye density of states per unit frequency per unit volume is given by

$$D_{1,j}(\nu) = \frac{2\nu^2}{u_{1,j}^3} \tag{9}$$

which leads to the cutoff frequency of mode j on side 1 being defined as [30]

$$\nu_{1,j}^c = u_{1,j}\left(\frac{3N_1}{4\pi}\right)^{1/3} \tag{10}$$

where N_1 is the total number of oscillators per unit volume of side 1. In cubic structures, such as Al, $N=\rho N_A/M$, where ρ is the mass density, N_A is Avogadro's number, and M is the atomic weight. The Bose–Einstein distribution function is defined as

$$n(\nu,T) = \frac{1}{\exp\left[\dfrac{h\nu}{k_B T}\right] - 1} \tag{11}$$

where k_B is Boltzmann's constant, and the phonon transmission coefficient from side 1 (Al) to side 2 (Si) under the three assumptions discussed above is defined as [27]

$$\alpha_1 = \frac{\sum_j u_{2,j}^{-2}}{\sum_j u_{1,j}^{-2} + \sum_j u_{2,j}^{-2}} \tag{12}$$

With Eqs. (8)–(12), R_{DMM} is calculated for an Al/Si interface as a function of temperature, as shown in Fig. 8. For these calculations, taking Al as side 1 and Si as side 2, the following thermophysical parameters were used [27]: $u_{1,L}=6240$ m s^{-1}, $u_{1,T}=3040$ m s^{-1}, $u_{2,L}=8970$ m s^{-1}, $u_{2,T}=5332$ m s^{-1}, $\rho_1=2700$ kg m^{-3}, and $M_1=0.027$ kg mol^{-1}.

The thermal boundary resistance determined from the comparison of the steady state and 3ω data (via Eq. (7)) shows agreement within an order of magnitude of the DMM calculations. This could be due to several aspects of the microbridge test samples not taken into account in DMM calculations such as temperature gradients in the bond pad due to Joule heating, changes in geometry at the bridge/bond pad junction, and additional carriers in the polysilicon due to the phosphorous dopants. The low temperature trends in the DMM are driven by phonon quantum state filling in accordance with the Bose–Einstein statistical distribution. The matching R trends in the Fig. 8 data at low temperatures suggest that the deviation in the temperature trends between the steady state and 3ω data are due to phonon-phonon scattering in thermal boundary conductance. At higher temperatures R rapidly decreases in the Eq. (7) calculations but approaches a constant value in the DMM calculations. The trend in the experimentally determined R could be due to electron-electron conductance at the interface, which contributes a linear temperature trend to thermal boundary resistance [31].

Although the discrepancies between the steady state and 3ω experimental measurements are explained, in part, by the thermal boundary resistance between the Al contact and the bond pad,

there are other experimental aspects that could be contributing to the different measurements. For example, the silicon microbridges are polycrystalline, and the differing sensitivities of the 3ω and steady state techniques to grain boundaries are relatively unknown. Also, the geometric change from the bond pad to the microbridge could lead to different types of responses. In addition, the steady state data show a length dependency, which could be due to analysis techniques on the raw data involving bond pad heating [24]. A similar analysis may be appropriate for the 3ω data.

5 Conclusions

Thermal conductivity measurements were made on polysilicon microbridges that were 10 μm wide and ranged from 200 μm to 500 μm long with the 3ω technique and compared with measurements made on the same structures with a steady state resistance technique. The measurements with the 3ω technique exhibit less of a dependence on length than the steady state measurements and agree much better with previously reported values of thermal conductivity of polysilicon microbridges. An explanation for the differences between the conductivities measured with the two different techniques is the thermal resistances of the Al and polysilicon layers in the bond pad.

Acknowledgment

The authors would like to thank Pam Norris at University of Virginia for her insight and arranging this collaboration, and Rebecca Clemens, Jaron Kuppers, Allen Gorby, and David Epp at Sandia for assistance with various aspects of the 3ω experimental setup. P.E.H. greatly appreciates financial support from the NSF graduate research fellowship program and a Sandia National Laboratories summer internship. Sandia is a multiprogram laboratory operated by Sandia Corporation, a Lockheed-Martin Co., for the United States Department of Energy's National Nuclear Security Administration under Contract No. DE-AC04-94AL85000.

Nomenclature

A = cross-sectional area, m^2
C = heat capacity, J m^{-3} K^{-1}
D = spectral phonon density of states, s m^{-3}
d = bridge thickness, m
g = radiation heat loss coefficient, s^{-1}
h = Planck's constant, J s
k = thermal conductivity, W m^{-1} K^{-1}
k_B = Boltzmann's constant, J K^{-1}
L = bridge length, m
M = atomic weight, kg mol^{-1}
N = oscillators per unit volume, m^{-3}
N_A = Avogrado's number, mol^{-1}
n = Bose–Einstein distribution function
R = electrical resistance, Ω
R_{BD} = thermal boundary resistance, W^{-1} m^2 K
T = temperature, K
t = time, s
u = phonon velocity, m s^{-1}
V = voltage, V
W = power loss per unit length, W m^{-1}
w = bridge width, m
x = positions, m

Greek Symbols

α = phonon transmission coefficient
Δ = impulse function, K
γ = thermal time constant, s
ε = emissivity
ν = phonon frequency, s^{-1}
ρ = mass density, kg m^{-3}
σ = Stefan–Boltzmann constant, W m^{-2} K^{-4}
ω = angular frequency, rad s^{-1}

Subscripts

1 = side 1
3ω = third harmonic
cl = convection loss
DMM = calculated with the DMM
i = intrinsic
j = phonon mode (longitudinal or transverse)
L = longitudinal mode
m = measured
T = transverse mode

Superscripts

c = cutoff

References

[1] Smith, A. N., and Calame, J. P., 2004, "Impact of Thin Film Thermophysical Properties on Thermal Management of Wide Bandgap Solid-State Transistors," Int. J. Thermophys., **25**, pp. 409–422.
[2] Cahill, D. G., Ford, W. K., Goodson, K. E., Mahan, G. D., Majumdar, A., Maris, H. J., Merlin, R., and Phillpot, S. R., 2003, "Nanoscale Thermal Transport," J. Appl. Phys., **93**, pp. 793–818.
[3] Mcconnell, A. D., Uma, S., and Goodson, K. E., 2001, "Thermal Conductivity of Doped Polysilicon Layers," J. Microelectromech. Syst., **10**, pp. 360–369.
[4] Cahill, D. G., Goodson, K. E., and Majumdar, A., 2002, "Thermometry and Thermal Transport in Micro/Nanoscale Solid-State Devices and Structures," ASME J. Heat Transfer, **124**, pp. 223–241.
[5] Uma, S., Mcconnell, A. D., Ashegi, M., Kurabayashi, K., and Goodson, K. E., 2001, "Temperature-Dependent Thermal Conductivity of Undoped Polycrystalline Silicon Layers," Int. J. Thermophys., **22**, pp. 605–616.
[6] Asheghi, M., Kurabayashi, K., Kasnavi, R., and Goodson, K. E., 2002, "Thermal Conduction in Doped Single-Crystal Silicon Films," J. Appl. Phys., **91**, pp. 5079–5088.
[7] Park, K., Marchenkov, A., Zhang, Z. M., and King, W. P., 2007, "Low Temperature Characterization of Heated Microcantilevers," J. Appl. Phys., **101**, p. 094504.
[8] Paul, O. M., Korvink, J., and Baltes, H., 1994, "Determination of the Thermal Conductivity of CMOS IC Polysilicon," Sens. Actuators, A, **41**, pp. 161–164.
[9] Von Arx, M., Paul, O., and Baltes, H., 2000, "Process-Dependent Thin-Film Thermal Conductivities for Thermal CMOS MEMS," J. Microelectromech. Syst., **9**, pp. 136–145.
[10] Volklein, F., and Baltes, H., 1992, "A Microstructure for Measurement of Thermal Conductivity of Polysilicon Thin Films," J. Microelectromech. Syst., **1**, pp. 193–196.
[11] Phinney, L. M., Kuppers, J. D., and Clemens, R. C., 2006, "Thermal Conductivity of SUMMiT™ V Polycrystalline Silicon," Sandia National Laboratories, Report No. SAND2006-7122.
[12] Tai, Y. C., Mastrangelo, C. H., and Muller, R. S., 1988, "Thermal Conductivity of Heavily Doped Low-Pressure Chemical Vapor Deposited Polycrystalline Silicon Films," J. Appl. Phys., **63**, pp. 1442–1447.
[13] Tai, Y. C., Mastrangelo, C. H., and Muller, R. S., 1989, "Erratum: 'Thermal Conductivity of Heavily Doped Low-Pressure Chemical Vapor Deposited Polycrystalline Silicon Films' [J. Appl. Phys. 63, 1442 (1988)]," J. Appl. Phys., **66**, pp. 3420.
[14] Cahill, D. G., 1990, "Thermal Conductivity Measurement From 30 to 750 K: The 3ω Method," Rev. Sci. Instrum., **61**, pp. 802–808.
[15] Cahill, D. G., 2002, "Erratum: 'Thermal Conductivity Measurement From 30 to 750 K: The 3ω Method' [Rev. Sci. Instrum. 61, 802 (1990)]," Rev. Sci. Instrum., **73**, p. 3701.
[16] Lee, S.-M., and Cahill, D. G., 1997, "Heat Transport in Thin Dielectric Films," J. Appl. Phys., **81**, pp. 2590–2595.
[17] Lee, S.-M., Cahill, D. G., and Venkatasubramanian, R., 1997, "Thermal Conductivity of Si-Ge Superlattices," Appl. Phys. Lett., **70**, pp. 2957–2959.
[18] Borca-Tasciuc, T., Kumar, A. R., and Chen, G., 2001, "Data Reduction in 3ω Method for Thin-Film Thermal Conductivity Determination," Rev. Sci. Instrum., **72**, pp. 2139–2147.
[19] Olson, B. W., Graham, S., and Chen, K., 2005, "A Practical Extension of the 3ω Method to Multilayer Structures," Rev. Sci. Instrum., **76**, p. 053901.
[20] Dames, C., and Chen, G., 2005, "1ω, 2ω, and 3ω Methods for Measurements of Thermal Properties," Rev. Sci. Instrum., **76**, p. 124902.
[21] Lu, L., Yi, W., and Zhang, D. L., 2001, "3ω Method for Specific Heat and Thermal Conductivity Measurements," Rev. Sci. Instrum., **72**, pp. 2996–3003.
[22] "SUMMiT V™: Five Level Surface Micromachining Technology and Design Manual," 2007, MEMS Technology Department, Sandia National Laboratories, Report No. SAND2007-D0446.
[23] Sniegowski, J. J., and De Boer, M. P., 2000, "IC-Compatible Polysilicon Surface Micromachining," Annu. Rev. Mater. Sci., **30**, pp. 299–333.
[24] Phinney, L. M., Piekos, E. S., and Kuppers, J. D., 2007, "Bond Pad Effects on Steady State Thermal Conductivity Measurement Using Suspended Micromachined Test Structures," *Proceedings of the 2007 ASME International Me-*

chanical Engineering Congress and Exposition, Seattle, WA, Paper No. 41349.
[25] Torczynski, J. R., Gallis, M. A., Piekos, E. S., Phinney, L. M., Serrano, J. R., and Gorby, A. D., 2008, "Validation of Thermal Models for a Prototypical MEMS Thermal Actuator," Sandia National Laboratories, Report No. SAND2008-D5749.
[26] Incropera, F., and Dewitt, D. P., 1996, *Fundamentals of Heat and Mass Transfer*, Wiley, New York.
[27] Swartz, E. T., and Pohl, R. O., 1989, "Thermal Boundary Resistance," Rev. Mod. Phys., **61**, pp. 605–668.
[28] Ho, C. Y., Powell, R. W., and Liley, P. E., 1972, "Thermal Conductivity of the Elements," J. Phys. Chem. Ref. Data, **1**, pp. 279–422.
[29] Hohlfeld, J., Wellershoff, S.-S., Gudde, J., Conrad, U., Jahnke, V., and Matthias, E., 2000, "Electron and Lattice Dynamics Following Optical Excitation of Metals," Chem. Phys., **251**, pp. 237–258.
[30] Cahill, D. G., Bullen, A., and Lee, S.-M., 2000, "Interface Thermal Conductance and the Thermal Conductivity of Multilayer Thin Films," High Temp. - High Press., **32**, pp. 135–142.
[31] Gundrum, B. C., Cahill, D. G., and Averback, R. S., 2005, "Thermal Conductance of Metal-Metal Interfaces," Phys. Rev. B, **72**, p. 245426.

Molecular Dynamics Based Analysis of Nucleation and Surface Energy of Droplets in Supersaturated Vapors of Methane and Ethane

Jadran Vrabec[1]
e-mail: jadran.vrabec@upb.de

Martin Horsch

Thermodynamik und Energietechnik,
Universität Paderborn,
Warburger Str. 100,
33098 Paderborn, Germany

Hans Hasse
Lehrstuhl für Thermodynamik,
Technische Universität Kaiserslautern,
Erwin-Schrödinger-Str. 44,
67663 Kaiserslautern, Germany

Homogeneous nucleation processes are characterized by the nucleation rate and the critical droplet size. Molecular dynamics simulation is applied for studying homogeneous nucleation during condensation of supersaturated vapors of methane and ethane. The results are compared with the classical nucleation theory (CNT) and the Laaksonen–Ford–Kulmala (LFK) model that introduces the size dependence of the specific surface energy. It is shown for the nucleation rate that the Yasuoka–Matsumoto method and the mean first passage time method lead to considerably differing results. Even more significant deviations are found between two other approaches to the critical droplet size, based on the maximum of the Gibbs free energy of droplet formation (Yasuoka–Matsumoto) and the supersaturation dependence of the nucleation rate (nucleation theorem). CNT is found to agree reasonably well with the simulation results, whereas LFK leads to large deviations at high temperatures. [DOI: 10.1115/1.3072909]

Keywords: phase transition, nucleation, molecular dynamics

1 Introduction

Nucleation processes in vapors at very high supersaturations, i.e., in the vicinity of the spinodal, cannot be studied with experimental methods because they are very fast, exhibiting rates that exceed the range accessible to measurement. Homogeneous nucleation supposes the absence not only of microscopic particles, but also of confining walls, a condition that is hard to approximate in experiments.

However, understanding homogeneous nucleation is required to develop an accurate theoretical approach to nucleation that extends to more complex and technically more relevant heterogeneous systems [1–3]. Molecular dynamics (MD) simulations can well be used to investigate the condensation of homogeneous vapors at high supersaturations.

The nucleation rate J is influenced to a large extent by the surface energy of emerging droplets, which also determines how many droplets are formed and from which size on they become stable. The accuracy of different theoretical expressions for the surface energy can be assessed by comparison to MD simulation results.

2 Nucleation Theory

CNT was developed by Volmer and Weber [4] in the 1920s and further extended by many contributions during the following decades [5]. It is founded on the capillarity approximation: droplets emerging during nucleation are assumed to have the same thermodynamic properties as the saturated bulk liquid. In particular, the specific surface energy ε of the emerging nanoscaled droplets is assumed to be the surface tension γ_0 of the planar phase boundary in equilibrium. Laaksonen et al. [6] (LFK) proposed a surface energy coefficient $\kappa(\iota)$ that depends on the number ι of molecules in the droplet, such that $\varepsilon = \kappa(\iota)\gamma_0$ with

$$\kappa(\iota) = 1 + \alpha_1(T)\iota^{-1/3} + \alpha_2(T)\iota^{-2/3} \tag{1}$$

Tanaka et al. [7] found that this expression leads to nucleation rates which agree with their simulation results.

It was shown both theoretically [8,9] and by simulation [10,11] that the surface tension acting in the curved interface of nanoscaled droplets is actually lower than in a planar interface. Figure 1 shows plots of the surface energy coefficient $\kappa(\iota)$ for methane and ethane at different temperatures. At low temperatures, LFK does indeed yield lower specific surface energies for $\iota \to 0$. However, at high temperatures of about 0.9 T_c, LFK assumes that small droplets have a *significantly higher* specific surface energy than the planar interface, cf. Fig. 1.

The Gibbs free energy of droplet formation,

$$\Delta G = A\varepsilon - V\rho_d k_B T \ln S_\mu - G_1 \tag{2}$$

with respect to the Gibbs free energy G_1 of a single-molecule "droplet," is composed of the positive surface contribution as discussed above, where the surface area is given by A, and a negative contribution of the volume V, where ρ_d is the density of the droplet and S_μ is the supersaturation of the vapor in terms of the chemical potential [4,5]. The relation between droplet size ι, surface area A, and volume V is given by assuming that all droplets are exactly spherical and have the same density ρ_d as the saturated bulk liquid.

The number N of small droplets with a Gibbs free energy of formation ΔG in metastable equilibrium with a supersaturated vapor consisting of N_1 molecules is given by [4]

$$N = N_1 \exp(-\Delta G/k_B T) \tag{3}$$

For relatively large droplets, however, the steady state distribution that is established in the initial nucleation stage of a condensation process is dominated by nonequilibrium phenomena. The steady

[1]Corresponding author.

Contributed by the Heat Transfer Division of ASME for publication in the JOURNAL OF HEAT TRANSFER. Manuscript received March 31, 2008; final manuscript received August 5, 2008; published online February 11, 2009. Review conducted by Robert D. Tzou. Paper Presented at the 2008 International Conference on Micro/Nanoscale Heat Transfer (MNHT2008), Tainan, Taiwan, January 6–9, 2008.

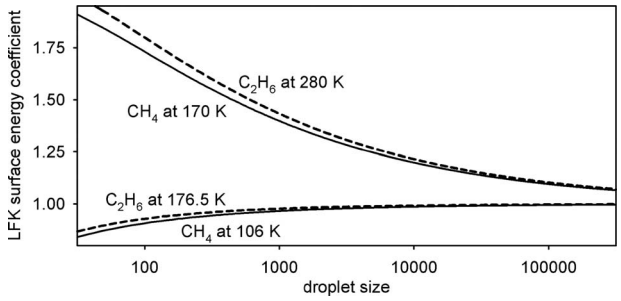

Fig. 1 Dependence of the LFK surface energy coefficient $\kappa(\iota)$ for methane (—) and ethane (- - -) on the droplet size ι

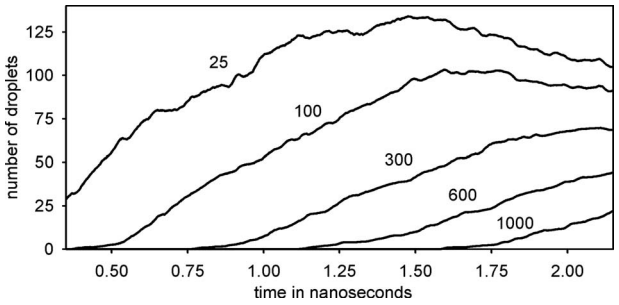

Fig. 2 Number of droplets containing at least 25, 100, …, 1000 molecules over simulation time [17]. Methane was regarded at 130 K and 1.606 mol/l in a volume of (63.7 nm)^3.

state probability $P(\iota)$ for a droplet to contain ι molecules can be related to the corresponding equilibrium probability $P_0(\iota)$ by

$$P(\iota) = \left(1 - J\int_1^{\iota} \frac{d\iota}{B(\iota)P_0(\iota)}\right)P_0(\iota) \tag{4}$$

as determined by Yasuoka and Matsumoto [12]. Therein, $B(\iota)$ is proportional to the frequency of size changes for a droplet containing ι molecules.

The critical droplet size ι^* is the number of molecules in a droplet for which the Gibbs free energy of formation assumes its maximal value ΔG^* [4,13]. The height of this energy barrier is the most influential parameter on the nucleation rate according to CNT [5].

$$J = N_1 \exp(-\Delta G^*/k_B T) A^* p^v \lambda h^{-1} Z\Theta \tag{5}$$

where A^* is the surface area of a critical droplet, p^v is the pressure of the supersaturated vapor, λ is the thermal wavelength, Z is the Zel'dovich factor, and Θ is the nonisothermal factor.

3 Simulation Method

Both the critical droplet size [14,15] and the nucleation rate [7,12,14,16–18] can be determined by molecular simulation. After an initial period of equilibration, the steady state distribution of droplets is established. The equilibrium distribution can then be obtained by Eq. (4), which transforms to

$$P_0(\iota) = \exp\left(J\int_1^{\iota} \frac{d\iota}{B(\iota)P(\iota)}\right)P(\iota) \tag{6}$$

according to Yasuoka and Matsumoto [12]. This translates to values for ΔG, cf. Eq. (3), from which ΔG^* and ι^* can be determined [14]. An approximation for the critical droplet size is also given by the "nucleation theorem" [19]:

$$\iota^* \approx \left(\frac{\partial \ln J}{\partial \ln S_\mu}\right)_T - 1 \tag{7}$$

Both of these methods for calculating ι^* require data on the nucleation rate J, i.e., the number of macroscopic droplets emerging per volume and time in a steady state at constant supersaturation. From an MD simulation of a supersaturated vapor, this rate can straightforwardly be extracted by counting the droplets that exceed a certain threshold size. This method was proposed by Yasuoka and Matsumoto [12] who found that as long as this threshold is significantly higher than the critical droplet size, its precise choice hardly affects the observed value of J.

Alternatively, the nucleation rate can also be estimated by fitting data on the mean first passage time, i.e., the temporal delay required for the first droplet of a given size to appear, to a predefined kinetic model [16].

To adequately evaluate these theories, it is furthermore necessary to determine the supersaturation in terms of the chemical potential:

$$S_\mu = \exp\left(\frac{1}{k_B T}\int_{p_s}^{p^v} \frac{dp}{\rho}\right) \tag{8}$$

based on an integral between the saturated vapor pressure p_s and the supersaturated pressure p^v along the isotherm of the metastable vapor, where ρ is the density of the vapor. That integral can, in principle, be evaluated by extrapolating from the stable to the metastable regime. However, it is both more reliable and more consistent to interpolate between MD results for the density dependence of the supersaturated vapor pressure [20,21]. An extended series of simulations including metastable states was recently carried out by Baidakov et al. [22] for the Lennard–Jones (LJ) fluid.

The present study of methane and ethane is based on MD simulation of supersaturated vapors. Methane was modeled as a simple LJ fluid with the size parameter $\sigma_{LJ}=3.7281$ Å and the energy parameter $\varepsilon_{LJ}/k_B=148.55$ K. For ethane, a rigid two-center LJ fluid model was used; both LJ centers had the parameters $\sigma_{LJ}=3.4896$ Å and $\varepsilon_{LJ}/k_B=136.99$ K with a distance of 2.3762 Å between them and a point quadrupole with a moment $Q=0.8277$ DÅ in the center of mass. These models were presented in previous work [23] and shown to reproduce data on the vapor pressure with an error of 3% or less, while for other key properties of systems with vapor-liquid coexistence, such as the saturated liquid density and the enthalpy of vaporization, the deviations are even lower.

Since simulated inhomogeneous systems are particularly affected by the choice of the cutoff radius [24,25], comparatively large values were specified in the present work: the cutoff radius was at least 1.75 nm for methane and 1.85 nm for ethane. All present MD simulations contained more than 100,000 molecules, which minimizes the influence of finite-size effects [16]. The simulations were conducted in the canonical ensemble, with constant number of molecules, volume, and temperature.

Based on these simulations, the critical droplet size was determined from ΔG maxima as well as the nucleation theorem. The required nucleation rates, published separately [17], were obtained according to the Yasuoka–Matsumoto method [12] with sufficiently large threshold sizes. Additionally, a system below the triple point was simulated to compare a published nucleation rate based on the mean first passage time (MFPT) method [16] with the corresponding result of the Yasuoka–Matsumoto method.

4 Simulation Results

Confirming the applicability of the Yasuoka–Matsumoto approach to the nucleation rate, Fig. 2 shows that larger droplets are formed at lower rates, but these rates are all within one order of magnitude [17]. This difference is negligible compared with the deviations observed for the theoretical predictions. Moreover, the pressure decreases over simulation time as more and larger droplets are formed and the vapor is depleted, which explains the lower rates observed at a later stage of the nucleation process.

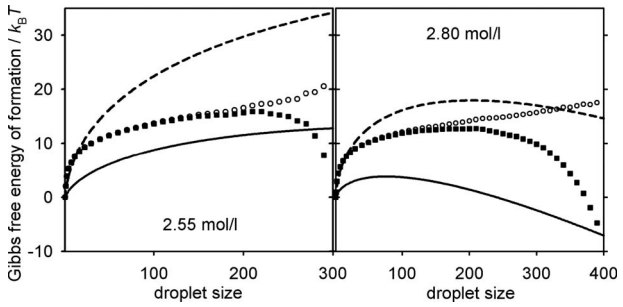

Fig. 3 Dependence of the Gibbs free energy of droplet formation on the droplet size for ethane at 280 K and two different densities, calculated from the metastable equilibrium (■) and the steady state distribution (○) as well as CNT (—) and LFK (- - -)

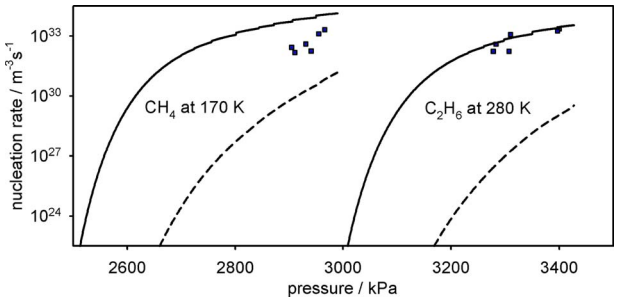

Fig. 5 Nucleation rates of methane and ethane at high temperatures (0.89 and 0.92 T_c) from simulation [17] according to the Yasuoka–Matsumoto method with different threshold sizes (■) as well as CNT (—) and LFK (- - -)

Wedekind et al. [16] simulated supersaturated vapors of the LJ fluid, interpreted, in their case, as a model for argon, and determined nucleation rates according to the MFPT method. Converted to values for methane, the MFPT nucleation rate is 10^{31} m^{-3} s^{-1} at 63.6 K and 0.1391 mol/l. In the present MD simulation with 1.26×10^6 molecules at the same conditions, the rate of formation for droplets exceeding a size of ten molecules was found to be 6×10^{30} m^{-3} s^{-1}. Data on larger droplets were insufficient to determine a nucleation rate. However, J must be even lower than that, because extremely small droplets are formed at higher rates than macroscopic ones [12]. Hence, the MFPT method deviates from the Yasuoka–Matsumoto nucleation rate in this case by at least a factor of two. This confirms results of Römer and Kraska [18] who observed a deviation of a factor of ten between the MFPT and Yasuoka–Matsumoto approach.

Plots of the Gibbs free energy of droplet formation for ethane at 280 K and different supersaturations are shown in Fig. 3. A maximum is clearly visible, if the equilibrium distribution is taken as a basis. For comparison, values estimated directly from the steady state, i.e., by assuming $P(\iota)=P_0(\iota)$ instead of Eq. (6), are indicated as well. These plots do not exhibit a maximum and, as expected, the steady state begins to diverge significantly from the equilibrium distribution only near the critical droplet size. The simulation results also show that both CNT and LFK are qualitatively correct in these cases. However, CNT underestimates ΔG while LFK overestimates it. Moreover, in both cases it is clearly visible that LFK is a good approximation for the smallest droplets that contain 20 or less molecules.

The nucleation rates from MD simulation confirm CNT, deviations are throughout lower than three orders of magnitude. The LFK model provides a better approach to systems at lower temperatures (Fig. 4), whereas near the critical point it leads to considerable deviations (Fig. 5).

Values of the critical droplet size obtained from ΔG maxima and the nucleation theorem are compared in Fig. 6. The results from both approaches deviate from each other roughly by a factor of two and the ΔG maxima agree particularly well with the LFK model.

5 Conclusion

The nucleation rate and the critical droplet size were studied for methane and ethane by MD simulation of supersaturated vapors. Different approaches for evaluating these simulations were compared with each other as well as with CNT and the LFK model.

Deviations in the order of a factor of two were found both for the MFPT approach to the nucleation rate and for the estimate of the critical droplet size based on the nucleation theorem, with respect to the corresponding methods proposed by Yasuoka and Matsumoto [12]. A factor of two is hardly relevant for practical purposes if it is applied to the nucleation rate, but in case of the critical droplet size such a deviation leads to qualitative errors. This is due to the fact that ι^* is roughly proportional to ΔG^*, which carries exponential weight in Eqs. (3) and (5) and similar expressions [4].

A particularly significant deviation was found between the nucleation rate from simulation and the LFK model at high temperatures. This may be due to the surface energy term of the LFK model, which assumes an unphysical increase in the specific surface energy for small droplets at high temperatures; as Tolman [8] showed, the surface tension $(\partial G/\partial A)_{p,T}$ converges to zero for $A\rightarrow0$. In particular, LFK overestimates ΔG^* at high temperatures and high supersaturations (conditions with $50<\iota^*<500$), which leads to the low predictions of J shown in Fig. 5.

However, for the Gibbs free energy of formation of extremely small droplets ($\iota<25$), consisting of a few molecules only, the

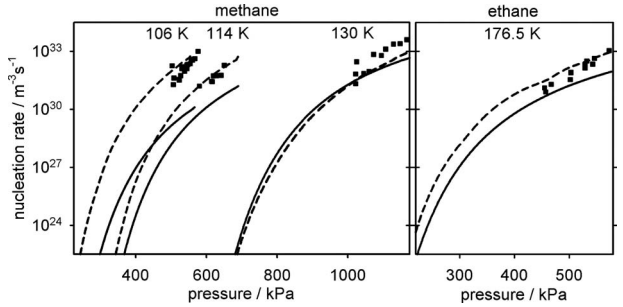

Fig. 4 Nucleation rates of methane and ethane at low temperatures from simulation [17] determined according to the Yasuoka–Matsumoto method with different threshold sizes (■) as well as CNT (—) and LFK (- - -)

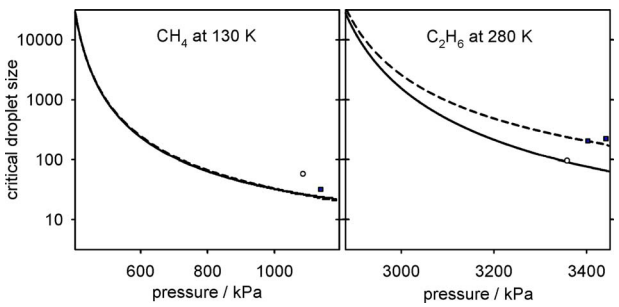

Fig. 6 Critical droplet size for methane and ethane from maxima of the Gibbs free energy of droplet formation (■) and the supersaturation dependence of the nucleation rate (○) as well as CNT (—) and LFK (- - -)

LFK model was found to be a good approximation even at high temperatures, although it assumes an unphysically high specific surface energy under these conditions.

This result can be explained by taking two phenomena into account: (1) All droplets are supposed to be exactly spherical, whereas the average area to volume ratio may actually be significantly increased for nanoscale droplets. Considering this, one obtains a higher surface energy, even for a lower surface tension. (2) According to the capillarity approximation, the chemical potential inside a droplet is assumed to be the saturated bulk chemical potential. On the other hand, the pressure is significantly increased due to the surface tension, which decreases the (negative) volume contribution to ΔG. This effect leads to a larger Gibbs free energy of droplet formation even if no additional surface effects are considered.

Acknowledgment

The authors thank Martin Bernreuther (High Performance Computing Center Stuttgart), Rodrigo Escobar (Pontificia Universidad Católica de Chile), Amador Guzmán (Universidad de Santiago de Chile), Nicolas Schmidt (Universität Stuttgart) and Jonathan Walter (Technische Universität Kaiserslautern), and Andrea Wix (Universität Karlsruhe) for valuable discussions, and Deutsche Forschungsgemeinschaft for funding by SFB 716. The simulations were performed on the HP XC6000 supercomputer at the Steinbuch Centre for Computing, Karlsruhe under the grant MMSTP.

Nomenclature

A = surface area
B = intensity of droplet size fluctuations
G = Gibbs free energy
G_1 = Gibbs free energy of a single-molecule droplet
J = nucleation rate
N = number of droplets
N_1 = number of vapor molecules
P = steady state probability
P_0 = equilibrium probability
Q = quadrupole moment
S_μ = supersaturation (with respect to the chemical potential)
T = temperature
T_c = critical temperature
V = volume
Z = Zel'dovich factor
h = Planck constant
k_B = Boltzmann constant
p = pressure
p_s = saturated vapor pressure
p^v = supersaturated vapor pressure
Θ = nonisothermal factor
α_1 and α_2 = parameters of the LFK model
γ = surface tension
γ_0 = surface tension of the planar phase boundary
ε = specific surface energy (with respect to the surface area)
$\varepsilon_{\mathrm{LJ}}$ = energy parameter of the Lennard–Jones potential
ι = number of molecules in a droplet
κ = LFK surface energy coefficient
λ = thermal wavelength
ρ = density
ρ_d = density of a droplet
σ_{LJ} = size parameter of the Lennard–Jones potential
$*$ = property of a critical droplet

References

[1] Lee, S.-H., Reeves, J. M., Wilson, J. C., Hunton, D. E., Viggiano, A. A., Miller, T. M., Ballenthin, J. O., and Lait, L. R., 2003, "Particle Formation by Ion Nucleation in the Upper Troposphere and Lower Stratosphere," Science, **301**, pp. 1886–1889.
[2] Määttänen, A., Vehkamäki, H., Lauri, A., Merikallio, S., Kauhanen, J., Savijärvi, H., and Kulmala, M., 2005, "Nucleation Studies in the Martian Atmosphere," J. Geophys. Res., **110**, p. E02002.
[3] Curtius, J., 2006, "Nucleation of Atmospheric Aerosol Particles," C. R. Phys., **7**, pp. 1027–1045.
[4] Volmer, M., and Weber, A., 1926, "Keimbildung in übersättigten Gebilden," Z. Phys. Chem. (Leipzig), **119**, pp. 277–301.
[5] Feder, J., Russell, K. C., Lothe, J., and Pound, G. M., 1966, "Homogeneous Nucleation and Growth of Droplets in Vapours," Adv. Phys., **15**(1), pp. 111–178.
[6] Laaksonen, A., Ford, I. J., and Kulmala, M., 1994, "Revised Parametrization of the Dillmann–Meier Theory of Homogeneous Nucleation," Phys. Rev. E, **49**(6), pp. 5517–5524.
[7] Tanaka, K. K., Kawamura, K., Tanaka, H., and Nakazawa, K., 2005, "Tests of the Homogeneous Nucleation Theory With Molecular-Dynamics Simulations," J. Chem. Phys., **122**, p. 184514.
[8] Tolman, R. C., 1949, "The Effect of Droplet Size on Surface Tension," J. Chem. Phys., **17**(3), pp. 333–337.
[9] Kirkwood, J. G., and Buff, F. P., 1949, "The Statistical Mechanical Theory of Surface Tension," J. Chem. Phys., **17**(3), pp. 338–343.
[10] Vrabec, J., Kedia, G. K., Fuchs, G., and Hasse, H., 2006, "Comprehensive Study on Vapour-Liquid Coexistence of the Truncated and Shifted Lennard–Jones Fluid Including Planar and Spherical Interface Properties," Mol. Phys., **104**(9), pp. 1509–1527.
[11] Napari, I., and Laaksonen, A., 2007, "Surface Tension and Scaling of Critical Nuclei in Diatomic and Triatomic Fluids," J. Chem. Phys., **126**, p. 134503.
[12] Yasuoka, K., and Matsumoto, M., 1998, "Molecular Dynamics of Homogeneous Nucleation in the Vapor Phase," J. Chem. Phys., **109**(19), pp. 8451–8470.
[13] Haber, F., 1922, "Über amorphe Niederschläge und krystallisierte Sole," Ber. Dtsch. Chem. Ges. B, **55**, pp. 1717–1733.
[14] Matsubara, H., Koishi, T., Ebisuzaki, T., and Yasuoka, K., 2007, "Extended Study of Molecular Dynamics Simulation of Homogeneous Vapor-Liquid Nucleation of Water," J. Chem. Phys., **127**, p. 214507.
[15] Nellas, R. B., Chen, B., and Siepmann, J. I., 2007, "Dumbbells and Onions in Ternary Nucleation," Phys. Chem. Chem. Phys., **9**, pp. 2779–2781.
[16] Wedekind, J., Reguera, D., and Strey, R., 2006, "Finite-Size Effects in Simulation of Nucleation," J. Chem. Phys., **125**, p. 214505.
[17] Horsch, M., Vrabec, J., Bernreuther, M., Grottel, S., Reina, G., Wix, A., Schaber, K., and Hasse, H., 2008, "Homogeneous Nucleation in Supersaturated Vapors of Methane, Ethane, and Carbon Dioxide Predicted by Brute Force Molecular Dynamics," J. Chem. Phys., **128**, p. 164510.
[18] Römer, F., and Kraska, T., 2007, "Homogeneous Nucleation and Growth in Supersaturated Zinc Vapor Investigated by Molecular Dynamics Simulation," J. Chem. Phys., **127**, p. 234509.
[19] Oxtoby, D. W., and Kashchiev, D., 1994, "A General Relation Between the Nucleation Work and the Size of the Nucleus in Multicomponent Nucleation," J. Chem. Phys., **100**(10), pp. 7665–7671.
[20] Linhart, A., Chen, C., Vrabec, J., and Hasse, H., 2005, "Thermal Properties of the Metastable Supersaturated Vapor of the Lennard–Jones Fluid," J. Chem. Phys., **122**, p. 144506.
[21] Nie, C., Geng, J., and Marlow, W. H., 2008, "Study of Thermal Properties of the Metastable Supersaturated Vapor With the Restricted Ensemble," Physica A, **387**, pp. 1433–1438.
[22] Baidakov, V. G., Protsenko, S. P., and Kozlova, Z. R., 2008, "Thermal and Caloric Equations of State for Stable and Metastable Lennard-Jones Fluids: I. Molecular-dynamics Simulations," Fluid Phase Equilib., **263**, pp. 55–63.
[23] Vrabec, J., Stoll, J., and Hasse, H., 2001, "A Set of Molecular Models for Symmetric Quadrupolar Fluids," J. Phys. Chem. B, **105**(48), pp. 12126–12133.
[24] Trokhymchuk, A., and Alejandre, J., 1999, "Computer Simulations of Liquid/Vapor Interface in Lennard–Jones Fluids: Some Questions and Answers," J. Chem. Phys., **111**(18), pp. 8510–8523.
[25] Shen, V. K., Mountain, R. D., and Errington, J. R., 2007, "Comparative Study of the Effect of Tail Corrections of Surface Tension Determined by Molecular Simulation," J. Phys. Chem. B, **111**(22), pp. 6198–6207.

Heat Transfer Augmentation of Aqueous Suspensions of Nanodiamonds in Turbulent Pipe Flow

Shuichi Torii
Department of Mechanical System Engineering,
Kumamoto University,
2-39-1, Kurokami,
Kumamoto 860-8550, Japan
e-mail: torii@mech.kumamoto-u.ac.jp

Wen-Jei Yang
Department of Mechanical Engineering,
University of Michigan,
Ann Arbor, MI 48109
e-mail: wjyang@engin.umich.edu

This paper aims to study the convective heat transfer behavior of aqueous suspensions of nanodiamond particles flowing through a horizontal tube heated under a constant heat flux condition. Consideration is given to the effects of particle concentration and Reynolds number on heat transfer enhancement. It is found that (i) significant enhancement of heat transfer performance due to suspension of nanodiamond particles in the circular tube flow is observed in comparison with pure water as the working fluid, (ii) the enhancement is intensified with an increase in the Reynolds number and the nanodiamond concentration, and (iii) substantial amplification of heat transfer performance is not attributed purely to the enhancement of thermal conductivity due to suspension of nanodiamond particles. [DOI: 10.1115/1.3072923]

Keywords: nanofluids, nanodiamond, convective heat transfer, Reynolds number, Nusselt number, effective thermal conductivity, viscosity

1 Introduction

Crystalline solids have thermal conductivities higher than fluids by one to three orders of magnitude. By intuition, one expects that thermal conductivities of particle-fluid mixtures are higher than those of pure fluids, as pointed out by Maxwell [1] more than a century ago. The conventional solid-liquid mixtures in which millimeter and/or micrometer-sized particles are added are known as slurries. It is known that slurries settle rapidly, clog flow channels, erode pipelines, and cause severe pressure drop and other undesirable problems. Therefore, fluids with suspended large particles have little practical application in heat transfer enhancement.

Modern technology makes it possible to produce particles <100 nm in diameter for suspending in conventional fluids such as water, engine oil, and ethylene glycol. This new class of fluids is referred to as "nanofluids," whose term is first named and used by Choi [2]. Compared with micron-sized particles, nanoparticles have much larger relative surface areas and a great potential for heat transfer enhancement. Based on this idea, many studies were conducted to explore superior properties of nanofluids, such as large surface-area-to-volume ratio, stable suspension, and no flow passage clogging, which are suitable in heat transfer applications. This is because the much larger surface areas of nanophase powders relative to those of conventional powders not only markedly improve conduction heat transfer capabilities but also increase the stability of suspensions.

Eastman et al. [3] demonstrated that oxide nanoparticles such as Al_2O_3 and CuO have excellent dispersion properties in water, oil, and ethylene glycol and form suspensions. Lee et al. [4] measured thermal conductivity of fluids containing Al_2O_3 and CuO particles so that for the copper oxide/ethylene glycol system, thermal conductivity can be enhanced by more than 20% at 4 vol %. In particular, they disclosed that the thermal conductivity of nanofluids depends on that of both the base fluids and particles. Using the measured thermal conductivity and viscosity data, Wang et al. [5] concluded that the increase in pressure drop is about the same as the increase in heat transfer for both laminar and turbulent flows in a circular tube for all of the fluid-particle mixtures. Most of these studies are on the effective thermal conductivity under macroscopically stationary conditions. There are very few studies on the other aspects related to nanofluids such as phase change behavior (for example, Ref. [6]) and convective heat transfer.

Lee and Choi [7] estimated the performance of microchannel heat exchangers with water, liquid nitrogen, and nanofluids as the working fluid and showed the superiority of a nanofluid-cooled microchannel heat exchanger. Pak and Choi [8] investigated convective heat transfer in the turbulent flow regime using the mixed fluids of water-Al_2O_3 and water-TiO_2. As for the mechanism of heat transfer enhancement of the nanofluid, Xuan and Roetzel [9] found that the effects of transport properties of the nanofluid and thermal dispersion are included. Xuan and Li [10] measured convective heat transfer of water-Cu nanofluids and found substantial heat transfer enhancement. Wen and Ding [11] reported an experimental work on the convective heat transfer of nanofluids made of water and γ-Al_2O_3 nanoparticles in the laminar flow region. They proposed that the enhancement of convective heat transfer is attributed to a nonuniform distribution of thermal conductivity and viscosity field and an attenuation of the thermal boundary layer thickness. The heat transfer behavior of aqueous suspensions of multiwalled carbon nanotubes (CNTs) in the laminar tube flow is experimentally studied by Ding et al. [12]. They proposed that enhancement of the convective heat transfer is ascribed to particle rearrangement, shear induced thermal conduction enhancement, reduction of thermal boundary layer thickness, and the higher aspect ratio of CNTs. A similar heat transfer argumentation in the convective flows is proposed by many researchers. On the contrary, there is no information on heat transfer characteristics of water-diamond nanofluids in the turbulent pipe flow.

The purpose of the present study is to investigate heat transfer characteristics of circular pipe flow including nanodiamond particles. Emphasis is placed on the effect of the suspension with the particles, i.e., the volume fraction of particles and Reynolds number on heat transfer performance in the turbulent flow.

Contributed by the Heat Transfer Division of ASME for publication in the JOURNAL OF HEAT TRANSFER. Manuscript received April 11, 2008; final manuscript received October 2, 2008; published online February 13, 2009. Review conducted by Robert D. Tzou. Paper presented at the 2008 International Conference on Micro/Nanoscale Heat Transfer (MNHT 2008), Tainan, Taiwan, January 6–9 2008.

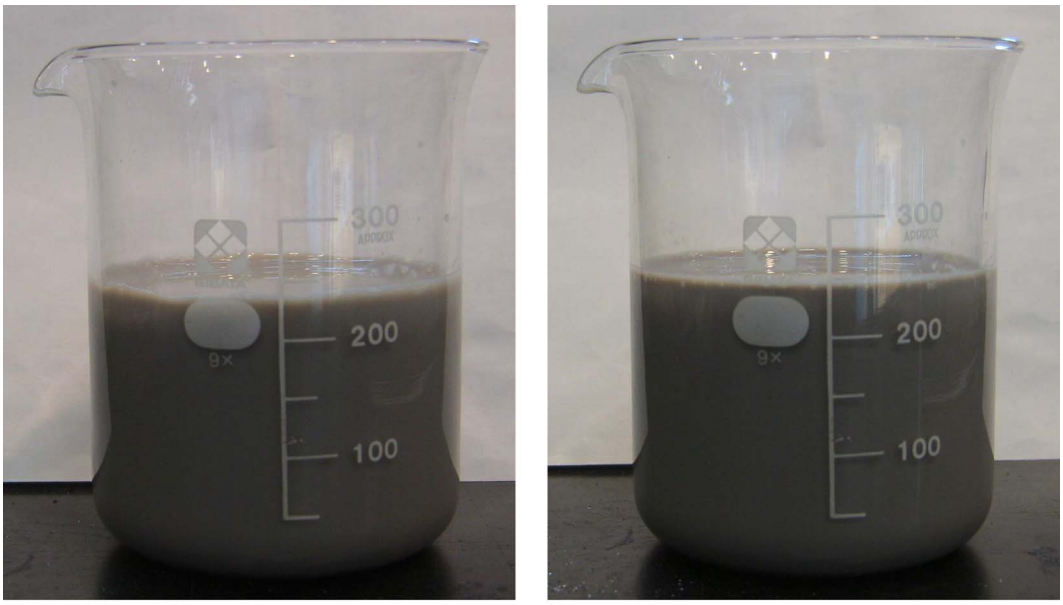

(*a*) (*b*)

Fig. 1 Nanofluids after 60 days (*a*) 0.4% (*b*) 1%

2 Experimental Setup and Measurement Methods

In general, the heat transfer coefficient of the thermal fluid flow including nanofluids is affected by the Reynolds number, thermal properties, and so on. In this work, the viscosity and thermal conductivity of nanodiamond fluids are considered here to study the effect of convective heat transfer. The nanoparticle dimension is ranged from 2 nm to 10 nm. Nanoparticle suspensions are far more stable than suspensions of larger particles [13]. One of the few methods of assessing nanofluid stability is to visually inspect fluid sample over an extended period of time. Figure 1 depicts the picture of 0.4% and 1% nanodiamond fluids after 60 days. The corresponding *p*H for two nanofluids is 6.62 and 6.35, respectively. One observes that no concentration gradient appears in both nanofluids. It implies no long-term degradation in thermal performance due to setting inside the cooling system's reservoir.

2.1 Measurement of Viscosity of Nanodiamond Nanofluids. The viscosity is measured by using the Cannon–Fenske viscometer. The measurements are done on nanofluids of different nanodiamond concentrations, i.e., a reverse tube capillary viscometer. The same measurement method is employed by Yang et al. [14]. At the same time, the relationship between the average particle size and the zeta potential in nanofluids was measured by using ELSZ-2 zeta potential and particle size analyzer (Otsuka Electronics Co., Ltd., Japan). For reference, a transmission electron microscope (TEM) image of the sample is depicted in Fig. 2. The electron micrograph shows that the particles are dispersed in the fluid and some are in the format of agglomerates.

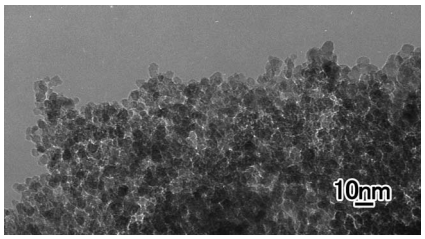

Fig. 2 TEM image of nanodiamond particles

2.2 Experimental Apparatus and Measurement Method of the Convective Heat Transfer Coefficient. The experimental system for measuring the convective heat transfer coefficient is illustrated schematically in Fig. 3. It consists of a flow loop, a power supply unit, a cooling device, and a flow measuring and control unit. The flow loop includes a pump, a digital flowmeter, a reservoir, a collection tank, and a test section. A straight seamless stainless tube with 1000 mm length, 4.0 mm inner diameter, and 4.3 mm outer diameter is used as the test section. The whole test section is heated with the aid of the Joule heating method through an electrode linked to a dc power supply. The power supply is adjustable and its maximum power is about 1000 W. Six K-type thermocouples (0.01 mm in diameter) are mounted on the test section at axial position of 150 mm from the inlet of the test section to measure the wall temperature distribution, and two further K-type thermocouples are inserted into the reservoir and collection tank at the inlet and exit of the test section to measure the bulk temperatures of nanofluid, respectively. The maximum flow

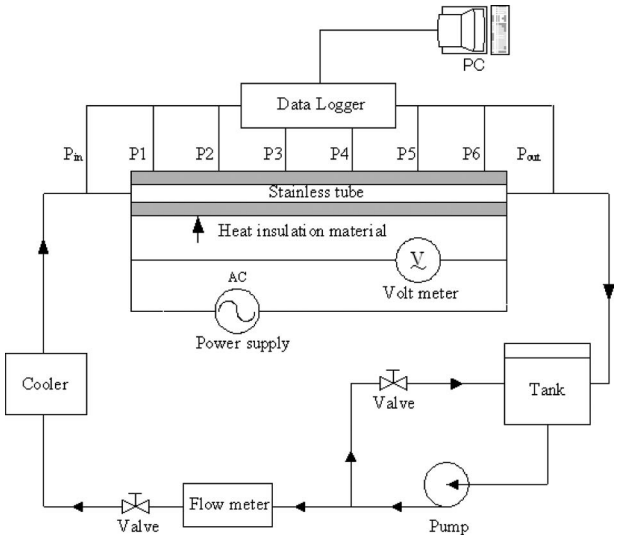

Fig. 3 Experimental apparatus

rate that the pump can deliver is 25 l/min. In the heat transfer experiments, the temperature readings from the eight thermocouples are recorded by a data logger system with a personal computer.

The local heat transfer coefficient h_x is defined as

$$h_x = \frac{q}{(T_{wx} - T_{mx})} \tag{1}$$

where x represents the axial distance from the entrance of the test section, q is the heat flux, T_{wx} is the measured wall temperature, and T_{mx} is the mixed mean temperature, i.e., the fluid temperature estimated by the following energy balance:

$$T_{mx} = T_{mo} + \frac{Q_x}{c_p W} \tag{2}$$

Here, c_p is the heat capacity, T_{mo} is the fluid temperature at the inlet. Also, Q_x and W are the heat rate from the heat wall surface and the average fluid velocity over the cross section, respectively. Note that Eq. (2) takes a heat loss through the insulation layer into account.

The local heat transfer coefficient h_x in Eq. (1) is usually expressed in the form of the Nusselt number Nu_x as

$$\mathrm{Nu}_x = \frac{h_x D}{k} \tag{3}$$

where D is the tube diameter, and k is the fluid thermal conductivity. In general, the Nu number is related to the Reynolds number (Re) and the Prandtl number (Pr). Thus, h_x is arranged in the form of Re versus Nu_x in Sec. 3, because only the nanodiamond nanofluid is employed. Notice that the thermal conductivity of nanofluid is strongly dependent on the nanoparticle volume fraction. Hamilton and Crosser [15] proposed a model for liquid-solid mixtures in which the ratio of conductivity of two phases is larger than 100 as

$$k = k_f \left[\frac{k_s + (n-1)k_f - (n-1)V(k_f - k_s)}{k_s + (n-1)k_f + V(k_f - k_s)} \right] \tag{4}$$

where k_s is the thermal conductivity of the discontinuous particle, k_f is the thermal conductivity of the fluid, V is the volume fraction of particle, and n is the empirical shape factor. V and n are defined by

$$V = \frac{V_s}{V_f + V_s} \tag{5}$$

and

$$n = \frac{3}{\psi} \tag{6}$$

respectively. Here ψ is the sphericity defined as the ratio of the surface area of a sphere with a volume equal to that of the particle to surface area of the particle. $\psi = 1$ is assumed in the present study because the nanoparticles are seen like a sphere, as seen in Fig. 2. In general, if the nanoparticles are dispersed in the pure solution, then there are a few agglomerated nanoparticles. Thus, the relationship between the average particle size and the zeta potential in nanofluid was measured by using ELSZ-2 zeta potential and particle size analyzer (Otsuka Electronics Co., Ltd., Japan). Based on the measured large zeta potential and Fig. 2, the nanoparticles employed here were assumed as spherical particles in the present study. In the preliminary experiment, the thermal conductivity was measured by using a KD2 thermal property meter (Labcell Ltd., UK). The discrepancy between the measured value and the result predicted by a Maxwell/Hamilton–Crosser type model was less 1% up to 1% of the particle volume fraction.

Three volumetric concentrations of nanodiamond fluid—0.1%, 0.4%, and 1%—are tested in the present study. The Reynolds number ranged from 3000 to 6000. An uncertainty analysis [16] yields the following results: the uncertainty in nanofluid flow rate is estimated to be ±1.5%, the uncertainty in the physical properties is less than 1%, and the uncertainty in the temperature measurement is estimated to be ±1.5%. The thermocouples were calibrated in a thermostat water bath and the accuracy was found to be within 0.1 K.

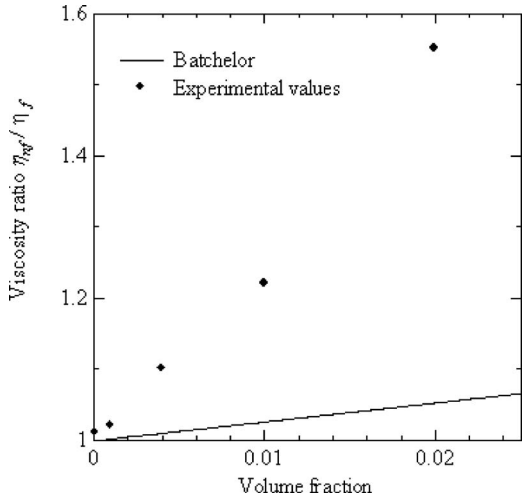

Fig. 4 Experimental and theoretical results of nanofluids viscosity for different volume fractions

3 Results and Discussion

3.1 Viscosity of Nanofluid. The viscosity of nanodiamond fluid was measured under various conditions. Figure 4 shows results for different concentrations. For comparison, the corresponding viscosities for different concentrations are theoretically estimated using the Batchelor model. The viscosity of nanofluids increases with increasing nanodiamond concentration. Such behavior is also observed by Kinloch et al. [17] for highly concentrated aqueous suspensions of multiwalled carbon nanotubes. The results have an important implication to nanodiamond fluids flowing through the tubular geometry used in this work. In other words, the viscosity of nanodiamond fluid is higher than the theoretical value over the wide range of volume fraction. Using the measured value, the Reynolds number is determined in the following. For reference, one observed that larger zeta potential appears in the range of volume fractions measured here, resulting in nanofluids with uniformly dispersed nanoparticles (10 nm in diameter) up to 1% of the particle volume fraction. He et al. [18] measured the viscosity of TiO_2 nanofluids by using a Bohlin CVO rheometer with a Mooney cell (Malvern Instruments, UK). They reported that the shear viscosity increases with increasing particle size. In other words, the effect of particle size on the viscosity increment becomes minor in nanofluids with substantially small particles. Putting these facts together, it is postulated that the discrepancy between the measured values and the viscosity of the suspension with a controlled-shear-rate viscometer becomes minor, because the nanofluid uniformly dispersed with 10 nm diamond particles is employed in the low volume concentration and the particle size is smaller than that used by He et al. [18].

3.2 Convective Heat Transfer Coefficient. Having established confidence in the experimental system, systematic experiments were performed at different flow conditions (Reynolds numbers) and different nanodiamond concentrations.

Figure 5 shows the effect of nanodiamond concentration on the local heat transfer coefficient at various axial distances from the entrance of the test section at Re=6000. Here, the local heat transfer coefficient is divided by that for the thermally and hydrodynamically fully developed region in the pure fluid pipe flow. It is

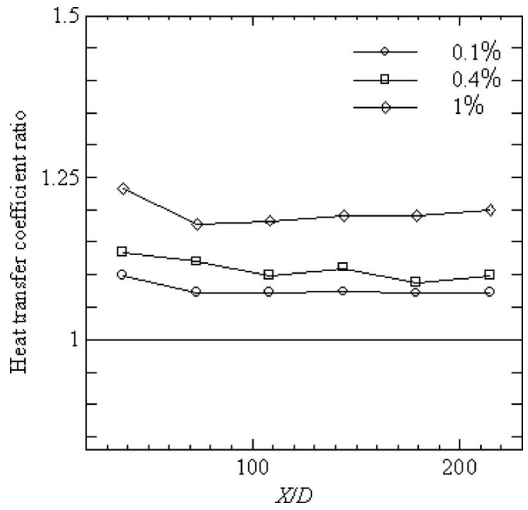

Fig. 5 Streamwise variation of heat transfer coefficient of nanofluids for different volume fractions

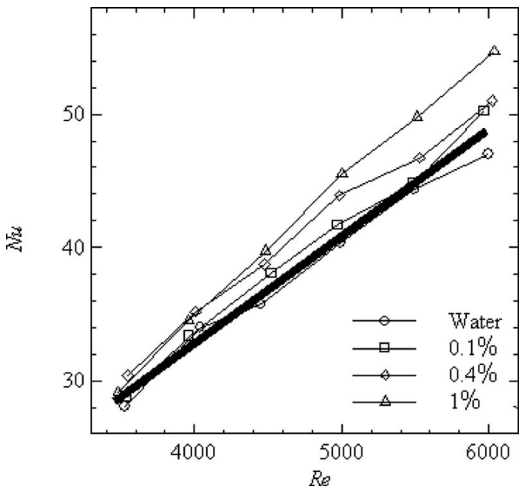

Fig. 7 Effect of nanoparticle concentration on Nusselt number as a function of Reynolds number

observed that (i) the presence of nanodiamond particles increases the convective heat transfer coefficient significantly, and the increase is more considerable at high nanodiamond concentrations; and (ii) at a given nanodiamond concentration, the heat transfer coefficient decreases with axial distance because of the entrance region. A similar trend but with less significant enhancement was obtained at different lower Reynolds numbers (not shown) and was also observed by Xuan and Li [10] in the turbulent flow regime and Wen and Ding [11] at the entrance region in the laminar glow regime. It is observed in Fig. 5 that the local heat transfer coefficient approaches the constant value along the axial direction, that is, the thermally fully developed region appears in the downstream region. In the following section, we study the effects of Reynolds number and nanodiamond concentration on heat transfer performance in the thermally fully developed region, i.e., at $x/D=180$. Notice that a comparison of nanofluid with pure fluid indicates that the enhancement of the local heat transfer coefficient is much more dramatic than that purely due to the enhancement of effective thermal conductivity. For reference, an increase in the thermal conductivity is depicted in Fig. 6 in the form of volume fraction versus dimensionless thermal conductivity with different nanoparticle materials as a parameter. Here, each thermal conductivity is normalized by one of the pure fluid. It is seen that the effective thermal conductivity increase with increasing nanoparticle concentration, and maximum enhancement is about 16% at 5% of the volume fraction.

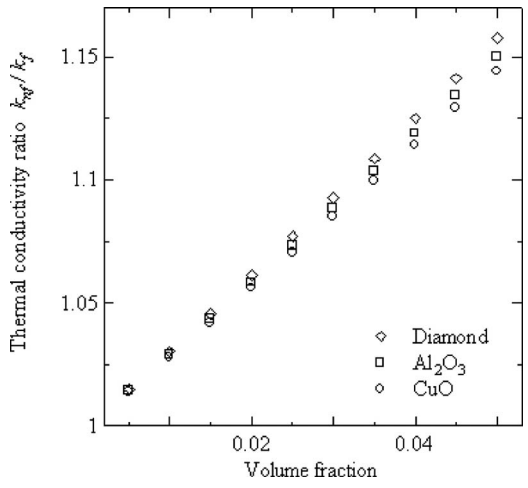

Fig. 6 Comparison of theoretical results of thermal conductivity for different nanoparticle materials

Figure 7 illustrates the effect of the Reynolds number on the heat transfer coefficient at $x/D=180$. The measured values are summarized in Fig. 7 in the form of Re versus Nu with the nanodiamond concentrations as the parameter. For comparison, the following well-known Gnielinski's correlation equation [19] under the constant heat flux boundary condition is superimposed in Fig. 7 as a solid line.

$$\mathrm{Nu} = \frac{(f/8)(\mathrm{Re}-1000)\mathrm{Pr}}{1.07+12.7\sqrt{f/8}(\mathrm{Pr}^{2/3}-1)} \tag{7}$$

Here, f is the friction factor as

$$f = [1.82\log_{10}(\mathrm{Re})-1.64]^{-2} \tag{8}$$

Figure 7 depicts the enhancement of the heat transfer coefficient with reference to pure fluid. It can be seen that the heat transfer enhancement increases with increasing Reynolds number. This trend becomes larger with an increase in the nanodiamond concentration with the Reynolds number fixed.

Next is to investigate the mechanisms of heat transfer enhancement. The heat transfer coefficient h is a macroscopic parameter describing heat transfer when a fluid flows across a solid surface of different temperature. The boundary layer increases with axial distance until fully developed after which the boundary layer thickness and hence the convective heat transfer coefficient is constant. This theory suggests that both an increase in the thermal conductivity k and/or a decrease in the thermal boundary layer thickness cause an amplification of the convective heat transfer coefficient. The maximum enhancement of the thermal conductivity under the conditions of the convective heat transfer experiments in this work does not exceed 16% for 5.0% nanodiamond fluid, as seen in Fig. 6. Meanwhile, Fig. 7 shows that the enhancement of the convective heat transfer coefficient is much greater than that due to the increase in the thermal conductivity, particularly at high nanodiamond concentrations and high Reynolds numbers. One may therefore simply attribute the large enhancement purely to a decrease in the thermal boundary layer thickness. No doubt, the reduction in the thermal boundary layer thickness could be an important factor, but further enhancement on the thermal conduction under dynamic conditions could be another important factor.

4 Summary

Experimental study has been performed to investigate the heat transfer behavior of aqueous suspensions of nanodiamond particles. Experimental and theoretical methods are employed to obtain the effective thermal conductivity, viscosity, and convective heat transfer coefficient. Consideration is given to the effect of particle concentration and Reynolds number on heat transfer enhancement. The effective results are summarized as follows.

(1) Significant enhancement of heat transfer performance due to suspension of nanodiamond particles in the circular tube flow is observed in comparison with pure water as the working fluid.
(2) The enhancement depends on the Reynolds number and the nanodiamond concentration. In other words, the maximum heat transfer enhancement in the thermally and hydrodynamically fully developed flow region takes places with an increase in the Reynolds number and nanodiamond concentration.
(3) Substantial amplification of heat transfer performance is not attributed purely to the enhancement of thermal conductivity due to the suspension of nanodiamond particles.

The above discussion is mostly from the macroscopic point of view. Microscopically, particle migration and rearrangement due to nonuniform shear rate over the pipe cross section could also be a reason for the observed large heat transfer enhancement. Thus further work is needed to disclose mechanisms of heat transfer enhancement.

Acknowledgment

The first author would like to express his thanks for the financial assistance provided through a Grand-in-Aid for Scientific Research (C) (Contract No. 16560153) by the Ministry of Education and Science of Japan for fiscal 2004-2005.

Nomenclature

c_p = specific heat, W/kg K
D = pipe diameter, m
f = friction factor, Eq. (8)
h_x = local heat transfer coefficient, Eq. (1)
k = thermal conductivity, Eq. (4)
k_f = thermal conductivity of the fluid
k_s = thermal conductivity of the discontinuous particle
n = empirical shape factor in Eq. (4)
Nu = Nusselt number, Eq. (7)
Nu_x = local Nusselt number, Eq. (3)
Pr = Prandtl number
Q_x = heating rate, W
q = heat flux, $\mathrm{W/m^2}$
Re = Reynolds number, WD/ν
T_{mo} = inlet fluid temperature
T_{mx} = mixed mean temperature, Eq. (2)
V = volume fraction of particle, %
W = mean velocity of fluid, m/s
x = coordinate, m
α = thermal diffusivity, $\mathrm{m^2/s}$
μ = viscosity, kg/ms
ν = kinematic viscosity, $\mathrm{m^2/s}$
ρ = density, $\mathrm{kg/m^3}$

Subscripts

f = fluid
mx = mean
s = solid or surface
wx = axial

References

[1] Maxwell, J. C., 1881, *A Treatise on Electricity and Magnetism*, Vol. 1, 2nd ed., Clarendon, Oxford, UK, p. 435.
[2] Choi, U. S., 1995, "Enhancing Thermal Conductivity of Fluids With Nanoparticles," *Developments and Applications of Non-Newtonian Fluids*, Vol. 231, D. A. Springer and H. P. Wang, eds., ASME FED, New York, pp. 6–12.
[3] Eastman, J. A., Choi, U. S., Li, S., Thompson, L. J., and Lee, S., 1997, "Enhanced Thermal Conductivity Through the Development of Nano-Fluids," *Proceedings of the Symposium on Nanophase and Nanocomposite Materials II*, Material Research Society, Boston, MA, Vol. 457, pp. 3–11.
[4] Lee, S. P., Choi, U. S., Li, S., and Eastman, J. A., 1999, "Measuring Thermal Conductivity of Fluids Containing Oxide Nanoparticles," ASME J. Heat Transfer, **121**, pp. 280–288.
[5] Wang, X., Xu, X., and Choi, U. S., 1999, "Thermal Conductivity of Nanoparticle-Fluid Mixture," J. Thermophys. Heat Transfer, **13**, pp. 474–480.
[6] Das, S. K., Putra, N., and Roetzel, W., 2003, "Pool Boiling Characteristics of Nanofluids," Int. J. Heat Mass Transfer, **46**, pp. 851–862.
[7] Lee, S. P., and Choi, U. S., 1996, "Application of Metallic Nanoparticle Suspensions in Advanced Cooling Systems," *Recent Advances in Solids/Structures and Application of Metallic Materials*, Vol. 342, Y. Kwon, D. Davis, and H. Chung, eds., ASME, New York, pp. 227–234.
[8] Pak, B. C., and Choi, Y. I., 1998, "Hydrodynamic and Heat Transfer Study of Dispersed Fluids With Submicron Metallic Oxide Particles," Exp. Heat Transfer, **11**, pp. 151–170.
[9] Xuan, Y., and Roetzel, W., 2000, "Conceptions for Heat Transfer Correlation of Nanofluids," Int. J. Heat Mass Transfer, **43**, pp. 3701–3707.
[10] Xuan, Y. M., and Li, Q., 2003, "Investigative Heat Transfer and Flow Features of Nanofluids," ASME J. Heat Transfer, **125**, pp. 151–155.
[11] Wen, D., and Ding, Y., 2004, "Experimental Investigation Into Convective Heat Transfer of Nanofluids at the Entrance Region Under Laminar Flow Conditions," Int. J. Heat Mass Transfer, **47**, pp. 5181–5188.
[12] Ding, Y., Alias, H., Wen, D., and Williams, R. A., 2006, "Heat Transfer of Aqueous Suspensions of Carbon Nanotubes (CNT Nanofluids)," Int. J. Heat Mass Transfer, **49**, pp. 240–250.
[13] Lee, J., and Mudawar, I., 2007, "Assessment of the Effectiveness of Nanofluids for Single-Phase and Two-Phase Heat Transfer in Micro-Channels," Int. J. Heat Mass Transfer, **50**, pp. 452–463.
[14] Yang, Y., Zhang, Z. G., Grulke, E. A., Anderson, W. B., and Wu, G., 2005, "Heat Transfer Properties of Nanoparticle-In-Fluid Dispersions (Nanofluids) in Laminar Flow," Int. J. Heat Mass Transfer, **48**, pp. 1107–1116.
[15] Hamilton, R. L., and Crosser, O. K., 1962, "Thermal Conductivity of Heterogeneous Two-Component Systems," Ind. Eng. Chem. Fundam., **1**, pp. 187–191.
[16] Kline, S. J., and McClintock, F. A., 1953, "Describing Uncertainties in Single-Sample Experiments," Mech. Eng., **75**, pp. 3–8.
[17] Kinloch, I. K., Roberts, S. A., and Windle, A. H., 2002, "A Theological Study of Concentrated Aqueous Nanotube Dispersions," Polymer, **43**, pp. 7483–7491.
[18] He, Y., Jin, Y., Chen, H., Ding, Y., Chang, D., and Lu, H., 2007, "Heat Transfer and Flow Behaviour of Aqueous Suspensions of TiO_2 Nanoparticles (Nanofluids) Flowing Upward Through a Vertical Pipe ," Int. J. Heat Mass Transfer, **50**, pp. 2272–2281.
[19] Kabelac, S., and Kuhnke, J. F., 1977, *Heat Transfer Mechanisms in Nanofluids: Experiment and Theory*, Helmut-Schmidt University of the Federal Armed Forces, Hamburg, Germany, pp. 12–18.

Experimental Study of Flow Critical Heat Flux in Alumina-Water, Zinc-Oxide-Water, and Diamond-Water Nanofluids

Sung Joong Kim

Tom McKrell

Jacopo Buongiorno
e-mail: jacopo@mit.edu

Lin-Wen Hu

Massachusetts Institute of Technology (MIT),
77 Massachusetts Avenue,
Cambridge, MA 02139-4307

It is shown that addition of alumina, zinc-oxide, and diamond particles can enhance the critical heat flux (CHF) limit of water in flow boiling. The particles used here were in the nanometer range (<100 nm) and at low concentration (≤0.1 vol %). The CHF tests were conducted at 0.1 MPa and at three different mass fluxes (1500 kg/m^2 s, 2000 kg/m^2 s, and 2500 kg/m^2 s). The thermal conditions at CHF were subcooled. The maximum CHF enhancement was 53%, 53%, and 38% for alumina, zinc oxide, and diamond, respectively, always obtained at the highest mass flux. A postmortem analysis of the boiling surface reveals that its morphology is altered by deposition of the particles during boiling. Additionally, the wettability of the surface is substantially increased, which seems to correlate well with the observed CHF enhancement.
[DOI: 10.1115/1.3072924]

Keywords: nanofluids, critical heat flux, flow boiling

1 Introduction

Nanofluids are dispersions, or colloidal suspensions, of nanoscale particles in a base liquid. Recent studies of pool boiling heat transfer have shown that highly diluted water-based nanofluids with metal oxide particles have great potential for enhancing the critical heat flux (CHF). For example, experimenting with alumina nanoparticles in water boiling on a copper plate, You et al. [1] observed a 200% enhancement in the CHF. Nanoparticles of various materials (silica, titania, ceria, and alumina) were studied in boiling experiments with heated nickel-chrome wires by Vassallo et al. [2], Milanova et al. [3], and Kim et al. [4], who measured CHF increases up to 60%, 170%, and 200%, respectively. Bang and Chang [5] used a stainless steel plate with boiling water and alumina nanoparticles to show that the CHF can be increased by 50%. In previous experiments with a steel wire at MIT, CHF gains of up to 80% were obtained with alumina, zirconia, and silica nanoparticles in water at concentrations as low as 0.001 vol % [6]. In these experiments it was also observed that nanoparticle deposition on the heater surface occurs upon boiling, thus increasing the surface wettability considerably, which could plausibly explain the large CHF enhancement in nanofluids [6,7]. Similar nanoparticle deposition was observed by other researchers [2–5,8]. Inspired by the notable outcomes of all these pool boiling studies, the applications of nanofluid coolants to nuclear reactors are being investigated at MIT [9]. However, the thermal and hydraulic condition of interest for nuclear reactors, as well as other potential applications of nanofluids, is *flow* boiling, for which the information in the nanofluid literature is very scarce. Preliminary flow CHF data reported in a recent article have shown that alumina nanoparticles can indeed enhance the flow boiling CHF of water [10]. On the other hand, Lee and Mudawar [11] observed premature burnout experimenting with high-concentration nanofluids (1 vol %) in microchannels at laminar conditions. Burnout in their experiments was due to clogging of the microchannels from nanoparticle deposition. No systematic studies of the effect of mass flux, quality, pressure, nanoparticle material, and concentration on the flow boiling and CHF of nanofluids are available in the literature. The present paper reports the results of new nanofluid flow boiling experiments that start to close some of these gaps.

2 Nanofluid Preparation and Characterization

Three nanoparticle materials were used, i.e., alumina, zinc oxide, and diamond. Alumina was selected for its wide use in the nanofluid literature. Zinc oxide was selected because zinc exists in reactor primary coolant through zinc injection. Diamond was selected for its expected colloidal stability in environments with aggressive chemistries and radiation fields. Concentrated water-based dispersions of alumina and zinc-oxide nanoparticles were acquired from Nyacol. The vendor-specified concentration was 20% by weight for alumina and 30% for zinc oxide. A concentrated diamond dispersion (4 wt %) was purchased from Plasma-Chem Gmbh. All dispersions were then diluted with de-ionized water to the concentrations of interest for the CHF experiments, i.e., 0.001%, 0.01%, and 0.1% by volume. No surfactant was added to the nanofluids during dilution. The size of the nanoparticles in the diluted nanofluids was measured with a dynamic light scattering analyzer and was found to be in the 40–50 nm range for alumina and 50–90 nm for zinc oxide. The vendor-specified average size of the diamond nanoparticles is 4 nm. Various properties were also measured including boiling point, surface tension, thermal conductivity, and viscosity and were found to be virtually identical to those of pure water, which was expected for such dilute nanofluids. The values of such properties for the alumina nanofluids are reported in Table 1.

Contributed by the Heat Transfer Division of ASME for publication in the JOURNAL OF HEAT TRANSFER. Manuscript received April 14, 2008; final manuscript received July 31, 2008; published online February 13, 2009. Review conducted by Satish G. Kandlikar. Paper presented at the Micro/Nanoscale Heat Transfer International Conference (MNHT2008).

Table 1 Measured properties for water and alumina nanofluid

	Concentration (vol %)	Boiling point (°C)	Thermal conductivity[a] W/m K	Surface tension[a] (mN/m)	Kinematic viscosity[a] (10^{-7} m^2/s)
Water (measured)	0.0	100.6	0.590	72.50	9.25
	0.001	100.7	0.586	74.78	9.27
Alumina nanofluid	0.01	100.8	0.588	73.44	9.29
(measured)	0.1	100.8	0.578	73.17	9.45
Water (NIST value)	0.0	99.6	0.602	72.43	9.57

[a]Thermal conductivity, viscosity, and surface tension measured by single-needle heat pulse technique (KD2 handheld meter), Cannon-Fenske capillary viscometer, and Wilhemly-Plate method (Sigma 703), respectively. Note that all the measurements were performed at room temperature.

3 Experiment

3.1 Experimental Apparatus. CHF was measured in the nanofluid flow loop shown in Fig. 1, which consists of a heated test-section assembly, a preheater, a cooler, a pump, and an accumulator. The loop is constructed with 25.4 mm o.d. (1 in.) stainless steel tubing. The test section consists of a tube made of stainless steel grade 316 with 6.35 mm (1/4 in.) o.d., 0.41 mm (0.016 in.) thickness, and 100 mm length (Fig. 2). The tube is electrically heated using two identical dc power supplies operating in parallel and connected to the tube ends by copper electrodes. The electric power supplied to the test section is measured with a calibrated voltmeter and inductive ammeter with an uncertainty of $<2\%$. Ten equidistant voltage taps along the tube length are used to confirm that the heat flux in the test section is reasonably uniform (Fig. 3). The heat flux delivered to the fluid in the test section, q'', is calculated as

$$q'' = \frac{VI}{\pi DL} \tag{1}$$

where V and I are the measured voltage and current, respectively, and D and L are the test-section inner diameter and length, respectively. The uncertainty on the calculated value of the heat flux is $<\pm 4\%$. The maximum heat flux achievable in the test section is about 9 MW/m^2. Two submerged K-type thermocouples (TCs) measure the fluid bulk temperatures at the entrance and exit of the test section, respectively. Other TCs are clamped on the outer surface of the test-section tube to measure the wall temperature at various axial locations. The inner wall temperature, T_w, is calculated assuming radial heat conduction within the tube wall. The heat transfer coefficient, h, is then calculated from knowledge of the heat flux, the inner wall temperature, and the bulk temperature T_b at the different axial locations

$$h = \frac{q''}{T_w - T_b} \tag{2}$$

The loop is equipped with a shell-and-tube cooler to reject the heat and control the test-section inlet subcooling. Pressure can be controlled by an accumulator and regulated nitrogen overpressure. However, for the experiments presented here the pressure was always atmospheric. Also, the accumulator is used to purge noncondensable gases at the beginning of each run. The flow rate in the loop is controlled with a centrifugal pump, and measured with a flowmeter of $<\pm 5\%$ uncertainty.

A series of preliminary tests with pure water (no nanoparticles present) was conducted to verify the reliability of the measurements obtained in the loop. The loop operation was first verified by measuring the single-phase convective heat transfer coefficient in the test section and comparing it to the well-known Gnielinski correlation [12]. The agreement between the experiments and the correlation is very reasonable (Fig. 4). The heat losses in the test section were quantified as follows. The percent heat loss (HL) is defined as the normalized difference between the electric power and the fluid thermal power

$$\mathrm{HL}(\%) \equiv \frac{VI - \dot{m}c_p(T_{\mathrm{out}} - T_{\mathrm{in}})}{VI} \times 100 \tag{3}$$

where $\dot{m}$ is the measured mass flow rate, T_{out} and T_{in} are the measured test-section outlet and inlet temperatures, respectively,

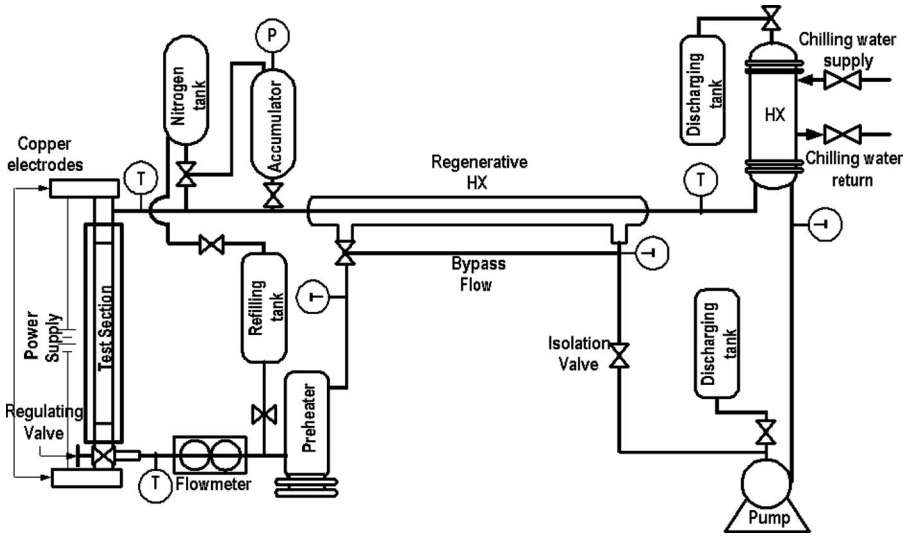

Fig. 1 Schematic of the flow loop

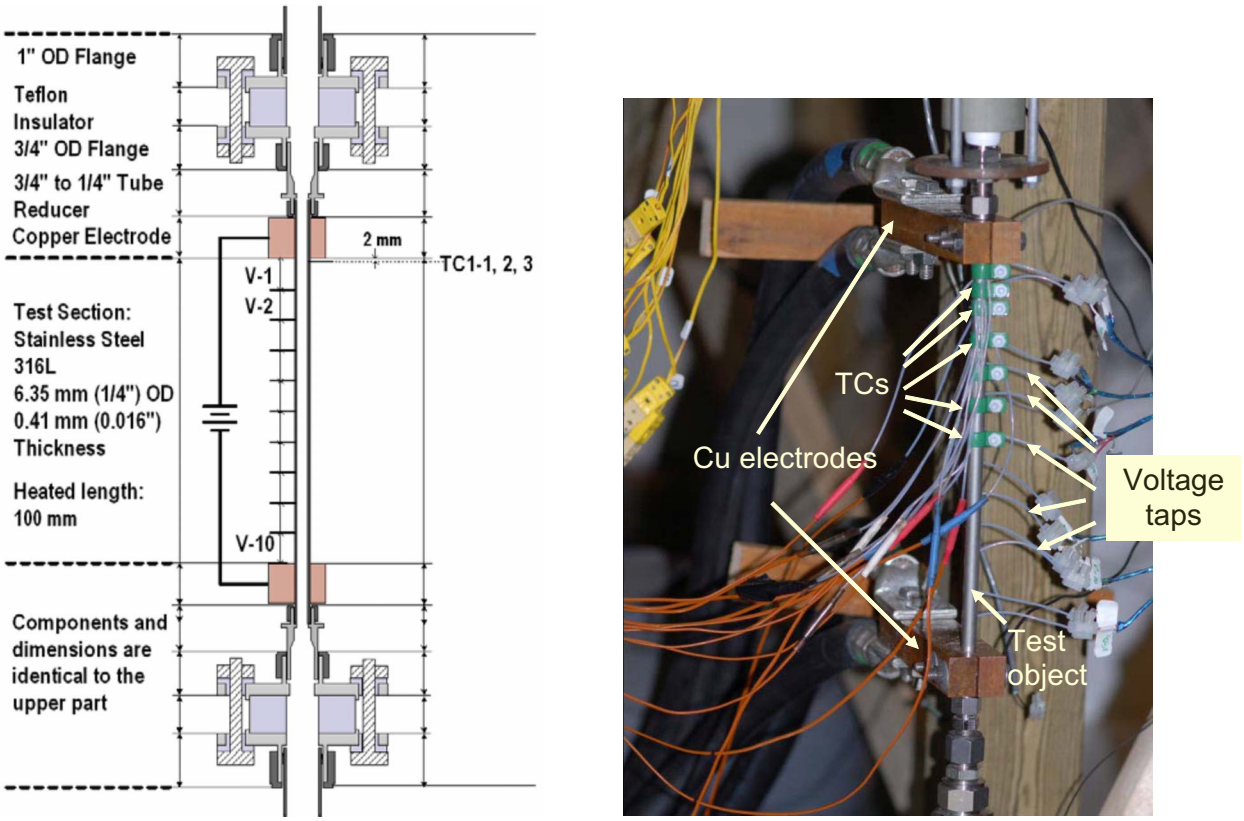

Fig. 2 The test-section schematic (*a*) and photo (*b*)

and c_p is the average specific heat of water between T_{in} and T_{out}. HL is less than 10% at low heat flux ($q'' < 1.0$ MW/m^2) and less than 1% at the high heat fluxes ($q'' > \sim 4$ MW/m^2) of interest to the CHF experiments (Fig. 5).

The experimental procedure for the CHF tests is as follows. After filling the loop with the test fluid, degassing is performed at 80°C for 1 h. Then, the desired flow rate is established and the power is raised in steps lasting a few minutes each until a new steady state is achieved (Fig. 6). The flow rate, test-section current and voltage, pressure, and wall and bulk temperatures are monitored and recorded at each power step. Since the heat flux is axially uniform, CHF occurs at the test-section exit and can be detected from the temperature excursion measured by the TCs near the exit. The control system automatically shuts down the power supply when any wall TC detects a runaway temperature excursion. Therefore, the experiment is arrested within 1–2 s of CHF occurrence. However, the test-section tube typically experiences burnout at the location of CHF (i.e., the exit), so it has to be replaced after every run. Prior to its use the inner surface of every new tube is cleaned with acetone to remove any dust, grease, or other contaminants that could affect CHF.

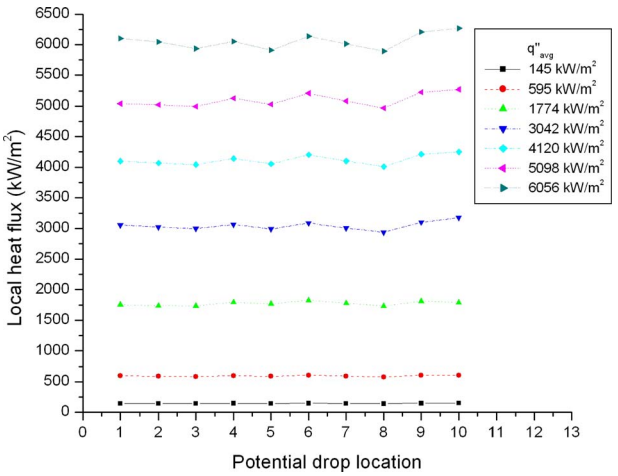

Fig. 3 Axial distribution of the heat flux at different power levels. Location 1 corresponds to the test-section exit and location 10 to the test-section entrance.

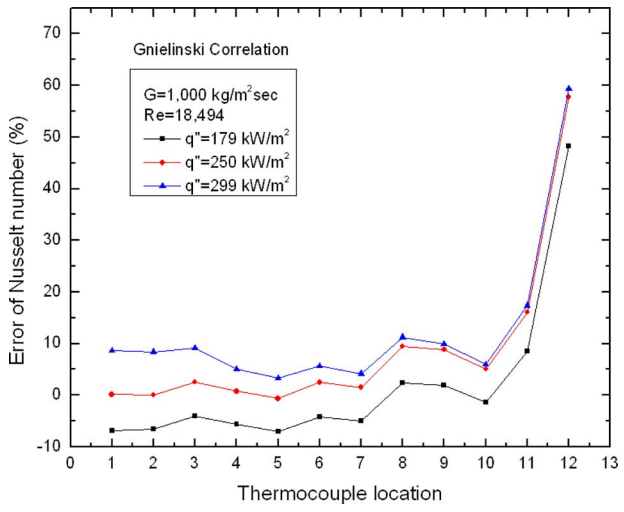

Fig. 4 Percentage difference between measured and predicted local Nusselt number. Location 1 corresponds to the test-section exit. The large discrepancy after the entrance (locations 11–12) is due to the thermal entrance effect, which is not accounted for in the Gnielinski correlation.

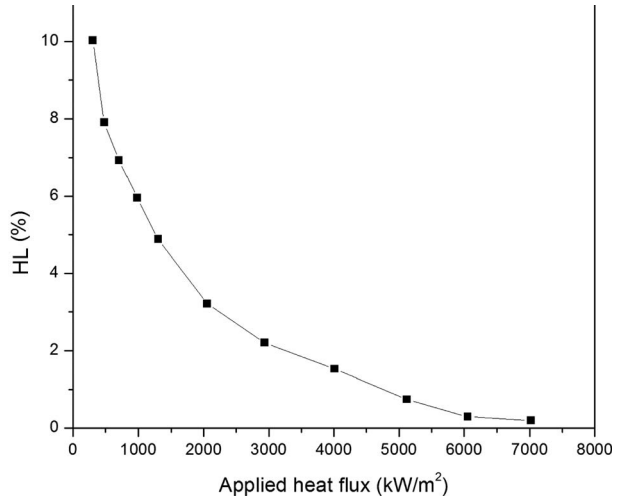

Fig. 5 Heat loss in the test section as a function of the heat flux

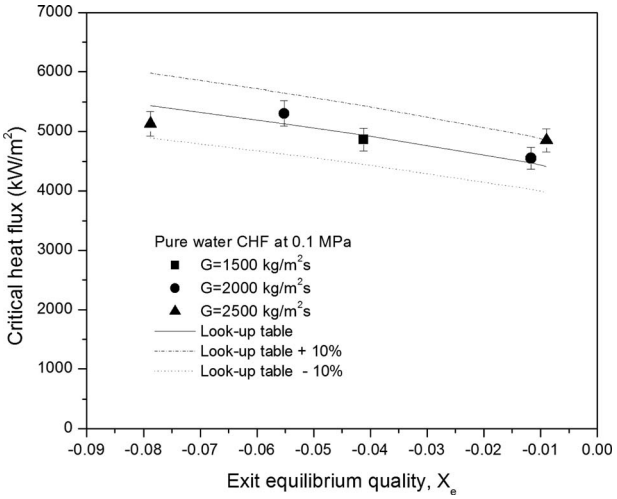

Fig. 7 Measured CHF values for water at atmospheric pressure

3.2 Results. Figure 7 shows the CHF experimental data for de-ionized water at three values of the mass flux (G), and compares them to the predictions of the CHF look-up table [13], which is the most accurate tool for predicting CHF in straight tubes. Our water data agree well with the predictions of the look-up table, within ±10%, which demonstrates that the loop is working properly. The exit equilibrium quality, x_e, is calculated as

$$x_e = \frac{c_p(T_{\text{out}} - T_{\text{sat}})}{h_{fg}} < 0 \tag{4}$$

where $T_{\text{sat}}=100\,^{\circ}\text{C}$ and $h_{\text{fg}}=2257$ kJ/kg are the water saturation temperature and heat of vaporization at atmospheric pressure, respectively.

The alumina nanofluid CHF experimental data are shown in Fig. 8, where the CHF is displayed as a function of the exit equilibrium quality for three values of the nanoparticle concentration and three values of the mass flux. The data for the low mass flux ($G=1500$ kg/m^2 s) fall within the look-up table ±10% "band," thus indicating that no CHF enhancement is present at these conditions. However, the data for the intermediate and high mass fluxes do show a significant enhancement, well above the estimated experimental uncertainty and the look-up table predictions. The enhancement increases with the mass flux and, to a lesser extent, with the nanoparticle concentration. The maximum enhancements for the 0.001 vol %, 0.01 vol %, and 0.1 vol % alumina nanofluids are 33%, 44%, and 53%, respectively, obtained at $G=2500$ kg/m^2 s in all three cases.

The results for the nanofluids with zinc oxide and diamond nanoparticles are shown in Fig. 9. The maximum measured CHF enhancement for zinc-oxide nanofluids is 53%, while for diamond nanofluids is 38%.

4 Data Interpretation

In Sec. 3 it was shown that the CHF of water is enhanced when nanoparticles of various materials are added to it. In this section we discuss some clues concerning the possible reasons for such enhancement. Since the most complete set of data is available for the alumina nanofluid tests, the following discussion will focus on the alumina nanofluids.

A change in CHF can be due to either changes in the thermophysical properties of the fluid or changes in the surface characteristics of the boiling surface. Since the thermophysical properties (thermal conductivity, viscosity, surface tension, etc.) of our nanofluids are almost identical to those of pure water (see Sec. 2), the CHF enhancement must come from a surface effect. The morphology of the heater inner surface, which is exposed to the test

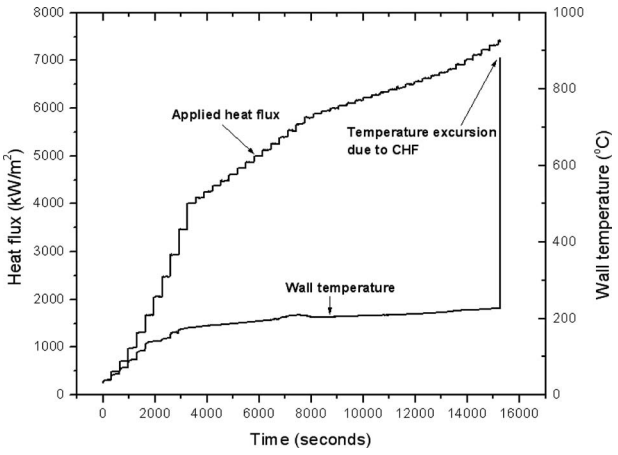

Fig. 6 Wall temperature and heat flux history in a typical CHF run

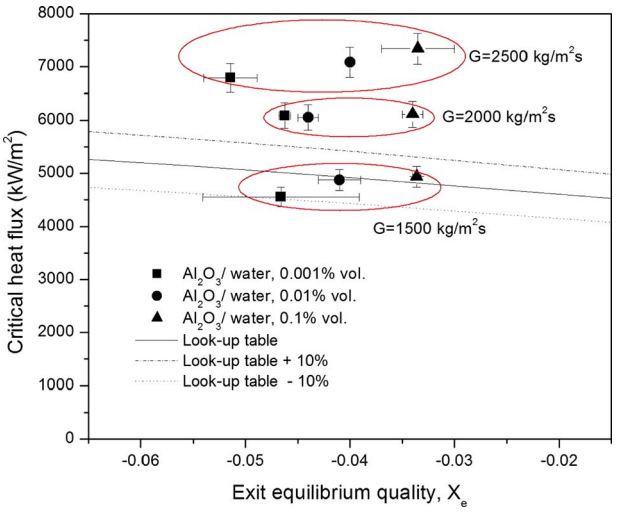

Fig. 8 Measured CHF values for alumina/water nanofluids at atmospheric pressure

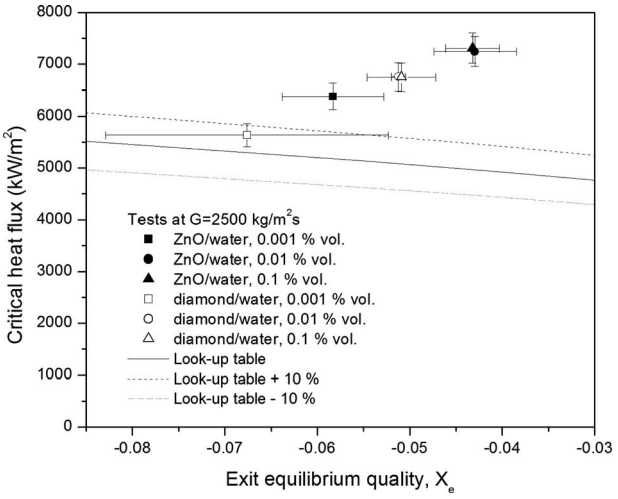

Fig. 9 Measured CHF values for zinc-oxide/water and diamond/water nanofluids at atmospheric pressure

fluid, is expected to change during a nanofluid run because of nanoparticle precipitation during nucleate boiling. This was confirmed by analyzing representative coupons of the test-section heaters, which were prepared by electron discharge machining (EDM) (Fig. 10). The coupons were then examined with a scanning electron microscope (SEM). SEM pictures of an as-purchased tube heater, as well as tube heaters boiled in pure water and 0.001 vol %, 0.01 vol %, and 0.1 vol % alumina nanofluids are shown in Fig. 11.

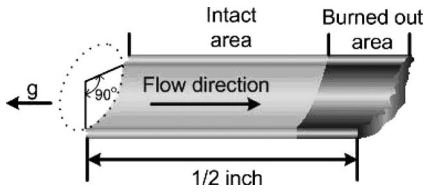

Fig. 10 Schematic of test coupons cut with EDM technique

It can be seen that the surface of the as-purchased heater is clean, and so is the surface after boiling in pure water. On the other hand, a substantial amount of nanoparticles was found to precipitate on the heater surface at all nanoparticle concentrations, forming a layer of aggregates. To confirm that this layer is indeed made of precipitated nanoparticles, energy dispersive X-ray spectroscopy (EDS) was used concurrently with the imaging capabilities of the SEM. The EDS is an instrument integrated with the SEM allowing for the imaging and subsequent elemental analysis of the features imaged. The EDS technique analyzes the X-rays that are emitted due to the interaction of a high energy electron beam and the surface atoms. Each element emits X-rays at discrete energy levels. Therefore, measurement of the X-ray spectrum emitted by the surface enables elemental identification of the surface. Figure 11(*f*) shows the EDS spectrum obtained for a surface boiled in nanofluids. The two large peaks in the spectrum correspond to aluminum and oxygen, supporting that the layer is made of aluminum oxide (alumina).

The two surface parameters that most affect CHF are *surface roughness*, which is related to the number of microcavities available for bubble nucleation, and *contact angle*, which is related to the wettability of the surface. Both parameters can be changed by the presence of the nanoparticles on the surface, as shown in previous papers [6,7]. Therefore it was decided to measure the surface roughness and contact angle for the test-section coupons. This was done by confocal microscopy at multiple locations on each coupon. The confocal microscope scans a laser beam over the sample's surface, creating a high resolution quantitative three-dimensional image of the surface. The results of this surface analysis are shown in Table 2 for some representative tests. Table 2 also shows the surface data for the as-purchased test section for comparison. It can be seen that the average surface roughness, R_a, is about 2 μm for all cases (as-purchased, water-boiled, and nanofluid-boiled coupons). No trend is evident, therefore, it must

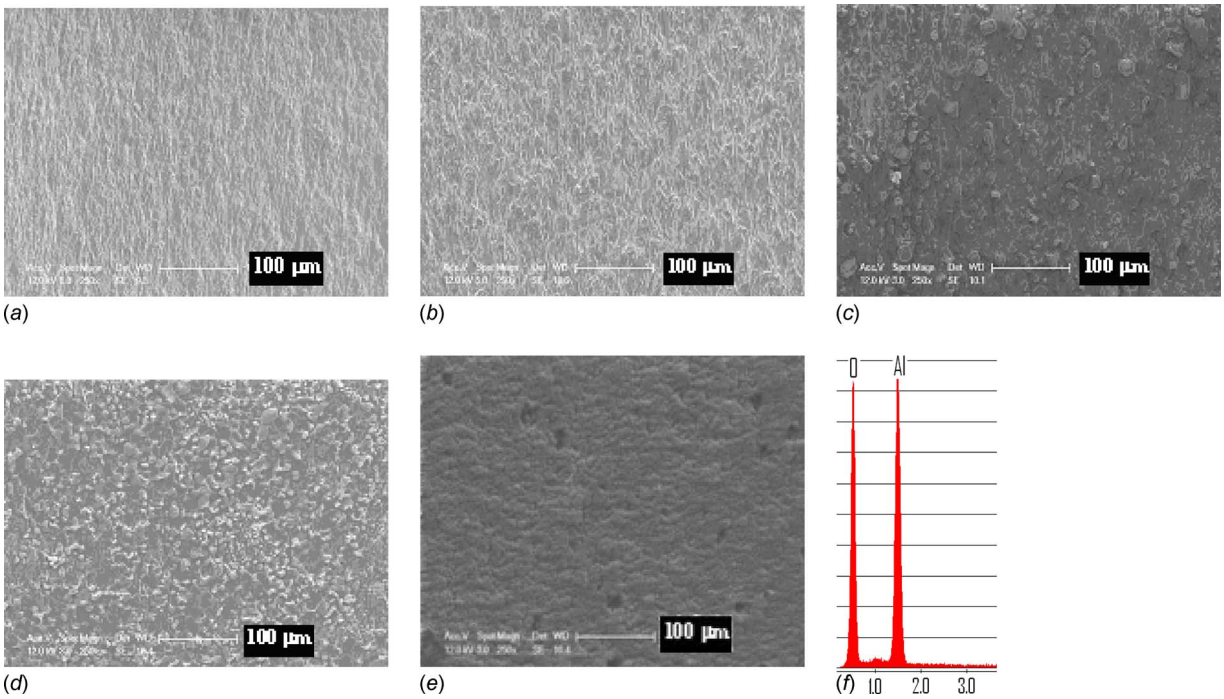

Fig. 11 SEM pictures of stainless steel test heaters (*a*) as-received, and after being boiled in (*b*) pure water, (*c*) 0.001 vol % Al_2O_3, (*d*) 0.01 vol % Al_2O_3, and (*e*) 0.1 vol % Al_2O_3. (*f*) EDS clearly shows the presence of alumina on a surface boiled in alumina nanofluid.

Table 2 Surface roughness and contact angle data for steel coupons cut from the loop test section after the CHF tests

Test-section surface condition	Roughness[a] R_a (μm)	Contact angle[b] (deg)
As-purchased	1.82	79
Used in water CHF test (G=2500 kg/m^2 s)	2.15	83
Used in 0.001 vol % Al_2O_3 nanofluid CHF test (G=2500 kg/m^2 s)	2.28	23
Used in 0.01 vol % Al_2O_3 nanofluid CHF test (G=2500 kg/m^2 s)	1.86	31
Used in 0.1 vol % Al_2O_3 nanofluid CHF test (G=2500 kg/m^2 s)	1.72	20

[a]Surface roughness was measured with confocal microscopy (measurement uncertainty ~0.01 μm).
[b]Contact angle values were measured using the water sessile droplet method (measurement uncertainty ±10 deg).

be concluded that the CHF enhancement does not come from a surface roughness change.

The contact angle data are much more interesting. The as-purchased coupon and the coupon boiled in water have contact angles of around 80 deg, while the coupons boiled in the alumina nanofluids all have a significantly lower contact angle, ~20–30 deg. These contact angles are the same whether deionized water or the alumina nanofluids are used in the measurement. Representative photos of the contact angles are shown in Fig. 12.

This increase in surface wettability can play an important role in enhancing the CHF. The nexus between contact angle and CHF is well known in *pool boiling*; for example, according to Kandlikar's model for a vertical heater [14]

$$q''_{\mathrm{CHF}} \propto (1 + \cos\beta) \tag{5}$$

where β is the contact angle. If the contact angle changes from about 80 deg to, say, 30 deg, Eq. (5) predicts a CHF enhancement of 60%, which is larger than but of the same order of magnitude as the CHF enhancement observed in our experiments. Models that relate contact angle to CHF in *flow boiling* are much less common. One that has been validated against a vast database (however, not with respect to its ability to predict the CHF dependence on contact angle) is that of Celata et al. [15]. This model hypothesizes that CHF corresponds to dry out of a liquid sublayer underneath a vapor clot that slides on the heated wall. The model is summarized by the following set of equations [15]

$$q''_{\mathrm{CHF}} = \frac{\rho_l \delta h_{\mathrm{fg}}}{L_B} U_B \tag{6}$$

$$\delta = y^* - D_B \tag{7}$$

$$D_B = \frac{32}{f}\frac{\sigma g(\beta)\rho_l}{G^2} \tag{8}$$

$$\frac{1}{\sqrt{f}} = 1.14 - 2.0\log\left(\frac{\varepsilon}{D} + \frac{9.35}{\mathrm{Re}\sqrt{f}}\right) \tag{9}$$

where ρ_l, h_{fg}, and σ are the liquid density, vaporization heat, and surface tension, respectively; U_B, L_B, and D_B are the vapor clot velocity, length, and diameter, respectively; δ and y^* are the thickness of the liquid sublayer and superheated layer, respectively; f is the friction factor, $g(\beta)$ is a function of the contact angle, ε is the surface roughness ($\sim R_a$), and D is the channel diameter. When the model of Celata et al. is applied to the flow conditions of our loop, and the contact angle is again changed from 80 deg to 30

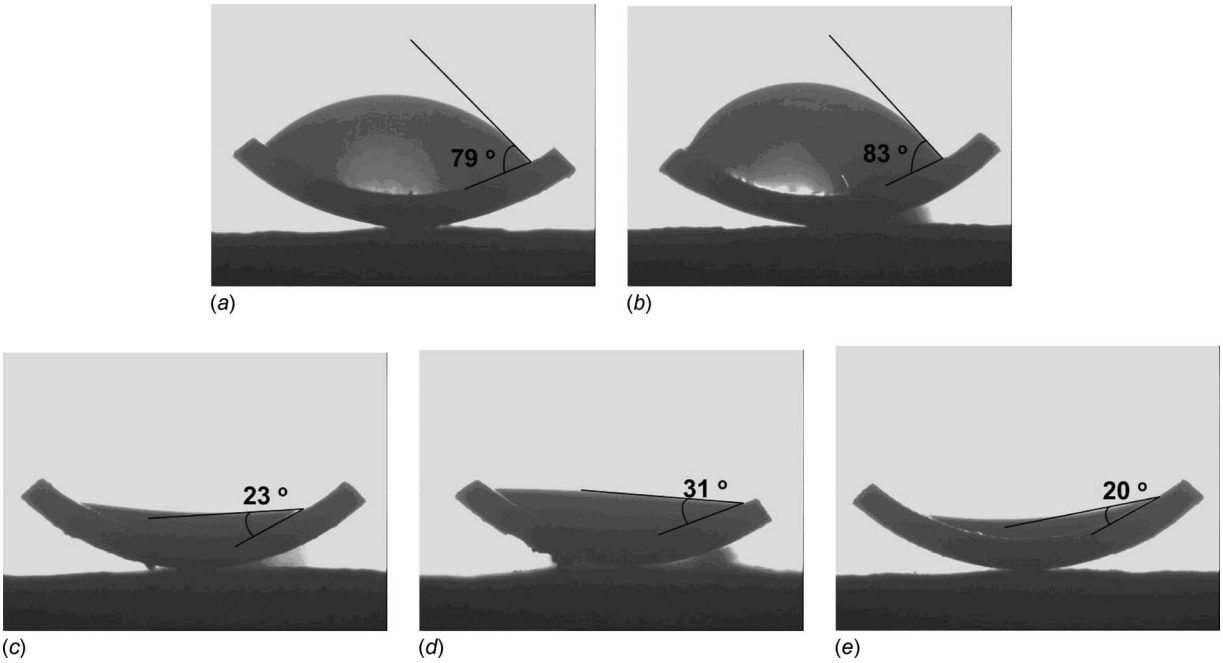

Fig. 12 Contact angle of water sessile droplets for test section (*a*) as-purchased, (*b*) boiled in water (at G =2500 kg/m^2 s), (c) boiled in 0.001 vol % alumina nanofluid (G=2500 kg/m^2 s), (*d*) boiled in 0.01 vol % alumina nanofluid (G=2500 kg/m^2 s), and (*e*) boiled in 0.1 vol % alumina nanofluid (G=2500 kg/m^2 s)

deg, Eqs. (6)–(9) (and the accompanying models in Ref. [12]) predict a CHF enhancement of about 50%, which is close to our experimentally observed CHF enhancement.

5 Conclusions

An experimental study of flow boiling CHF in water-based nanofluids with alumina, zinc-oxide, and diamond nanoparticles was presented. The main findings were as follows.

- The nanofluids exhibited a significant CHF enhancement (up to 40–50%) with respect to pure water at high mass flux (2000–2500 kg/m^2 s).
- The enhancement did not occur at lower mass flux (1500 kg/m^2 s).
- The enhancement appeared to be weakly dependent on nanoparticle concentration for the alumina nanofluids, while it increased more pronouncedly with nanoparticle concentration for the zinc-oxide and diamond nanofluids.
- Some nanoparticles were deposited on the boiling surface during the experiments. It was shown that such particle deposition increased the wettability of the boiling surface. Models exist that support the observed trend between reduced wettability and increased CHF.

Future research directions should focus on a definitive explanation of the CHF enhancement mechanism in flow boiling. Also, the possibility of precoating the boiling surface with nanoparticles as a CHF enhancement technique should be investigated.

Acknowledgment

The authors are grateful to AREVA (PO 1007021110), the DOE Nuclear Engineering Education Research Program (DE-FG07-07ID14765), and the DOE Innovation in Nuclear Infrastructure and Education Program (DE-FG07-02ID14420) for their sponsorship of this work. The Korea Science and Engineering Foundation is acknowledged for Mr. Kim's doctoral fellowship. Dr. T.S. Ramakrishnan of Schlumberger Ltd. is acknowledged for granting the use of their Olympus LEXT confocal microscope.

Nomenclature

c_p = specific heat, J/kg K
D = inner diameter, m
D_B = vapor clot diameter, m
f = friction factor
G = mass flux, kg/m^2 s
$g(\beta)$ = contact angle function
h = heat transfer coefficient, W/m^2 K
h_{fg} = heat of vaporization, J/kg
I = current, A
L = length, m
L_B = vapor clot length, m
$\dot{m}$ = mass flow rate, kg/s
o.d. = outer diameter, m
q'' = heat flux, W/m^2
R_a = average surface roughness, μm
T = temperature, °C
U_B = vapor clot velocity, m/s
V = voltage, V
vol = volume, m^3
wt = weight, kg
x_e = exit equilibrium quality
y^* = thickness of the superheated layer, m

Subscripts

b = bulk
CHF = critical heat flux
in = test-section inlet
out = test-section outlet
sat = saturation
w = wall

Greek Letters

β = contact angle, deg
δ = thickness of the liquid sublayer, m
ε = surface roughness, μm
ρ_l = liquid density, kg/m^3
σ = surface tension, N/m

References

[1] You, S. M., Kim, J., and Kim, K. H., 2003, "Effect of Nanoparticles on Critical Heat Flux of Water in Pool Boiling Heat Transfer," Appl. Phys. Lett., **83**(16), pp. 3374–3376.
[2] Vassallo, P., Kumar, R., and D'Amico, S., 2004, "Pool Boiling Heat Transfer Experiments in Silica-Water Nano-Fluids," Int. J. Heat Mass Transfer, **47**, pp. 407–411.
[3] Milanova, D., Kumar, R., Kuchibhatla, S., and Seal, S., 2006, "Heat Transfer Behavior of Oxide Nanoparticles in Pool Boiling Experiment," *Proceedings of the Fourth International Conference on Nanochannels, Microchannels and Minichannels*, Limerick, Ireland, Jun. 19–21.
[4] Kim, H., Kim, J., and Kim, M., 2006, "Experimental Study on CHF Characteristics of Water-TiO_2 Nano-Fluids ," Nuclear Engineering and Technology, An International Journal of the Korean Nuclear Society, **38**(1), pp. 61–68.
[5] Bang, I. C., and Chang, S. H., 2005, "Boiling Heat Transfer Performance and Phenomena of Al_2O_3 -Water Nano-Fluids From a Plain Surface in a Pool," Int. J. Heat Mass Transfer, **48**, pp. 2407–2419.
[6] Kim, S. J., Bang, I. C., Buongiorno, J., and Hu, L. W., 2007, "Surface Wettability Change During Pool Boiling of Nanofluids and Its Effect on Critical Heat Flux," Int. J. Heat Mass Transfer, **50**, pp. 4105–4116.
[7] Kim, S. J., Bang, I. C., Buongiorno, J., and Hu, L. W., 2006, "Effects of Nanoparticle Deposition on Surface Wettability Influencing Boiling Heat Transfer in Nanofluids," Appl. Phys. Lett., **89**, p. 153107.
[8] Jackson, J. E., Borgmeyer, B. V., Wilson, C. A., Cheng, P., and Bryan, J. E., 2006, "Characteristics of Nucleate Boiling With Gold Nanoparticles in Water," *Proceedings of IMECE 2006*, Chicago, IL, Nov. 5–10.
[9] Buongiorno, J., Hu, L. W., Kim, S. J., Hannink, R., Truong, B., and Forrest, E., 2008, "Nanofluids for Enhanced Economics and Safety of Nuclear Reactors: An Evaluation of the Potential Features, Issues and Research Gaps," Nucl. Technol., **162**, pp. 80–91.
[10] Kim, S. J., McKrell, T., Buongiorno, J., and Hu, L. W., 2008, "Alumina Nanoparticles Enhance the Flow Critical Heat Flux of Water at Low Pressure," ASME J. Heat Transfer, **130**, p. 044501.
[11] Lee, J., and Mudawar, I., 2007, "Assessment of the Effectiveness of Nanofluids for Single-Phase and Two-Phase Heat Transfer in Micro-Channels," Int. J. Heat Mass Transfer, **50**, pp. 452–463.
[12] Gnielinski, V., 1976, "New Equations for Heat and Mass Transfer in Turbulent Pipe and Channel Flow," Int. Chem. Eng., **16**, pp. 359–368.
[13] Groeneveld, D. C., Leung, L. K. H., Kirillov, P. L., Bobkov, V. P., Smogalev, I. P., Vinogradov, V. N., Huang, X. C., and Royer, E., 1996, "The 1995 Look-Up Table for Critical Heat Flux in Tubes," Nucl. Eng. Des., **163**, pp. 1–23.
[14] Kandlikar, S. G., 2001, "A Theoretical Model to Predict Pool Boiling CHF Incorporating Effects of Contact Angle and Orientation," ASME J. Heat Transfer, **123**, pp. 1071–1079.
[15] Celata, G. P., Cumo, M., and Mariani, A., 1994, "Rationalization of Existing Mechanistic Models for the Prediction of Water Subcooled Flow Boiling Critical Heat Flux," Int. J. Heat Mass Transfer, **37**, pp. 347–360.

Effect of CuO Nanoparticle Concentration on R134a/ Lubricant Pool-Boiling Heat Transfer

M. A. Kedzierski
National Institute of Standards and Technology,
Building 226, Room B114,
Gaithersburg, MD 20899

This paper quantifies the influence of copper (II) oxide (CuO) nanoparticle concentration on the boiling performance of R134a/polyolester mixtures on a roughened horizontal flat surface. Nanofluids are liquids that contain dispersed nanosize particles. Two lubricant-based nanofluids (nanolubricants) were made with a synthetic polyolester and 30 nm diameter CuO particles to 1% and 0.5% volume fractions, respectively. As reported in a previous study for the 1% volume fraction nanolubricant, a 0.5% nanolubricant mass fraction with R134a resulted in a heat transfer enhancement relative to the heat transfer of pure R134a/polyolester (99.5/0.5) between 50% and 275%. The same study had shown that increasing the mass fraction of the 1% volume fraction nanolubricant resulted in smaller, but significant, boiling heat transfer enhancements. The present study shows that the use of a nanolubricant with half the concentration of CuO nanoparticles (0.5% by volume) resulted in either no improvement or boiling heat transfer degradations with respect to the R134a/polyolester mixtures without nanoparticles. Consequently, significant refrigerant/lubricant boiling heat transfer enhancements are possible with nanoparticles; however, the nanoparticle concentration is an important determining factor. Further research with nanolubricants and refrigerants is required to establish a fundamental understanding of the mechanisms that control nanofluid heat transfer.
[DOI: 10.1115/1.3072926]

Keywords: additives, boiling, copper (II) oxide, enhanced heat transfer, nanotechnology, refrigerants, refrigerant/lubricant mixtures

1 Introduction

In recent years, the U.S. National Nanotechnology Initiative (NNI) has, in large part, driven the deluge of heat transfer property investigations of liquids with dispersed nanosize particles called nanofluids. Much of the justification for nanofluid heat transfer research rests on the potential improvement in the thermal conductivity of the fluids due to nanoparticles. For example, Eastman et al. [1] found that more than a 40% increase in the thermal conductivity of a liquid could be achieved by adding nanoparticles to a volume fraction of approximately 0.4%. Most nanofluid boiling heat transfer studies have been conducted with water-based nanofluids [2–4]. Although You et al. [4] and Bang and Chang [2] did not observe a pool-boiling enhancement with water-based nanofluids, Wen and Ding [3] did.

Kedzierski and Gong [5] also obtained a boiling heat transfer enhancement with nanofluids for refrigerant/lubricant mixtures by using a lubricant-based nanofluid (nanolubricant). The study obtained between 50% and 275% improvement in the boiling heat transfer with a nanolubricant where 1% of the volume was occupied by 30 nm diameter CuO nanoparticles. Not much is presently known about how the material of the particles, their shape, size, distribution, and concentration affect refrigerant/lubricant boiling performance. Consequently, this study is a first step toward the understanding of how one of the aforementioned parameters influence heat transfer: nanoparticle concentration.

In order to investigate the influence of nanoparticle concentration on refrigerant/lubricant pool boiling, the boiling heat transfer of three R134a/nanolubricant mixtures on a roughened, horizontal flat (plain), copper surface was measured. A commercial polyolester lubricant (RL68H)[1] with a measured kinematic viscosity of 65.5 $\mu m^2/s \pm 0.5$ $\mu m^2/s$ at 313.15 K was the base lubricant that was mixed with nominally 30 nm diameter copper (II) oxide (CuO) nanoparticles. Copper (II) oxide (79.55 g/mol) has many commercial applications including its use as an optical glass-polishing agent. A manufacturer used a proprietary surfactant at a mass between 5% and 15% of the mass of the CuO as a dispersant for the RL68H/CuO mixture (nanolubricant). The manufacturer made the mixture such that 10% of the volume was CuO particles. The mixture was diluted at NIST to a 0.5% volume fraction of CuO by adding neat RL68H and ultrasonically mixing the solution for approximately 24 h. The particle size and dispersion were verified by a light scattering technique and were found to be 37 nm $\pm$ 1 nm and well dispersed with little particle agglomeration [6]. The RL68H/CuO (99.5/0.5)[2] volume fraction mixture, also known as RL68H2Cu, was mixed with pure R134a to obtain three R134a/RL68H2Cu mixtures at nominally 0.5%, 1%, and 2% mass fractions for the boiling tests. The present measurements were compared with measurements from Ref. [5][3] that were obtained with an identical experimental method with the exception that the volume fraction of the nanolubricant was 1% (R134a/

Contributed by the Heat Transfer Division of ASME for publication in the JOURNAL OF HEAT TRANSFER. Manuscript received April 16, 2008; final manuscript received August 8, 2008; published online February 13, 2009. Review conducted by Robert D. Tzou. Paper presented at the 2008 International Conference on Micro/Nanoscale Heat Transfer (MNHT2008), Tainan, Taiwan, January 6–9, 2008.

[1]Certain commercial equipment, instruments, or materials are identified in this paper in order to specify the experimental procedure adequately. Such identification is not intended to imply recommendation or endorsement by the National Institute of Standards and Technology, nor is it intended ti imply that the materials or equipment identified are necessarily the best available for the purpose.

[2]The equivalent mixture is RL68H/CuO (97.1/2.9) in terms of mass.

[3]The error in the volume fraction in Ref. [5] has been corrected in this manuscript.

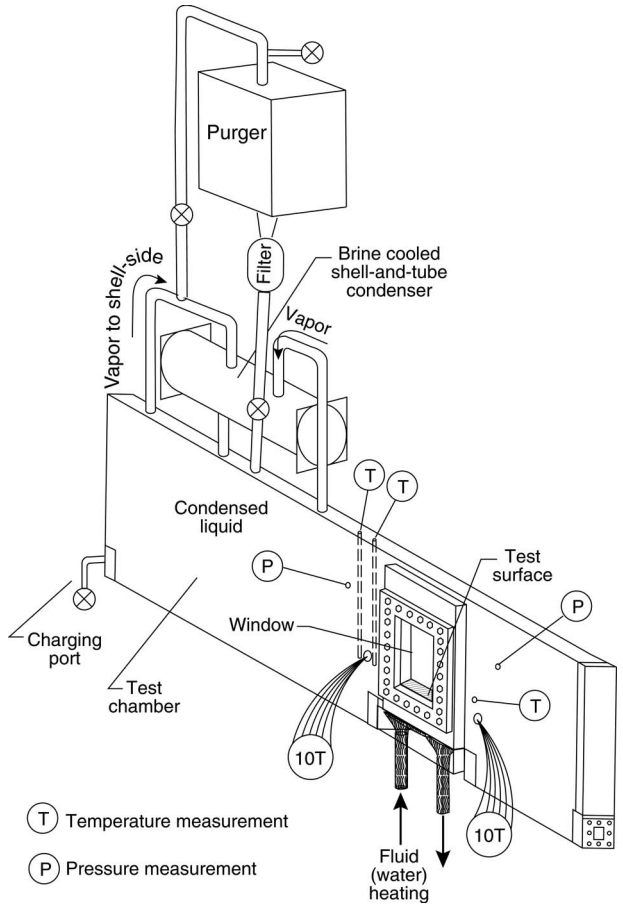

Fig. 1 Schematic of test apparatus

RL68H1Cu) rather than 0.5%.[4] In addition, the boiling heat transfer of three R134a/RL68H mixtures (0.5%, 1%, and 2% mass fractions), without nanoparticles, was obtained from the previous study to serve as a baseline for comparison.

2 Apparatus

Figure 1 shows a schematic of the apparatus that was used to measure the pool-boiling data of this study. More specifically, the apparatus was used to measure the liquid saturation temperature (T_s), the average pool-boiling heat flux (q''), and the wall temperature (T_w) of the test surface. The three principal components of the apparatus were the test chamber, the condenser, and the purger. The internal dimensions of the test chamber were 25.4 mm $\times$257 mm$\times$1.54 m. The test chamber was charged with approximately 7 kg of refrigerant, giving a liquid height of approximately 80 mm above the test surface. As shown in Fig. 1, the test section was visible through two opposing flat 150×200 mm^2 quartz windows. The bottom of the test surface was heated with high velocity (2.5 m/s) water flow. The vapor produced by liquid boiling on the test surface was condensed by the brine-cooled shell-and-tube condenser and returned as liquid to the pool by gravity. Further details of the test apparatus can be found in Refs. [7,8].

3 Test Surface

Figure 2 shows the oxygen-free high-conductivity (OFHC) copper flat test plate used in this study. The test plate was machined

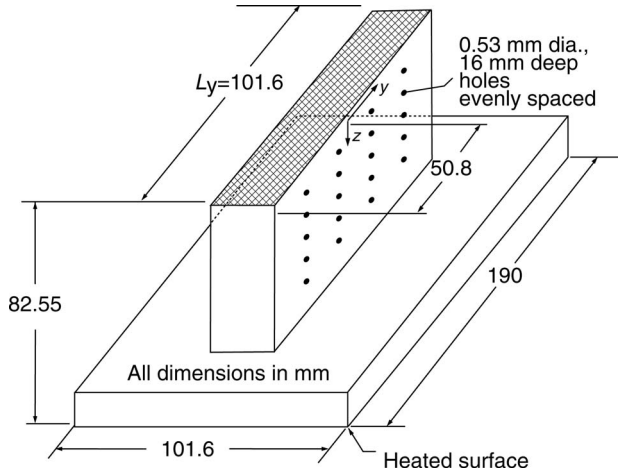

Fig. 2 OFHC copper flat test plate with crosshatched surface and thermocouple coordinate system

out of a single piece of OFHC copper by electric discharge machining (EDM). A tub grinder was used to finish the heat transfer surface of the test plate with a crosshatch pattern. Average roughness measurements were used to estimate the range of average cavity radii for the surface to be between 12 μm and 35 μm. The relative standard uncertainty of the cavity measurements were approximately $\pm$12%. Further information on surface characterization can be found in Ref. [8].

4 Measurements and Uncertainties

The standard uncertainty (u_i) is the positive square root of the estimated variance u_i^2. The individual standard uncertainties are combined to obtain the expanded uncertainty (U), which is calculated from the law of propagation of uncertainty with a coverage factor. All measurement uncertainties are reported at 95% confidence level, except where specified otherwise. For the sake of brevity, only an outline of the basic measurements and uncertainties is given below. Complete details on the heat transfer measurement techniques and uncertainties can be found in Refs. [9,10], respectively.

All of the copper-Constantan thermocouples and the data acquisition system were calibrated against a glass-rod standard platinum resistance thermometer (SPRT) and a reference voltage to a residual standard deviation of 0.005 K. Considering the fluctuations in the saturation temperature during the test and the standard uncertainties in the calibration, the expanded uncertainty of the average saturation temperature was no greater than 0.04 K. Consequently, it is believed that the expanded uncertainty of the temperature measurements was less than 0.1 K.

Twenty 0.5 mm diameter thermocouples were force fitted into the wells of the side of the test plate shown in Fig. 2. The heat flux and the wall temperature were obtained by regressing the measured temperature distribution of the block to the governing two-dimensional conduction equation (Laplace equation). In other words, rather than using the boundary conditions to solve for the interior temperatures, the interior temperatures were used to solve for the boundary conditions following a backward stepwise procedure given in Ref. [11]. The origin of the coordinate system was centered on the surface with respect to the y-direction at the heat transfer surface. Centering the origin in the y-direction reduced the uncertainty of the wall heat flux and temperature calculations by reducing the number of fitted constants involved in these calculations.

Fourier's law and the fitted constants from the solution to the Laplace equation, which represented the temperature field, were used to calculate the average heat flux (q'') normal to and evalu-

[4]At 313.15 K, the measured kinematic viscosities of RL68H1Cu and RL68H2Cu were 71.8 μm^2/s$\pm$0.2 μm^2/s and 68.1 μm^2/s$\pm$0.1 μm^2/s, respectively.

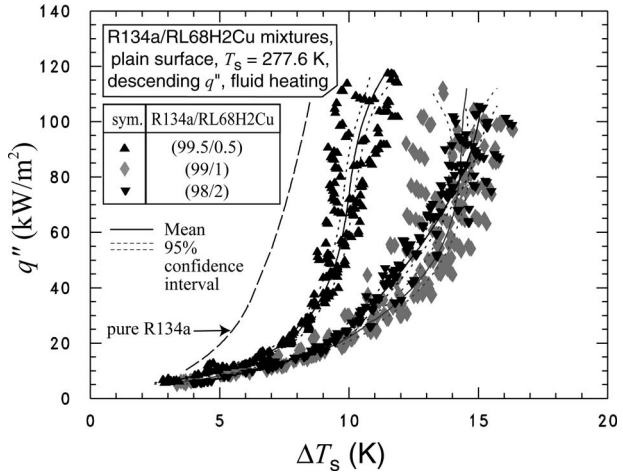

Fig. 3 R134a/RL68H with 0.5% volume CuO nanoparticle mixtures boiling curves for plain surface

ated at the heat transfer surface based on its projected area. The average wall temperature (T_w) was calculated by integrating the local wall temperature (T). The wall superheat was calculated from T_w and the measured temperature of the saturated liquid (T_s). Considering this, the relative expanded uncertainty in the heat flux ($U_{q''}$) was greatest at the lowest heat fluxes, approaching 20% of the measurement near 10 kW/m^2. In general, the $U_{q''}$ remained approximately within 6% for heat fluxes greater than 40 kW/m^2. The average random error in the wall superheat (U_{T_w}) was between 0.05 K and 0.2 K. Plots of $U_{q''}$ and U_{T_w} versus heat flux can be found in Ref. [10].

5 Experimental Results

The heat flux was varied approximately between 10 kW/m^2 and 120 kW/m^2 to simulate a range of possible operating conditions for R134a chillers. All pool-boiling tests were taken at 277.6 K saturated conditions. The data were recorded consecutively starting at the largest heat flux and descending in intervals of approximately 4 kW/m^2. The descending heat flux procedure minimized the possibility of any hysteresis effects on the data, which would have made the data sensitive to the initial operating conditions. Tabulated data of the measured heat flux and wall superheat for all the measurements of this study are given in Ref. [10].

The mixtures were prepared by charging the test chamber (see Fig. 1) with pure R134a to a known mass. Next, a measured mass of nanolubricant or lubricant was injected with a syringe through a port in the test chamber. The refrigerant/lubricant solution was mixed by flushing pure refrigerant through the same port where the lubricant was injected. All compositions were determined from the masses of the charged components and are given on a mass fraction basis. The maximum uncertainty of the composition measurement is approximately 0.02%, e.g., the range of a 2.0% composition is between 1.98% and 2.02%. Nominal or target mass compositions are used in the discussion. For example, the "actual" mass composition of the RL68H2Cu in the R134a/RL68H2Cu (99.5/0.5) mixture was $0.51\% \pm 0.02\%$. Likewise, the RL68H2Cu mass fractions for R134a/RL68H2Cu (99/1) and the R134a/RL68H2Cu (98/2) mixtures were $0.99\% \pm 0.02\%$ and $2.00\% \pm 0.02\%$, respectively.

The effect of mass fraction on R134a/RL68H2Cu pool boiling for the 0.5% volume fraction nanolubricant (RL68H2Cu) is shown in Fig. 3. Figure 3 is a plot of the measured heat flux (q'') versus the measured wall superheat (T_w-T_s) for the R134a/RL68H2Cu mixtures at a saturation temperature of 277.6 K. The solid lines shown in Fig. 3 are cubic best-fit regressions or estimated means of the data. Five of the 243 measurements were removed before fitting because they were identified as "outliers" based on having both high influence and high leverage [12]. Table 1 gives the constants for the cubic regression of the superheat versus the heat flux for the fluids tested here. Kedzierski [10] presented the residual standard deviation of the regressions. The dashed lines to either side of the mean represent the lower and upper 95% simultaneous (multiple-use) confidence intervals for the mean. From the confidence intervals, the expanded uncertainty of the estimated mean wall superheat was on average approximately 0.27 K.

Figure 3 shows that the means of the R134a/RL68H2Cu (99/1) and the R134a/RL68H2Cu (98/2) superheat measurements are

Table 1 Estimated parameters for cubic boiling curve fits for plain copper surface $\Delta T_s = A_0 + A_1 q'' + A_2 q''^2 + A_3 q''^3$ ΔT_s in Kelvin and q'' in W/m^2

Fluid	A_0	A_1	A_2	A_3
R134a/RL68H2Cu (99.5/0.5)				
4.3 K $\le \Delta T_s \le$ 8.5 K	-7.73305×10^{-1}	7.30718×10^{-4}	-1.90704×10^{-8}	1.65931×10^{-13}
8.5 K $\le \Delta T_s \le$ 10.2 K	4.88641	1.77973×10^{-4}	-2.19853×10^{-9}	9.84361×10^{-15}
R134a/RL68H2Cu (99/1)				
4.7 K $\le \Delta T_s \le$ 9.5 K	-1.35217	9.95281×10^{-4}	-2.86155×10^{-8}	3.07861×10^{-13}
9.5 K $\le \Delta T_s \le$ 11.3 K	4.66547	3.07933×10^{-4}	-3.31686×10^{-9}	1.21057×10^{-14}
R134a/RL68H2Cu (99/2)				
4.1 K $\le \Delta T_s \le$ 9.5 K	1.13092	5.80570×10^{-4}	-5.24572×10^{-9}	-1.77277×10^{-13}
9.5 K $\le \Delta T_s \le$ 10.3 K	7.13263	1.21866×10^{-4}	-2.70100×10^{-10}	-1.61515×10^{-15}
R134a/RL68H1Cu (99.5/0.5)				
3.4 K $\le \Delta T_s \le$ 8.2 K	7.52004×10^{-1}	3.15645×10^{-4}	-4.69784×10^{-9}	2.20673×10^{-14}
R134a/RL68H1Cu (99/1)				
3.5 K $\le \Delta T_s \le$ 9 K	6.0058×10^{-1}	3.28260×10^{-4}	-1.31501×10^{-9}	-4.42454×10^{-14}
9 K $\le \Delta T_s \le$ 10.7 K	4.51615	1.84658×10^{-4}	-2.18782×10^{-9}	9.58136×10^{-15}
R134a/RL68H1Cu (99/2)				
3.5 K $\le \Delta T_s \le$ 8.75 K	3.00385×10^{-2}	6.44828×10^{-4}	-1.79772×10^{-8}	1.78650×10^{-13}
8.75 K $\le \Delta T_s \le$ 12 K	7.65055	-2.18447×10^{-5}	1.37521×10^{-9}	-7.45213×10^{-15}

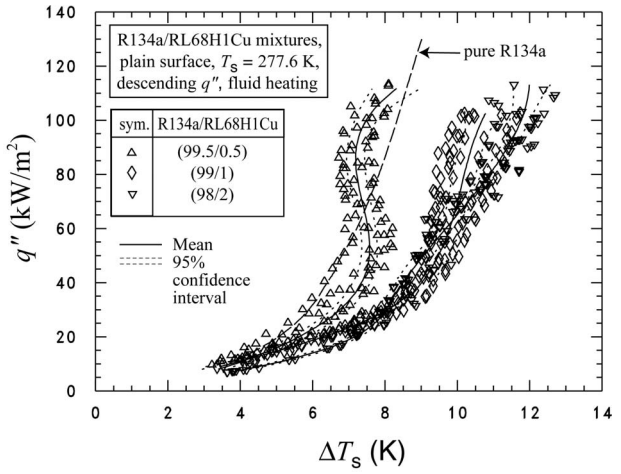

Fig. 4 R134a/RL68H with 1% volume CuO nanoparticle mixtures boiling curves for plain surface [5]

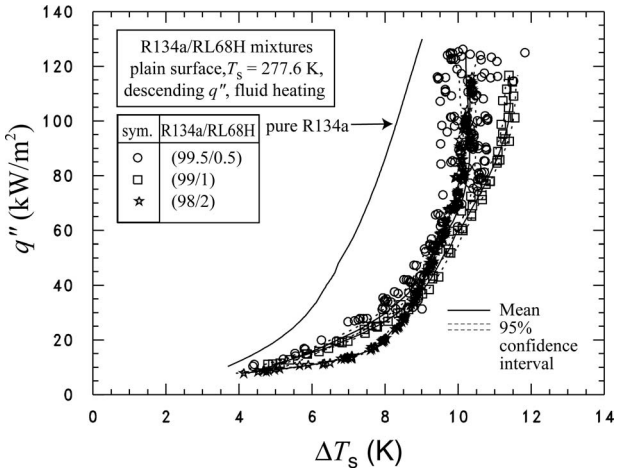

Fig. 5 R134a/RL68H mixtures boiling curves for plain surface [5]

within approximately 1 K for the entire heat flux range that was tested. For heat fluxes less than approximately 75 kW/m^2, the R134a/RL68H2Cu (99/1) mixture mean superheat is less than that of the R134a/RL68H2Cu (98/2) mixture. For heat fluxes larger than 75 kW/m^2, the R134a/RL68H2Cu (98/2) mixture exhibits the unusual characteristic of having an enhanced boiling performance as compared with the R134a/RL68H2Cu (99/1) mixture. However, the confidence intervals coincide for heat fluxes larger than 75 kW/m^2 indicating that no difference can be discerned between the two data sets. For most heat fluxes, the R134a/RL68H2Cu (99.5/0.5) superheat measurements, represented by the closed triangles, are as much as 4 K less than those of the 99/1 and the 98/2 mixtures. For comparison, the mean of the pure R134a boiling curve taken from Ref. [5] is provided as a coarsely dashed line.

The effect of the 1% volume fraction nanolubricant (RL68H1Cu) mass fraction on R134a/RL68H1Cu pool boiling is shown in Fig. 4. Figure 4 is a plot of the measured heat flux (q'') versus the measured wall superheat (T_w-T_s) for the R134a/RL68H1Cu mixtures at a saturation temperature of 277.6 K taken from Ref. [5]. The means of the R134a/RL68H1Cu (99/1) and the R134a/RL68H1Cu (98/2) superheat measurements are within approximately 1 K for the entire heat flux range that was tested. For heat fluxes less than approximately 30 kW/m^2 and greater than approximately 60 kW/m^2, the R134a/RL68H1Cu (99/1) mixture mean superheat is less than that of the R134a/RL68H1Cu (98/2) mixture. For heat fluxes between these limits, the R134a/RL68H1Cu (98/2) mixture exhibits the unusual characteristic of having an enhanced boiling performance as compared with the R134a/RL68H1Cu (99/1) mixture. For most heat fluxes, the R134a/RL68H1Cu (99.5/0.5) superheat measurements, represented by the open triangles, are significantly less than those of the 99/1 and the 98/2 mixtures. The average expanded uncertainty of the estimated mean wall superheat for the three refrigerant/nanolubricant mixtures was 0.23 K.

Figure 5 is a plot of the measured heat flux (q'') versus the measured wall superheat (T_w-T_s) for three R134a/RL68H mixtures at a saturation temperature of 277.6 K taken from Ref. [5]. Figure 5 illustrates the effect of the pure lubricant mass fraction on R134a/lubricant pool boiling. Comparison of the three mean boiling curves shows that the superheats are within approximately 1 K of each other for heat fluxes between approximately 30 kW/m^2 and 90 kW/m^2. For the same heat flux range, the superheat for the pure R134a is roughly 3 K less than that for the mixtures translating into heat transfer degradation with respect to R134a.

A more precise examination of the effect of CuO nanoparticle concentration on boiling performance, for a given R134a/nanolubricant mass fraction, is given in Figs. 6–8. Each figure compares the relative performance of the R134a/RL68H1Cu and the R134a/RL68H2Cu for one of the target mass fractions. A heat transfer enhancement exists where the heat flux ratio is greater than 1 and the 95% simultaneous confidence intervals (depicted by the shaded regions) do not include the value of 1.

Figure 6 plots the ratio of the R134a/RL68H2Cu heat flux to the R134a/RL68H heat flux (q''_{CuO}/q''_{PL}) versus the R134a/RL68H2Cu mixture heat flux (q''_{CuO}) at the same wall superheat for the 99.5/0.5 mixture composition. The heat flux ratio varies between roughly 0.73 and 1.12 for the R134a/RL68H2Cu (99.5/0.5) mixture for heat fluxes between 7 kW/m^2 and 93 kW/m^2. The R134a/RL68H2Cu (99.5/0.5) mixture shows a maximum heat flux ratio of approximately 1.12; however, the maximum resides in a region between 50 kW/m^2 and 93 kW/m^2 where no difference can be established between the two fluids because the confidence intervals include the value of 1. Overall, the average heat flux ratio for the R134a/RL68H2Cu (99.5/0.5) mixture from approximately 7 kW/m^2 to 93 kW/m^2 was 0.91. In contrast, Fig. 6 shows that a significant boiling heat transfer enhancement over that of the R134a/RL68H (99.5/0.5) mixture without nanoparticles is obtained when the nanoparticle volume faction of the lubricant

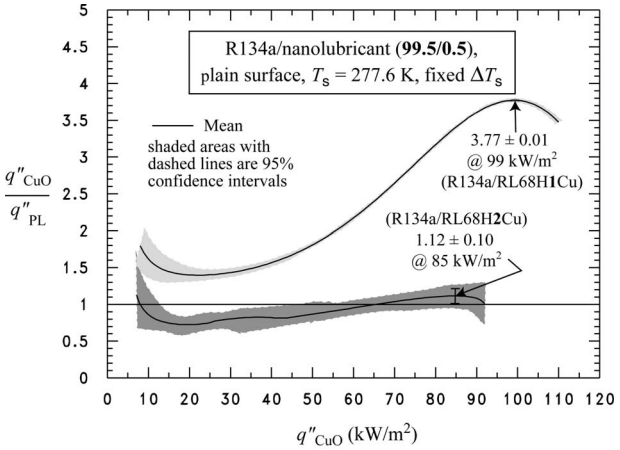

Fig. 6 Heat flux of R134a/RL68H mixtures with CuO nanoparticles relative to that of R134a/RL68H mixtures without CuO nanoparticles for the 99.5/0.5 composition

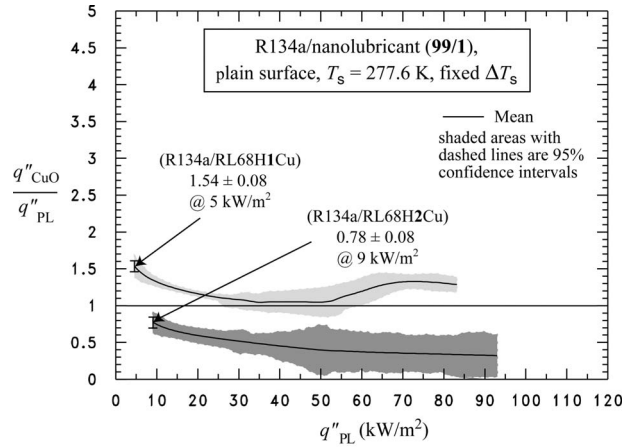

Fig. 7 Heat flux of R134a/RL68H mixtures with CuO nanoparticles relative to that of R134a/RL68H mixtures without CuO nanoparticles for the 99/1 composition

is increased from 0.5% to 1%. More specifically, the heat flux ratio for the R134a/RL68H1Cu (99.5/0.5) mixture varies between roughly 1.5 and 3.75 for heat fluxes between 10 kW/m^2 and 110 kW/m^2. Overall, the average heat flux ratio for the R134a/RL68H1Cu (99.5/0.5) mixture from approximately 8 kW/m^2 to 94 kW/m^2 was 2.15. Consequently, the average heat flux ratio for the 1% CuO volume fraction mixture was nearly 2.4 times larger than that for the 0.5% CuO volume fraction mixture for approximately the same heat flux range.

Figure 7 plots the ratio of the R134a/RL68H2Cu heat flux to the R134a/RL68H heat flux (q''_{CuO}/q''_{PL}) versus the R134a/RL68H mixture heat flux (q''_{PL}) at the same wall superheat for the 99/1 mixture. The heat flux ratio varies roughly between 0.78 and 0.33 for the R134a/RL68H2Cu (99/1) mixture for heat fluxes between 9 kW/m^2 and 93 kW/m^2. The R134a/RL68H2Cu (99/1) mixture shows a maximum heat flux ratio of approximately 0.78 at a heat flux of approximately 9 kW/m^2. Overall, the average heat flux ratio for the R134a/RL68H2Cu (99/1) mixture from approximately 9 kW/m^2 to 93 kW/m^2 was 0.44. In contrast, Fig. 7 shows that a significant boiling heat transfer enhancement over that of the R134a/RL68H (99/1) mixture without nanoparticles is obtained when the nanoparticle volume faction of the lubricant is increased from 0.5% to 1%. More specifically, the heat flux ratio for the R134a/RL68H1Cu (99/1) mixture varies roughly between 1.54 and 1.05 for heat fluxes between 5 kW/m^2 and 85 kW/m^2. Overall, the average heat flux ratio for the R134a/RL68H1Cu (99/1) mixture from approximately 5 kW/m^2 to 85 kW/m^2 was 1.19. For a shared heat flux range between 9 kW/m^2 and 85 kW/m^2, the average heat flux ratio for the 1% CuO volume fraction mixture was approximately 2.6 times larger than that for the 0.5% CuO volume fraction mixture.

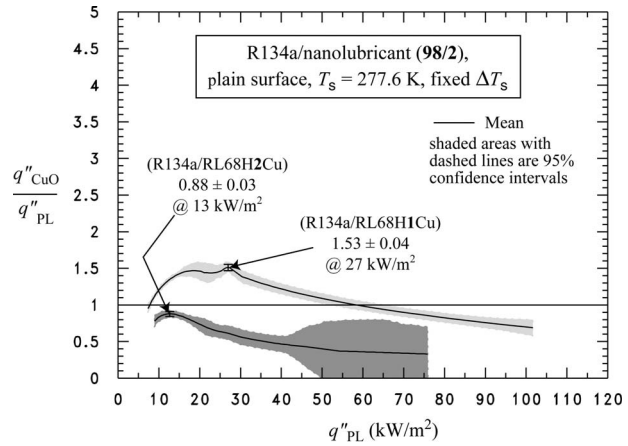

Fig. 8 Heat flux of R134a/RL68H mixtures with CuO nanoparticles relative to that of R134a/RL68H mixtures without CuO nanoparticles for the 98/2 composition

Figure 8 plots the ratio of the R134a/RL68H2Cu heat flux to the R134a/RL68H heat flux (q''_{CuO}/q''_{PL}) versus the R134a/RL68H mixture heat flux (q''_{PL}) at the same wall superheat for the 98/2 mixture. The heat flux ratio varies roughly between 0.88 and 0.33 for the R134a/RL68H2Cu (98/2) mixture for heat fluxes between 9 kW/m^2 and 76 kW/m^2. The R134a/RL68H2Cu (98/2) mixture shows a maximum heat flux ratio of approximately 0.88 at a heat flux of approximately 13 kW/m^2. Overall, the average heat flux ratio for the R134a/RL68H2Cu (98/2) mixture from approximately 9 kW/m^2 to 76 kW/m^2 was 0.51. In contrast, Fig. 8 shows that when the nanoparticle volume faction of the lubricant is increased from 0.5% to 1% a boiling heat transfer enhancement over that of the R134a/RL68H (98/2) mixture is obtained for heat fluxes less than approximately 60 kW/m^2. More specifically, the heat flux ratio for the R134a/RL68H1Cu (98/2) mixture varies roughly between 1.53 and 0.70 for heat fluxes between 7 kW/m^2 and 100 kW/m^2. Overall, the average heat flux ratio for the R134a/RL68H1Cu (98/2) mixture from approximately 9 kW/m^2 to 76 kW/m^2 was 1.17. As a result, the average heat flux ratio for the 1% CuO volume fraction mixture was nearly 2.3 times larger than that for the 0.5% CuO volume fraction mixture for approximately the same heat flux range.

6 Discussion

The heat transfer results summarized in Figs. 6–8 show that use of the 0.5% CuO volume fraction nanolubricant with R134a results in a significantly smaller pool-boiling heat flux than that exhibited with R134a and the nanolubricant with the 1% CuO volume fraction. Overall, mixtures with the 1% volume fraction nanolubricant had boiling heat fluxes (for a given superheat) that were on average 140% larger than those for mixtures with the 0.5% CuO volume fraction nanolubricant. In fact, for most heat fluxes, the 0.5% CuO volume fraction nanolubricant caused heat transfer degradation with respect to the R134a/POE boiling performance, while the 1% CuO volume fraction nanolubricant caused an enhancement relative to R134a/POE. Although the addition of nanoparticles has caused an increase in the viscosity of the lubricant, the refrigerant/lubricant boiling heat transfer correlation of Kedzierski [13] suggested that the viscosity increase can be responsible for approximately a 1% increase in the heat transfer. Likewise, Kedzierski and Gong [5] showed that improvement in nanolubricant thermal conductivity appears to be of secondary importance in its influence on boiling enhancement. Of primary importance in the enhancement of refrigerant/lubricant boiling, for this particular data set, appears to be the interaction of nanoparticles with bubbles. The fact that nanoparticles at a 0.5% volume fraction in the lubricant did not provide a boiling heat transfer enhancement while a 1% volume fraction did, may suggest a critical nanoparticle volume fraction that is necessary for boiling enhancement. It may be necessary for a nanoparticle volume fraction threshold to be exceeded before there are sufficient number of nanoparticles to influence bubble growth and formation. A similar synergistic behavior of nanofluids was also seen by Prasher [14] in his examination of a maximum enhancement of nanofluid thermal conductivity being achieved if there were sufficient nanoparticles to give an agglomeration rate of approximately 35%.

The critical volume fraction of nanoparticles depends on the distribution of the nanoparticles among the excess layer, the surface, and the bulk of the boiling refrigerant/nanolubricant mixture. For this reason, it is speculated that a boiling enhancement or a boiling degradation was realized for the present tests based on the

coupling of the following three heat transfer mechanisms: (1) boiling enhancement via nanoparticle interaction with bubbles, (2) improved thermal conductivity of the lubricant excess layer by the accumulation of highly conductive nanoparticles, and (3) loss of nanosize nucleation sites due to nanoparticle filling of cavities. The last mechanism, the loss of nanosize sites, induces a loss in boiling performance. The surface cavities become saturated with nanoparticles leaving the remaining particles not trapped by the surface to be available for use in the first and second mechanisms. Some volume fraction greater than what is necessary to attain the saturated surface state is believed to be the critical or threshold nanoparticle volume fraction for achieving a boiling enhancement. The second mechanism, improved thermal conductivity of the excess layer, may improve boiling or even degrade it by the loss of wall superheat due to improved conduction from the surface. The first mechanism, the nanoparticle interaction with bubbles, is believed to be the primary contributor to improved boiling.

The above discussion brings to light the likelihood that filling the cavities of the surface caused the boiling heat transfer degradation measured for the R134a/RL68H2Cu mixtures of this study. Das et al. [15] conjectured that the boiling heat transfer degradation that they measured for a water-based nanofluid was caused by nanoparticles plugging the surface, which caused a decrease in nucleation sites. Their conclusion was drawn from an analogy with water deposits that are typically found on surfaces used for boiling water. In order for a smoothing of the surface to decrease boiling, it must reduce the number of active boiling sites.

Following the critical radius criterion given by Carey [16], the calculated range of active cavity radii for saturated R134a boiling at the present test conditions is between 50 μm and 0.1 μm. The R_a roughness of the new clean test surface before its use was 3.39 μm as measured by the NIST Precision Engineering Division [7]. In addition, R_a roughness measurements were also made after boiling tests with a portable contacting stylus device while the boiling surface was in the test apparatus. The average R_a roughness of the surface after boiling the (98/2) RL68H1Cu mixture, with the test fluid removed from the apparatus, and while the nanolubricant excess layer was still on the surface, was approximately 2.9 μm. The average R_a roughness of the surface after it was then cleaned with acetone was approximately 3.0 μm. A statistical comparison supported the conclusion that no difference between the clean and the dirty roughness values could be claimed. In addition, given that the original roughness measurement and the measurements made on the installed test surface were done with different instruments, there would be little or no justification for claiming that R_a roughness has changed as far as the resolution and methodology of these instruments are concerned. Consequently, it is speculated that the nanoparticles smoothed the surface on the nanoscale without changing the gross roughness characteristics because the cavities are an order of magnitude larger than the nanoparticles. This suggests that cavities smaller than those predicted by the critical radius criterion for R134a are active sites for boiling R134a/lubricant mixtures.

Future research is required to investigate the influence of the particle material, its shape, size, distribution, and concentration on refrigerant boiling performance. Not only should the bulk concentration be studied, the distribution of the concentration of the nanoparticles within a particular system should be investigated along with the influence of nanoparticles on boiling surface roughness. Further investigation into the above effects may lead to a theory that can be used to develop nanolubricants that improve boiling heat transfer for the benefit of the refrigeration and air-conditioning industry.

7 Conclusions

The influence of CuO nanoparticle concentration on the boiling performance of R134a/polyolester mixtures on a roughened, horizontal flat surface was investigated. The measurements show that use of the 0.5% CuO volume fraction nanolubricant with R134a results in a significantly smaller pool-boiling heat flux than that exhibited with R134a and the nanolubricant with the 1% CuO volume fraction. Overall, mixtures with the 1% volume fraction nanolubricant had boiling heat fluxes (for a given superheat) that were on average 140% larger than those for mixtures with the 0.5% volume fraction nanolubricant. It was speculated that the 1% CuO volume fraction was greater than some threshold CuO volume fraction resulting in sufficiently more nanoparticles for interaction with bubbles, thus resulting in a significant boiling heat transfer enhancement as compared with boiling without nanoparticles. Conversely, the 0.5% CuO volume fraction apparently was less than the required threshold CuO volume fraction, which resulted in reduced active boiling sites causing a corresponding degradation in the boiling heat transfer as compared with boiling without nanoparticles. For example, the average heat flux ratio for the R134a/RL68H2Cu (99.5/0.5), the R134a/RL68H2Cu (99/1), and the R134a/RL68H2Cu (98/2) mixtures from approximately 10 kW/m^2 to 90 kW/m^2 was 0.91, 0.44, and 0.51, respectively.

It was speculated that enhancement or a boiling degradation was realized for the present tests based on the coupling of the following three heat transfer mechanisms: (1) boiling enhancement via nanoparticle interaction with bubbles, (2) improved thermal conductivity of lubricant excess layer by the accumulation of highly conductive nanoparticles, and (3) loss of nanosize nucleation sites due to nanoparticle filling of cavities. The total number of nanoparticles in the test fluid is split between those within the nanosize cavities of the surface, those in the lubricant excess layer, those on the adiabatic surfaces, and those in the bulk liquid. Nanoparticles not trapped on the surfaces are available to interact with bubbles and possibly induce a boiling enhancement. An overall improvement in the boiling heat transfer will result if the enhancement due to nanoparticle interactions more than compensates for the boiling heat transfer degradation as caused by the filling of boiling cavities with nanoparticles.

Acknowledgment

This work was funded by NIST. Thanks go to the following NIST personnel for their constructive criticism of the first draft of this manuscript: Dr. S. Treado and Dr. P. Domanski. Thanks go to Mr. N. Sawant of the Catholic University of America for his constructive criticism of the second draft of the manuscript. Furthermore, the author extends appreciation to W. Guthrie and Mr. A. Heckert of the NIST Statistical Engineering Division for their consultations on the uncertainty analysis. Boiling heat transfer measurements were taken by Mr. David Wilmering of KT Consultants. The RL68H (EMKARATE RL 68H) was donated by Dr. S. Randles of Uniqema. The RL68H2Cu was manufactured by Nanophase Technologies with a copper (II) oxide and dispersant in RL68H especially for NIST.

Nomenclature

English Symbols

A_n = regression constant in Table 1 $n=0,1,2,3$
L_y = length of test surface (Fig. 2), m
q'' = average wall heat flux, W m^{-2}
T = temperature, K
T_w = temperature at roughened surface, K
U = expanded uncertainty
u_i = standard uncertainty
y = test surface coordinate (Fig. 2), m

Greek Symbols

ΔT_s = wall superheat (T_w-T_s), K

English Subscripts

CuO = R134a/RL68H2Cu or R134a/RL68H1Cu mixture
L = nanolubricant

PL = R134a/RL68H mixture
q'' = heat flux
s = saturated state
T_w = wall temperature
w = wall, heat transfer surface

References

[1] Eastman, J. A., Choi, S. U. S., Li, S., Yu, W., and Thompson, L. J., 2001, "Anomalously Increased Effective Thermal Conductivities of Ethylene Glycol-Based Nanofluids Containing Copper Nanoparticles," Appl. Phys. Lett., **78**, pp. 718–720.

[2] Bang, I. C., and Chang, S. H., 2004, "Boiling Heat Transfer Performance and Phenomena of Al_2O_3–Water Nanofluids From a Plain Surface in a Pool," *Proceedings of ICAPP*, Pittsburgh, PA, pp. 1437–1443.

[3] Wen, D., and Ding, Y., 2005, "Experimental Investigation Into the Pool Boiling Heat Transfer of Aqueous Based γ-Alumina Nanofluids," J. Nanopart. Res., **7**, pp. 265–274.

[4] You, S. M., Kim, J. H., and Kim, K. H., 2003, "Effect of Nanoparticles on Critical Heat Flux of Water in Pool Boiling Heat Transfer," Appl. Phys. Lett., **83**(16), pp. 3374–3376.

[5] Kedzierski, M. A., and Gong, M., 2007, "Effect of CuO Nanolubricant on R134a Pool Boiling Heat Transfer With Extensive Measurement and Analysis Details," U.S. Department of Commerce, Paper No. NISTIR 7454.

[6] Sung, L., 2006, private communication.

[7] Kedzierski, M. A., 2002, "Use of Fluorescence to Measure the Lubricant Excess Surface Density During Pool Boiling," Int. J. Refrig., **25**, pp. 1110–1122.

[8] Kedzierski, M. A., 2001, "Use of Fluorescence to Measure the Lubricant Excess Surface Density During Pool Boiling," U.S. Department of Commerce, Paper No. NISTIR 6727.

[9] Kedzierski, M. A., 2000, "Enhancement of R123 Pool Boiling by the Addition of Hydrocarbons," Int. J. Refrig., **23**, pp. 89–100.

[10] Kedzierski, M. A., 2007, "Effect of CuO Nanoparticle Concentration on R134a/Lubricant Pool Boiling Heat Transfer With Extensive Analysis," U.S. Department of Commerce, Paper No. NISTIR 7450.

[11] Kedzierski, M. A., 1995, "Calorimetric and Visual Measurements of R123 Pool Boiling on Four Enhanced Surfaces," U.S. Department of Commerce, Paper No. NISTIR 5732.

[12] Belsley, D. A., Kuh, E., and Welsch, R. E., 1980, *Regression Diagnostics: Identifying Influential Data and Sources of Collinearity*, Wiley, NY.

[13] Kedzierski, M. A., 2001, "The Effect of Lubricant Concentration, Miscibility and Viscosity on R134a Pool Boiling," Int. J. Refrig., **24**(4), pp. 348–366.

[14] Prasher, R., 2006, "Effect of Colloidal Chemistry on the Thermal Conductivity of Nanofluids," ASME Paper No. IMECE2006-13142.

[15] Das, S. K., Putra, N., and Roetzel, W., 2003, "Pool Boiling of Nano-Fluids on Horizontal Narrow Tubes," Int. J. Multiphase Flow, **29**, pp. 1237–1247.

[16] Carey, V. P., 1992, *Liquid-Vapor Phase-Change Phenomena*, Hemisphere, New York, pp. 186–191.

Atomic-Scale Three-Dimensional Phononic Crystals With a Very Low Thermal Conductivity to Design Crystalline Thermoelectric Devices

Jean-Numa Gillet[1]
e-mail: jngillet@gmail.com

Yann Chalopin

Sebastian Volz[2]
e-mail: volz@em2c.ecp.fr

Laboratoire d'Energétique Moléculaire et Macroscopique, Combustion and Centre National de la Recherche Scientifique (EM2C, CNRS UPR 288), Ecole Centrale Paris, Grande Voie des Vignes, 92295 Châtenay-Malabry Cedex, France

Superlattices with thermal-insulating behaviors have been studied to design thermoelectric materials but affect heat transfer in only one main direction and often show many cracks and dislocations near their layer interfaces. Quantum-dot (QD) self-assembly is an emerging epitaxial technology to design ultradense arrays of germanium QDs in silicon for many promising electronic and photonic applications such as quantum computing, where accurate QD positioning is required. We theoretically demonstrate that high-density three-dimensional (3D) arrays of molecular-size self-assembled Ge QDs in Si can also show very low thermal conductivity in the three spatial directions. This physical property can be considered in designing new silicon-based crystalline thermoelectric devices, which are compatible with the complementary metal-oxide-semiconductor (CMOS) technologies. To obtain a computationally manageable model of these nanomaterials, we investigate their thermal-insulating behavior with atomic-scale 3D phononic crystals: A phononic-crystal period or supercell consists of diamond-cubic (DC) Si cells. At each supercell center, we substitute Si atoms by Ge atoms in a given number of DC unit cells to form a boxlike nanoparticle (i.e., QD). The nanomaterial thermal conductivity can be reduced by several orders of magnitude compared with bulk Si. A part of this reduction is due to the significant decrease in the phonon group velocities derived from the flat dispersion curves, which are computed with classical lattice dynamics. Moreover, according to the wave-particle duality at small scales, another reduction is obtained from multiple scattering of the particlelike phonons in nanoparticle clusters, which breaks their mean free paths (MFPs) in the 3D nanoparticle array. However, we use an incoherent analytical model of this particlelike scattering. This model leads to overestimations of the MFPs and thermal conductivity, which is nevertheless lower than the minimal Einstein limit of bulk Si and is reduced by a factor of at least 165 compared with bulk Si in an example nanomaterial. We expect an even larger decrease in the thermal conductivity than that predicted in this paper owing to multiple scattering, which can lead to a ZT much larger than unity. [DOI: 10.1115/1.3072927]

Keywords: quantum dot, nanoparticle, phononic crystal, superlattice, thermal conductivity, thermoelectric device

1 Introduction

The design of new semiconducting materials with an ultralow thermal conductivity λ is currently one of the most active areas of research in solid-state physics [1–16]. Indeed, the energy-conversion performance of a thermoelectric material is given by its thermoelectric figure of merit ZT, which varies as the inverse of λ, since $ZT=S^2\sigma T/\lambda$, where S, σ, and T are the Seebeck coefficient, electrical conductivity, and absolute temperature of the material, respectively [1]. Superlattices, which consist of periodic layers of thin films, have been extensively studied to design materials with $ZT>1$. Indeed, because of phonon confinement and reflection on layer interfaces, the thermal conductivity of a superlattice can be several orders of magnitude smaller than that of a bulk material [2,7,10]. The same behavior has also been observed in one-dimensional nanowires and two-dimensional (2D) nanocomposites [3–6]. However, because of two major drawbacks, the design of a material with a ZT superior to the alloy limit usually fails with the superlattices [1]. First, a lattice mismatch can occur between the different layers of a superlattice as in the Ge/Si superlattices. This mismatch leads to the formation of cracks and dislocations, which reduces σ and avoids the increase in ZT compared with the alloy limit. Second, the superlattices mainly decrease heat conduction in the perpendicular direction to the thin-layer interfaces, which is not convenient in designing three–dimensional (3D) thermoelectric devices.

Phononic crystals were inspired by the remarkable optical properties of photonic crystals. These materials have recently received an increasing interest because they show band gaps of acoustic

[1]Corresponding author. Present address: Department of Physics, Institut d'Electronique, de Microélectronique et de Nanotechnologie (IEMN, CNRS UMR 8520), Université des Sciences et Technologies de Lille 1, Av. Poincaré, BP 60069, 59652 Villeneuve d'Ascq Cedex, France.

[2]Present address: Institute of Industrial Science (IIS), University of Tokyo, Center for International Research on MicroMechatronics (CIRMM), and Centre National de la Recherche Scientifique, LIMMS, UMI CNRS 2820-IIS, Dw 304, 4-6-1 Komaba, Meguro-ku, Tokyo 153-8505, Japan.

Contributed by the Heat Transfer Division of ASME for publication in the JOURNAL OF HEAT TRANSFER. Manuscript received May 23, 2008; final manuscript received October 27, 2008; published online February 20, 2009. Review conducted by Robert D. Tzou.

wave propagation owing to their periodic elastic structures [17–26]. Usual phononic crystals are fabricated with a periodic structure of elastic rods—for 2D crystals [17–21] or beads for 3D crystals [22–26]—within a solid matrix or a fluid. However, the lattice constant of these elastic structures is usually of the order of ~ 1 mm. Therefore, band gaps cannot occur at frequencies that are higher than ~ 1 MHz in the dispersion curves of those materials. Recently, colloidal crystals with a lattice constant of ~ 1 μm, which are made up of mesoscopic particles dispersed in a continuous medium, have been used to obtain 3D phononic crystals showing band gaps at hypersonic frequencies of the order of ~ 1 GHz [26], which remains too low in designing solid-state thermoelectric materials.

Due to their compatibility with the present complementary metal-oxide-semiconductor (CMOS) technologies, self-assembled germanium quantum dots (QDs) in a silicon matrix constitute an emerging epitaxial technology in designing room-temperature quantum devices that operate with single electrons, holes, or photons [27–35]. Because accurate positioning of the QDs is required in designing electronic and photonic architectures for a number of applications such as quantum computing, lithographic patterning and liquid precursors have been already used to fabricate periodic arrays of self-assembled Ge QDs in Si with a size smaller than 10 nm. Their 3D fabrication can also be achieved by epitaxial layer superposition but shows very few cracks and dislocations differently from the Ge/Si superlattices. Moreover, with their necessary down-scaling in the design of ultracompact quantum device architectures with enhanced quantum effects, major efforts are currently achieved to fabricate ultradense Ge QD arrays with a size of only some nanometers.

In this paper, using a model ordered nanomaterial, we theoretically demonstrate that high-density 3D arrays of self-assembled Ge QDs with a size and spacing of some nanometers in Si can show thermal conductivity, which can be much smaller than that of bulk Si in the three spatial directions. This significant result was obtained from an atomistic model based on classical lattice dynamics as well as semiclassical Boltzmann transport equation with the relaxation-time approximation. The model nanomaterial used for our demonstration consists of a 3D periodic array of Ge boxlike nanoparticles (i.e., the QDs) with a size and spacing of some nanometers in Si. This nanomaterial forms an atomic-scale 3D phononic crystal with a lattice constant equal to a given number of interatomic distances. In this 3D nanomaterial, we compute by classical lattice dynamics flat dispersion curves in the terrahertz range with miniband gaps. These flat branches result in small phonon group velocities. This significant reduction in the group velocities compared with bulk Si cannot be obtained with the traditional continuum elastic models, which are based on the plane-wave decomposition as well as the finite-element (FEM) and finite-difference time-domain (FDTD) methods [36]. Indeed, these models cannot capture the discrete behavior of the atoms inside each nanomaterial supercell and between the supercells.

The wavelike effect of the small phonon group velocities is not the only cause of the decrease in the thermal conductivity in our atomic-scale 3D phononic crystal. Indeed, owing to the wave-particle duality at small scales, an additional ensemble effect of multiple scattering of the particlelike phonons exists in our phononic crystal and increases the total scattering probability according to the Matthiessen rule. This probabilistic effect, which is due to multiple reflections and diffusions of the phonon-particle interference functions arising in 3D nanoparticle clusters, breaks the MFPs and constitutes another reduction factor of the thermal conductivity in our phononic crystal.

We show that the thermal conductivity of the atomic-scale 3D phononic crystal can be decreased by a factor of at least 165 compared with bulk Si in an example nanomaterial. At room temperature, we obtain an upper limit of only 0.95 W/mK for the thermal conductivity of a phononic crystal where each supercell is made up of a nanoparticle of 344 Ge atoms inside a cage of 656 Si atoms. This value is lower than the classical Einstein limit of 0.99 W/mK for disordered bulk Si [37]. However, the present model predicts an overestimation of the thermal conductivity. Indeed, to obtain this upper limit, the cross sections of the scatterers are considered independent of each other in an incoherent-scattering analytical model based on a perturbation quantum theory [38]. An even larger reduction in the thermal conductivity is expected when multiple-scattering effects will be taken into account.

The thermal-insulating behavior of high-density 3D arrays of molecular-size self-assembled Ge QDs, which are investigated from the model of the atomic-scale 3D phononic crystal, is an important property in designing new thermoelectric devices with a large ZT and using very large scale integration (VLSI) technologies borrowed from CMOS microelectronics. Indeed, these silicon-based nanomaterials are crystalline, and their power factor ($S^2\sigma$) can be increased by doping with no significant modification of their thermal conductivity [36]. Possible applications concern the design of new energy-conversion devices, which could be used, for instance, in highly efficient hybrid (thermal/electric) engines for automobiles or Peltier refrigerators for domestic use as well as in the power management of microelectronic portable devices with an extremely high-density of transistors, which is not possible with other recently proposed thermoelectric nanomaterials because they are not CMOS-compatible [1].

2 Dispersion Curves

As shown in Fig. 1(a), we use atomic-scale 3D phononic crystals with a lattice constant of several interatomic distances as model nanomaterials to investigate the thermal properties of high-density 3D arrays of molecular-size self-assembled Ge QDs in Si. A period of our atomic-scale 3D phononic crystal consists of $N \times N \times N = N^3$ diamond-cubic (DC) cells of Si atoms forming a cubic supercell. While larger nanostructures can be envisioned, we restrict to $N=5$ in this paper owing to the computational cost of classical lattice dynamics (as well as by didacticism). Therefore, each supercell is composed of 125 DC unit cells, and our nanomaterial has a lattice constant $d=5\times 0.5431$ nm$=2.7155$ nm. Since the number of atoms per Si unit cell is 8, the total number of atoms forming a supercell is $125\times 8=1000$. At each supercell center, we substitute a cluster of Si atoms by Ge atoms to obtain a 3D periodic heterostructure Ge/Si. In three possible atomic configurations, we substitute the Si atoms contained in $M\times M\times M = M^3$ cells at each supercell center by Ge atoms to form boxlike Ge nanoparticles of different sizes with $M=1$, 2, or 3. When $M=1$, the central cell of each supercell contain 28 Ge atoms, which are surrounded by 972 Si atoms in the 124 other cells. When $M=2$, each supercell has $2\times 2\times 2=8$ cells of 126 Ge atoms at its center and 117 peripheral cells of 874 Si atoms. As shown in Fig. 1(b), when $M=3$, each supercell is composed of 344 Ge atoms at its center forming a boxlike nanoparticle of $3\times 3\times 3=27$ cells, which are surrounded by 98 cells of 656 Si atoms. In Fig. 1(b), the Ge and Si atoms in a supercell are colored black and gray, respectively. The periodic spatial repetition of supercells forms an atomic-scale 3D phononic crystal, as shown in Fig. 1(a).

We use classical lattice dynamics for atomistic computation of the dispersion curves of the atomic-scale 3D phononic crystal. This discrete model is usually based on the harmonic approximation of the energy function between two neighbor atoms [39]. However, to obtain a more realistic model, we use the Stillinger–Weber potential to describe the potential energy of the interaction between two and three neighbor atoms [40,41]. Moreover, we optimize the equilibrium positions of the atoms in the lattice as a function of the respective masses of the Si and Ge atoms. Each phononic crystal shows 3000 dispersion curves, since we have $3\times 1000=3000$ vibration degrees of freedom in a supercell with $N=5$. To obtain the 3000 dispersion curves, we use the general utility lattice program (GULP) [42]. Since the dispersive effect of each atom in a supercell is considered in this discrete model, we

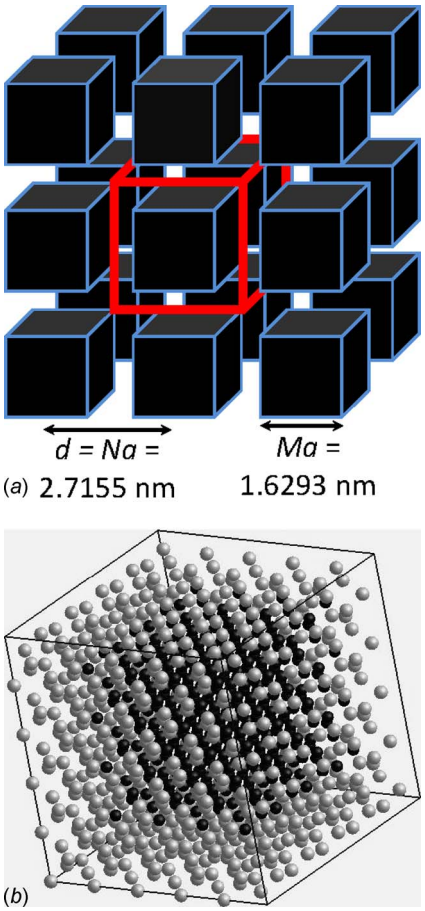

Fig. 1 Schematics at two different scales of an atomic-scale 3D phononic crystal with *N*=5 and *M*=3. In the continuous mediumlike drawing in (*a*), the nanoparticles with an edge length of 3*a*=1.6293 nm and spacing of *d*=5*a*=2.7155 nm are shown by periodic black cubes with highlighted edges. In (*a*), the central transparent cube with bold thick edges displays one of the nanomaterial supercells. The discrete mediumlike drawing of a supercell is presented in (*b*), where the 344 Ge atoms forming each boxlike nanoparticle in (*a*) are colored in black while the 656 peripheral Si atoms are colored in gray in the remainder of the supercell.

obtain dispersion curves in the terrahertz range for the atomic-scale 3D phononic crystal. Figure 2 shows 80 of the 3000 computed dispersions curves of an atomic-scale 3D phononic crystal with the parameters $N=5$ and $M=3$ (schematized in Fig. 1). The 2997 curves of the optical folded modes are very flat, which result in very low group velocities since they are obtained by derivation of the branches with respect to the wave-vector amplitude in a particular direction. By using the atomic-scale 3D phononic crystal, we can therefore reduce heat conduction in the three spatial directions. As discussed in Secs. 3–5, the thermal conductivity of our nanomaterial therefore is much lower than that of its related bulk material.

3 Thermal-Conductivity Model

With a general equation (Eq. (2)), which does not use the Debye approximation, we obtain the thermal conductivity λ of a 3D crystalline material from its phonon relaxation times as well as its acoustic and optical dispersion curves, which were computed by classical lattice dynamics. The mathematical demonstration of Eq. (2) is given in the Appendix. We derive this equation from a semiclassical formulation of the heat flux q_x in a given direction x [43,44]. For a 3D crystalline material, this heat flux, which is

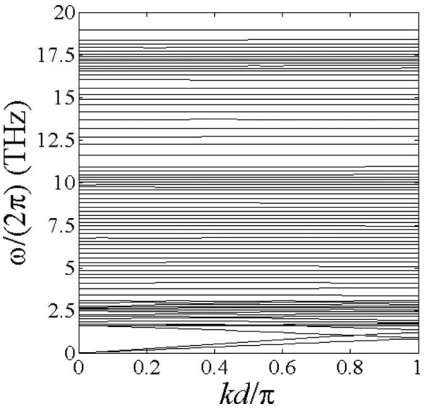

Fig. 2 80 branches chosen among the 3000 dispersion curves of an atomic-scale 3D phononic crystal with *N*=5, *M*=3, and *d*=5*a*=2.715 nm

carried by the phonons with the energies $\hbar\omega_{\mathbf{k},m}$, angular frequencies $\omega_{\mathbf{k},m}$, and group-velocity vectors $\mathbf{v}_{\mathbf{k},m}$, can be determined from the following summation over all possible phonon modes $(\mathbf{k},m)$:

$$q_x = \frac{1}{V}\sum_{m=1}^{N_m}\sum_{\mathbf{k}} \hbar\omega_{\mathbf{k},m} n_{\mathbf{k},m} \mathbf{v}_{\mathbf{k},m}\cdot\hat{x} \tag{1}$$

In Eq. (1), $\hbar=h/(2\pi)$ is the reduced Planck constant, V is the material volume, and m is the index of one branch of the N_m dispersion curves to which the mode $(\mathbf{k},m)$ belongs with a wave vector $\mathbf{k}$ and a nonequilibrium number of phonons $n_{\mathbf{k},m}$. Then, as shown in the Appendix, we obtain the following equation for λ with the relaxation-time approximation of the semiclassical Boltzmann transport equation:

$$\lambda = \frac{1}{3}\sum_{m=1}^{N_m}\int_0^{k_{\max}} l_{k,m} v_{k,m} \hbar\omega_{k,m} \frac{\partial n_{k,m}^{(0)}}{\partial T} g_k dk \tag{2}$$

where $N_m=3000$ for the atomic-scale 3D phononic crystals with the parameter $N=5$, $n_{k,m}^{(0)}$ is the Bose–Einstein equilibrium phonon distribution, and the group-velocity amplitudes $v_{k,m}$ are computed by the derivation of the dispersion curves with respect to the radial wave number $k=|\mathbf{k}|$ as $v_{k,m}=|d\omega_{k,m}/dk|$. In Eq. (2), g_k is the density of states (DOS) per volume unit. As shown in the Appendix, we obtain the conventional relationship $g_k=k^2/(2\pi^2)$ in the case of isotropic group velocities. This DOS is a good approximation for a face-centered cubic (FCC) bulk material as bulk silicon. However, for a nanomaterial with nonspherical supercells, the DOS $g_k=f_k k^2/(2\pi^2)$, where f_k is a nondimensional geometric factor, is a better approximation. Since $K=2^{1/2}K_x$ is the radius of the sphere circumscribing the cube with the edge length $2K_x$ in the [1 0 0] direction of the reciprocal space, as shown in Fig. 3, we can set the constant value $f_k=2$ for any k, with a good approximation, in the case of our atomic-scale 3D phononic crystal owing to the cubic shape of its supercells.

The dispersion curves, which are introduced in Eq. (2) to obtain λ, are computed by classical lattice dynamics, as explained in Sec. 2. Differently from a recent ab initio approach [45], we consider the modal dependence of the phonon mean free paths (MFPs) such as $l_{k,m}=v_{k,m}\tau_{k,m}$, where $\tau_{k,m}$ are the phonon relaxation times of the modes (k,m). The integral in Eq. (2) is taken over the finite interval $[0, k_{\max}]$, where $k_{\max}$ is the right boundary of the first Brillouin zone (BZ). For a FCC bulk material, this boundary is given by $k_{\max}=2\pi/a$. The lattice constant is $a=0.5431$ nm for bulk Si. Differently, owing to the cubic shape of its supercells, we use $k_{\max}=\pi/d$ in Eq. (2) to obtain the thermal conductivity of our atomic-scale 3D phononic crystal. As explained in Sec. 2, $d=Na$

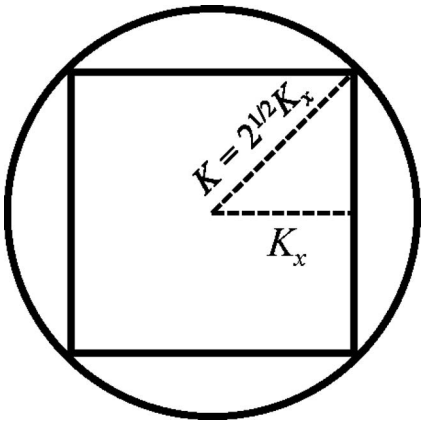

Fig. 3 2D view in the reciprocal plane formed by the directions [1 0 0] and [0 1 0] of a cube with the edge length $2K_x$. The smallest sphere circumscribing this cube has a radius $K=2^{1/2}K_x$, which explains the use of the constant geometric factor of $f_k=2$ in the DOS g_k in Eq. (2).

is the edge length of a supercell, where N is the number of interatomic distances forming this length. As a consequence, in the case of our atomic-scale 3D phononic crystals, the dispersion curves are integrated with Eq. (2) over the finite interval $[0, \pi/d]$, which corresponds to half of the first folded BZ. Because we set $N=5$ in this paper, the size of the folded BZ is one-tenth of that of the bulk Si since $(2\pi/a)/(\pi/d)=2N=10$.

Equation (2) is different from a preceding formulation of the thermal conductivity where integration is over the angular frequency ω instead of the wave number k, which is not trivial to compute [44]. In this formulation, prior to integration, an additional nonanalytical model would be required to obtain the DOS g_ω as a function of ω, since the Debye approximation $\omega \approx v_g k$ is not valid for our atomic-scale 3D phononic crystal. Indeed, even in the isotropic case, the following assumption (where v_g is the mode group velocity):

$$g_\omega d\omega = \frac{k^2}{2\pi^2}\frac{dk}{d\omega}d\omega \approx \frac{1}{2\pi^2}\frac{\omega^2}{v_g^3}d\omega \tag{3}$$

leads to a wrong DOS g_ω (per volume unit) in our nanomaterial owing to its large number of optical dispersion curves (2997 compared with only 3 acoustic curves when $N=5$).

From Eq. (2), we can define an effective value $\langle l \rangle$ of the MFPs $l_{k,m}$ in order to quantify their effect on the thermal conductivity:

$$\lambda(T) = \frac{1}{3}\langle l \rangle \langle Cv \rangle \quad \text{with} \quad \langle Cv \rangle = \sum_{m=1}^{N_m} \int_0^{k_{\max}} v_{k,m}\hbar\omega_{k,m}\frac{\partial n_{k,m}^{(0)}}{\partial T} g_k dk$$

and

$$\langle l \rangle = \frac{3\lambda}{\langle Cv \rangle} = \frac{\sum_{m=1}^{N_m} \int_0^{k_{\max}} l_{k,m} v_{k,m}\hbar\omega_{k,m}\frac{\partial n_{k,m}^{(0)}}{\partial T} g_k dk}{\sum_{m=1}^{N_m} \int_0^{k_{\max}} v_{k,m}\hbar\omega_{k,m}\frac{\partial n_{k,m}^{(0)}}{\partial T} g_k dk} \tag{4}$$

In Eq. (4), the average product $\langle Cv \rangle$ depends on the absolute temperature T but is independent of the phonon MFPs. This factor is analog to the Cv product in the classical formula of λ for a bulk material, which is based on the kinetic theory and given by $\lambda_{\text{bulk}}=(1/3)l_{\text{bulk}}Cv$ where l_{bulk} is the effective phonon MFP, C is the specific heat capacity, and v is the speed of sound. For bulk semiconductors, the lattice thermal conductivity in Eq. (2) can be considered as the total thermal conductivity used to compute ZT, since the electronic thermal conductivity λ_e is negligible in the case of a usual doping [36].

4 Scattering Relaxation Times

To compute the thermal conductivity of our atomic-scale 3D phononic crystal with Eq. (2), we use an analytical model of the total phonon relaxation times $\tau_{k,m}=l_{k,m}/v_{k,m}$ of the modes (k,m), which are derived from the Matthiessen rule and scattering cross sections in a phonon-particle approach. Only resistive scattering processes are considered since our nanomaterial is semiconducting. Therefore, according to the Matthiessen rule, $1/\tau_{k,m}$ is proportional to the summation of three scattering probabilities as

$$\frac{1}{\tau_{k,m}} = \frac{1}{\tau_{k,m}^{(d)}} + \frac{1}{\tau_{k,m}^{(u)}} + \frac{1}{\tau_{k,m}^{(p)}} \tag{5}$$

For a high-purity nanomaterial, the scattering probability related to the relaxation time $\tau_{k,m}^{(d)}$ in Eq. (5) due to punctual defects and isotopes is a second-order effect, which can be neglected compared with the summation of the two other probabilities that is proportional to $1/\tau_{k,m}^{(u)}+1/\tau_{k,m}^{(p)}$. To compute the relaxation time $\tau_{k,m}^{(u)}$ of the Umklapp process (or U-process), we use a common formulation given in Refs. [46,47] with the average Grüneisen parameter $\gamma=1.5$ of bulk Si, so that $1/\tau_{k,m}^{(u)} \approx b_u(T)\omega_{k,m}^2/v_{k,m}^2$, where the empirical function $b_u(T)$ of T is independent of the phonon band structure, and the Debye approximation is not used. A power dependence in ω^α (where α is an integer) of the U-process probability was verified in a FCC crystal using molecular dynamics in a recent paper [48].

In Eq. (5), $\tau_{k,m}^{(p)}$ is the particlelike relaxation time due multiple scattering of the corpuscular phonons at the atomic scale. Indeed, the duality principle in quantum mechanics stipulates that a particle can exhibit both wave- and particlelike properties at small scales. Therefore, the wave function of a corpuscular phonon in our atomic-scale 3D phononic crystal must be a solution of the Schrödinger equation. In this perspective, multiple scattering of a corpuscular phonon in our nanomaterial can be approximately viewed as a stochastic walk, with multiple deflection, tunneling, and confinement probabilities, in a 3D periodic potential-energy landscape. Solving this multiple-scattering quantum problem to obtain the scattering cross section requires computation of the pseudoparticle wave function for all scattering paths [49], which can be computationally intractable because the number of possible paths can be infinite in three dimensions. An approximate method to obtain the multiple-scattering cross section $\sigma_k^{(p)}$ as a function of k must be used.

In this paper, we use the perturbation approach developed by Kim and Majumdar [38] to obtain an approximate analytical model of $\sigma_k^{(p)}$. Indeed, the square amplitude $|c_2(\mathbf{q},\mathbf{q}')|^2$ of the matrix element, which couples the annihilation and creation quantum operators of the incoming and scattered particles (with the wave vectors $\mathbf{q}$ and $\mathbf{q}'$, respectively) in the perturbed Hamiltonian H', is related to the scattering relaxation time, as shown by Klemens and co-workers [50–52]. This approach considers an individual scatterer and is therefore valid for incoherent (or independent) scattering where the scatterers can be considered as far from each other, so that they do not interact with each other. This absence of interaction is different from multiple scattering arising in our atomic-scale 3D phononic crystal. However, the use of an incoherent-scattering model leads to an underestimate $\sigma_{k,m}^{(\text{inc})} < \sigma_{k,m}^{(p)}$ of the phonon-particle cross section, which enables us to compute an upper limit $\lambda_{\max}$ of the thermal conductivity in our atomic-scale 3D phononic crystal with Eq. (2). Indeed, the phonon-particle relaxation time should obey, for any mode (k,m), the following inequality $\tau_{k,m}^{(\text{inc})} > \tau_{k,m}^{(p)}$ because

$$1/\tau_{k,m}^{(\mathrm{inc})} = \eta \sigma_{k,m}^{(\mathrm{inc})} v_{k,m} \tag{6}$$

where $\eta = 1/d^3$ is the nanoparticle volumic density. In the case of a 3D nanoparticle array, where nanoparticles deviates from the periodicity with, for instance, a mean characteristic nanoparticle radius $\bar{R}$ and standard deviation ΔR, $\sigma_{k,m}^{(\mathrm{inc})}$ has to be weighted by a statistical distribution $w(R,\bar{R},\Delta R)$, so that

$$\bar{\sigma}_{k,m}^{(\mathrm{inc})} = \frac{\int_0^{R_{\mathrm{cutoff}}} \sigma_{k,m}^{(\mathrm{inc})}(R) w(R,\bar{R},\Delta R) dR}{\int_0^{R_{\mathrm{cutoff}}} w(R,\bar{R},\Delta R) dR} \tag{7}$$

The spatially averaged cross section $\bar{\sigma}_{k,m}^{(\mathrm{inc})}$ has to be used in Eq. (6) instead of $\sigma_{k,m}^{(\mathrm{inc})}$ when the 3D nanoparticle array is not fully periodic.

We first consider the incoherent cross section $\sigma_k^{(\mathrm{inc})}$ obtained with the analytical model in Ref. [38] in the framework of the Debye approximation. Therefore, $\sigma_k^{(\mathrm{inc})}$ is independent of the phonon-branch index m and connects the Rayleigh-type far-field ($\sigma_k^{(\mathrm{far\ field})}$) and near-geometrical ($\sigma_k^{(\mathrm{near\ geom})}$) cross sections arising when $k \to 0$ and $k \to \infty$, respectively, with the following interpolation:

$$\frac{1}{\sigma_k^{(\mathrm{inc})}} = \frac{1}{\sigma_k^{(\mathrm{far\ field})}} + \frac{1}{\sigma_k^{(\mathrm{near\ geom})}} \quad \text{with}$$

$$\sigma_k^{(\mathrm{far\ field})}/G = \chi^4 h_1(\chi, \Delta A/A, \Delta K/K)$$

and

$$\sigma_k^{(\mathrm{near\ geom})}/G = 2h_2(\chi, \Delta A/A, \Delta K/K) \tag{8}$$

In Eq. (8), we find back the traditional fourth-power dependence of the Rayleigh cross section $\sigma_k^{(\mathrm{far\ field})} \sim \chi^4$ when $k \to 0$, where $\chi = kR$ is the size parameter for a scatterer with the characteristic radius R. Moreover, $\sigma_k^{(\mathrm{near\ geom})} = 2G = 2\pi R^2$ is the geometrical cross section, which becomes independent of k when $k \to \infty$ and is twice the projected area G of the scatterer according to the extinction paradox [38,53]. The nondimensional trigonometric-type functions h_1 and h_2 in Eq. (8) depend on χ as well as the atomic mass A and elastic constant K of the matrix in which the scatterer is embedded with an atomic mass and elastic constant that differ from those of the matrix by the quantities ΔA and ΔK, respectively [38]. To compute the incoherent cross section $\sigma_k^{(\mathrm{inc})}$, we apply Eq. (8) to a Ge nanoparticle of volume $V_p = (Ma)^3$ with $\Delta A/A = (A_{\mathrm{Ge}} - A_{\mathrm{Si}})/A_{\mathrm{Si}} = 1.5849$ where $A_{\mathrm{Ge}} = 72.61$ and $A_{\mathrm{Si}} = 28.09$ are the atomic masses in atomic mass unit (AMU) of the Ge embedded scatterer and Si matrix, respectively. The ratio $\Delta K/K$ is small compared with $\Delta A/A$ for a Ge nanoparticle embedded in a Si matrix since it is computed as $\Delta C_{11}/C_{11} \approx 0.24$, where C_{11} is the first diagonal element of the Si elastic tensor and ΔC_{11} is the difference between those of Si and Ge. Owing to mass conservation, the equivalent spherical radius R of each Ge nanoparticle, to be used in Eq. (8), is defined as $R = [3/(4\pi)]^{1/3}\ Ma = 0.6204\ Ma$.

In Fig. 4(*a*), the three curves of the incoherent-scattering efficiency $Q_k^{(\mathrm{inc})} = \sigma_k^{(\mathrm{inc})}/G$ as a function of the reduced wave number kd/π for the smallest ($M=1$), middle ($M=2$), and largest ($M=3$) Ge nanoparticle sizes in a phononic-crystal supercell are plotted with the dashed-dotted, dashed, and solid lines, respectively. From Fig. 4(*a*), we conclude that particlelike phonon scattering is an effect appearing close to the border of the first folded half BZ (limited by the first thin vertical dashed line in the plot left-hand side) where the allowed phonon wavelengths are the shortest. Indeed, the modes with $k > \pi/d$ in the high-order folded BZs, where $Q_k^{(\mathrm{inc})}$ reaches the geometrical limit of 2 (given by the thin top horizontal dashed line), are forbidden. For the phonon wavelengths larger than four times the supercell period, $Q_k^{(\mathrm{inc})}$ becomes smaller for the largest ($M=3$) and middle ($M=2$) nanoparticle sizes, so that scattering is dominated by the Umklapp process when $k < \pi/(2d)$ and we find back the classical case with $\tau_{k,m} \approx \tau_{k,m}^{(u)}$ in this zone. For the smallest nanoparticle size ($M=1$), $Q_k^{(\mathrm{inc})}$ never reaches a value higher than 0.0332, so that the Umklapp process is always dominant as in bulk Si, and the decrease in the thermal conductivity will not be so impressive than that obtained when $M=3$ (as shown in Sec. 5). For the middle ($M=2$) and largest ($M=3$) nanoparticle sizes, $Q_k^{(\mathrm{inc})}$ increases to the significant values of 0.3161 and 0.8819, respectively, obtained at the right border of the first folded BZ ($k=\pi/d$). The scattering efficiency is the strongest for the largest ($M=3$) nanoparticle size, since its curve is the first to reach its global maximum (obtained in the half of the second folded BZ) compared with the cases with $M=2$ and $M=1$. Indeed, $Q_k^{(\mathrm{inc})}$ monotonically decreases with M because N is restricted to 5 in this paper. After their global maxima, the three curves $Q_k^{(\mathrm{inc})}$ in Fig. 3(*a*) converge with damped oscillations to the geometrical limit of 2, as in the van de Hulst approximation in optics [54]. Fig. 4(*b*) shows the gradual quasi-linear increase in the scattering efficiency $Q_{k=\pi/d}^{(\mathrm{inc})}$ computed at the right border of the first folded BZ with respect to the Ge relative concentration x in each supercell from 0 (in the case of bulk Si) to 0.8819 (when $x=0.344$ or $M=3$).

In our calculations, we avoid the Debye approximation, used for the simplicity of the discussion in the precedent, by replacing the proportionality factor k^4 in $\sigma_k^{(\mathrm{far\ field})}$ in Eq. (8) by $(\omega_{k,m}/v_{k,m})^4$ in accordance with the developments in Ref. [38]. This replacement leads to an incoherent-scattering cross section, which shows a modal dependency of both k and m, but involves a correction of only some percentage of the thermal conductivity. Indeed, in the incoherent approach, scattering of the optical phonons is minor.

5 Modeling Results

We are interested in both wave- and particlelike effects on the decrease in the thermal conductivity in our atomic-scale 3D phononic crystal, which can be investigated from the effective product $\langle Cv \rangle$ and MFP $\langle l \rangle$. In this paper, we compute an upper limit $\lambda_{\max}$ of the thermal conductivity as a function of T since an incoherent approach is used to obtain the particlelike scattering cross section, which also leads to an overestimate $\langle l \rangle_{\max}$ of the effective MFP. Differently, the predicted $\langle Cv \rangle$ is more realistic since this quantity is independent of the phonon relaxation times.

In the log-log plot of Fig. 5(*a*), the dashed-dotted, dashed, and solid thick curves (from the top to bottom) are the computed upper limits $\lambda_{\max}$ of the thermal conductivity for the atomic-scale 3D phononic crystals with the smallest ($M=1$), middle ($M=2$), and largest ($M=3$) nanoparticle sizes in the supercells with the edge length $5a$, respectively. The top circles (which are interpolated by the thin top dashed curve) denote experimental measurements of the thermal conductivity of bulk Si from Ref. [46] for comparison. The thin bottom dashed horizontal line references to the classical Einstein limit for disordered bulk Si with an asymptotical value of 0.99 W/mK when $T \geq 300$ K [37]. The strongest thermal-conductivity decrease is obtained for the atomic-scale 3D phononic crystal with the largest nanoparticle size ($M=3$). In the latter, $\lambda_{\max}$ is lower than the Einstein limit for disordered bulk Si at usual to high temperatures from $T=260$ K to the melting point. This limit is not beaten by the nanomaterials with smaller nanoparticle sizes ($M=1$ and 2). Indeed, particlelike scattering is less significant when the nanoparticles become smaller, and the phonon group velocities increase as well. Below $T=20$ K, the decreasing slope of bulk Si is faster than those of the nanomaterials when T is reduced, since boundary scattering becomes predominant owing to the large effective MFP of bulk Si.

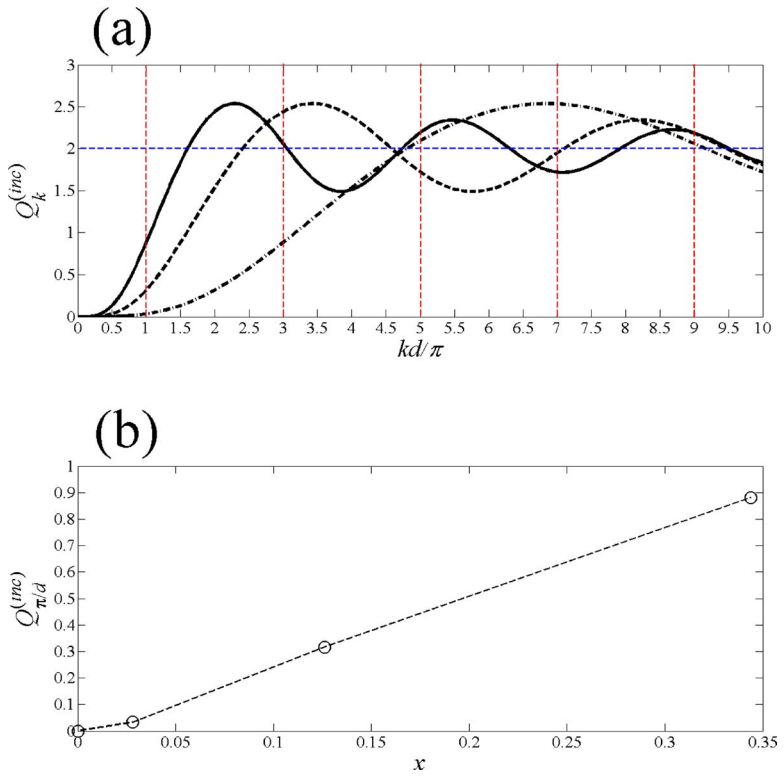

Fig. 4 Diagrams in (*a*) of the incoherent-scattering efficiency $Q_k^{(inc)}$ versus wave number *k* for three atomic-scale 3D phononic crystals: The curves displayed by the dashed-dotted, dashed, and solid black lines are for the nanomaterials with the smallest (*M*=1), middle (*M*=2), and largest (*M*=3) nanoparticle sizes. The thin top dashed horizontal line in (*a*) references to the geometrical limit with the value of 2. The thin dashed vertical lines in (*a*) give the right boundaries of the first, second, third, fourth, and fifth folded BZs from the left-hand side to the right-hand side. In (*a*), the allowed modes are only in the first folded BZ at the left of the first thin dashed vertical line (from the left-hand side). In (*b*), the maximal allowed $Q_k^{(inc)}$ at the right boundary of the first folded BZ, where $k=\pi/d$, is given as a function of the Ge relative concentration *x* in the supercells, where *x* varies from 0 for bulk Si to 0.344 for the nanomaterial with the largest nanoparticle size (*M*=3).

Figure 5(*a*) has to be matched up with Fig. 5(*b*), where the upper-limit curves of the effective MFPs of the atomic-scale 3D phononic crystals are displayed in a log-log plot by the dashed-dotted ($M=1$), dashed ($M=2$), and solid ($M=3$) thick lines. A gradual decrease in $\langle l\rangle_{\max}$ is observed for an increased T owing to Umklapp scattering. Owing to significant particlelike scattering in the nanomaterial with the largest nanoparticle size ($M=3$), $\langle l\rangle_{\max}$ becomes lower than only 8 nm when $T\geq 300$ K, which is much lower than the effective MFP of bulk Si of 100 nm at 300 K. However, in the nanomaterial with $M=1$, the $\langle l\rangle_{\max}$ curve is approximately superposed with that of the effective MFP of bulk Si (obtained by interpolation of the top circles with the thin top dashed line). Indeed, in this nanomaterial, the nanoparticles are made up of a unique DC Si cell. Therefore, they are too small to generate significant particlelike scattering compared with bulk Si.

Figure 6 is a zoom of the $\lambda_{\max}$ curve for the atomic-scale 3D phononic crystal with the largest nanoparticle size ($M=3$) and the most significant thermal-conductivity decrease with respect to bulk Si. At $T=65$ K, we observe a peak of the curve with $\lambda_{\max}=1.23$ W/mK. This maximal value is referenced by the thin top dashed horizontal line. Below this temperature, Umklapp scattering becomes insignificant and $\lambda_{\max}$ abruptly falls to 0 W/mK. In contrast, we observe a more gradual decrease in $\lambda_{\max}$ above 65 K owing to Umklapp scattering. At $T=300$ K, $\lambda_{\max}$ reaches the value of only 0.95 W/mK, which is smaller than the thermal conductivity of bulk Si (156 W/mK) by a factor of 165. Close to the melting point, at $T=1400$ K, $\lambda_{\max}$ decreases to the value of 0.5038 W/mK, which is referenced by the thin bottom dashed horizontal line. This value is twice smaller than the Einstein limit for disordered bulk Si shown by the thin middle dashed horizontal line for comparison.

In the bottom of Fig. 7(*a*), the circles interpolated by a thick dashed line is a log-log plot of the ratio $\lambda_{\max}/\lambda_{\text{bulk}}$ of the upper-limit thermal conductivity of the atomic-scale 3D phononic crystal with the largest nanoparticle size ($M=3$) with respect to the bulk-Si thermal conductivity λ_{bulk}. This ratio gradually increases from $1/4401=0.00023$ at $T=20$ K to $1/50=0.02$ close to the melting point, while it reaches $1/165=0.0061$ at $T=300$ K. The two above plots with the upward and downward triangles (interpolated by thick dashed lines) show the ratios $\langle l\rangle_{\max}/\langle l\rangle_{\text{bulk}}$ and $\langle Cv\rangle/\langle Cv\rangle_{\text{bulk}}$, respectively, where $\langle l\rangle_{\max}$ and $\langle Cv\rangle$ are the respective effective-MFP upper limit and average product Cv in the nanomaterial with the largest nanoparticle size ($M=3$) in contrast to the effective MFP $\langle l\rangle_{\text{bulk}}$ and average product $\langle Cv\rangle_{\text{bulk}}$ in bulk Si. We observe a monotonic increase in $\langle l\rangle_{\max}/\langle l\rangle_{\text{bulk}}$ (owing to Umklapp scattering) for an increased T as well as a monotonic decrease in $\langle Cv\rangle/\langle Cv\rangle_{\text{bulk}}$. The two curves intersect at $T=300$ K and have the same ratios of $\approx 1/13=0.077$ at this temperature. This reference ratio is displayed by the thin top dashed horizontal

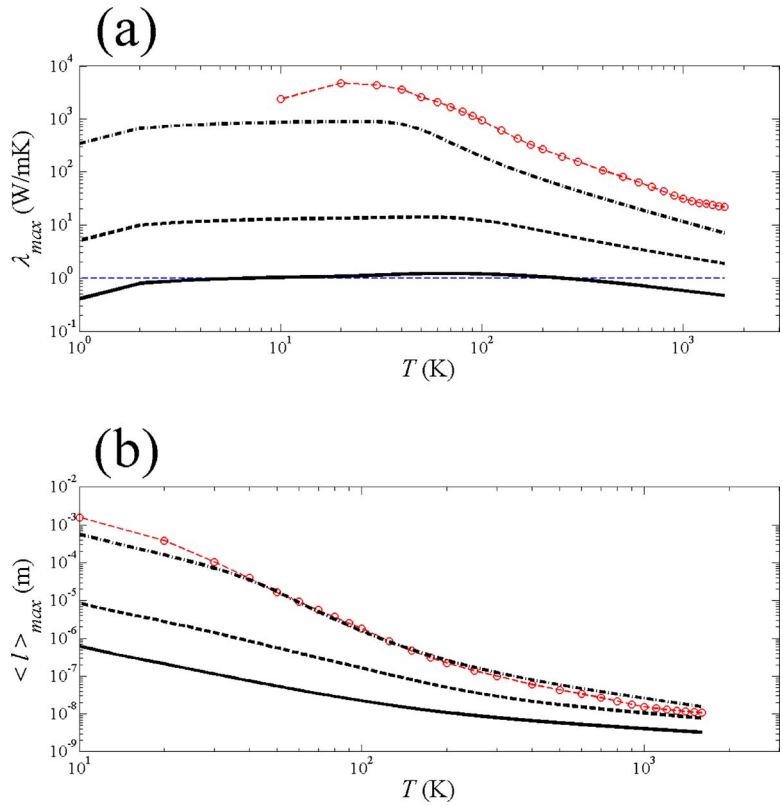

Fig. 5 Diagrams in (*a*) of the upper limits λ_{max} of the thermal conductivity versus temperature *T* for three atomic-scale 3D phononic crystals: The curves displayed by the dashed-dotted, dashed, and solid black lines are for the nanomaterials with the smallest (*M*=1), middle (*M*=2), and largest (*M*=3) nanoparticle sizes, respectively. The thin bottom dashed horizontal line in (*a*) is a reference to the Einstein limit of 0.99 W/mK (for disordered bulk Si). The top circles interpolated by the thin top dashed line are experimental measurements of the thermal conductivity of bulk Si for comparison. In (*b*), the upper limits $\langle l \rangle_{max}$ of the effective MFP versus *T* are displayed by the dashed-dotted, dashed, and solid black lines for nanomaterials with *M*=1, *M*=2, and *M*=3, respectively. The top circles interpolated by the thin top dashed line give the curve of the effective MFP of bulk Si for comparison.

line. At higher temperatures, we observe that the $\langle Cv \rangle$ decreases predominantly over that of $\langle l \rangle_{\max}$. At $T < 300$ K, we obtain the opposite case owing to the predominance of particlelike over wavelike effects. The ratio $\langle Cv \rangle / \langle Cv \rangle_{\text{bulk}}$ converge to a horizontal curve, which is almost superposed to the thin dashed horizontal reference line, when $T > 300$ K. Indeed, the average specific heat capacities of both nanomaterial and bulk Si converge to the same constant classical limit at high temperatures while the group velocities are assumed to be independent of *T*.

From the bottom to the top of Fig. 7(*b*), we display the semilog

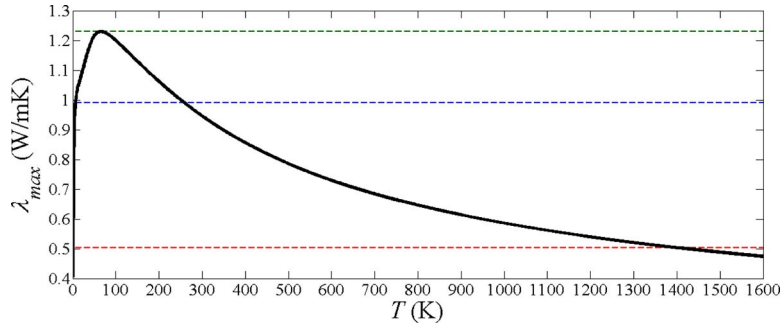

Fig. 6 Diagram of the upper limits λ_{max} of the thermal conductivity versus temperature *T* for the atomic-scale 3D phononic crystal with the largest nanoparticle size (*M*=3). This curve shows a peak at *T*=65 K with the value of 1.23 W/mK, which is referenced by the thin top horizontal dashed line. The middle and bottom thin dashed horizontal lines are references to the Einstein limit of 0.99 W/mK (for disordered bulk Si) and upper limit λ_{max} =0.50 W/mK (for the nanomaterial) close to the melting point, respectively.

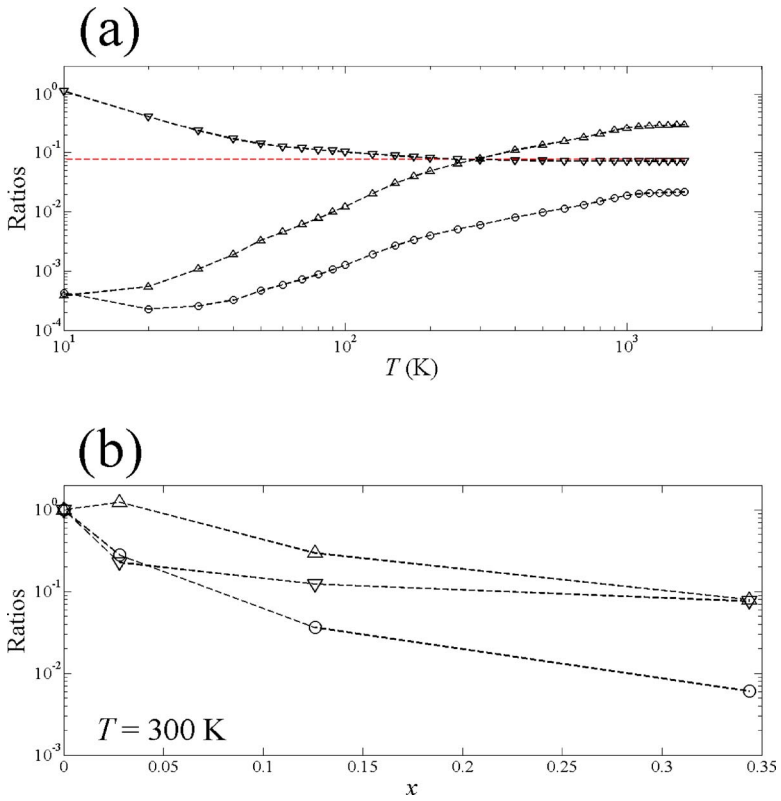

Fig. 7 Diagrams in (*a*) of the ratios $\lambda_{max}/\lambda_{bulk}$ (black circles), $\langle l\rangle_{max}/\langle l\rangle_{bulk}$ (black upward triangles) and $\langle Cv\rangle/\langle Cv\rangle_{bulk}$ (black downward triangles) versus temperature *T* for the atomic-scale 3D phononic crystals with the largest nanoparticle size (*M*=3). Data of the same group are interpolated by a black dashed line. The thin top dashed horizontal line is a reference to the intersection point of the curves $\langle l\rangle_{max}/\langle l\rangle_{bulk}$ and $\langle Cv\rangle/\langle Cv\rangle_{bulk}$ at *T*=300 K, where these ratios have the value of 1/13=0.077. In (*b*), the ratios $\lambda_{max}/\lambda_{bulk}$ (black circles), $\langle l\rangle_{max}/\langle l\rangle_{bulk}$ (black upward triangles) and $\langle Cv\rangle/\langle Cv\rangle_{bulk}$ (black downward triangles) are plotted at *T*=300 K versus the Ge relative concentration *x*, where *x* varies from 0 for bulk Si to 0.344 for the atomic-scale 3D phononic crystal with the largest nanoparticle size (*M*=3). In (*b*), the curves $\langle l\rangle_{max}/\langle l\rangle_{bulk}$ and $\langle Cv\rangle/\langle Cv\rangle_{bulk}$ intersect when *x*=0.344, as also seen in (*a*).

plots of the ratios $\lambda_{max}/\lambda_{bulk}$, $\langle Cv\rangle/\langle Cv\rangle_{bulk}$, and $\langle l\rangle_{max}/\langle l\rangle_{bulk}$, at $T=300$ K, which are displayed by circles, downward triangles, and upward triangles, respectively (where these symbols are interpolated by dashed lines). The three ratios are plotted versus the Ge relative concentration x in the supercells, which vary from 0 (in the case of bulk Si) to 0.344 (in the nanomaterial with $M=3$ showing the largest nanoparticle size). We observe monotonic reductions of $\lambda_{max}/\lambda_{bulk}$ and $\langle Cv\rangle/\langle Cv\rangle_{bulk}$ from 1 to $1/165=0.0061$ and 1 to $1/13=0.077$, respectively. The ratio $\langle l\rangle_{max}/\langle l\rangle_{bulk}$ only begins to decrease when $x>0.028$ (or $M>1$). Indeed, for the nanomaterial with the smallest nanoparticles made up of only one DC Si cell ($M=1$), particlelike scattering is insignificant so that the λ reduction is weak and only due to the average product $\langle Cv\rangle$. However, when $x=0.344$ (or $M=3$), the $\langle Cv\rangle/\langle Cv\rangle_{bulk}$ and $\langle l\rangle_{max}/\langle l\rangle_{bulk}$ curves intersect. As a result, particlelike scattering in the incoherent approach becomes as significant as the wavelike effect only for the atomic-scale 3D phononic crystal with the largest nanoparticle size ($M=3$). In the right-hand side of the diagram, we see the intersection point (at $T=300$ K) of the curves $\langle Cv\rangle/\langle Cv\rangle_{bulk}$ and $\langle l\rangle_{max}/\langle l\rangle_{bulk}$ with the same ratio of $1/13=0.077$.

6 Conclusion

We theoretically demonstrate that high-density 3D arrays of molecular-size self-assembled Ge QDs in Si show a thermal conductivity, which can be lower by several orders of magnitude than that of bulk Si. This physical property can have important consequences on the design of new room-temperature quantum device architectures and CMOS-compatible thermoelectric devices. We model the thermal-insulating behavior of these crystalline nanomaterials using atomic-scale 3D phononic crystals. A phononic-crystal period or supercell consists of N^3 DC unit cells of Si atoms with $N=5$ here. A 3D periodic nanocomposite of $8N^3=1000$ atoms is formed, since we substitute a cluster of Si atoms by Ge atoms in M^3 DC unit cells at each supercell center. By varying M from 1 to 3, we obtain boxlike Ge QDs of different sizes at each supercell center. With the dispersion curves computed by classical lattice dynamics and a semi-analytical equation based on the relaxation-time approximation of the Boltzmann transport equation, we obtain the thermal conductivity of the atomic-scale 3D phononic crystals. Compared with single-crystal bulk Si, we show that the thermal conductivity in an example nanomaterial can be lower than the classical Einstein limit and can be reduced by a factor of at least 165 (when $N=5$ and $M=3$), which can lead to a much larger ZT than unity owing to the nanomaterial crystallinity. This reduction is not only due to the significant decrease of the phonon group velocities and incoherent scattering of the particlelike phonons. Indeed, we expect an even larger decrease than that predicted in the present model owing to phonon multiple scattering.

Acknowledgment

We acknowledge the French Research National Agency (ANR) ThermaEscape under the program PNANO for its financial support as well as the Centre National de la Recherche Scientifique (CNRS). We also thank Professor J.D. Gale and his group for the development of GULP under a free license.

Appendix

Using a semiclassical formulation [43,44], the heat flux q_x in a direction x, which is carried by the phonons with the energy $\hbar\omega_{\mathbf{k},m}$ and group-velocity vector $\mathbf{v}_{\mathbf{k},m}$ can be determined for a crystalline material with a volume V by the following summation over all possible phonon modes $(\mathbf{k},m)$:

$$q_x = \frac{1}{V}\sum_{m=1}^{N_m}\sum_{\mathbf{k}} \hbar\omega_{\mathbf{k},m} n_{\mathbf{k},m} \mathbf{v}_{\mathbf{k},m}\cdot\hat{x} \tag{A1}$$

where $\hbar = h/(2\pi)$ is the reduced Planck constant, and m is the index of one branch of the N_m dispersion curves to which belongs the mode $(\mathbf{k},m)$ with a number of phonons $n_{\mathbf{k},m}$ and wave vector $\mathbf{k}$. However, in the relaxation-time approximation [43,44], the semiclassical Boltzmann transport equation in the steady state simplifies to

$$\frac{n^{(0)}_{\mathbf{k},m} - n_{\mathbf{k},m}}{\tau_{\mathbf{k},m}} = \mathbf{v}_{\mathbf{k},m}\cdot\nabla n_{\mathbf{k},m} \tag{A2}$$

where we take into consideration the modal dependence of the phonon relaxation times $\tau_{\mathbf{k},m}$. In Eq. (A2), $n^{(0)}_{\mathbf{k},m}$ is the Bose–Einstein equilibrium distribution:

$$n^{(0)}_{\mathbf{k},m} = \frac{1}{\exp\left(\dfrac{\hbar\omega_{\mathbf{k},m}}{k_B T}\right) - 1} \tag{A3}$$

where k_B is the Boltzmann constant. Moreover, a simplification in the advection term in Eq. (A2), given by $\nabla n_{\mathbf{k},m} = \nabla T(\partial n^{(0)}_{\mathbf{k},m}/\partial T)$, is commonly used in the steady state for a material with dimensions larger than the effective phonon MFP [44,55,56]. Therefore, by substitution of Eq. (A2) into Eq. (A1) and noting $v_{\mathbf{k},m} = |\mathbf{v}_{\mathbf{k},m}|$, we obtain

$$q_x = -\frac{dT}{dx}\frac{1}{V}\sum_m\sum_{\mathbf{k}} \tau_{\mathbf{k},m}(v_{\mathbf{k},m}\cos\theta)^2\hbar\omega_{\mathbf{k},m}\frac{\partial n^{(0)}_{\mathbf{k},m}}{\partial T} \tag{A4}$$

because the equilibrium term in $n^{(0)}_{\mathbf{k},m}$ from Eq. (A2) produces a zero heat flux (since $\mathbf{v}_{-\mathbf{k},m} = -\mathbf{v}_{\mathbf{k},m}$), and the heat flux is in the x direction so that $\nabla T = (dT/dx)\hat{x}$. In Eq. (A4), θ is the angle between $\mathbf{v}_{\mathbf{k},m}$ and the heat flux direction. If we consider isotropic group velocities, which is a common approximation [44], $v_{\mathbf{k},m}$ can be considered as independent of the wave-vector orientation (ϕ,θ) in spherical coordinates. This simplification is acceptable for materials with several isotropic directions. Using this approximation, Eq. (A4) becomes

$$\begin{aligned} q_x &= -\frac{dT}{dx}\frac{1}{V}\sum_m \frac{V}{(2\pi)^3}\int_0^{k_{\max}} k^2 dk\,\tau_{k,m}(v_{k,m})^2\hbar\omega_{k,m}\frac{\partial n^{(0)}_{k,m}}{\partial T} \\ &\quad\times\int_0^{2\pi} d\phi\int_0^{\pi}\sin\theta d\theta(\cos\theta)^2 \\ &= -\frac{dT}{dx}\frac{1}{3}\sum_m\int_0^{k_{\max}}\tau_{k,m}(v_{k,m})^2\hbar\omega_{k,m}\frac{\partial n^{(0)}_{k,m}}{\partial T}\frac{k^2}{2\pi^2}dk \end{aligned} \tag{A5}$$

where $k = |\mathbf{k}|$, and $(2\pi)^3/V$ is the $\mathbf{k}$-space volume occupied by each mode. In Eq. (A5), the integration is limited by the maximum wave number $k_{\max}$, which corresponds to the right boundary of the first BZ. From Eq. (A5), we can derive the thermal conductivity λ from the Fourier law: $q_x = -\lambda(dT/dx)$. We consider the mode dependence of the phonon MFP $l_{k,m}$, which is given by the following relationship: $\tau_{k,m} = l_{km}/v_{k,m}$. Therefore, from Eq. (A5), we obtain the following relationship for λ:

$$\lambda = \frac{1}{3}\sum_m\int_0^{k_{\max}} l_{k,m}v_{k,m}\hbar\omega_{k,m}\frac{\partial n^{(0)}_{k,m}}{\partial T}g_k dk \tag{A6}$$

where the group velocities $v_{k,m}$ are computed from the dispersion curves as $v_{k,m} = |d\omega_{k,m}/dk|$, and the DOS per volume unit is $g_k = k^2/(2\pi^2)$ for a bulk material in the isotropic approximation. Equation (A6) is the same as Eq. (2).

References

[1] Kim, W., Zide, J., Gossard, A., Klenov, D., Stemmer, S., Shakouri, A., and Majumdar, A., 2006, "Thermal Conductivity Reduction and Thermoelectric Figure of Merit Increase by Embedding Nanoparticles in Crystalline Semiconductors," Phys. Rev. Lett., **96**, p. 045901.
[2] Chen, G., 1999, "Phonon Wave Heat Conduction in Thin Films Superlattices," ASME J. Heat Transfer, **121**(4), pp. 945–953.
[3] Hochbaum, A. I., Chen, R., Delgado, R. D., Liang, W., Garnett, E. C., Najarian, M., Majumdar, A., and Yang, P., 2008, "Enhanced Thermoelectric Performance of Rough Silicon Nanowires," Nature (London), **451**, pp. 163–167.
[4] Boukai, A. I., Bunimovich, Y., Tahir-Kheli, J., Yu, J.-K., Goddard, W. A., III, and Heath, J. R., 2008, "Silicon Nanowires as Efficient Thermoelectric Materials," Nature (London), **451**, pp. 168–171.
[5] Volz, S., and Chen, G., 1999, "Molecular Dynamics Simulation of Thermal Conductivity of Silicon Nanowires," Appl. Phys. Lett., **75**(14), pp. 2056–2058.
[6] Yang, R., and Chen, G., 2004, "Thermal Conductivity Modeling of Periodic Two-Dimensional Nanocomposites," Phys. Rev. B, **69**, p. 195316.
[7] Chiritescu, C., Cahill, D. G., Nguyen, N., Johnson, D., Bodapati, A., Keblinski, P., and Zschack, P., 2007, "Ultralow Thermal Conductivity in Disordered, Layered WSe_2 Crystals," Science, **315**, pp. 351–353.
[8] Hsu, K. F., Loo, S., Guo, F., Chen, W., Dyck, J. S., Uher, C., Hogan, T., Polychroniadis, E. K., and Kanatzidis, M. G., 2004, "Cubic $AgPb_mSbTe_{2+m}$: Bulk Thermoelectric Materials With High Figure of Merit," Science, **303**, pp. 818–821.
[9] Harman, T. C., Taylor, P. J., Walsh, M. P., and LaForge, B. E., 2002, "Quantum Dot Superlattice Thermoelectric Materials and Devices," Science, **297**, pp. 2229–2232.
[10] Venkatasubramanian, R., Siivola, E., Colpitts, T., and O'Quinn, B., 2001, "Thin-Film Thermoelectric Devices With High Room-Temperature Figures of Merit," Nature (London), **413**, pp. 597–602.
[11] Volz, S., Lemonnier, D., and Saulnier, J. B., 2001, "Clamped Nanowire Thermal Conductivity Based on Phonon Transport Equation," Microscale Thermophys. Eng., **5**, pp. 191–207.
[12] Jeng, M.-S., Yang, R., Song, D., and Chen, G., 2008, "Modeling the Thermal Conductivity and Phonon Transport in Nanoparticle Composites Using Monte Carlo Simulation," ASME J. Heat Transfer, **130**, p. 042410.
[13] Chen, G., and Shakouri, A., 2002, "Heat Transfer in Nanostructures for Solid-State Energy Conversion," ASME J. Heat Transfer, **124**(2), pp. 242–342.
[14] Yu, C., Saha, S., Zhou, J., and Shi, L., 2006, "Thermal Contact Resistance and Thermal Conductivity of a Carbon Nanofiber," ASME J. Heat Transfer, **128**(3), pp. 234–239.
[15] Liu, W., and Asheghi, M., 2006, "Thermal Conductivity Measurements of Ultra-Thin Single Crystal Silicon Layers," ASME J. Heat Transfer, **128**(1), pp. 75–83.
[16] Bulusu, A., and Walker, D. G., 2007, "Modeling of Thermoelectric Properties of Semi-Conductor Thin Films With Quantum and Scattering Effects," ASME J. Heat Transfer, **129**(4), pp. 492–499.
[17] Bonello, B., Charles, C., and Ganot, F., 2007, "Lamb Waves in Plates Covered by a Two-Dimensional Phononic Film," Appl. Phys. Lett., **90**, p. 021909.
[18] Sun, J.-H., and Wu, T.-T., 2006, "Propagation of Surface Acoustic Waves Through Sharply Bent Two-dimensional Phononic Crystal Waveguides Using a Finite-Difference Time-Domain Method," Phys. Rev. B, **74**, p. 174305.
[19] Wu, T.-T., Hsu, C.-H., and Sun, J.-H., 2006, "Design of a Highly Magnified Directional Acoustic Source Based on the Resonant Cavity of Two-Dimensional Phononic Crystals," Appl. Phys. Lett., **89**, p. 171912.
[20] Wu, T.-T., Huang, Z.-G., and Lin, S., 2004, "Surface and Bulk Acoustic Waves in Two-Dimensional Phononic Crystal Consisting of Materials With General Anisotropy," Phys. Rev. B, **69**, p. 094301.
[21] Khelif, A., Choujaa, A., Benchabane, S., Djafari-Rouhani, B., and Laude, V., 2004, "Guiding and Bending of Acoustic Waves in Highly Confined Phononic Crystal Waveguides," Appl. Phys. Lett., **84**(22), pp. 4400–4402.
[22] Chen, H., Luo, X., and Ma, H., 2007, "Scattering of Elastic Waves by Elastic Spheres in a NaCl-Type Phononic Crystal," Phys. Rev. B, **75**, p. 024306.
[23] Yang, S., Page, J. H., Liu, Z., Cowan, M. L., Chan, C. T., and Sheng, P., 2004, "Focusing of Sound in a 3D Phononic Crystal," Phys. Rev. Lett., **93**, p. 024301.
[24] Yang, S., Page, J. H., Liu, Z., Cowan, M. L., Chan, C. T., and Sheng, P., 2002, "Ultrasound Tunneling Through 3D Phononic Crystals," Phys. Rev. Lett., **88**,

p. 104301.
[25] Liu, Z., Chan, C. T., Sheng, P., Goertzen, A. L., and Page, J. H., 2000, "Elastic Wave Scattering by Periodic Structures of Spherical Objects: Theory and Experiment," Phys. Rev. B, **62**(4), pp. 2446–2457.
[26] Tommaseo, G., Petekidis, G., Steffen, W., Fytas, G., Schofield, A. B., and Stefanou, N., 2007, "Hypersonic Acoustic Excitations in Binary Colloidal Crystals: Big Versus Small Hard Sphere Control," J. Chem. Phys., **126**, p. 014707.
[27] Yakimov, A. I., Dvurechenskii, A. V., and Nikiforov, A. I., 2006, "Germanium Self-Assembled Quantum Dots in Silicon for Nano- and Optoelectronics," J. Nanoelectron. Optoelectron., **1**(2), pp. 119–175.
[28] Guise, O., Yates, J. T., Jr., Levy, J., Ahner, J., Vaithyanathan, V., and Schlom, D. G., 2005, "Patterning of Sub-10-nm Ge Islands on Si(100) by Directed Self-Assembly," Appl. Phys. Lett., **87**, p. 171902.
[29] Berbezier, I., Karmous, A., Ronda, A., Sgarlata, A., Balzarotti, A., Castrucci, P., Scarselli, M., and De Crescenzi, M., 2006, "Growth of Ultrahigh-Density Quantum-Confined Germanium Dots on SiO_2 Thin Films," Appl. Phys. Lett., **89**, p. 063122.
[30] Gray, J. L., Hull, R., and Floro, J. A., 2006, "Periodic Arrays of Epitaxial Self-Assembled SiGe Quantum Dot Molecules Grown on Patterned Si Substrates," J. Appl. Phys., **100**, p. 084312.
[31] Kiravittaya, S., Heidemeyer, H., and Schmidt, O. G., 2005, "Lateral Quantum-Dot Replication in Three-Dimensional Quantum-Dot Crystals," Appl. Phys. Lett., **86**, p. 263113.
[32] Kar, G. S., Kiravittaya, S., Stoffel, M., and Schmidt, O. G., 2004, "Material Distribution Across the Interface of Random and Ordered Island Arrays," Phys. Rev. Lett., **93**, p. 246103.
[33] Karmous, A., Cuenat, A., Ronda, A., Berbezier, I., Atha, S., and Hull, R., 2004, "Ge Dot Organization on Si Substrates Patterned by Focused Ion Beam," Appl. Phys. Lett., **85**, pp. 6401–6403.
[34] Zhong, Z., Halilovic, A., Fromherz, T., Schäffler, F., and Bauer, G., 2003, "Two-Dimensional Periodic Positioning of Self-Assembled Ge Islands on Prepatterned Si (001) Substrates," Appl. Phys. Lett., **82**(26), pp. 4779–4781.
[35] Lee, H., Johnson, J. A., He, M. Y., Speck, J. S., and Petroff, P. M., 2001, "Strain-Engineered Self-Assembled Semiconductor Quantum Dot Lattices," Appl. Phys. Lett., **78**(1), pp. 105–107.
[36] Khitun, A., Balandin, A., Liu, J. L., and Wang, K. L., 2000, "In-Plane Lattice Thermal Conductivity of a Quantum-Dot Superlattice," J. Appl. Phys., **88**(2), pp. 696–699.
[37] Cahill, D. G., Watson, S. K., and Pohl, R. O., 1992, "Lower Limit to the Thermal Conductivity of Disordered Crystals," Phys. Rev. B, **46**(10), pp. 6131–6140.
[38] Kim, W., and Majumdar, A., 2006, "Phonon Scattering Cross Section of Polydispersed Spherical Nanoparticles," J. Appl. Phys., **99**, p. 084306.
[39] Dove, M. T., 1993, *Introduction to Lattice Dynamics* (Cambridge Topics in Mineral Physics and Chemistry Vol. 4), Cambridge University Press, Cambridge, UK.
[40] Jian, Z., Kaiming, Z., and Xide, X., 1990, "Modification of Stillinger–Weber Potentials for Si and Ge," Phys. Rev. B, **41**(18), pp. 12915–12918.
[41] Chalopin, Y., Gillet, J.-N., and Volz, S., 2008, "Predominance of Thermal Contact Resistance in a Silicon Nanowire on a Planar Substrate," Phys. Rev. B, **77**(23), p. 233309.
[42] http://www.ivec.org/GULP/.
[43] Ziman, J. M., 1960, "Electrons and Phonons: The Theory of Transport Phenomena in Solids," *Oxford Classic Texts in the Physical Sciences*, Oxford University Press, Oxford, UK.
[44] Majumdar, A., 1993, "Microscale Heat Conduction in Dielectric Thin Films," ASME J. Heat Transfer, **115**(1), pp. 7–16.
[45] Vo, T. T. M., Williamson, A. J., Lordi, V., and Galli, G., 2008, "Atomistic Design of Thermoelectric Properties of Silicon Nanowires," Nano Lett., **8**(4), pp. 1111–1114.
[46] Glassbrenner, C. J., and Slack, G. A., 1964, "Thermal Conductivity of Silicon and Germanium From 3 K to the Melting Point," Phys. Rev., **134**(4A), pp. A1058–A1069.
[47] Slack, G. A., and Galginaitis, S., 1964, "Thermal Conductivity and Phonon Scattering by Magnetic Impurities in CdTe," Phys. Rev., **133**(1A), pp. A253–A268.
[48] McGaughey, A. J. H., and Kaviany, M., 2004, "Quantitative Validation of the Boltzmann Transport Equation Phonon Thermal Conductivity Model Under the Single-Mode Relaxation Time Approximation," Phys. Rev. B, **69**, p. 094303.
[49] Feynman, R. P., and Hibbs, A. R., 1965, *Quantum Mechanics and Path Integrals*, McGraw-Hill, New York.
[50] Klemens, P. G., 1955, "The Scattering of Low-Frequency Lattice Waves by Static Imperfections," Proc. Phys. Soc., London, Sect. A, **68**, pp. 1113–1128.
[51] Klemens, P. G., 1958, *Solid State Physics*, Vol. 7, F. Seitz and D. Turn, eds., Academic, New York.
[52] Turk, L. A., and Klemens, P. G., 1974, "Phonon Scattering by Impurity Platelet Precipitates in Diamond," Phys. Rev. B, **9**(10), pp. 4422–4428.
[53] Bohren, C. F., and Huffman, D. R., 1998, *Absorption and Scattering of Light by Small Particles*, Wiley, New York.
[54] van de Hulst, H. C., 1981, *Light Scattering by Small Particles*, Dover, New York.
[55] Berman, R., Foster, E. L., and Ziman, J. M., 1956, "The Thermal Conductivity of Dielectric Crystals: The Effect of Isotopes," Proc. R. Soc. London, Ser. A., **237**, pp. 344–354.
[56] Kittel, C., 2005, *Introduction to Solid State Physics*, 8th ed., Wiley, New York.

Examining Interfacial Diffuse Phonon Scattering Through Transient Thermoreflectance Measurements of Thermal Boundary Conductance

Pamela M. Norris[1]
e-mail: pamela@virginia.edu

Patrick E. Hopkins[2]

Department of Mechanical and Aerospace Engineering,
University of Virginia,
P.O. Box 400746,
Charlottesville, VA 22904-4746

Today's electronic and optoelectronic devices are plagued by heat transfer issues. As device dimensions shrink and operating frequencies increase, ever-increasing amounts of thermal energy are being generated in smaller and smaller volumes. As devices shrink to length scales on the order of carrier mean free paths, thermal transport is no longer dictated by the thermal properties of the materials comprising the devices, but rather the transport of energy across the interfaces between adjacent materials in the devices. In this paper, current theories and experiments concerning phonon scattering processes driving thermal boundary conductance (h_{BD}) are reviewed. Experimental studies of thermal boundary conductance conducted with the transient thermoreflectance technique challenging specific assumptions about phonon scattering during thermal boundary conductance are presented. To examine the effects of atomic mixing at the interface on h_{BD}, a series of Cr/Si samples was fabricated subject to different deposition conditions. The varying degrees of atomic mixing were measured with Auger electron spectroscopy. Phonon scattering phenomena in the presence of interfacial mixing were observed with the trends in the Cr/Si h_{BD}. The experimental results are reviewed and a virtual crystal diffuse mismatch model is presented to add insight into the effect of interatomic mixing at the interface. The assumption that phonons can only transmit energy across the interface by scattering with a phonon of the same frequency—i.e., elastic scattering, can lead to underpredictions of h_{BD} by almost an order of magnitude. To examine the effects of inelastic scattering on h_{BD}, a series of metal/dielectric interfaces with a wide range of vibrational similarity is studied at temperatures above and around materials' Debye temperatures. Inelastic scattering is observed and new models are developed to predict h_{BD} and its relative dependency on elastic and inelastic scattering events.
[DOI: 10.1115/1.3072928]

Keywords: thermal boundary conductance, pump probe transient thermoreflectance technique, diffuse phonon scattering, material diffusion, Auger electron spectroscopy, elemental characterization, elastic scattering, inelastic scattering, nanoscale solid-solid interfaces

1 Introduction

The ongoing trend of miniaturization on the nanoscale has created many new thermal challenges for device engineers and scientists. In many solid state devices, increased power densities in combination with continued size reductions are giving rise to thermal processes that cannot be predicted by traditional macroscopic laws and models. For example, as transistor gate lengths are continuously decreasing in an effort to continue the trends projected by Moore's law, power dissipation is becoming a growing concern. Moore's law is commonly reported as the doubling of transistor density on an integrated circuit (IC) every 18 months. As seen from the trends of the Intel® microprocessors since the turn of the 21st century, IC engineers have met and exceeded expectations of Moore's law [1]. Much of this progress is attributed to the ability of engineers and scientists to effectively manage the thermal issues that arise from the continued size reduction of the components in the ICs. However, in the most current and envisioned applications of nanostructures and nanodevices, thermal management is a serious issue that is impeding development and productivity [2].

With the continued reduction of feature sizes in these nanosystems, theories and predictions based on macroscopic principles must be abandoned in order to accurately deal with the thermal issues. This is a consequence of the characteristic lengths of materials in nanodevices reducing to sizes on the order of the mean free path, Λ, of the primary energy carriers in solids at device operating temperatures. As operating speeds increase, for example, the characteristic sizes of the transistors in the ICs are approaching dimensions on the order of 10 nm. Since multiple carrier-carrier scattering events do not occur when characteristic lengths are on the order of the mean free path, a local temperature gradient cannot be established, and therefore Fourier's law does not apply. This presents an increased challenge for managing the

[1]Corresponding author.
[2]Present address: Engineering Sciences Center, Sandia National Laboratories, P.O. Box 5800, Albuquerque, NM 87185-0346.

Contributed by the Heat Transfer Division of ASME for publication in the JOURNAL OF HEAT TRANSFER. Manuscript received June 12, 2008; final manuscript received October 8, 2008; published online February 20, 2009. Review conducted by Robert D. Tzou. Paper presented at the 2008 International Conference on Macro/Nanoscale Heat Transfer (MNHT2008), Tainan, Taiwan, January 6–9, 2008.

energy transport in these devices, since ultimately, heat is undesirable and must be removed from the active regions of these devices that are generating energetic carriers.

Although this nanoscale size effect poses a major problem for understanding energy transfer through materials in a device [3,4], as these materials become smaller, more critical to the thermal management of many nanoscale devices is understanding how energy is transferred *across the interfaces* of the many materials that make up a device. As device dimensions shrink, it is becoming more likely that an energy carrier will scatter at an interface between two adjacent materials, where the resistance to energy transfer at this interface is much higher than in the materials that form the interface [2]. This thermal boundary resistance, R_{BD} (the inverse of thermal boundary conductance, h_{BD}), gives rise to a temperature drop, ΔT, across the interface of materials where energy transport occurs.

Thermal boundary conductance, sometimes termed Kapitza conductance, was first observed by Kaptiza in 1941 [5] between copper and liquid helium by observing that in the presence of a heat flux across the copper/liquid helium boundary, a temperature discontinuity existed. This phenomenon can be caused by, for example, the differing transport properties of the materials adjacent to the interface [6] or a disordered region of the materials resulting from device fabrication conditions [7]. The thermal boundary conductance, h_{BD}, relates the heat flux to the temperature drop ΔT across the interface.

$$q = h_{BD}\Delta T \tag{1}$$

The consideration of h_{BD} is vital in the design of nanostructures used in, for example, IC design, thermal interface materials [8–10], thermoelectric devices [11,12], thin-film high temperature superconductors [13,14], vertical cavity surface emitting lasers [15], optical data storage media [16], ultrashort pulsed laser systems [17,18], and high power density field effect transistors [19,20].

In this paper, current theories and experiments concerning phonon scattering processes driving thermal boundary conductance (h_{BD}) are reviewed. Traditional models make assumptions about phonon scattering that limit their range of applicability. These models and assumptions are discussed in Sec. 2 along with the transient thermoreflectance (TTR) technique, a measurement technique common in measuring interfacial thermal conductance. The remainder of the paper will review experimental studies of thermal boundary conductance conducted with the TTR technique challenging specific assumptions about phonon scattering during interfacial heat transfer. The experimental results are summarized and several new models, developed as a result of these experiments, are reviewed.

2 Phonon Interfacial Transport: Theory and Measurements

Although much work has been done in the area of interfacial thermal transport, most of the work has been done at low temperatures (<10 K) and for liquid-solid interfaces. While there have been a few proposed theories for room temperature application, most of which are adaptations of the low temperature models, there is no model that reliably captures the variability in measured interfacial thermal conductance. An understanding of the basic transport mechanisms involved in interfacial transport is critical to the design and engineering of nanostructured material systems used in a wide range of technologies, from state-of-the-art nanoelectronics, to thermoelectric modules, to thermal barrier coatings used in turbine engines.

Thermal energy is transported in metallic materials nearly completely by the electron system, whereas in nonmetals, the energy is stored and transported by phonons. Phonon scattering, the main transport mechanism across a wide range of device interfaces, has been successfully predicted by various models in limiting cases. These models are based on the specular or diffuse nature of phonon scattering at the interface. When a phonon undergoes specular scattering, the angle of the incident phonon equals the reflected angle and the angle of the transmitted phonons can be determined by Snell's law. When a phonon undergoes diffuse scattering, the scattering event is completely independent of any information about the particle before the scattering event, such as the angle of incidence. The particle scatters with equal probability in all directions. The specularity parameter, p, estimates the probability that phonons are specularly scattered [21];

$$p = \exp\left[-\frac{16\pi^2\delta^2}{\lambda^2}\right] \tag{2}$$

where δ is the roughness parameter and λ is the phonon wavelength. In the case of interfaces, the roughness parameter, δ, is the mean square deviation of the height of the surface from the reference plane [22]. A representative wavelength of the phonon system approaching the interface can be estimated by the thermal coherence length, $\mathcal{L}_{\text{th}}$, which assuming a thermal spread of k_BT, can be calculated by [22]

$$\mathcal{L}_{\text{th}} = \frac{2\pi\hbar v}{k_BT} \tag{3}$$

Here k_B is Boltzmann's constant, $\hbar$ is Planck's constant, and v is the phonon group velocity. At low temperatures, $\mathcal{L}_{\text{th}}$ is large and p approaches 1 (completely specular scattering). As temperature increases, $\mathcal{L}_{\text{th}}$ decreases, which decreases the probability of specular scattering (increases the probability of diffuse scattering).

Specular scattering is most likely experienced by long wavelength phonons (which represent the majority of phonons that are excited at low temperatures) at perfectly smooth interfaces. For example, consider an acoustically hard material, such as diamond, at 5 K. The diamond phonons approach an interface with only one monolayer of roughness (the lattice constant of diamond is $\approx$3.57 Å). Given an average phonon velocity of $v_{\text{diamond}} = 14,367$ m s^{-1} [23], a specularity parameter of $p=0.997$ is calculated for the diamond phonon scattering. However, as temperature is increased up to 300 K, the specularity parameter drops down to $p=0$, indicating that all phonons will undergo diffuse scattering events.

To predict h_{BD} in the event of purely specular scattering, Little proposed the acoustic mismatch model (AMM) [24,25]. In the AMM the transmissivity, that is, the percentage of the incident phonons that will be transmitted across the interface, is calculated based on the ratio of acoustic impedances of the materials on either side of the interface. The AMM has proven successful at predicting h_{BD} at low temperatures ($T<7$ K) and at ideal interfaces [7]. However, this ideal case only represents a very limited population of interfaces in modern devices, which often operate at higher temperatures and have disordered regions near the interface that would induce diffuse scattering. To account for this type of phonon scattering, Swartz and Pohl [26] developed the diffuse mismatch model (DMM) to predict h_{BD} at more realistic interfaces.

To apply the DMM in its simplest form, the following assumptions must be made: (1) phonons are elastically scattered—i.e., a phonon from side 1 with frequency ω can only emit a phonon into side 2 with the same frequency ω after the scattering event (for discussions, side 1 will refer to the softer material with lower phonon velocities and side 2 will refer to the stiffer material with higher phonon velocities); (2) phonon scattering is completely diffuse—i.e., a scattered phonon has no memory of the mode (longitudinal or transverse) or direction of the incident phonon; and (3) the materials on both sides of the interface are elastically isotropic—i.e., the longitudinal and transverse acoustic velocities are constant in all crystallographic directions. The DMM is mathematically stated as

$$h_{BD}^{\mathrm{DMM}} = \frac{1}{4}\sum_j \int_0^{\omega_{i,j}^c} v_{i,j}\hbar\omega D_{i,j}(\omega)\frac{\partial f^0(\omega,T)}{\partial T}\zeta^{i\to 3-i}(\omega)d\omega \quad (4)$$

where the transmissivity from side i to side $3-i$, $\zeta^{i\to 3-i}$, has no angular or phonon mode dependence because of the nature of diffuse scattering, $D(\omega)$ is the density of states, ω is the phonon frequency, and v is the phonon velocity. The generalized notation of superscript $3-i$ denotes the side opposite to side i, so that the side opposite to side 1 is 2 and the side opposite to side 2 is 1 [26]. The subscripts i and j refer to the side and the phonon mode (longitudinal or transverse), respectively, and the superscript 0 on f^0 refers to an equilibrium distribution. Diffuse scattering will rethermalize the phonon system (thermalizing black boundaries) [4] so the phonon system can be described by the equilibrium Bose–Einstein distribution ($f^0(\omega,T)$) and can therefore be characterized by a temperature at the interface, T. The cutoff frequency, ω^c, of each phonon mode j can be calculated for the separate phonon modes assuming an isotropic Debye solid, $\omega_j^c = v_j(6\pi^2 N)^{1/3}$, where N is the total number of phonons per unit volume [27]. Assuming a Debye density of states, the transmission probability is calculated by [26]

$$\zeta^{i\to 3-i}(\omega) = \frac{\sum_j \frac{1}{v_{3-i,j}^2}}{\sum_j \frac{1}{v_{i,j}^2} + \sum_j \frac{1}{v_{3-i,j}^2}} = \frac{\frac{1}{v_{3-i,L}^2} + \frac{2}{v_{3-i,T}^2}}{\frac{1}{v_{i,L}^2} + \frac{2}{v_{i,T}^2} + \frac{1}{v_{3-i,L}^2} + \frac{2}{v_{3-i,T}^2}} = \zeta^{i\to 3-i} \quad (5)$$

which is a result of applying the principle of detailed balance [28] to the phonon fluxes from sides i and $3-i$ approaching a perfect interface and assuming single phonon elastic scattering.

This model has been shown to predict conductance across higher temperature interfaces ($T>15$ K) relatively well [7,26]. However, at much higher temperatures (such as the operating temperatures of high frequency microelectronic devices), the DMM has been shown to either underpredict or overpredict experimental data, depending on the material systems [6]. Neither the AMM and DMM accurately predict h_{BD} in most practical material systems at conditions of technological interest.

Another model for h_{BD}, the phonon radiation limit (PRL), estimates the maximum conductance for interfacial transport from elastic scattering [29]. Development of the PRL is very similar to that of the DMM. However, the PRL assumes that all of the phonons in side $3-i$ up to the cutoff frequency in side i (assuming $\omega_i^c < \omega_{3-i}^c$) contribute to thermal transport though elastic collisions ($\zeta^{3-i\to i}=1$). With these assumptions, the PRL is given as

$$h_{BD}^{\mathrm{PRL}} = \frac{1}{4}\sum_j \int_0^{\omega_{i,j}^c} v_{3-i,j}\hbar\omega D_{3-i,j}(\omega)\frac{\partial f^0(\omega,T)}{\partial T}d\omega \quad (6)$$

which represents the maximum conductance due to elastic scattering. Since the PRL represents the upper limit of the elastic contribution to thermal transport, it will always predict a higher h_{BD} than the DMM. The DMM and PRL predict a constant h_{BD} at temperatures approaching the Debye temperature, θ_D, of the lower Debye temperature material (acoustically "softer" material or the material with the lower phonon velocity). This has to do with the change in the phonon population of the metal film as a function of temperature, and the fundamental assumption of elastic scattering employed in the DMM and PRL.

3 Experimental Measurement of h_{BD} Using the Transient Thermoreflectance Technique

There are many different techniques that have been used to measure thermal boundary conductance. An in-depth review of these techniques put into historical context is given by Swartz and Pohl [26]. This paper reviews studies by several groups who have used the TTR technique to measure h_{BD} for a wide range of material interfaces. The TTR technique employs a "pump" light pulse that is focused to a small spot on the surface of a metallic film that, upon absorption of the incident photons by the electrons in the metal, creates a temperature rise in the electron system. This change in temperature of the film produces a proportional change in the reflectivity. The change in the reflectivity as the film cools by conduction into the underlying structures is measured with a time-delayed "probe" light pulse, which is focused onto the center of the heated region of the film.

The experimental results presented here were obtained using the TTR experimental setup shown schematically in Fig. 1. The primary laser output emanates from a Coherent RegA 9000 amplifier (seeded with a Coherent MIRA 900 oscillator) operating at a 250 kHz repetition rate with about 4 μJ/pulse and a 150 fs pulse width at 800 nm (1.55 eV), which is split at a 9:1 pump to probe ratio. The pump beam, which is modulated at 125 kHz by an acousto-optic modulator (AOM), provides a modulated sequence of excitation events on the sample surface. The probe beam passes through a half-wave plate, rotating the polarization by 90 deg relative to the pump, which enables improved noise filtering. The length of the probe path is set by precise control of a dovetail prism mounted on a variable delay stage, with a total maximum delay between the pump and probe pulses of 1500 ps. The probe is directed through a polarizing filter, oriented such that only the probe light is passed and not the pump, which is positioned before a silicon photodiode, which monitors the reflection of the probe beam off the sample. A lock-in amplifier triggered at the modulation frequency of the pump monitors the photodiode response to the modulation in intensity of the probe beam. The radii of the pump and probe beams are measured with a sweeping knife edge technique [30]. Although the low repetition rate of the RegA system and the "one shot on–one shot off" modulation rate of the pump beam ensure minimal residual heating between pump pulses, the phase of the signal must still be taken into account to account for electronic noise. Phase correction is performed by the procedures for signal phase adjustment outlined by Stevens et al. [30]. The thermal boundary conductance is determined by fitting the TTR data to a lumped capacitance thermal model with h_{BD} as the free parameter, as outlined in Refs. [31,32].

4 Inability of the DMM to Accurately Predict h_{BD}

The TTR method has been used to determine h_{BD} on a wide variety of interfaces and experimental measurements show a wide range of agreement with the DMM. This is easily seen in Fig. 2, which shows the ratio of measured h_{BD} with the TTR technique to predict h_{BD} with the DMM calculated via Eqs. (4) and (5) as a function of the ratio of the materials' Debye temperatures. The ratio of the two materials' Debye temperatures gives a quantitative value to compare the degree of differing vibrational states between two materials. If the ratio is close to unity, then the materials have very similar cutoff frequencies, and are considered acoustically matched. If the ratio is much smaller or greater than unity, then the samples are considered acoustically mismatched.

Figure 2 clearly demonstrates the inability of the DMM to accurately predict h_{BD}. It is seen that in acoustically well-matched material systems with a Debye temperature ratio close to 1, the DMM overpredicts the boundary conductance while for mismatched systems the DMM underpredicts the conductance by as much as an order of magnitude. It should be noted, however, that the interfaces of these samples were not abrupt junctions, and the influence of the possible formation of a finite-size mixing or two-phase region at the interface could not be determined. This work investigates the underprediction and overprediction of the DMM by systematically investigating two effects, interatomic mixing and inelastic scattering. These investigations seek to further explore the validity of the *single phonon elastic scattering assumption*.

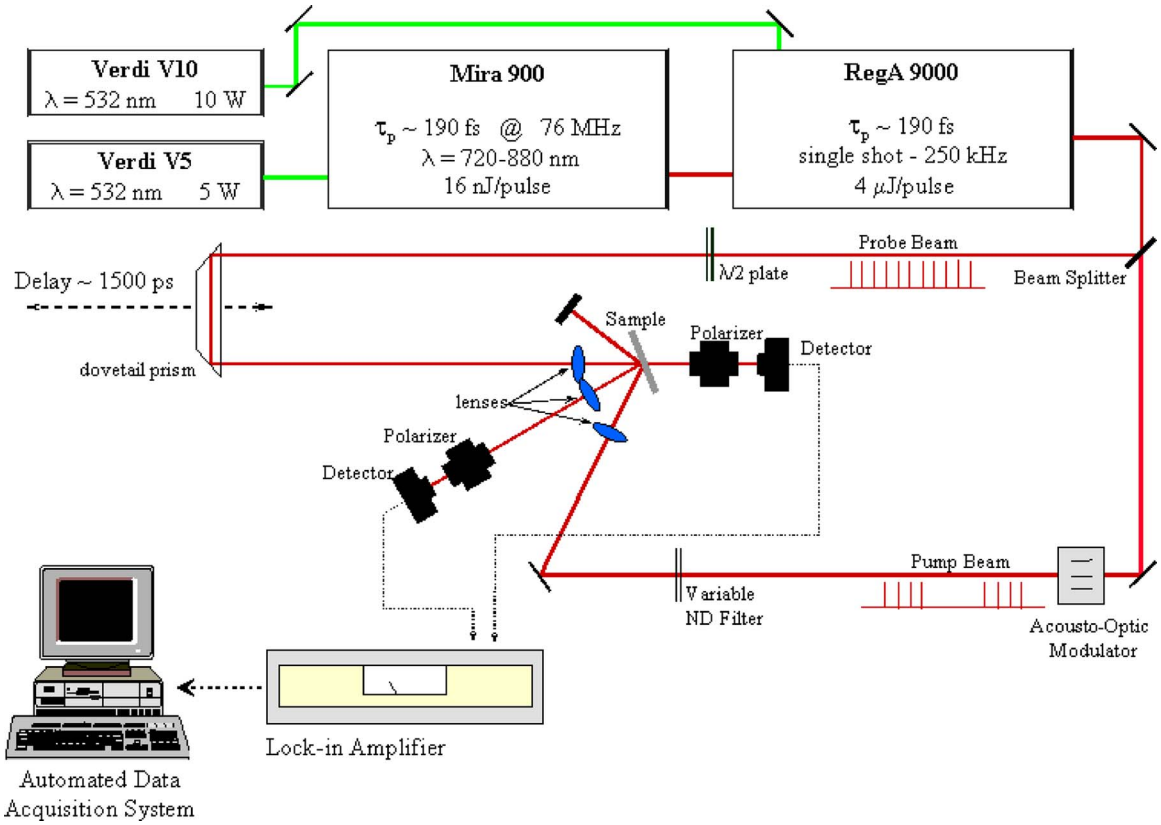

Fig. 1 Schematic of the transient thermoreflectance setup at the University of Virginia's Microscale Heat Transfer Laboratory

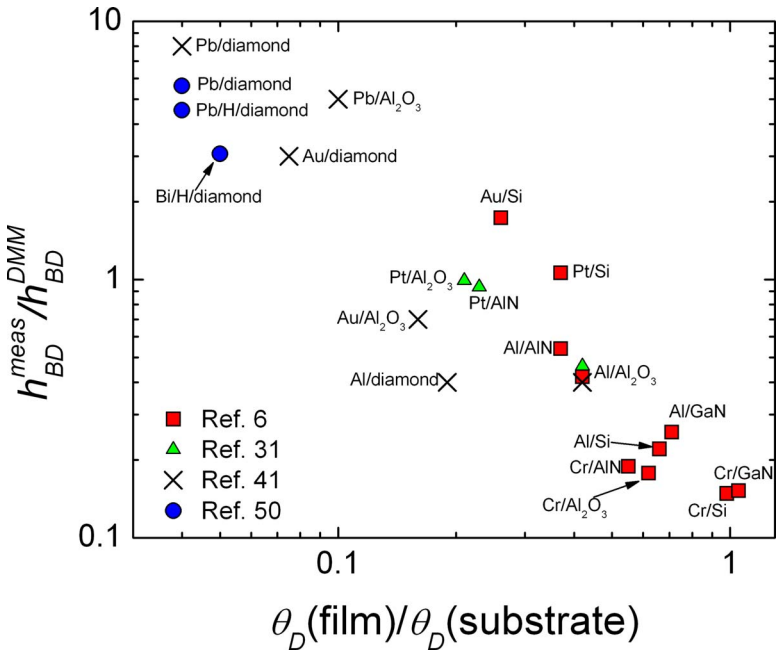

Fig. 2 Ratio of measured h_{BD}, h_{BD}^{meas}, to h_{BD} predicted from the DMM, h_{BD}^{DMM}, versus the ratios of the Debye temperatures of the metal film to the dielectric substrate. The data presented in this figure are selected results from Stevens et al. [6], Lyeo and Cahill [50], Stoner and Maris [41], and Hopkins et al. [31]. Some of the diamond substrates were subject to hydrogen termination before metal film deposition represented by the "H/diamond" after the metal film. The general trend shows that the DMM underpredicts measurements on acoustically mismatched samples and overpredicts measurements on acoustically matched samples.

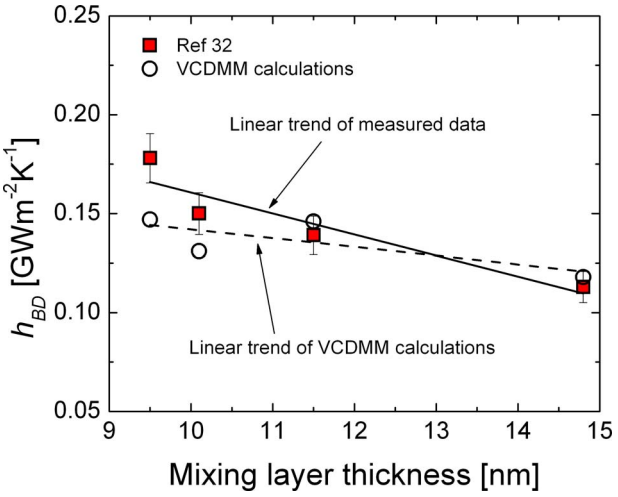

Fig. 3 Thermal boundary conductance measurements on various Cr/Si interfaces from Hopkins et al. [32] and corresponding VCDMM calculations from Beechem et al. [34]. Where the DMM predicts h_{BD} that is almost eight times larger (0.86 GW m^{-2} K^{-1}) than that measured on the samples with no dependence on mixing layer thickness or compositions, the VCDMM calculations are within 18% of the measured values and show similar trends with mixing layer thickness when taking into account the change in Si composition in the mixing region.

5 Effects of Interatomic Mixing on Thermal Boundary Conductance

In realistic nanodevices, pronounced interdiffusion or reactions at the interface can occur on the order of the characteristic length of the device, even at room temperature [33]. This interdiffusion results in the presence of a disordered and two-phase region at the interface of two materials, which contributes to the overall h_{BD} [26]. The effect of disorder, or a two-phase region, on h_{BD} has been the focus of many numerical studies [34–38], but the lack of experimental observation has led to conflicting theoretical results for h_{BD} as a result of multiphase and diffusion regions. For example, the scattering-mediated acoustic mismatch model, which assumes complete specular scattering, predicts a decrease in h_{BD} [39], while calculations by Kozorezov et al. [40] indicate an increase. Lattice dynamics calculations have offered insight into phonon interfacial transmission and h_{BD}, but these only apply to specific interfacial structures. There have been limited experimental studies on the role of mixing on h_{BD}, but the Norris Laboratory just recently was the first to publish quantitative experimental results relating thickness of the interdiffusion region to changes in measured h_{BD} [32].

Hopkins et al. [32] measured h_{BD} across different Cr/Si interfaces subjected to various fabrication conditions with the TTR technique. Chromium and Si represent acoustically matched materials with nearly identical Debye temperatures (θ_D(Cr)=630 K and θ_D(Si)=640 K) [27] and therefore have similar cutoff frequencies. The interfaces were characterized with Auger electron spectroscopy (AES) to quantify the thickness of material mixing and elemental concentration in the mixing region. The interfacial mixing observed in these AES profiles ensures completely diffuse scattering, so the DMM can be compared with the experimental data. The DMM predicts h_{BD} of 0.855 GW m^{-2} K^{-1} using a Debye approximation. The measured h_{BD} ranged from 0.178 GW m^{-2} K^{-1} in the sample with a 9.5 nm mixing layer thickness to 0.113 GW m^{-2} K^{-1} in the sample with 14.8 nm of mixing as shown in Fig. 3. The DMM overpredicts the measured h_{BD}, which has often been associated with poor interface quality and substrate damage [6,7,26,41].

A portion of the difference between the measured h_{BD} and that calculated from the DMM in well-matched samples such as Cr/Si could result from varying degrees of mixing. The DMM does not take into account an interfacial mixing layer. Although the scattering-mediated acoustic mismatch model accounts for multiple scattering events that could result from interfacial disorder [39], it assumes specular phonon reflection, which clearly is not a valid assumption in this case since the interfacial region was observed to be significantly disordered.

At an ideal interface with no mixing, a phonon from the Cr film scatters at the Cr/Si interface, and is either transmitted into the Si or reflected back into the Cr. From Eq. (5) the phonon transmission probability for the Cr/Si interface is $\zeta^{\mathrm{Cr}\rightarrow\mathrm{Si}}=37\%$, meaning that at the ideal interface, 37% of the phonons are transmitted from the Cr into the substrate. In the event of interfacial mixing, the phonons must propagate across a finite amount of space to conduct energy into the substrate. When these phonons scatter with Si at the beginning of the mixing layer, a certain percentage of the phonons are transmitted deeper into the mixing layer. As the thickness of the interfacial mixing layer increases, the probability that a phonon will scatter more than once increases thereby decreasing h_{BD}, which is expected with increased diffuse scattering in well-matched materials. Thus, the presence of an interfacial mixing region causing multiple elastic scattering events, which are not accounted for, may be the cause of the overestimation of the DMM in well-matched material systems with Debye temperature ratios close to 1.

6 Predicting the Interfacial Mixing Dependency of h_{BD} With the VCDMM

Beechem et al. [34] presented a virtual crystal diffuse mismatch model (VCDMM) to predict the influence of mixing region thickness and composition on h_{BD}. This model introduces a simple correction to the DMM through use of a virtual crystal to account for the manner by which energy propagates through the interfacial region. In this manner multiple scattering events occurring at the interface can be quantified allowing for more accurate prediction of h_{BD} as well as insight into the effect of interfacial quality on overall heat transfer.

To account for a finite interfacial thickness, the VCDMM replaces the interfacial region with a third material, the virtual crystal, which has properties that are a blend of the bulk materials on either side [42] and a thickness equal to the length of disorder. Incorporating the virtual crystal modifies the DMM to account for both the interaction between each of the bulk materials and interface as well as the now finite thickness of the interface.

The interaction between the two materials and the disordered region is investigated by estimating the conductance between each of the bulk materials and the virtual crystal. This is accomplished by applying the DMM for each of the now two interfaces with a modification of the transmission coefficient to account for the virtual crystal so that the transmission is calculated at the i/virtual crystal and $3-i$/virtual crystal interfaces. Again, this calculation assumes all solids are Debye solids. It follows that h_{BD} for the two-interface system is given by

$$h_{BD}^{\mathrm{VCDMM}}=\left[\frac{1}{h_{BD}^{i\rightarrow\mathrm{VC}}}+\frac{1}{h_{BD}^{3-i\rightarrow\mathrm{VC}}}\right]^{-1} \tag{7}$$

The above relation accounts for only the efficiency by which energy transfers from the bulk to the interface but does not analyze the ease by which energy propagates through the interfacial region. To examine this effect, the results of Eq. (7) are scaled according to the depth factor, Ξ, which is a ratio of the interfacial thickness, δ, to the mean free path of the virtual crystal, Λ_{VC} ($\Xi=\delta/\Lambda_{\mathrm{VC}}$). The interfacial thickness, δ, is also the roughness parameter used in Eq. (2). Using kinetic theory with the virtual crystal approximation for thermal conductivity [42] to estimate

the mean free path along with the measured thickness of the Cr/Si interface, the depth factor is calculated allowing for the estimation of h_{BD} from the VCDMM by

$$h_{BD}^{\mathrm{VCDMM}} = \left[\frac{\Xi}{h_{BD}^{i\to \mathrm{VC}}} + \frac{\Xi}{h_{BD}^{3-i\to \mathrm{VC}}} \right]^{-1} = \frac{\Lambda_{\mathrm{VC}}}{\delta} \left[\frac{1}{h_{BD}^{i\to \mathrm{VC}}} + \frac{1}{h_{BD}^{3-i\to \mathrm{VC}}} \right]^{-1} \tag{8}$$

Equation (8) describes the effect of interatomic mixing around the interface on phonon interfacial transport. However, in acoustically matched metal/dielectric material systems such as Cr/Si, another channel of energy transport associated with electron-phonon nonequilibrium could significantly affect interfacial energy transport [43]. In well-matched material systems, the thermal resistance associated with phonon-phonon interfacial transport, $R_{pp}=1/h_{pp}$, is relatively small and on the same order as the resistance associated with an electron-phonon nonequilibrium in the film near the interface, $R_{ep}=1/h_{ep}$, where this electron-phonon boundary conductance is given by [43]

$$h_{ep} = \sqrt{k_{pp} G} \tag{9}$$

where k_{pp} is the phonon thermal conductivity in the metal and G is the electron-phonon coupling factor of the metal [44–47]. Therefore, in acoustically matched material systems, R_{ep} must also be taken into account, which leads to

$$h_{BD}^{\mathrm{VCDMM}} = \left\{ \frac{1}{\sqrt{k_{pp} G}} + \Xi_j \left[\frac{1}{h_{BD}^{i\to \mathrm{VC}}} + \frac{1}{h_{BD}^{3-i\to \mathrm{VC}}} \right] \right\}^{-1} \tag{10}$$

Shown in Fig. 3 is a comparison of the virtual crystal model to the experimental data from Hopkins et al. [32]. The virtual crystal approach is within 18% of the measured values whereas the predicted h_{BD} of the DMM, which does not account for any interfacial mixing, is about eight times these values. In both prediction and measurement, there is a distinct trend of decreasing h_{BD} with increasing interfacial thickness. This results from the additional scattering, which occurs as the phonons must propagate through the disordered region.

7 Influence of Inelastic Phonon Scattering on Thermal Boundary Conductance

In an attempt to investigate the underpredictive trends of the DMM as seen in Fig. 2, several computational and experimental efforts have been undertaken. In 1993, Stoner and Maris [41] reported h_{BD} at a range of acoustically mismatched interfaces from 50 K to 300 K. As expected from the DMM, the measured h_{BD} decreased with an increase in sample mismatch and the change in h_{BD} decreased with temperature. In the sample with the greatest mismatch, Pb/diamond, values of h_{BD} were measured that exceeded the DMM prediction by two orders of magnitude. One possible explanation offered for the underestimate of h_{BD} by the DMM was the occurrence of inelastic scattering—i.e., one or more phonons of frequency ω_1 on side 1 were emitting one or more phonons of frequency ω_2 on side 2—thereby offering additional channels for transport not accounted for in the DMM. At a Pb/diamond interface, a high frequency diamond phonon could scatter at the interface and emit low frequency phonons on the Pb side.

As the interface temperature increases above the Debye temperature of the softer material (i.e., in the classical limit), the DMM predicts that h_{BD} is relatively constant. This is a result of the change in phonon population with temperature predicted by the Bose–Einstein distribution function. At temperatures close to a material's Debye temperature, the change in phonon population with temperature becomes linear. The DMM is a function of the temperature derivative of the Bose–Einstein distribution, which results in the constant h_{BD} predicted at higher temperatures ($T > \theta_D$) when elastic scattering is assumed. Assuming only elastic scattering and a Debye solid, the transmission coefficient is independent of temperature.

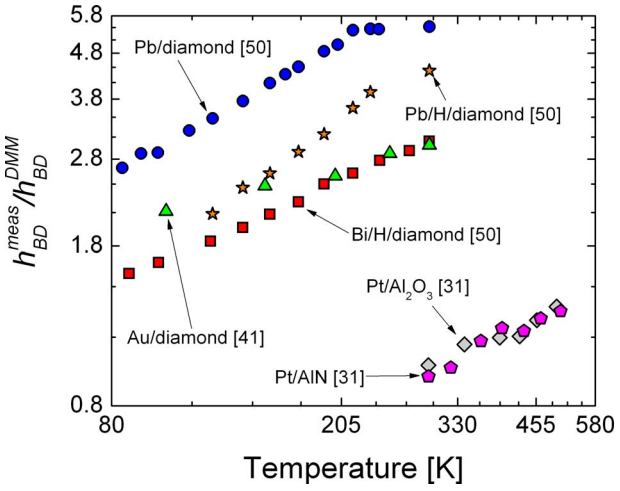

Fig. 4 Ratio of measured h_{BD}, h_{BD}^{meas}, to h_{BD} predicted from the DMM, h_{BD}^{DMM}, versus temperature for six different acoustically mismatches samples. The data presented in this figure are selected results of Lyeo and Cahill [50], Stoner and Maris [41], and Hopkins et al. [31]. Some of the diamond substrates were subject to hydrogen termination before metal film deposition represented by the H/diamond. The general trend shows that the increase in h_{BD} observed with temperature over the temperature range for each sample is much greater than the increase with temperature predicted by the DMM. These data show a linear trend in h_{BD} with temperature, which is evidence of inelastic scattering.

To check the temperature dependence of h_{BD}, Stevens et al. [37] performed molecular dynamics (MD) simulations at a range of temperatures. The simulations were conducted on both highly and lightly mismatched interfaces with Debye temperature ratios of 0.2 and 0.5. A strong linear relationship was observed in the h_{BD} results for the temperature range considered, with h_{BD} varying by nearly a factor of 4. This strong linear temperature dependence suggests a thermal transport mechanism that is dependent on temperature in the classical limit. The most likely explanation for this discrepancy is that while MD simulation accounts for both elastic and inelastic scattering at the interface, the DMM accounts only for elastic scattering. Chen et al. [48] used MD simulations to examine a Kr/Ar nanowire interface, showing a linear increase in h_{BD} with an increase in temperature from 35 K to 55 K, which they ascribed to anharmonic processes. Kosevich [49] considered the role of inelastic scattering on the phonon transmission probability using a multiharmonic model to show that inelastic scattering makes a greater contribution to h_{BD} than elastic scattering for interfaces with very different vibrational spectra.

Evidence of inelastic scattering has been observed experimentally by Lyeo and Cahill [50] at low temperatures ($T \leq T_{\mathrm{room}}$) and Hopkins et al. [31] at high temperatures ($T \geq T_{\mathrm{room}}$). Lyeo and Cahill [50] observed an approximately linear increase in h_{BD} over a temperature range of 80–300 K on carefully prepared Pb and Bi thin films on diamond substrates. Hopkins et al. [31] observed a linear trend in h_{BD} over temperatures from 300 K to 500 K on several different samples, including the heavily mismatched Pt/Al_2O_3 and Pt/AlN interfaces. The linear trends observed in these experimental works match the aforementioned simulation results, which suggested that multiple-phonon processes (inelastic scattering) can play a significant role in interface thermal conductance. However, these data do not agree with the trends predicted by the DMM. Selected data from Stoner and Maris [41], Lyeo and Cahill [50], and Hopkins et al. [31] are shown in Fig. 4, which

shows the ratio of measured h_{BD} to that predicted from the DMM for six different samples over a 200 K temperature range. It is apparent that in these mismatched samples, the measured data show an increasing linear trend, which is much greater than the slightly increasing if not constant predictions from the DMM.

The presence of inelastic scattering events, which add an additional channel of interfacial energy transport, may be the cause of the underestimation of the DMM in mismatched material systems with distinctly different Debye temperatures. In well-matched material systems, such as Cr/Si as previously studied, the difference between the modes in the film and substrate is very small, so the joint vibrational modes near the interface are most likely present in both the film and substrate making elastic scattering highly probable.

8 Joint Frequency Diffuse Mismatch Model

An underlying assumption governing the DMM is that a phonon transmits energy across an interface by emitting a phonon with the same frequency, i.e., the phonons are elastically scattered. Therefore, as the interface temperature increases above the Debye temperature of the softer material, the DMM predicts that h_{BD} is relatively constant. This implies that the DMM predicts a constant h_{BD} above ~ 100 K for Pb/diamond since $\theta_D(\mathrm{Pb}) = 105$ K [27]. In fact, the DMM predicts a constant h_{BD} above 100 K for any Pb interface regardless of the substrate. However, if inelastic phonon processes occur (i.e., a phonon with frequency $\omega^c_{\mathrm{diamond}}$ scatters into several phonons with frequencies below ω^c_{Pb}), then the change in h_{BD} with temperature would be related to the change in the diamond phonon population in addition to the Pb population.

Hopkins and Norris [51] developed a simple correction to the DMM to account for the discrepancy between the DMM and the experimental data in the event of inelastic scattering. By blending the vibrational spectra of the film and substrate materials, an approximation for the contribution of the inelastic modes was developed with a diffuse scattering assumption, the joint frequency diffuse mismatch model (JFDMM). The JFDMM assumes the same form as the DMM but uses a modified phonon velocity that is taken as a weighted average of the velocities of the phonon systems from sides 1 and 2. Consequently, this results in a weighted average of the phonon spectra used in the h_{BD} calculation, given by

$$D_{\mathrm{mod},j} = \frac{\omega^2}{2\pi^2 v^3_{\mathrm{mod},j}}, \quad \omega \leq \omega^c_{\mathrm{mod},j} \tag{11}$$

$$\omega^c_{\mathrm{mod},j} = v_{\mathrm{mod},j}\{6\pi^2(\xi_i N_i + \xi_{3-i} N_{3-i})\}^{1/3} \tag{12}$$

$$v_{\mathrm{mod},j} = \xi_i v_i + \xi_{3-i} v_{3-i} \tag{13}$$

where the weighting factor ξ_i is simply a percentage of the composition of the phonons in each material in the unit volume, expressed mathematically as

$$\xi_i = \frac{\dfrac{N_i}{N_{3-i}} M_i}{\dfrac{N_i}{N_{3-i}} M_i + M_{3-i}} \tag{14}$$

where M_i is the atomic mass of side i. Since the DMM is calculated per unit volume, to better estimate the percent composition of the joint vibrating atoms near the interface, the relative number of phonons on each side must be taken into account by including the number of oscillators per unit volume, N. This is similar to calculating the percent composition of atoms in any compound (for example, the %O in H_2O). This approximation introduces high frequency phonons that are available in the vibrational spectrum in side 2 (stiffer material or the substrate in the aforementioned data) but not side 1 (softer material or the film in the aforementioned data) into the incident heat flux. The JFDMM increases the prediction of h_{BD} by a factor that is proportional to the side 2 vibrational spectrum, giving an approximation for inelastic scattering. The transmission coefficient for the JFDMM is still assumed to be calculated with Eq. (5); note that this relaxes the assumption of detailed balance since the JFDMM assumes a modified phonon flux.

Figure 5 compares the predictions from the DMM and JFDMM to experimental TTR data shown in Fig. 4. Figure 5 shows the ratio of measured h_{BD} to the predicted h_{BD} by the DMM and JFDMM. This figure compares predictive trends for data on Pt/AlN [31], Pt/Al_2O_3 [31], Au/diamond [41], Bi/H/diamond [50], and Pb/diamond and Pb/H/diamond [50]. The model calculations use elastic constants to calculate phonon velocities and material properties to calculate the cutoff frequencies [23]; the material properties used in these calculations are listed in Table 1. The ratio of measured data to DMM predictions is shown by the filled symbols and the ratio of measured data to the JFDMM is represented by the outline of the symbols with no fill. Note that the models cannot distinguish between different depositions or interface conditions [32,52], so the predictions by the models on the hydrogen terminated diamond and non-hydrogen-terminated substrates are the same. The JFDMM predicts a closer value and better temperature dependent trend to the experimental data than the DMM. The JFDMM shows a different temperature dependent trend than the DMM, which is more in line with the experimental data since it assumes that phonons with frequencies higher than the cutoff frequency in side 1 can participate in h_{BD}. These data sets represent material systems that show evidence of inelastic scattering at these temperatures. The agreement between the JFDMM and the experimental data is much closer in the heavily mismatched materials than the not-as-heavily mismatched materials. This could be due to the contributions of inelastic scattering to h_{BD} being much greater in the heavily mismatched material systems [53].

9 Inelastic and Elastic Scattering Contributions to Thermal Boundary Conductance

Although the JFDMM shows improvement in h_{BD} predictions in the event that inelastic phonon scattering dominates interfacial transport, this method makes necessary assumptions about phonon transport that deserve further attention. The main assumption of the JFDMM is that a fraction of the available phonon states in the substrate are present in the film. In actuality, the atoms around the interface are vibrating at joint modes by Newton's law of motion [54]. The maximum allowable frequency for these joint modes is the substrate cutoff frequency. However, dampening of these modes will occur due to the differing interatomic forces of the film and substrate. This prevents the joint modes from oscillating at certain frequencies. This continuum phenomenon is paralleled quantum mechanically in the JFDMM through the weighted average of the two materials' phonon states in the incident flux. The weighting factor, ξ, reflects the dampening of the substrate modes, and is used to enhance the incident phonon flux to take into account the joint vibrations that are allowed after dampening effects. However, without computationally expensive computer simulations or a rigorous theoretical treatment, this weighting factor cannot be explicitly determined for every phonon mode, and therefore should be viewed as an estimation of the joint modes participating in h_{BD}. The JFDMM can be viewed as a starting point for estimating the maximum h_{BD} due to inelastic scattering.

Consider atoms vibrating at joint modes around the interface with no dampening effects. These atoms can therefore vibrate at all allowable frequencies up to the maximum allowed frequency in the substrate. Atoms on sides 1 and 2 will be coupled in joint vibrational modes with frequencies up to the cutoff frequency of side 2. This is paralleled in the JFDMM by making the weighting factors (Eq. (14)) $\xi_1 = 0$ and $\xi_2 = 1$, which conceptually is treating h_{BD} as a function of the incident phonon flux from side 2 transmitted into side 1. This simplifies Eqs. (11)–(13) to $D_{\mathrm{mod},j} = D_{2,j}$,

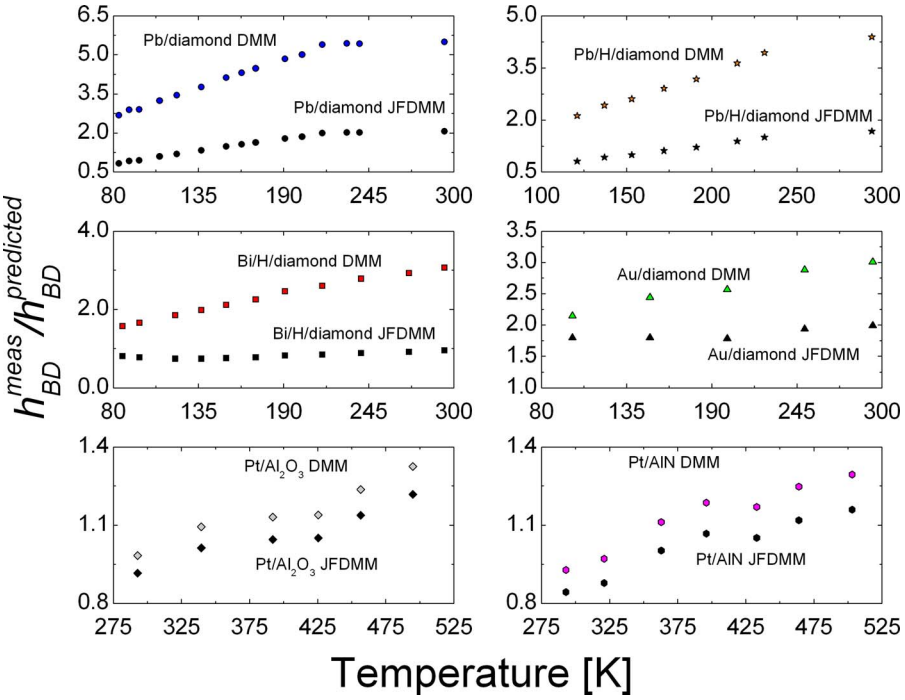

Fig. 5 Ratio of measured h_{BD}, h_{BD}^{meas}, to h_{BD} predicted from the DMM and JFDMM versus temperature for six different acoustically mismatched samples. The data presented in this figure are selected results of Lyeo and Cahill [50], Stoner and Maris [41], and Hopkins et al. [31]. The JFDMM captures the temperature trends in the data that exhibit inelastic scattering, and predicts h_{BD} values that are more in line with the experimental measurements.

$\omega_{\text{mod},j}^{c}=\omega_{2,j}^{c}$, and $v_{\text{mod},j}=v_{2,j}$, respectively, and redefines Eq. (4) in terms of the flux transmitted from side 2 to side 1, given as [53]

$$h_{BD}^{\text{inel}}=\frac{1}{4}\sum_{j}\int_{0}^{\omega_{2,j}^{c}} v_{3-i,j}\hbar\omega D_{3-i,j}(\omega)\frac{\partial}{\partial T}[f^{0}(\omega,T)\zeta_{3-i}^{\text{inel}}(T)]d\omega \tag{15}$$

From the nature of diffuse scattering, the inelastic transmission probability is $\zeta_{2}^{\text{inel}}(T)=1-\zeta_{1}^{\text{inel}}(T)$, which is different from the elastic transmission probability calculated with Eq. (5). Equation (15) allows higher frequency phonons that do not exist in the film to participate in h_{BD}. Without knowledge of the explicit temperature dependence of $\zeta_{2}^{\text{inel}}(T)$, h_{BD} cannot be calculated. However, the use of Eq. (15) along with experimental data can give important insights into the role of inelastic phonon scattering in thermal boundary conductance.

Hopkins and Norris [53] used Eq. (15) to develop the inelastic phonon radiation limit (IPRL). Consider the case where all available substrate phonons are participating in h_{BD}. In this case, the probability that a phonon on side 2 is inelastically transmitted (i.e., scatters into lower frequency phonons and is transmitted into side 1) is unity. By letting $\zeta_{2}^{\text{inel}}(T)=1$, Eq. (15) becomes an expression for the largest allowable thermal boundary conductance due to inelastic scattering, or the IPRL, expressed as

$$h_{BD}^{\text{IPRL}}=\frac{1}{4}\sum_{j}\int_{0}^{\omega_{2,j}^{c}} v_{2,j}\hbar\omega D_{2,j}(\omega)\frac{\partial f^{0}(\omega,T)}{\partial T}d\omega \tag{16}$$

The IPRL assumes that all side 2 phonons are transmitted into the film, and does not explicitly take into account elastic or inelastic scattering processes. However, by allowing all frequencies of phonons in side 2 to transmit energy into side 1, which has the lower cutoff frequency, inelastic scattering is implied. Note that in this limit, similar to the JFDMM, which also takes into account some inelastic scattering, the assumption of equilibrium is relaxed and therefore the principle of detailed balance is not enforced.

From the trends in the IPRL as compared with the PRL and experimental data, the relative contributions of elastic and inelastic scattering can be examined [53]. Above the film's Debye temperature, it is apparent that contributions from elastic scattering

Table 1 Pertinent thermophysical properties of materials in this work: from top to bottom: molar mass—M [23], molar density—n [23], longitudinal and transverse phonon velocities (which were calculated from the elastic lattice constants), v_L and v_T [23], Debye temperature—θ_D [27], and mass density—ρ [23]

	Al_2O_3	AlN	Au	Bi	Cr	Diamond	Pb	Pt	Si
M (kg mol^{-1})	0.102	0.0203	0.197	0.209	0.052	0.012	0.207	0.195	0.028
n (mol m^{-3})	38,922	160,345	97,970	46,794	138,269	290,008	55,990	110,872	83,214
v_L (m s^{-1})	10,890	11,120	3,390	1,543	6,980	17,500	2,350	4,174	8,970
v_T (m s^{-1})	6,450	6,267	1,290	1,107	4,100	12,800	970	1,750	5,332
θ_D (K)	1,043	1,150	165	119	630	2,230	105	240	645
ρ (kg m^{-3})	3,970	3,255	19,300	9,780	7,190	3,512	11,590	21,620	2,330

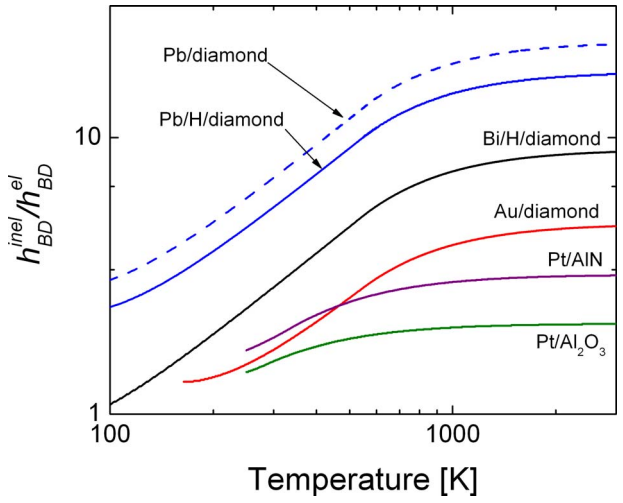

Fig. 6 Relative magnitude of inelastic scattering on h_{BD}. This ratio compares the inelastic contribution to h_{BD} to the elastic contribution. Details of these calculations are found in Ref. [53]. The role of inelastic phonon scattering increases as the acoustic mismatch of the film and substrate becomes greater. The range in which h_{BD} should increase linearly with temperature due to inelastic scattering also increases with acoustic mismatch.

will result in a constant h_{BD}. However, inelastic scattering events will drive the linear trend in h_{BD}. Therefore, the total thermal boundary conductance in the classical limit ($T > \theta_D$) will be a blend of both the constant elastic contribution and the temperature dependent inelastic phonon scattering contributions. To demonstrate the relative contribution to h_{BD} due to inelastic scattering as compared with that due to elastic scattering, the ratio $h_{BD}^{\text{inel}}/h_{BD}^{\text{el}}$ is plotted versus temperature in the classical regime in Fig. 6 for the six interfaces studied. As expected, the inelastic contributions compared with the elastic contributions to h_{BD} in Pb, Bi, and Au on diamond are more temperature dependent than the relative contribution in the Pt/Al_2O_3 and Pt/AlN samples due to the higher Debye temperature of diamond than Al_2O_3 and AlN. This also leads to the inelastic contributions becoming independent of temperature at higher temperatures in the diamond samples as compared with the Al_2O_3 and AlN substrate samples. In fact, the high temperature limits of the diamond substrate samples are not reached until the interface temperatures are driven above the melting temperature of the metal, meaning that in nanostructures composed of these interfaces, h_{BD} will continually increase with temperature until melting. Also, in the high temperature limit, as the mismatch between the materials adjacent to the interface grows, the contributions of inelastic phonon scattering to thermal boundary conductance increase.

10 Conclusions

The ongoing trend of miniaturization on the nanoscale has created many new thermal challenges for device engineers and scientists. An understanding of nanoscale energy transport is becoming increasingly important as standard device sizes continually decrease and classical heat transfer laws fail to predict energy transfer processes in a growing number of nanodevices. In nanodevices, it is more likely that energy carriers will scatter at an interface between two adjacent materials, where the resistance to energy transfer is much higher, than in the materials that form the interface. Traditionally used models do not adequately predict the rate of energy transfer across these interfaces, which is governed by the thermal boundary conductance, h_{BD}. The most commonly used model of h_{BD}, the DMM, overpredicts h_{BD} in well-matched material systems with a Debye temperature ratio close to 1 and underpredicts h_{BD} for mismatched material systems by as much as an order of magnitude. The major limiting assumptions in the DMM are examined using experimental results obtained using the TTR technique, and several new models are presented.

A study of the interfacial transport in the presence of atomic mixing at the boundary between two materials lends insights into the effect of multiple-phonon scattering. The presence of an interfacial mixing region causing multiple elastic scattering events that are not accounted for may be the cause of the overestimation of the DMM in well-matched material systems with Debye temperature ratios close to 1. The VCDMM, which introduces a mixing region to the DMM, offers insight into the scattering processes that affect h_{BD} at these imperfect interfaces.

Experimental measurements of h_{BD} at elevated temperatures ($T \geq \theta_D$) enable exploration of the influence of inelastic scattering mechanisms. A linear trend in h_{BD} has been observed in several samples, even when the temperature is driven above the Debye temperature of the softer film material. Since the DMM only accounts for elastic scattering, the h_{BD} calculations from the DMM predict a relatively constant temperature trend. The measured linear trend shows that inelastic scattering contributes to interfacial transport at temperatures around and above the Debye temperature of a material adjacent to a solid interface.

To further understand the role of inelastic and elastic scattering events in interfacial transport, the JFDMM was developed, which takes into account the contributions of inelastic scattering to h_{BD} by considering the phonon flux at the interface to consist of frequencies that exist in both solids. The JFDMM shows improved values and trends in h_{BD} predictions from the DMM. From the basic assumptions of the JFDMM, an upper limit to h_{BD} was derived assuming all phonons are participating in energy transfer through inelastic scattering—the IPRL. To further understand inelastic scattering, experimental data on several interfaces were quantitatively compared, and the relative contributions of inelastic and elastic scattering to h_{BD} at these different interfaces were observed. The relative contribution of inelastic scattering to h_{BD} decreases as the materials adjacent to the interface become vibrationally similar.

Acknowledgment

The authors gratefully acknowledge financial support from the Office of Naval Research MURI program, Grant No. N00014-07-1-0723. P.E.H. also gratefully acknowledges support from the NSF Graduate Student Research Program.

Nomenclature

D = spectral phonon density of states per unit volume
f = phonon statistical distribution of energy states
G = electron-phonon coupling factor, W m^{-3} K^{-1}
$\hbar$ = Planck's constant divided by 2π, J s
h_{BD} = thermal boundary conductance, W m^{-2} K^{-1}
k_B = Boltzmann's constant, J K^{-1}
$\mathcal{L}_{\text{th}}$ = thermal coherence length, m
M = molar mass, kg mol^{-1}
N = phonon number density, m^{-3}
n = molar density, mol m^{-3}
p = specularity parameter
R_{BD} = thermal boundary resistance, W^{-1} m^2 K^1
T = temperature, K
v = group velocity, m s^{-1}

Greek Symbols

δ = interfacial roughness (thickness), m
θ_D = Debye temperature, K
ζ = interfacial transmission probability
Λ = mean free path, m
λ = wavelength, m

ρ = mass density, kg m^{-3}
Ξ = interfacial depth factor
ω = angular frequency of vibration, s^{-1}
ξ = weight factor for vibrational states

Subscripts

ep = due to electron-phonon scattering
i = side i
j = polarization (longitudinal or transverse)
L = longitudinal mode
mod = modified to account for joint vibrational states
pp = due to phonon-phonon scattering
T = transverse mode

Superscripts

0 = equilibrium
c = cutoff
DMM = calculated with the diffuse mismatch model
el = accounting for elastic processes
$i \rightarrow 3-i$ = from side i to side $3-i$
$i \rightarrow$ VC = from side i to the virtual crystal
inel = accounting for inelastic processes
IPRL = calculated with the inelastic phonon radiation limit
meas = measured with the TTR technique
PRL = calculated with the phonon radiation limit
VCDMM = calculated with the virtual crystal diffuse mismatch model

References

[1] Foster, L. E., 2006, *Nanotechnology: Science, Innovation, and Opportunity*, Pearson Education, Inc., Upper Saddle River, NJ.
[2] Cahill, D. G., Ford, W. K., Goodson, K. E., Mahan, G. D., Majumdar, A., Maris, H. J., Merlin, R., and Phillpot, S. R., 2003, "Nanoscale Thermal Transport," J. Appl. Phys., **93**, pp. 793–818.
[3] Tien, C. L., Majumdar, A., and Gerner, F. M., 1998, *Microscale Energy Transport*, Taylor and Francis, Washington, DC.
[4] Majumdar, A., 1993, "Microscale Heat Conduction in Dielectric Thin Films," ASME J. Heat Transfer, **115**, pp. 7–16.
[5] Kapitza, P. L., 1941, "The Study of Heat Transfer in Helium II," Zh. Eksp. Teor. Fiz. Pis'ma Red., **11**, pp. 1–31.
[6] Stevens, R. J., Smith, A. N., and Norris, P. M., 2005, "Measurement of Thermal Boundary Conductance of a Series of Metal-Dielectric Interfaces by the Transient Thermoreflectance Technique," ASME J. Heat Transfer, **127**, pp. 315–322.
[7] Swartz, E. T., and Pohl, R. O., 1987, "Thermal Resistances at Interfaces," Appl. Phys. Lett., **51**, pp. 2200–2202.
[8] Chung, D. D. L., 2001, "Thermal Interface Materials," J. Mater. Eng. Perform., **10**, pp. 56–59.
[9] Prasher, R. S., 2006, "Thermal Interface Materials: Historical Perspective, Status, and Future Directions," Proc. IEEE, **94**, pp. 1571–1586.
[10] Singhal, V., Siegmund, T., and Garimella, S. V., 2004, "Optimization of Thermal Interface Materials for Electronics Cooling Applications," IEEE Trans. Compon. Packag. Technol., **27**, pp. 244–252.
[11] Da Silva, L. W., and Kaviany, M., 2004, "Micro-Thermoelectric Cooler: Interfacial Effects on Thermal and Electrical Transport," Int. J. Heat Mass Transfer, **47**, pp. 2417–2435.
[12] Mahan, G. D., and Woods, L. M., 1998, "Multilayer Thermionic Refrigeration," Phys. Rev. Lett., **80**, pp. 4016–4019.
[13] Phelan, P. E., Song, Y., Nakabeppu, O., Ito, K., Hijikata, K., Ohmori, T., and Torikoshi, K., 1994, "Film/Substrate Thermal Boundary Resistance for an Er-Ba-Cu-O High-T_C Thin Film," ASME J. Heat Transfer, **116**, pp. 1038–1041.
[14] Phelan, P. E., 1998, "Application of Diffuse Mismatch Theory to the Prediction of Thermal Boundary Resistance in Thin-Film High-T_C Superconductors," ASME J. Heat Transfer, **120**, pp. 37–43.
[15] Chen, G., Tien, C. L., Wu, X., and Smith, J. S., 1994, "Thermal Diffusivity Measurement of GaAs/AlGaAs Thin-Film Structures," ASME J. Heat Transfer, **116**, pp. 325–331.
[16] Kim, E.-K., Kwun, S.-I., Lee, S.-M., Seo, H., and Yoon, J.-G., 2000, "Thermal Boundary Resistance at $Ge_2Sb_2Te_5/ZnS:SiO_2$ Interface," Appl. Phys. Lett., **76**, pp. 3864–3866.
[17] Qiu, T. Q., and Tien, C. L., 1994, "Femtosecond Laser Heating of Multi-Layer Metals—I. Analysis," Int. J. Heat Mass Transfer, **37**, pp. 2789–2797.
[18] Qiu, T. Q., Juhasz, T., Suarez, C., Bron, W. E., and Tien, C. L., 1994, "Femtosecond Laser Heating of Multi-Layer Metals—II. Experiments," Int. J. Heat Mass Transfer, **37**, pp. 2799–2808.
[19] Smith, A. N., and Calame, J. P., 2004, "Impact of Thin Film Thermophysical Properties on Thermal Management of Wide Bandgap Solid-State Transistors," Int. J. Thermophys., **25**, pp. 409–422.
[20] Majumdar, A., Fushinobu, K., and Hijikata, K., 1995, "Effect of Gate Voltage on Hot-Electron and Hot-Phonon Interaction and Transport in a Submicrometer Transistor," J. Appl. Phys., **77**, pp. 6686–6694.
[21] Zhang, Z., 2007, *Nano/Microscale Heat Transfer*, McGraw-Hill, New York.
[22] Chen, G., 2005, *Nanoscale Energy Transport and Conversion: A Parallel Treatment of Electrons, Molecules, Phonons, and Photons*, Oxford University Press, New York.
[23] Gray, D. E., 1972, *American Institute of Physics Handbook*, McGraw-Hill, New York.
[24] Cheeke, J. D. N., Ettinger, H., and Hebral, B., 1976, "Analysis of Heat Transfer Between Solids at Low Temperatures," Can. J. Phys., **54**, pp. 1749–1771.
[25] Little, W. A., 1959, "The Transport of Heat Between Dissimilar Solids at Low Temperatures," Can. J. Phys., **37**, pp. 334–349.
[26] Swartz, E. T., and Pohl, R. O., 1989, "Thermal Boundary Resistance," Rev. Mod. Phys., **61**, pp. 605–668.
[27] Kittel, C., 1996, *Introduction to Solid State Physics*, Wiley, New York.
[28] Vincenti, W. G., and Kruger, C. H., 2002, *Introduction to Physical Gas Dynamics*, Krieger, Malabar, FL.
[29] Snyder, N. S., 1970, "Heat Transport Through Helium II: Kapitza Conductance," Cryogenics, **10**, pp. 89–95.
[30] Stevens, R. J., Smith, A. N., and Norris, P. M., 2006, "Signal Analysis and Characterization of Experimental Setup for the Transient Thermoreflectance Technique," Rev. Sci. Instrum., **77**, p. 084901.
[31] Hopkins, P. E., Stevens, R. J., and Norris, P. M., 2008, "Influence of Inelastic Scattering at Metal-Dielectric Interfaces," ASME J. Heat Transfer, **130**, p. 022401.
[32] Hopkins, P. E., Norris, P. M., Stevens, R. J., Beechem, T., and Graham, S., 2008, "Influence of Interfacial Mixing on Thermal Boundary Conductance Across a Chromium/Silicon Interface," ASME J. Heat Transfer, **130**, p. 062402.
[33] Poate, J. M., Tu, K. N., and Mayer, J. W., 1978, *Thin Films—Interdiffusion and Reactions*, Wiley, New York, pp. 1–12.
[34] Beechem, T. E., Graham, S., Hopkins, P. E., and Norris, P. M., 2007, "The Role of Interface Disorder on Thermal Boundary Conductance Using a Virtual Crystal Approach," Appl. Phys. Lett., **90**, p. 054104.
[35] Kechrakos, D., 1991, "The Role of Interface Disorder in the Thermal Boundary Conductivity Between Two Crystals," J. Phys.: Condens. Matter, **3**, pp. 1443–1452.
[36] Ren, S.-F., Cheng, W., and Chen, G., 2006, "Lattice Dynamics Investigations of Phonon Thermal Conductivity of Si/Ge Superlattices With Rough Interfaces," J. Appl. Phys., **100**, p. 103505.
[37] Stevens, R. J., Zhigilei, L. V., and Norris, P. M., 2007, "Effects of Temperature and Disorder on Thermal Boundary Conductance at Solid-Solid Interfaces: Nonequilibrium Molecular Dynamics Simulations," Int. J. Heat Mass Transfer, **50**, pp. 3977–3989.
[38] Kechrakos, D., 1990, "The Phonon Boundary Scattering Cross Section at Disordered Crystalline Interfaces: A Simple Model," J. Phys.: Condens. Matter, **2**, pp. 2637–2652.
[39] Prasher, R. S., and Phelan, P. E., 2001, "A Scattering-Mediated Acoustic Mismatch Model for the Prediction of Thermal Boundary Resistance," ASME J. Heat Transfer, **123**, pp. 105–112.
[40] Kozorezov, A. G., Wigmore, J. K., Erd, C., Peacock, A., and Poelaert, A., 1998, "Scattering-Mediated Transmission and Reflection of High-Frequency Phonons at a Nonideal Solid-Solid Interface," Phys. Rev. B, **57**, pp. 7411–7414.
[41] Stoner, R. J., and Maris, H. J., 1993, "Kapitza Conductance and Heat Flow Between Solids at Temperatures From 50 to 300 K," Phys. Rev. B, **48**, pp. 16373–16387.
[42] Abeles, B., 1963, "Lattice Thermal Conductivity of Disordered Semiconductor Alloys at High Temperatures," Phys. Rev., **131**, pp. 1906–1911.
[43] Majumdar, A., and Reddy, P., 2004, "Role of Electron-Phonon Coupling in Thermal Conductance of Metal-Nonmetal Interfaces," Appl. Phys. Lett., **84**, pp. 4768–4770.
[44] Kaganov, M. I., Lifshitz, I. M., and Tanatarov, L. V., 1957, "Relaxation Between Electrons and the Crystalline Lattice," Sov. Phys. JETP, **4**, pp. 173–178.
[45] Qiu, T. Q., and Tien, C. L., 1993, "Size Effects on Nonequilibrium Laser Heating of Metal Films," ASME J. Heat Transfer, **115**, pp. 842–847.
[46] Qiu, T. Q., and Tien, C. L., 1993, "Heat Transfer Mechanisms During Short-Pulse Laser Heating of Metals," ASME J. Heat Transfer, **115**, pp. 835–841.
[47] Hostetler, J. L., Smith, A. N., Czajkowsky, D. M., and Norris, P. M., 1999, "Measurement of the Electron-Phonon Coupling Factor Dependence on Film Thickness and Grain Size in Au, Cr, and Al," Appl. Opt., **38**, pp. 3614–3620.
[48] Chen, Y., Li, D., Yang, J., Wu, Y., Lukes, J., and Majumdar, A., 2004, "Molecular Dynamics Study of the Lattice Thermal Conductivity of Kr/Ar Superlattice Nanowires," Physica B, **349**, pp. 270–280.
[49] Kosevich, Y. A., 1995, "Fluctuation Subharmonic and Multiharmonic Phonon Transmission and Kapitza Conductance Between Crystals With Very Different Vibrational Spectra," Phys. Rev. B, **52**, pp. 1017–1024.
[50] Lyeo, H.-K., and Cahill, D. G., 2006, "Thermal Conductance of Interfaces Between Highly Dissimilar Materials," Phys. Rev. B, **73**, p. 144301.

[51] Hopkins, P. E., and Norris, P. M., 2007, "Effects of Joint Vibrational States on Thermal Boundary Conductance," Nanoscale Microscale Thermophys. Eng., **11**, pp. 247–257.
[52] Hopkins, P. E., and Norris, P. M., 2006, "Thermal Boundary Conductance Response to a Change in Cr/Si Interfacial Properties," Appl. Phys. Lett., **89**, p. 131909.
[53] Hopkins, P. E., and Norris, P. M., 2009, "Relative Contributions of Inelastic and Elastic Diffuse Phonon Scattering to Thermal Boundary Conductance Across Solid Interfaces," ASME J. Heat Transfer, **131**, p. 022402.
[54] Huberman, M. L., and Overhauser, A. W., 1994, "Electronic Kapitza Conductance at a Diamond-Pb Interface," Phys. Rev. B, **50**, pp. 2865–2873.

Contribution of Ballistic Electron Transport to Energy Transfer During Electron-Phonon Nonequilibrium in Thin Metal Films

Patrick E. Hopkins[1]

Pamela M. Norris[2]
e-mail: pamela@virginia.edu

Department of Mechanical and Aerospace Engineering,
University of Virginia,
Charlottesville, VA 22904-4746

With the ever decreasing characteristic lengths of nanomaterials, nonequilibrium electron-phonon scattering can be affected by additional scattering processes at the interface of two materials. Electron-interface scattering would lead to another path of energy flow for the high-energy electrons other than electron-phonon coupling in a single material. Traditionally, electron-phonon coupling in transport is analyzed with a diffusion (Fourier) based model, such as the two temperature model (TTM). However, in thin films with thicknesses less than the electron mean free path, ballistic electron transport could lead to electron-interface scattering, which is not taken into account in the TTM. The ballistic component of electron transport, leading to electron-interface scattering during ultrashort pulsed laser heating, is studied here by a ballistic-diffusive approximation of the Boltzmann transport equation. The results for electron-phonon equilibration times are compared with calculations with TTM based approximations and experimental data on Au thin films. [DOI: 10.1115/1.3072929]

Keywords: electron-phonon coupling, ultrashort pulsed laser heating, Boltzmann transport equation, ballistic-diffusive treatment, electron-interface scattering, thin films

1 Introduction

With the continued progress in development and production of nanostructures and nanosystems also comes development of high-powered high-precision measurement systems. Ultrashort pulsed laser systems are now commercially manufactured and marketed with optical pulses as short as a few femtoseconds. At these ultrashort time scales, ultrafast phenomena that are crucial in many nanoscale applications are directly observable, such as ablation and laser machining of materials [1–3], spin dynamics in magnetic materials [4–8], electron relaxation in metals [9–12], electron-phonon heat transfer in thin metal films [13–17], and electron-carrier processes in semiconductors [18,19]. These ultrafast phenomena often induce electron-phonon nonequilibrium, where the temperature of the free electron system can reach several thousands of Kelvin with just a few degrees of temperature increase in the lattice system. However, as engineers continue to fabricate materials and devices with decreasing characteristic lengths, the ultrafast processes become increasingly difficult to observe and characterize with femtosecond optical techniques due to the presence of material interfaces. For example, Hopkins and Norris [14] showed that electron-interface scattering affects transient thermoreflectance (TTR) [20] measurements of the electron-phonon coupling factor in thin Au films. They attributed this interference to ballistic electron transport resulting from the ultrashort femtosecond pulse leading to a thermal penetration depth of the electron system stretching to the Au film-substrate interface [13]. Therefore, during electron-phonon thermalization, the electron system also scatters at the Au/substrate interface and loses energy to the substrate, so the observed electron-phonon coupling factor is greater than that predicted via traditional models [21]. This suggests that during ultrashort pulsed laser heating, when the film thickness is less than the ballistic penetration depth of the electrons, there are two competing electron scattering processes affecting the equilibration of the "electron gas" with the surrounding media: electron-phonon scattering in the film due to diffusive electron transport and electron-interface scattering at the film/substrate interface due to ballistic electron transport.

In this report, the effects of ballistic electron transport after ultrashort pulsed laser heating are compared with the diffusive electron transport that contributes to electron-phonon coupling in thin metal films. Different effects of ballistic electron transport during electron-phonon nonequilibrium have been experimentally observed in Au by several groups [13,14,22,23], but the relative effects of ballistic and diffuse electron transport and subsequent scattering mechanisms have yet to be considered separately; this is possible by considering electron transport during electron-phonon nonequilibrium with the ballistic-diffusive approximation (BDA) [24,25] to the Boltzmann transport equation (BTE) [26].

2 Background

2.1 Two Temperature Model. Energy transport during electron-phonon nonequilibrium is described with the two temperature model (TTM) [27]. In thin metal films with thicknesses less than the thermal (ballistic) [13] penetration depths, δ, the TTM can be expressed in the simplified form that assumes the thermal gradient of the electron system is minimal [13,14], which, after short pulse absorption, is given by

$$C_e \frac{\partial T_e}{\partial t} = -G[T_e - T_L] \tag{1}$$

[1]Present address: Engineering Sciences Center, Sandia National Laboratories, P.O. Box 5800, Albuquerque, NM 87185-0346.

[2]Corresponding author.

Contributed by the Heat Transfer Division of ASME for publication in the JOURNAL OF HEAT TRANSFER. Manuscript received June 15, 2008; final manuscript received September 10, 2008; published online February 20, 2009. Review conducted by Robert D. Tzou. Paper presented at the 2008 International Conference on Micro/Nanoscale Heat Transfer (MNHT2008), Tainan, Taiwan, January 6–9, 2008.

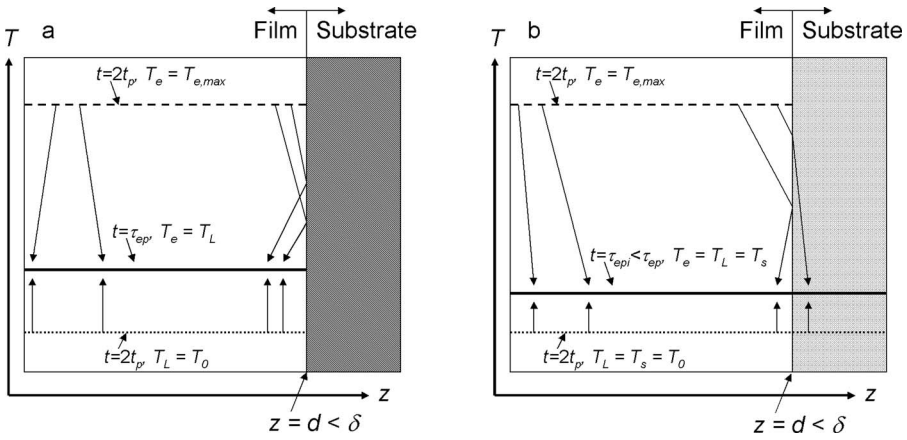

Fig. 1 Schematic of temperature changes of electron and lattice systems immediately after short-pulsed laser heating, in the case when the film thickness is less than the ballistic penetration depth. (*a*) Insulated boundary between the film and substrate: electron-phonon coupling will dominate the electron scattering events and drive electron cooling. Although electrons will traverse to the film/substrate interface, assuming an insulated boundary, the electrons will elastically reflect off the interface and travel back into the film and scatter with phonons in the film. (*b*) Uninsulated boundary between the film and substrate; electrons can inelastically scatter at the interface creating another form of energy loss from the electron system in addition to electron-phonon scattering in the film.

$$C_L \frac{\partial T_L}{\partial t} = G[T_e - T_L] \tag{2}$$

where C_e is the electron system heat capacity, T_e is the temperature of the electron system, G the electron-phonon coupling factor, C_L is the lattice heat capacity, and T_L the temperature of the lattice. Equation (1) is subject to $T_e(t=0)=T_{e,\max}$ and Eq. (2) is subject to $T_L(t=0)=T_0$, where $T_{e,\max}$ is the maximum electron temperature after laser absorption and T_0 is the initial temperature of the thin metal film. A schematic illustrating the change in electron and phonon temperatures at various times after pulse absorption (represented by $t=0$) up to the electron-phonon thermalization time, τ_{ep}, of the thermal processes described by Eqs. (1) and (2) are shown in Fig. 1(*a*). The scattering processes and temperature changes driving electron-phonon thermalization are illustrated by the arrows in this figure. In this thermal process, since the film-substrate boundary is considered "insulative" (i.e., any electron scattering occurring at the boundary is completely elastic and reflective) and since the ballistic penetration depth is greater than the film thickness, the thermal gradient in the electron system is considered negligible, and volumetric electron-phonon coupling is the primary mode of electron thermalization with the surrounding medium (being the film's lattice). Since $d<\delta$, there will be electron-interface scattering, but as previously mentioned, electrons elastically reflect off the interface then penetrate back into the film and scattering with phonons. In addition, note that the arrows representing the electron scattering processes are drawn slightly skewed from the vertical. This represents the fact that, although there is no net thermal gradient in the electron system, electrons still travel in all directions with different velocities (the net of which is zero), resulting in electron-phonon scattering. Also, since the ballistic penetration depth (which is related to the elastic electron mean free path, since multiple electron scattering events will give rise to electron relaxation into a Fermi distribution) is a statistical quantity, not all electrons will penetrate to a depth δ before electron-phonon scattering. This is depicted by the arrows in Fig. 1(*a*) that are not "reflecting" at the interface.

The electron cooling process in Fig. 1(*a*), which is mathematically explained by the TTM, describes energy exchange between a hot electron system and a colder lattice system via electron-phonon scattering events with the electron-phonon coupling factor, which is a function of the electron-phonon relaxation time [28]. These scattering events make this thermal process diffusive by nature, and the TTM can be derived from the BTE under the relaxation time approximation using the electron-phonon relaxation time as the time it takes for the electron system to return to an equilibrium Fermi distribution [29]. However, the ballistic transport that occurs in the electron system, immediately after pulsed laser heating [13,22], can influence the electron scattering dynamics and energy transfer in thin films with thicknesses less than the ballistic penetration depth due to inelastic electron-interface scattering at the film/substrate interface [14]. Evidence of this inelastic electron-interface scattering affecting electron cooling has been shown even in thermally insulative substrates [14]. In this case, inelastic electron scattering at the film/substrate interface would cause energy loss from the film electron system and increase the electron-phonon thermalization time, since the electrons could loose energy to (1) the substrate via electrons traveling ballistically and inelastically scattering at the interface and (2) the film lattice via electrons traveling diffusely and scattering with phonons. When considering inelastic electron-interface scattering (and neglecting phonon-interface scattering typically associated with phonon thermal boundary resistance [30]), the electron-phonon-interface thermalization time, τ_{epi}, would be driven by the scattering processes and temperature changes illustrated by the arrows in Fig. 1(*b*), which depicts electrons inelastically scattering at the interface and transferring energy away from the film media. Note that Fig. 1(*b*) depicts the final temperature of the film to be less than that depicted in Fig. 1(*a*) due to the inelastic electron-interface scattering events transferring more film electron energy away from the film into the substrate.

Although the thermal effects of the ballistic electron-interface scattering have been indirectly studied with a three temperature model (3TM) [14], the 3TM approach still assumes complete diffusive transport. Therefore, the explicit contribution of ballistic electron transport and subsequent scattering processes on electron system relaxation other than electron-phonon scattering (such as inelastic electron-interface scattering at a film-substrate interface) cannot be studied with these diffusive treatments.

2.2 Ballistic-Diffusive Approximations for the BTE. Studying the ballistic nature of electron transport during electron-phonon nonequilibrium must start with the BTE for electrons [29], given by

$$\frac{\partial f}{\partial t} + \boldsymbol{v}\nabla_{\boldsymbol{r}} f + \frac{e}{m}\boldsymbol{E}\cdot\nabla_{\boldsymbol{v}} f = \left(\frac{\partial f}{\partial t}\right)_c \tag{3}$$

where f is the nonequilibrium electron distribution, $\boldsymbol{v}$ the velocity vector, $\boldsymbol{r}$ the position vector, e the electric charge, m the mass of an electron, $\boldsymbol{E}$ the electric field, the quantity $e\boldsymbol{E}$ the Lorentz force resulting from the electric field, and the term $(\partial f/\partial t)_c$ the time rate of change of the nonequilibrium electron distribution due to electron collisions. Assuming one-dimensional (1D) heat flow, which is often assumed in ultrashort pulsed laser heating analyses [28,31], Eq. (3) becomes

$$\frac{\partial f}{\partial t} + v_z\frac{\partial f}{\partial z} + \frac{F_z}{m}\frac{\partial f}{\partial v_z} = \left(\frac{\partial f}{\partial t}\right)_c \tag{4}$$

where z is the direction perpendicular to the film surface, and F_z represents the Lorentz force. As previously mentioned, estimating the collision term of Eq. (4) with the relaxation time approximation and taking the relaxation time as the electron-phonon thermalization time leads to the traditional TTM [27], as outlined by Chen et al. [29].

However, in the event of ultrashort pulsed laser absorption by the electron system and subsequent ballistic penetration to a depth greater than the film thicknesses, the electrons traveling ballistically can scatter at the film/substrate interface and significantly change the electron relaxation dynamics [14]. In order to understand the relative contributions of the ballistic electron-interface scattering and the diffusive electron-phonon scattering, the BDA must be employed to the BTE [24,25]. The BDA separates the intensity of energy carriers, I, at any point into two parts: the ballistic intensity, I_b, which represents carriers originating from the boundaries and experiencing out-scattering only, and the diffusive intensity, I_m, which represents carriers originating from inside the medium due to the excitation and the boundary contribution converted into scattered or emitted carriers after absorption. This solution technique has been used to study phonon transport and ballistic phonon scattering under a single relaxation time approximation [24,25,32], transforming the distribution function notation of the BTE into intensity notation [33]. In this work, in the limiting case of $d < \delta$ and assuming no thermal gradient, the BTE for electrons will be used to calculate the ballistic and diffusive electron intensities and to compare the relative contributions of inelastic interface scattering from ballistic transport and phonon scattering from diffusive transport to electron-media thermalization.

3 Separation of Ballistic and Diffusive Electron Scattering

3.1 The Equation of Electron Energy Transfer. The 1D BTE for electrons is given by Eq. (4). When $d < \delta$, no thermal gradient exists in the electron system, and therefore Eq. (4) becomes

$$\frac{\partial f}{\partial t} = \left(\frac{\partial f}{\partial t}\right)_c \tag{5}$$

Paralleling the equation of phonon radiative transport (EPRT) [33], the equation of electron energy transfer (EEET) is established by multiplying each term in Eq. (5) by the product $\varepsilon D(\varepsilon)$, where ε is the electron energy and $D(\varepsilon)$ is the electron density of states yielding

$$\frac{\partial U}{\partial t} = \left(\frac{\partial U}{\partial t}\right)_c \tag{6}$$

where U is the volumetric electron energy density, defined as $U = \varepsilon D(\varepsilon) f$, and Eq. (6) is subject to the following initial condition:

$$U(0) = S = \frac{(1-R)J}{d} \tag{7}$$

In this case, the initial condition S is the energy absorbed by electrons per unit volume. This is related to $T_{e,\max}$ in Eq. (1) by $\int_{T_0}^{T_{\max}} C_e(T_e)dT = S$. The source term assumes that the incident energy is absorbed instantaneously and homogeneously throughout the depth of the film (the energy is actually absorbed in the optical penetration depth, but then stretched out into the film thickness by electrons traveling ballistically if $d < \delta$). Applying the relaxation time approximation [26] to the EEET yields

$$\frac{\partial U}{\partial t} = -\frac{U - U_0}{\tau} \tag{8}$$

where U_0 is the equilibrium electron energy density per unit energy in the film defined as $U_0 = \int_\varepsilon \varepsilon D(\varepsilon) f_0 d\varepsilon$, where f_0 is the Fermi–Dirac distribution function. Here, τ is the relaxation time of the electrons in the metal films, which for purely diffusive transport (i.e., a completely insulative substrate, as discussed with respect to Fig. 1(*a*)) and for the temperatures and time scales of interest is the electron-phonon thermalization time, τ_{ep}.

In this work, only electron temperatures less than 4000 K will be considered to directly compare with pump probe experimental data on Au [14]. Therefore, this analysis will focus on free electron (noble) metals, and this temperature range ensures the following:

(1) a linear heat capacity [34] so $C_e(T_e) = \gamma T_e$ and therefore the maximum electron temperature after pulse absorption can be estimated by $T_{e,\max} = \sqrt{2S/\gamma + T_0^2}$
(2) a relatively constant chemical potential, μ, that is approximately equal to the Fermi energy, ε_F [34]
(3) a relatively constant electron-phonon coupling factor in the free electron metal [21,34]
(4) an electron spectral energy range participating in thermal processes within $\varepsilon \pm k_B T_e$, where k_B is the Boltzmann constant [35]
(5) an unmodified lattice from the incident laser pulse (i.e., no ablation or spallation [1])
(6) a parabolic conduction band leading to a conduction electron density of states per unit energy given by $D(\varepsilon) = (3n/2)(\varepsilon/\varepsilon_F)^{1/2}(1/\varepsilon_F)$ [35], where n is the conduction electron number density (a derivation of this less-often-used form of the density of states is given in the Appendix)

3.2 Complete Elastic Electron Interface Scattering (i.e., No Electron Energy Loss to the Substrate). Applying the BDA to electron transport after short-pulsed laser heating uses a slightly different approach than previous works applying the BDA to phonon transport [24,25,32]—specifically the single relaxation time approximation. Electron-phonon nonequilibrium resulting from pulsed laser heating can be divided into two characteristic time intervals [13,36]. The earliest of the time intervals, the duration of which is termed the electron-electron relaxation time, τ_{ee}, is typically on the order of 10–100 fs for metals [31]. This time represents the time it takes for the excited electrons to relax into a Fermi distribution through *e-e* (electron-electron) collisions, which dominate *e-p* (electron-phonon) collisions during this time interval. Ballistic transport of the electrons occurs over this time. Once equilibrium is achieved within the electron system, the higher temperature electrons transmit energy to the lattice through *e-p* scattering processes over the electron-phonon relaxation time (often referred to as the electron-phonon thermalization time), τ_{ep}.

The heat transferred via these *e-p* interactions is governed by Eqs. (1) and (2). Thermalization time is typically on the order of 1 ps for metals and is inversely related to the electron-phonon coupling factor [28]. Due to the differing relaxation times governing ballistic and diffusive (electron-phonon) transport processes, ballistic electron transport must be modeled with τ_{ee} and diffusive electron transport must be modeled with τ_{ep}.

Therefore, to separate ballistic and diffusive electron transport, the EEET (Eq. (6)) can be rewritten as

$$\frac{\partial U}{\partial t} = \frac{\partial}{\partial t}(U_b + U_m) = \left(\frac{\partial U_b}{\partial t}\right)_c + \left(\frac{\partial U_m}{\partial t}\right)_c \tag{9}$$

or by applying the relaxation time approximation

$$\frac{\partial U}{\partial t} = \frac{\partial}{\partial t}(U_b + U_m) = -\frac{U_b - U_m}{\tau_{ee}} - \frac{U_m - U_0}{\tau_{ep}} \tag{10}$$

Note in Eq. (10), since $\tau_{ee} < \tau_{ep}$, the ballistic component relaxes to the diffusive component over τ_{ee}, which in turn relaxes to the equilibrium distribution over τ_{ep}. Also, Eq. (8) can in fact be approximated with a single relaxation time approximation, following previous BDAs relating to phonon transport with the stipulation that $U_b=0$ when $t > \tau_{ee}$. Relating the ballistic and diffusive terms, and recognizing that S is absorbed by the ballistically traveling electrons, yields

$$\frac{\partial U_b}{\partial t} = -\frac{U_b - U_m}{\tau_{ee}} \tag{11}$$

and

$$\frac{\partial U_m}{\partial t} = -\frac{U_m - U_0}{\tau_{ep}} \tag{12}$$

where Eqs. (11) and (12) are subject to

$$U_b(0) = S \tag{13}$$

and

$$U_m(0) = U_b(\tau_{ee}) \tag{14}$$

respectively. Technically, there is a time delay in the development of the diffusively scattering electron system since the ballistic system relaxes to the diffusive system, and therefore Eq. (14) should read $U_m(\tau_{ee}) = U_b(\tau_{ee})$. However, this work is not focused on *when* the energy is transferred but *how* the energy is transferred, and therefore for ease of calculation and discussion, the diffusive component to the electron energy is prescribed to begin at $t=0$. Therefore, by imposing Eq. (14) as an initial condition, Eq. (12) is rewritten as

$$\frac{\partial U_m}{\partial t} = -\frac{U_m - U_0}{\tau_{ep} - \tau_{ee}} \tag{15}$$

The solution of the ballistic component is given by

$$U_b(t) = U_m\left(1 - \exp\left[-\frac{t}{\tau_{ee}}\right]\right) + S\exp\left[-\frac{t}{\tau_{ee}}\right] \tag{16}$$

and the diffusive component is given by

$$U_m(t) = \frac{U_0\left(1 - \exp\left[-\dfrac{t}{\tau_{ep} - \tau_{ee}}\right]\right) + S\exp\left[-\dfrac{t}{\tau_{ep} - \tau_{ee}} - 1\right]}{1 - \exp\left[-\dfrac{t}{\tau_{ep} - \tau_{ee}}\right] + \exp\left[-\dfrac{t}{\tau_{ep} - \tau_{ee}} - 1\right]} \tag{17}$$

Equations (11) and (15) subject to Eqs. (13) and (14) represent the "BDA" of the EEET for the electron system excited by an ultrashort laser pulse in which ($d < \delta$) and elastic electron-interface scattering occurs (shown in Fig. 1(*a*)). The solutions are given by Eqs. (16) and (17). The average energy densities over the thermalization times of the ballistic and diffusive components are given by

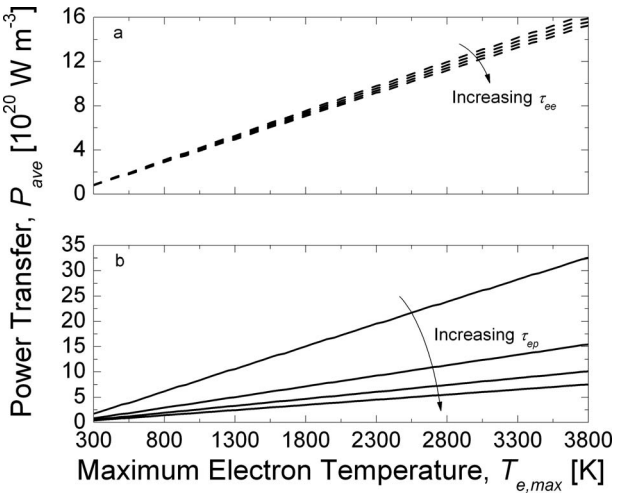

Fig. 2 Average power density transferred from the electron system assuming no energy loss to the substrate (elastic electron-interface scattering) as a function of maximum electron temperature in the (*a*) ballistic regime assuming τ_{ee} of 50 fs, 200 fs, 350 fs, and 500 fs and τ_{ep} of 4 ps (Eq. (20)) and (*b*) diffusive regime (electron-phonon coupling) assuming τ_{ee} of 200 fs and τ_{ep} of 2 ps, 4 ps, 6 ps, and 8 ps (Eq. (21)).

$$U_{b,\mathrm{avg}} = \frac{1}{\tau_{ee}}\int_0^{\tau_{ee}} U_b(t)dt \tag{18}$$

and

$$U_{m,\mathrm{avg}} = \frac{1}{\tau_{ep} - \tau_{ee}}\int_0^{\tau_{ep}-\tau_{ee}} U_m(t)dt \tag{19}$$

Therefore, the average power density transferred from the ballistic and diffusive electron systems over each system's respective thermalization time is given by

$$P_{b,\mathrm{avg}} = \frac{U_{b,\mathrm{avg}}}{\tau_{ee}} \tag{20}$$

$$P_{m,\mathrm{avg}} = \frac{U_{m,\mathrm{avg}}}{\tau_{ep} - \tau_{ee}} \tag{21}$$

Figures 2(*a*) and 2(*b*) show the power density transferred from the ballistic and diffusive electron system in a Au film over their respective thermalization times as a function of maximum electron temperature assuming $S = (\gamma(T_{e,\max}^2 - T_0^2))/2$. These calculations assume elastic electron-interface scattering, and therefore all the energy from S remains in the electron system during the ballistic transport regime. For Au, $\gamma = 71.4$ J m^{-3} K^{-2}, $\varepsilon_F = 5.53$ eV, and $n = 5.9 \times 10^{28}$ m^{-3} [37]. Figure 2(*a*) shows ballistic power density calculations assuming a constant τ_{ep} of 4 ps with various τ_{ee}'s (50 fs, 200 fs, 350 fs, and 500 fs). Figure 2(*b*) shows diffusive power density calculations assuming a constant τ_{ee} of 200 fs with various τ_{ep}'s (2 ps, 4 ps, 6 ps, and 8 ps). The electron-electron relaxation times were chosen since τ_{ee} in Au has been theoretically calculated to be as low as about 50 fs [31] and experimentally measured to be as large as 500 fs [12]. The power density of the ballistic contribution weakly depends on electron-electron thermalization time, where the diffusive contribution is strongly dependent on thermalization time. This diffusive electron

power density dependency on electron-phonon thermalization time is expected since the electron-phonon coupling factor is inversely related to τ_{ep} via $G=\gamma T_e/\tau_{ep}$ [38].

The electron-phonon coupling factor in metals has been extensively studied, and the temperature functionality of G has been well studied numerically [21,34,39]. In the case of Au in the temperature range of interest in this work, G is a constant value of about 2.4×10^{16} W m^{-3} K^{-1}, which has been verified experimentally [13,16,40,41]. Since G represents the diffusive electron-phonon scattering in this work, the power transferred by the electron system by diffusive scattering events (Eq. (21)) can be recast into terms of G as

$$P_{m,\mathrm{avg}}=\frac{1}{\left(\frac{\gamma T_{e,\max}}{G}-\tau_{ei}\right)^2}\int_0^{\gamma T_{e,\max}/G-\tau_{ee}}\left(\int_{\varepsilon_F-k_B}^{\varepsilon_F+k_B}\varepsilon D(\varepsilon)f_0 d\varepsilon\frac{\left(1-\exp\left[-\frac{t}{\frac{\gamma T_{e,\max}}{G}-\tau_{ee}}\right]\right)+S\exp\left[-\frac{t}{\frac{\gamma T_{e,\max}}{G}-\tau_{ee}}-1\right]}{1-\exp\left[-\frac{t}{\frac{\gamma T_{e,\max}}{G}-\tau_{ee}}\right]+\exp\left[-\frac{t}{\frac{\gamma T_{e,\max}}{G}-\tau_{ee}}-1\right]}\right)dt \quad (22)$$

where Eq. (22) takes into account a change in electron-phonon thermalization time based on the maximum electron temperature achieved after laser heating through $\tau_{ep}=\gamma T_{e,\max}/G$. This assumption keeps calculations in line with the definition of the laser source term, S. Figure 3 shows the ratio of the ballistic power density to the diffusive power density as a function of electron temperature using Eqs. (20) and (22). Figure 3 shows calculations of $P_{b,\mathrm{avg}}/P_{m,\mathrm{avg}}$ for four different τ_{ee}'s (50 fs, 200 fs, 350 fs, and 500 fs). The calculations show that, for this case of elastic electron-interface scattering leading to electron-electron then electron-phonon thermalization, the power transferred from the electrons traveling ballistically is approximately equal to the power transferred from the thermalized electron system to the phonons during electron-phonon thermalization at high electron temperatures. At relatively low electron temperatures (close to room temperature) the power transferred during ballistic processes is less than that during diffusive electron-phonon processes.

3.3 Inelastic Electron Interface Scattering (i.e., Electron Energy Loss to the Substrate). Technically, since Eq. (11) represents the ballistic carriers scattering among themselves to relax into a thermal distribution, the term BDA is used loosely. Although the ballistic and diffusive components to electron transport are separated, they are effectively separated by considering two different EEETs: one for the electron-electron relaxation and one for the electron-phonon relaxation. However, in the case of inelastic electron-interface scattering, the ballistic carriers that inelastically scatter at the film/substrate interface experience no internal scattering. The energy of these carriers originates from the pulse absorption from the surface. In this case, the BDA of the EEET takes a slightly different form, more in line with the original BDA of the EPRT developed by Chen [24,25].

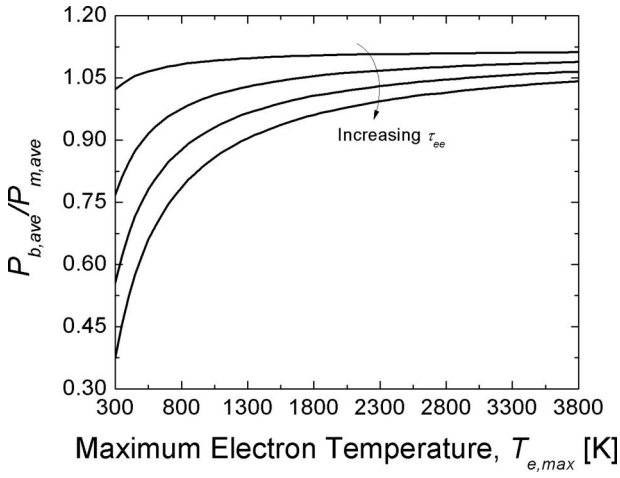

Fig. 3 Ratio of average power density transferred from ballistic processes to diffusive processes (ratio of Eq. (20) to Eq. (22)) as a function of maximum electron temperature. These calculations assume a temperature dependent electron-phonon relaxation time of $\tau_{ep}=\gamma T_{e,\max}/G$ and no energy loss to the substrate. Calculations shown assume τ_{ee} of 50 fs, 200 fs, 350 fs, and 500 fs.

As with the purely elastic scattering case, the ballistically and diffusively traveling electrons are considered as two separate systems, but to consider inelastic electron energy loss to the substrate as a result of electron-interface scattering, a new relaxation time, the electron-interface relaxation time, τ_{ei}, is applied to the ballistic system. If electrons elastically reflect off the interface, then they will eventually thermalize and scatter with phonons. Since the goal of this work is to compare the effects of inelastic interface scattering from ballistic electron transport to electron-phonon thermalization from diffusive electron transport, the elastically reflected electrons can be lumped in with the diffusive electron-phonon relaxation term. With this in mind, Eq. (6) can be rewritten as

$$\frac{\partial U}{\partial t}=\frac{\partial}{\partial t}(U_{bi}+U_m)=-\frac{U_{bi}}{\tau_{ei}}-\frac{U_m-U_0}{\tau_{ep}-\tau_{ee}} \quad (23)$$

where the subscript "*bi*" refers to the ballistic component inelastically scattering at the interface. Note that the inelastically interfacially scattered electrons do not relax to any particular energy since the energy of these electrons leave the film system; they experience out-scattering only as prescribed for the ballistic carriers in the original BDA development [24,25]. Again, the ballistic and diffusive terms on each side of Eq. (23) can be related yielding

$$\frac{\partial U_{\mathrm{bi}}}{\partial t}=-\frac{U_{\mathrm{bi}}}{\tau_{ei}} \quad (24)$$

and

$$\frac{\partial U_m}{\partial t}=-\frac{U_m-U_0}{\tau_{ep}-\tau_{ee}} \quad (25)$$

subject to

$$U_{\mathrm{bi}}(0)=S \quad (26)$$

and

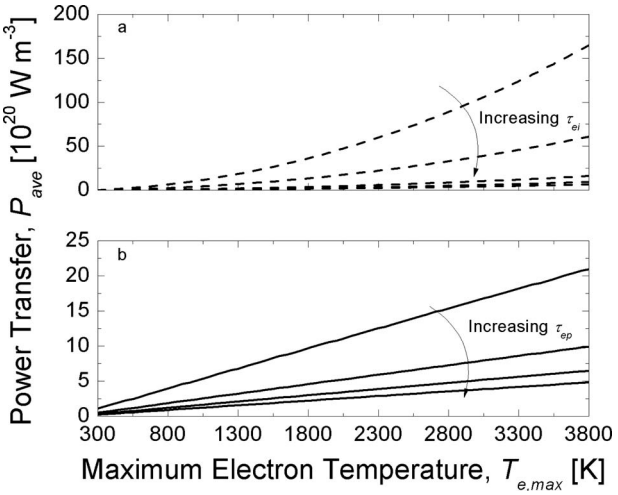

Fig. 4 Average power density transferred from the electron system assuming energy loss to the substrate (inelastic electron-interface scattering) as a function of maximum electron temperature in the (*a*) ballistic regime assuming τ_{ei} of 15 fs, 50 fs, 200 fs, 350 fs, and 500 fs and τ_{ep} of 4 ps (Eq. (30)) and (*b*) diffusive regime (electron-phonon coupling) assuming τ_{ee} of 200 fs and τ_{ep} of 2 ps, 4 ps, 6 ps, and 8 ps (Eq. (31)).

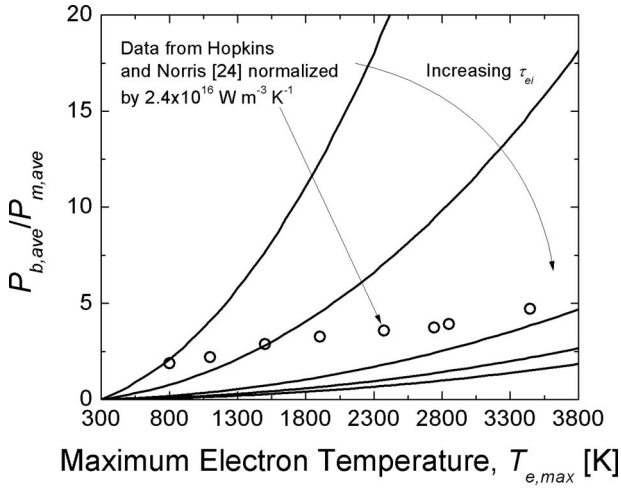

Fig. 5 Ratio of average power density transferred from ballistic processes to diffusive processes (ratio of Eq. (30) to Eq. (32)) as a function of maximum electron temperature. These calculations assume a temperature dependent electron-phonon relaxation time of $\tau_{ep}=\gamma T_{e,\max}/G$ and energy loss to the substrate from inelastic electron-interface scattering events during electron-electron thermalization. Calculations shown assume τ_{ei} of 15 fs, 50 fs, 200 fs, 350 fs, and 500 fs. Also shown in the figure are experimental pump probe *G*s measured on 20 nm Au films on Si substrates as a function of maximum electron temperature as measured by Hopkins and Norris [14]. Their data are normalized by the accepted value of *G* in Au, $G=2.4\times10^{16}$ W m^{-3} K^{-1}. The experimental work from Hopkins and Norris concluded that electron-interface scattering could increase the rate of electron-phonon equilibration in the film by providing another channel of energy transfer. This same conclusion is apparent in the calculations shown in this figure.

$$U_m(0) = S - U_{\rm bi}(\tau_{ei}) \tag{27}$$

Again, Eq. (25) assumes that $t=0$ is the time when the electron system in the film has reached a thermal Fermi distribution. These equations also assume that $\tau_{ei} < \tau_{ee}$, which is valid since the flight time of an electron in a thin film during Fermi relaxation is on the order to $t_{\rm flight}=d/v_F$, where v_F is the Fermi velocity. The solutions to Eqs. (24) and (25) are given by

$$U_{bi}(t) = S\exp\left[-\frac{t}{\tau_{ei}}\right] \tag{28}$$

and

$$U_m(t) = U_0\left(1-\exp\left[-\frac{t}{\tau_{ep}-\tau_{ei}}\right]\right) + S\left(\exp\left[-\frac{t}{\tau_{ep}-\tau_{ei}}\right]-\exp\left[-\frac{t}{\tau_{ep}-\tau_{ei}}-1\right]\right) \tag{29}$$

The average energy densities of the ballistic and diffusive components are calculated with equations analogous to Eqs. (18) and (19). Therefore, following Eqs. (20) and (21), the power densities transferred during scattering in ballistic and diffusive transport assuming inelastic electron-interface scattering are given by

$$P_{bi,\rm avg}=\frac{1}{\tau_{ei}^2}\int_0^{\tau_{ei}} S\exp\left[-\frac{t}{\tau_{ei}}\right]dt \tag{30}$$

and

$$P_{m,\rm avg} = \frac{1}{(\tau_{ep}-\tau_{ei})^2}\times\int_0^{\tau_{ep}-\tau_{ee}}\left(\left\{\int_{\varepsilon_F-k_B}^{\varepsilon_F+k_B}\varepsilon D(\varepsilon)f_0 d\varepsilon\left(1-\exp\left[-\frac{t}{\tau_{ep}-\tau_{ei}}\right]\right)\right\} + S\left(\exp\left[-\frac{t}{\tau_{ep}-\tau_{ei}}\right]-\exp\left[-\frac{t}{\tau_{ep}-\tau_{ei}}-1\right]\right)\right)dt \tag{31}$$

Figures 4(*a*) and 4(*b*) show the power density transferred from the electron system due to ballistic-inelastic interface scattering and diffusive electron-phonon scattering in a Au film over their respective thermalization times using Eqs. (30) and (31). These calculations use the same parameters as the calculations shown in Figs. 2(*a*) and 2(*b*), only this time including an electron-interface relaxation time of 15 fs to simulate the time-of-flight of an electron in a Au lattice traversing across a 20 nm film ($t_{\rm flight}=d/v_F$ $=20$ nm$/(1.4\times10^6$ m s$^{-1})\approx15$ fs). A similar trend is seen with the diffusive component as compared with that in Fig. 2(*b*). However, the ballistic power transfer is much larger in this case of inelastic electron-interface scattering and electron system energy loss compared with no electron system energy loss as modeled in Fig. 2(*a*), especially at high temperatures and low electron-interface relaxation times.

Following Eq. (22), Eq. (31) can be recast in terms of G as

$$P_{m,\rm avg} = \frac{1}{\left(\frac{\gamma T_{e,\max}}{G}-\tau_{ei}\right)^2}\times\int_0^{\gamma T_e/G-\tau_{ee}}\left(\left\{\int_{\varepsilon_F-k_B}^{\varepsilon_F+k_B}\varepsilon D(\varepsilon)f_0 d\varepsilon\left(1-\exp\left[-\frac{t}{\frac{\gamma T_{e,\max}}{G}-\tau_{ei}}\right]\right)\right\} + S\left(\exp\left[-\frac{t}{\frac{\gamma T_{e,\max}}{G}-\tau_{ei}}\right]-\exp\left[-\frac{t}{\frac{\gamma T_{e,\max}}{G}-\tau_{ei}}-1\right]\right)\right)dt \tag{32}$$

Figure 5 shows the ratio of ballistic to diffusive power densities (ratio of Eq. (30) to Eq. (32)) for the five different electron-

interface relaxation times shown in Fig. 4(*a*). These calculations assume that energy is being lost from the electron system in the film due to inelastic electron-interface scattering. The results show that the power transferred from the electron system through ballistic electron scattering can be much greater than the power transferred via diffusive electron scattering at high electron temperatures (4000 K) and low thermalization times.

These results agree well with the trends seen in electron-phonon coupling measurements in 20 nm Au films on Si substrates as measured by Hopkins and Norris [14]. At low electron temperatures (low incident fluence), they measured G of 2.3×10^{16} W m^{-3} K^{-1}. At high electron temperatures (3500 K), they measured G of 11.23×10^{16} W m^{-3} K^{-1}. They attributed this increase to electron-interface scattering due to the large ballistic penetration depth in Au. The measured Gs by Hopkins and Norris divided by the theoretically accepted value of G (2.4×10^{16} W m^{-3} K^{-1}) as a function of maximum electron temperature are also shown in Fig. 5. The agreement between the data and the calculations in this paper suggest that inelastic electron-interface scattering can affect electron-phonon thermalization by decreasing the amount of energy in the electron system during electron-electron relaxation processes.

4 Conclusions

In nanodevices, ballistic transport of hot energy carriers can play a significant role in thermal processes. In this work, the effects of ballistic transport and subsequent electron cooling after short-pulsed laser heating are studied. The equation of electron energy transfer is established from the electron Boltzmann transport equation. The ballistic and diffusive contributions to electron thermal transport are studied by applying the ballistic-diffusive approximation to the EEET. In this development, electron-interface scattering is treated with the ballistic-diffusive approximation to the BTE, and the diffusive processes are assumed as electron-phonon scattering. The power transferred from the electron system during ballistic transport due to inelastic interface scattering can be over an order of magnitude greater than the diffusive component at high electron temperatures (4000 K). The temperature trends and values of ballistic to diffusive power transfer agree very well with previous experiments.

Acknowledgment

The authors gratefully acknowledge financial support from the Office of Naval Research MURI program, Grant No. N00014-07-1-0723. P.H. also gratefully acknowledges support from the NSF Graduate Student Research Program. The authors would like to thank Rich Salaway, Jennifer Simmons, John Duda, Justin Smoyer, and Mike Fish for insightful discussions.

Nomenclature

- C = heat capacity, J m^{-3} K^{-1}
- $D(\varepsilon)$ = electron density of states per unit energy, m^{-3} J^{-1}
- d = film thickness, m
- E = electric field, V m^{-1}
- e = fundamental electric charge, C
- F = Lorentz force, N
- f = nonequilibrium electron statistical distribution function
- f_0 = Fermi–Dirac distribution function
- G = electron-phonon coupling factor, W m^{-3} K^{-1}
- $\hbar$ = Planck's constant divided by 2π, J s
- J = incident laser fluence, J m^{-2}
- m = mass of an electron, kg
- n = conduction electron number density, m^{-3}
- P = power density, W m^{-3}
- R = optical reflectivity
- S = source term describing volumetric power absorbed from laser pulse, W m^{-3}
- T = temperature, K
- t = time, s
- t_p = pulse width, s
- U = electron energy density, J m^{-3}
- v = electron velocity, m s^{-1}

Greek Symbols

- δ = ballistic penetration depth, m
- ε = electron energy, J
- ε_F = Fermi energy, J
- γ = linear coefficient to electronic heat capacity (Sommerfeld constant), J m^{-3} K^{-2}
- τ = thermalization or relaxation time, s

Subscripts

- 0 = equilibrium
- avg = time averaged
- d = contribution from electrons traveling ballistically
- c = collision
- e = electron
- ei = electron-interface
- ep = electron-phonon
- L = lattice
- m = contribution from electron traveling diffusively in the medium
- r = position
- v = velocity
- z = z direction

Appendix

Beginning with the familiar expression for the Fermi energy given (Chap. 6, Eq. (17) in Ref. [37])

$$\varepsilon_F = \frac{\hbar^2}{2m}(3\pi^2 n)^{2/3} \tag{A1}$$

where $\hbar$ is Planck's constant divided by 2π, and recognizing that the density of states per unit energy per unit volume, assuming a parabolic conduction band, is given by (Chap. 6, Eq. (20) in Ref. [37])

$$D(\varepsilon) = \frac{1}{2\pi^2}\left(\frac{2m}{\hbar^2}\right)^{3/2}\varepsilon^{1/2} \tag{A2}$$

Equation (A1) can be rearranged and inserted into Eq. (A2) to give

$$D(\varepsilon) = \frac{3n}{2}\left(\frac{\varepsilon}{\varepsilon_F}\right)^{1/2}\frac{1}{\varepsilon_F} \tag{A3}$$

which is the expression for the electron density of states per unit energy per unit volume used in the calculations in this work.

References

[1] Ivanov, D. S., and Zhigilei, L. V., 2003, "Combined Atomistic-Continuum Modeling of Short-Pulse Laser Melting and Disintegration of Metal Films," Phys. Rev. B, **68**, p. 064114.

[2] Wellershoff, S.-S., Hohlfeld, J., Gudde, J., and Matthias, E., 1999, "The Role of Electron-Phonon Coupling in Femtosecond Laser Damage of Metals," Appl. Phys. A: Mater. Sci. Process., **69**, pp. S99–S107.

[3] Wellershoff, S.-S., Gudde, J., Hohlfeld, J., Muller, J. G., and Matthias, E., 1998, "The Role of Electron-Phonon Coupling in Femtosecond Laser Damage of Metals," Proc. SPIE, **3343**, pp. 378–387.

[4] Beaurepaire, E., Merle, J.-C., Daunois, A., and Bigot, J.-Y., 1996, "Ultrafast Spin Dynamics in Ferromagnetic Nickel," Phys. Rev. Lett., **76**, pp. 4250–4253.

[5] Guidoni, L., Beaurepaire, E., and Bigot, J.-Y., 2002, "Magneto-Optics in the Ultrafast Regime: Thermalization of Spin Populations in Ferromagnetic Films," Phys. Rev. Lett., **89**, p. 017401.

[6] Hohlfeld, J., Matthias, E., Knorren, R., and Bennemann, K. H., 1997, "Nonequilibrium Magnetization Dynamics of Nickel," Phys. Rev. Lett., **78**, pp.

4861–4864.
[7] Koopmans, B., Van Kampen, M., Kohlhepp, J. T., and De Jonge, W. J. M., 2000, "Femtosecond Spin Dynamics of Epitaxial Cu(111)/Ni/Cu Wedges," Appl. Phys. Lett., **87**, pp. 5070–5072.
[8] van Kampen, M., Kohlhepp, J. T., de Jonge, W. J. M., Koopmans, B., and Coehoorn, R., 2005, "Sub-Picosecond Electron and Phonon Dynamics in Nickel," J. Phys.: Condens. Matter, **17**, pp. 6823–6834.
[9] Fann, W. S., Storz, R., Tom, H. W. K., and Bokor, J., 1992, "Direct Measurement of Nonequilibrium Electron-Energy Distributions in Subpicosecond Laser-Heated Gold Films," Phys. Rev. Lett., **68**, pp. 2834–2837.
[10] Del Fatti, N., Voisin, C., Achermann, M., Tzortzakis, S., Christofilos, D., and Vallee, F., 2000, "Nonequilibrium Electron Dynamics in Noble Metals," Phys. Rev. B, **61**, pp. 16956–16966.
[11] Sun, C. K., Vallee, F., Acioli, L., Ippen, E. P., and Fujimoto, J. G., 1993, "Femtosecond Investigation of Electron Thermalization in Gold," Phys. Rev. B, **48**, pp. 12365–12368.
[12] Sun, C. K., Vallee, F., Acioli, L., Ippen, E. P., and Fujimoto, J. G., 1994, "Femtosecond-Tunable Measurement of Electron Thermalization in Gold," Phys. Rev. B, **50**, pp. 15337–15348.
[13] Hohlfeld, J., Wellershoff, S.-S., Gudde, J., Conrad, U., Jahnke, V., and Matthias, E., 2000, "Electron and Lattice Dynamics Following Optical Excitation of Metals," Chem. Phys., **251**, pp. 237–258.
[14] Hopkins, P. E., and Norris, P. M., 2007, "Substrate Influence in Electron-Phonon Coupling Measurements in Thin Au Films," Appl. Surf. Sci., **253**, pp. 6289–6294.
[15] Hostetler, J. L., Smith, A. N., Czajkowsky, D. M., and Norris, P. M., 1999, "Measurement of the Electron-Phonon Coupling Factor Dependence on Film Thickness and Grain Size in Au, Cr, and Al," Appl. Opt., **38**, pp. 3614–3620.
[16] Qiu, T. Q., Juhasz, T., Suarez, C., Bron, W. E., and Tien, C. L., 1994, "Femtosecond Laser Heating of Multi-Layer Metals—II. Experiments," Int. J. Heat Mass Transfer, **37**, pp. 2799–2808.
[17] Qiu, T. Q., and Tien, C. L., 1994, "Femtosecond Laser Heating of Multi-Layer Metals—I. Analysis," Int. J. Heat Mass Transfer, **37**, pp. 2789–2797.
[18] Klopf, J. M., and Norris, P. M., 2005, "Subpicosecond Observation of Photoexcited Carrier Thermalization and Relaxation in InP-Based Films," Int. J. Thermophys., **26**, pp. 127–140.
[19] Klopf, J. M., and Norris, P. M., 2007, "Probing Nonequilibrium Dynamics With White Light Femtosecond Pulses," Appl. Surf. Sci., **253**, pp. 6305–6309.
[20] Norris, P. M., Caffrey, A. P., Stevens, R. J., Klopf, J. M., Mcleskey, J. T., and Smith, A. N., 2003, "Femtosecond Pump-Probe Nondestructive Examination of Materials," Rev. Sci. Instrum., **74**, pp. 400–406.
[21] Chen, J. K., Latham, W. P., and Beraun, J. E., 2005, "The Role of Electron-Phonon Coupling in Ultrafast Laser Heating," J. Laser Appl., **17**, pp. 63–68.
[22] Brorson, S. D., Fujimoto, J. G., and Ippen, E. P., 1987, "Femtosecond Electronic Heat-Transport Dynamics in Thin Gold Films," Phys. Rev. Lett., **59**, pp. 1962–1965.
[23] Hohlfeld, J., Muller, J. G., Wellershoff, S.-S., and Matthias, E., 1997, "Time-Resolved Thermoreflectivity of Thin Gold Films and Its Dependence on Film Thickness," Appl. Phys. B: Lasers Opt., **64**, pp. 387–390.
[24] Chen, G., 2002, "Ballistic-Diffusive Equations for Transient Heat Conduction From Nano to Macroscales," ASME J. Heat Transfer, **124**, pp. 320–328.
[25] Chen, G., 2001, "Ballistic-Diffuse Heat-Conduction Equations," Phys. Rev. Lett., **86**, pp. 2297–2300.
[26] Vincenti, W. G., and Kruger, C. H., 2002, *Introduction to Physical Gas Dynamics*, Krieger, Malabar, FL.
[27] Kaganov, M. I., Lifshitz, I. M., and Tanatarov, L. V., 1957, "Relaxation Between Electrons and the Crystalline Lattice," Sov. Phys. JETP, **4**, pp. 173–178.
[28] Smith, A. N., Hostetler, J. L., and Norris, P. M., 1999, "Nonequilibrium Heating in Metal Films: An Analytical and Numerical Analysis," Numer. Heat Transfer, Part A, **35**, pp. 859–873.
[29] Chen, J. K., Tzou, D. Y., and Beraun, J. E., 2006, "A Semiclassical Two-Temperature Model for Ultrafast Laser Heating," Int. J. Heat Mass Transfer, **49**, pp. 307–316.
[30] Swartz, E. T., and Pohl, R. O., 1989, "Thermal Boundary Resistance," Rev. Mod. Phys., **61**, pp. 605–668.
[31] Qiu, T. Q., and Tien, C. L., 1993, "Heat Transfer Mechanisms During Short-Pulse Laser Heating of Metals," ASME J. Heat Transfer, **115**, pp. 835–841.
[32] Yang, R., Chen, G., Laroche, M., and Taur, Y., 2005, "Simulation of Nanoscale Multidimensional Transient Heat Conduction Problems Using Ballistic-Diffusive Equations and Phonon Boltzmann Equation," ASME J. Heat Transfer, **127**, pp. 298–306.
[33] Majumdar, A., 1993, "Microscale Heat Conduction in Dielectric Thin Films," ASME J. Heat Transfer, **115**, pp. 7–16.
[34] Lin, Z., Zhigilei, L. V., and Celli, V., 2008, "Electron-Phonon Coupling and Electron Heat Capacity of Metals Under Conditions of Strong Electron-Phonon Nonequilibrium," Phys. Rev. B, **77**, p. 075133.
[35] Chen, G., 2005, *Nanoscale Energy Transport and Conversion: A Parallel Treatment of Electrons, Molecules, Phonons, and Photons*, Oxford University Press, New York.
[36] Chowdhury, I. H., and Xu, X., 2003, "Heat Transfer in Femtosecond Laser Processing of Metal," Numer. Heat Transfer, Part A, **44**, pp. 219–232.
[37] Kittel, C., 1996, *Introduction to Solid State Physics*, Wiley, New York.
[38] Qiu, T. Q., and Tien, C. L., 1992, "Short-Pulse Laser Heating on Metals," Int. J. Heat Mass Transfer, **35**, pp. 719–726.
[39] Smith, A. N., and Norris, P. M., 1998, "Numerical Solution for the Diffusion of High Intensity, Ultrashort Laser Pulses Within Metal Films," *Proceedings of the 11th International Heat Transfer Conference (Korean Society of Mechanical Engineers)*, Vol. 5, p. 241–246.
[40] Hostetler, J. L., Smith, A. N., and Norris, P. M., 1997, "Thin-Film Thermal Conductivity and Thickness Measurements Using Picosecond Ultrasonics," Microscale Thermophys. Eng., **1**, pp. 237–244.
[41] Smith, A. N., and Norris, P. M., 2001, "Influence of Intraband Transitions on the Electron Thermoreflectance Response of Metals," Appl. Phys. Lett., **78**, pp. 1240–1242.

Numerical Study of Thermally Targeted Liposomal Drug Delivery in Tumor

Aili Zhang

Xipeng Mi

Geer Yang

Department of Biomedical Engineering,
Shanghai Jiao Tong University,
Shanghai 200240, P.R. China

Lisa X. Xu

Department of Biomedical Engineering,
and Med-X Research Institute,
Shanghai Jiao Tong University,
Shanghai 200240, P.R. China

The efficacy of cancer chemotherapy can be greatly enhanced by thermally targeted nanoparticle liposome drug delivery system. A new theoretical model coupling heat and mass transfer has been developed to study the spatial and transient drug distributions. In this model, the influence of tumor cell apoptosis and necrosis in drug transport is also considered, in addition to the tumor microvasculature permeability to nanoliposomes. The model predictions agree well with our previous experimental results, and it has been used to simulate the nanoparticle drug distribution in the tumor under hyperthermic conditions. Results show that hyperthermia alone only enhances drug accumulation in the periphery of a tumor with 1 cm in radius, and the tumor cells in the central region are hardly damaged due to poor drug diffusion. Apoptosis or necrosis of the tumor cells could significantly influence the drug penetration and should be accounted for in drug diffusion modeling to accurately predict the therapeutic effect. Simulation study on the combined radio frequency ablation and liposomal doxorubicin delivery shows more effective treatment outcome, especially for larger tumors. The present model can be used to predict the treatment outcome and optimize the clinical protocol.
[DOI: 10.1115/1.3072952]

Keywords: thermally targeted drug delivery, hyperthermia, nanoparticle liposomes, RF ablation

1 Introduction

Improvement of the therapeutic efficacy while minimizing the side effects of antitumor drug on normal healthy tissues has been a long struggling goal of many researchers. Encapsulating drug with liposomes of certain sizes is proven to prolong the drug circulation time, reduce the drug accumulation in normal tissues, and thus, enhance the targeted drug delivery to the tumor [1,2]. This is in part attributed to the incomplete and leaky wall of the vessels in a tumor. The optimal liposome size is found to be between 90 nm and 200 nm in diameter, as both the circulation time and accumulation in the tumor are considered [3,4].

To further increase the antitumor drug delivery efficiency, mild heating (i.e., hyperthermia) is used locally. Study of the thermally targeted liposomal drug delivery has been reported to enhance antitumor efficacy [5,6]. During hyperthermia, the local blood perfusion and the permeability of the tumor vasculature to macromolecules are significantly increased, resulting in massive extravasation of nanoparticle liposomal drug [7–10]. Moreover, thermally sensitive liposomes can also be used to release drug at the locally elevated temperature for better therapeutic index [11,12]. The final outcome of the chemotherapeutic treatment depends on an adequate drug distribution throughout the tumor. Survival of some tumor cells might lead to tumor recurrence or metastasis. However, it is very difficult to observe the local drug concentration in vivo even with the most advanced imaging techniques. Thus, modeling and numerical simulations of the drug delivery process become necessary and useful.

Several models have been developed to describe the drug delivery process for different applications [13–15]. Ward et al. studied the drug transport and tumor growth at the same time using a mathematical model to describe small molecules drug and nutrition transported from the tumor edge to the center through diffusion only (no advection through vascular network taken into account). Considering the characteristics of breast cancer, Lankelma et al. [16,17] studied the doxorubicin activity in islets of breast cancer by assuming drug transport through both transcellular (the cellular network) and paracellular (the intercellular interstitium) pathways. Magni et al. [18] built a mathematical model to describe the cancer growth dynamics in response to anticancer agents in xenograft. In this model, the tumor cell growth, division, and death are all considered, and the change of tumor in response to chemotherapy is assumed to be determined by the balance between the cell proliferation and death. El-Kareh and Secomb [19–21] presented models accounting for the cellular pharmacodynamics of drug, and numerically studied the intraperitoneal delivery of cisplatin in tumor and investigated the influence of hyperthermia on the drug penetration distance.

Unlike small molecule drug transport, the delivery process of liposomal drug is much more complex. The liposome encapsulated drug selectively extravasates into the tumor region from blood vessels [22]. Hyperthermia has been found to remarkably improve the extravasation of liposome nanoparticles [4,12]. As the liposome breaks, the antitumor drug releases and diffuses throughout the tumor region. Without taking the spatial nonuniformity of the tumor into consideration, El-Kareh and Secomb [23] developed a model to compare the different delivery methods of bolus injection, continuous infusion, and liposomal delivery of doxorubicin. The model has been used to study the liposome leakage from the tumor vasculature, the breakage of liposomes, and the cellular uptake of free drug simultaneously, but the diffusion effect is neglected. In fact, the heterogeneous distribution of tumor vessels causes nonuniform extravasation of liposomal drugs, which could in turn significantly affect the drug concentration gradient [24]. The effect of tumor cell necrosis and apoptosis induced by the antitumor drugs [25] should also be considered in modeling. Furthermore, as local heating is imposed on the tumor,

Contributed by the Heat Transfer Division of ASME for publication in the JOURNAL OF HEAT TRANSFER. Manuscript received September 9, 2008; final manuscript received December 9, 2008; published online February 24, 2009. Review conducted by Robert D. Tzou. Paper presented at the 2008 International Conference on Micro/Nanoscale Heat Transfer (MNHT2008), Tainan, Taiwan, January, 6–9, 2008.

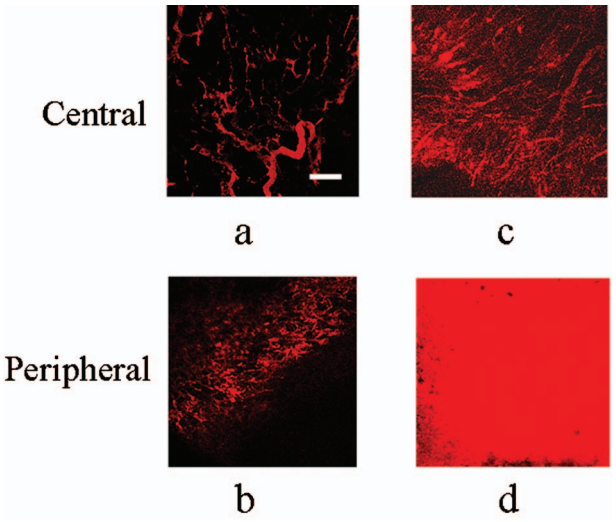

Fig. 1 Vasculature fluorescent images in the tumor center and periphery before and after thermal treatments. Bar: 200 μm. (*a*) and (*b*): before treatment and (*c*) and (*d*): heated at 42°C for 1 h [8].

tissue temperature distributions are normally not uniform, and the drug delivery is coupled with heat and mass transfer.

To precisely study the liposomal delivery and free drug distribution inside the tumor during hyperthermia, the coupled heat and mass transport process has been investigated and modeled based on our previous experimental results. In this model, the heterogeneous tumor morphology, vascular permeability to liposome nanoparticles, and the drug gradients are all considered. The treatment efficacy is quantified and compared with the experimental results. Influences of some key parameters, such as the liposome rupture rate, the apoptosis induced diffusivity change on drug penetration, are studied. The model is further used to investigate the radio frequency (RF) ablation combined liposome drug treatment for larger tumors by coupling heat and mass transfer.

2 Experimental Study of Nanoparticle Liposome Extravasation In Vivo

In our previous experimental study, the extravastion of liposomes in the 4T1 tumor of nude mice has been quantified, and the microvascular sensitivity to hyperthermia studied [8]. Tumor is implanted into the skin tissue within the window chamber on the dorsal flap of the nude mouse. After 10 days of growth, the tumor becomes 1–2 mm in diameter and 150 μm thick. Densely distributed and incomplete angiogenesis is found in the tumor peripheral region, while there are only few vessels in a more ordered branching pattern in the tumor central region through histological study. The vasculature in the tumor peripheral region is found to be much more sensitive to hyperthermia than that in the center. Stabilized long-circulating polyethyleneglycol (PEG) liposome is prepared by the lipid film hydration and extrusion method. Liposome with a narrow size distribution (average of 90–120 nm) has been used. A 200 ul suspension of the liposomal doxorubicin (encapsulated Dox of concentration 0.1 mg/ml) is injected into the tail vein of the anesthetized mouse (average weight of 20 g). The tumor is heated to 42°C using a water bath mounted to the window chamber for 1 h, and the temperatures are monitored using thermocouples. The extravasation of liposomes are observed and imaged by confocal microscopy shown in Fig. 1. The fluorescence intensity indicating the liposome concentration in the tumor interstitial is quantified three-dimensionally and results are compared with those without heating (when the mouse body temperature at 34°C), as shown in Fig. 2.

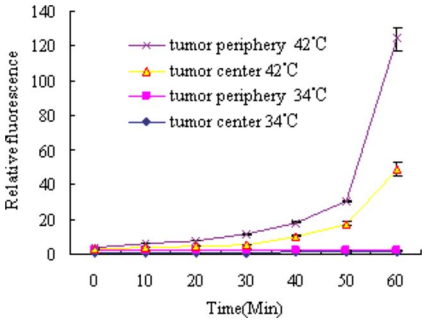

Fig. 2 HT-induced extravasation of 100 nm liposome nanoparticles at 42°C or 34°C for 1 h in different tumor regions. The largest HT enhancement of extravasation was seen at tumor periphery. Values are mean and standard error (SE) (n=11 for each group) [8].

As seen in Fig. 2, hyperthermia has caused a large increase in liposomal Dox extravasation in the peripheral region, while only a small increase is found in the tumor center as compared with those at the body temperature. Different thermal sensitivities of the newly formed and incomplete vessels in the tumor periphery and the relatively mature vascular network could have contributed to the heterogeneous extravasation of the nanoparticle liposomal drug.

3 Model Development

As previously observed in our experimental studies [8], few vessels exist in the central region of the tumor, while abundant vessels are found in the peripheral region. For modeling purposes, a tumor with radius of R can be divided into two parts: the central region within $r<R_c$ without any vessels and the peripheral region of $R_c<r<R$ with microvasculature evenly distributed, as illustrated in Fig. 3. The surrounding normal tissue is assumed to be infinite.

The liposomal doxorubicin is injected through the rat tail vein, and transports in the vasculature before reaching the tumor. Due to the elimination effect, the liposome concentration in plasma decreases exponentially with time and can be expressed as [23]

$$C_{L,V}=\frac{M}{M_g}(A_1e^{-k_1t}+A_2e^{-k_2t}) \tag{1}$$

where M is the drug dose (mg/m^2 or ug/g), M_g is the dose (mg/m^2 or ug/g) used to fit the experimental data and to obtain the plasma pharmacokinetic parameters for the liposome: A_1, A_2, k_1, and k_2 [2,23]. Here, the concentration of liposomal drug is assumed to scale linearly to the dose M. The first term in the

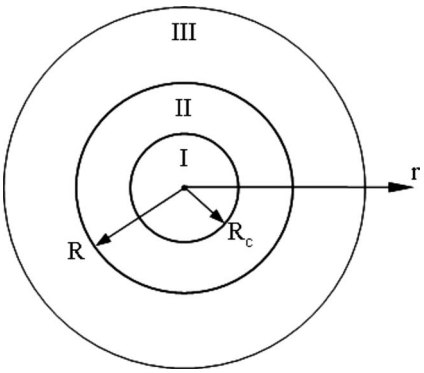

Fig. 3 Schematics of the tumor, I: central region of the tumor, II: peripheral region of the tumor, and III: surrounding normal tissue

Table 1 Parameters used in modeling

Parameters		Value
k_t		0.51 W/m K [27]
$(\rho c)_t$, $(\rho c)_b$		4180 J/m^3 K [28]
q_{met}		30,000 W/m^3 for tumor [28]
		450 W/m^3 for normal breast [29]
T_b		37°C
w_{b_37}		0 ml/s/ml in tumor central region
		0.009 ml/s/ml in tumor periphery [30]
		0.00018 ml/s/ml in normal tissue [30]
Mouse	M_g	6 μg/g [31]
	A_1	0
	A_2	90 μg/ml [31]
	k_1	0
	k_2	0.00033 min^{-1} [31]
Human	M_g	50 mg/m^2 [23]
	A_1	6.9 μg/ml [23]
	A_2	12.2 μg/ml [23]
	k_1	0.00502 min^{-1} [23]
	k_2	0.00025 min^{-1} [23]
$D_{L,\text{app}}$		2.4×10^{-9} cm^2/s [32]
P_{L_37}		2.0×10^{-8} cm/s [33]
S_t		200 cm^{-1} in tumor periphery [23]
		0 cm^{-1} in other regions
$D_{D,0}$		6.7×10^{-7} cm^2/s [34]
φ_{e0}		0.12 in central tumor [8]
		0.23 in tumor periphery [8]
		0.3 in normal tissue [35]
τ_r		24 h [23]
$v_{\max}$		2.8 μg/ml/min [23]
k_i		13.7 μg/ml [23]
k_e		0.219 μg/ml [23]
k_d		8.53×10^{-8} ml/μg/s [36]
C_1		743×10^8 [37]
α		0.000529 mm^{-1} [37]

brackets on the right hand side of the equation represents an initial rapid distribution phase of drug, where a minor fraction of the injected dose (A_1) is cleared through circulation with the kinetic parameter k_1. The second term is an extended distribution phase, where the rest of the dose (A_2) is cleared with the parameter k_2. Previous experimental research has found different values of pharmacokinetic parameters (k_1,k_2) in mouse and in human [26], which are listed in Table 1.

The liposomal drug in blood transports across the leaky wall of vessels and into the tumor interstitial through both diffusion and convection [38,39]. The apparent permeability $P_{L,\text{app}}$ of the vasculature is normally used to quantify the transvascular transport [40]. According to the definition, transvascular mass transfer of liposomal drug is proportional to the apparent vascular permeability, the concentration difference across the vessel wall, and the vessel surface area. A source term is used to describe the vascular leakage in the tumor peripheral region ($R_c < r < R$). In reference to the greatly enhanced extravasation of liposome previously found during hyperthermia [12], an increase of 76-fold in $P_{L,\text{app}}$ from its original value at 37°C is assumed. After the extravasation, liposomal drug transports in the interstitial space in both directions toward the central region and the surrounding normal tissue, respectively, owing to the concentration gradient (diffusion) and the motion of interstitial fluid (convection). For macromolecules like liposome, the magnitude of diffusion is comparable to the convection, and both should be considered. As it is hard to separate the diffusion and convection, an apparent diffusivity, $D_{L,\text{app}}$, is used to describe the interstitial transport process. In the mean time, the liposome ruptures and releases free antitumor drugs. This process is assumed to follow the first-order kinetics with the decaying time constant τ_r [23]. Thus, the concentration of the liposomal drug in the interstitial of the peripheral region can be determined by

$$\frac{\partial C_{L,E}}{\partial t} = D_{L,\text{app}} \cdot \nabla^2 C_{L,E} + P_{L,\text{app}} \cdot A_t (C_{L,V} - C_{L,E}) - C_{L,E}/\tau_r \quad (2)$$

where $C_{L,E}$ is the drug concentration in liposome form in the extracellular space (milligrams per milliliter of total tumor volume); the first term on the right hand side of the equation represents apparent diffusion of liposomal drug in tumor tissue, the second term the penetrative transport across the vessel wall, and the third term the rupture of liposome. A_t is the effective surface area of the vasculature per unit tumor volume.

Released from liposome, the antitumor drug (i.e., doxorubicin) transports in the interstitial space and is up-taken by the cells. For small molecules, such as doxorubicin, diffusion is dominant while convection is relatively smaller [41]. Moreover, high interstitial pressure in the tumor interior impedes convective transport of the drug. Therefore, convection is negligible for free doxorubicin transport. By considering tumor tissue as a porous material, the effective diffusivity of free drug D_D can be determined from the drug diffusivity in the interstitial fluid $D_{D,0}$ and the interstitial volume fraction φ_e [42]

$$D_D = \frac{2\varphi_e}{3 - \varphi_e} D_{D,0} \quad (3)$$

As more and more tumor cells undergo necrosis or apoptosis during or post-treatment, the interstitial volume fraction φ_e increases [43] and is assumed to change linearly with tumor cell survival rate S

$$\varphi_e = 1 - (1 - \varphi_{e0}) \times S \quad (4)$$

where φ_{e0} is the initial volume fraction of interstitial space before drug treatment. Through the histological study, different values of φ_{e0} have been found in different regions of the tumor. S is the survival rate of the tumor cells.

Thus, the transport of free drug released from liposome can be expressed as

$$\frac{\partial C_{D,E}}{\partial t} = D_D \cdot \nabla^2 C_{D,E} + \frac{C_{L,E}}{\tau_r} - \frac{\partial C_{D,I}}{\partial t}(1 - \varphi_e) \quad (5)$$

where $C_{D,E}$ is the free drug concentration in the extracellular space (milligrams per milliliter of total tumor volume); the first term on the right hand side represents free drug diffusion in tissue, the second term the drug released from liposome, and the third the cellular uptake of drug by the tumor cells, where $C_{D,I}$ is the intracellular bound drug concentration.

The drug is believed to transport passively across the cell membrane, and the cellular uptake is the carrier-mediated transport, which can be expressed as [23]

$$\frac{\partial C_{D,I}}{\partial t} = v_{\max}\left(\frac{C_{D,E}}{C_{D,E} + k_e} - \frac{C_{D,I}}{C_{D,I} + k_i}\right) \quad (6)$$

where $C_{D,I}$ is the intracellular bound drug concentration (milligrams per milliliter of intracellular volume). $v_{\max}$ is the maximal cellular uptake rate, and k_i and k_e are pharmacodynamics parameters.

Tumor is treated with both heating and drug. Since in vitro experimental studies have showed no significant tumor cell death under the hyperthermic condition at 42°C alone, cell killing is assumed mainly due to the drug effect, $S = S_d$. According to the drug killing mechanism, the cell survival rate decreases exponentially with the area under the drug concentration curve, the time integral of $C_{D,I}$ (AUC). Thus, S_d is expressed as [36]

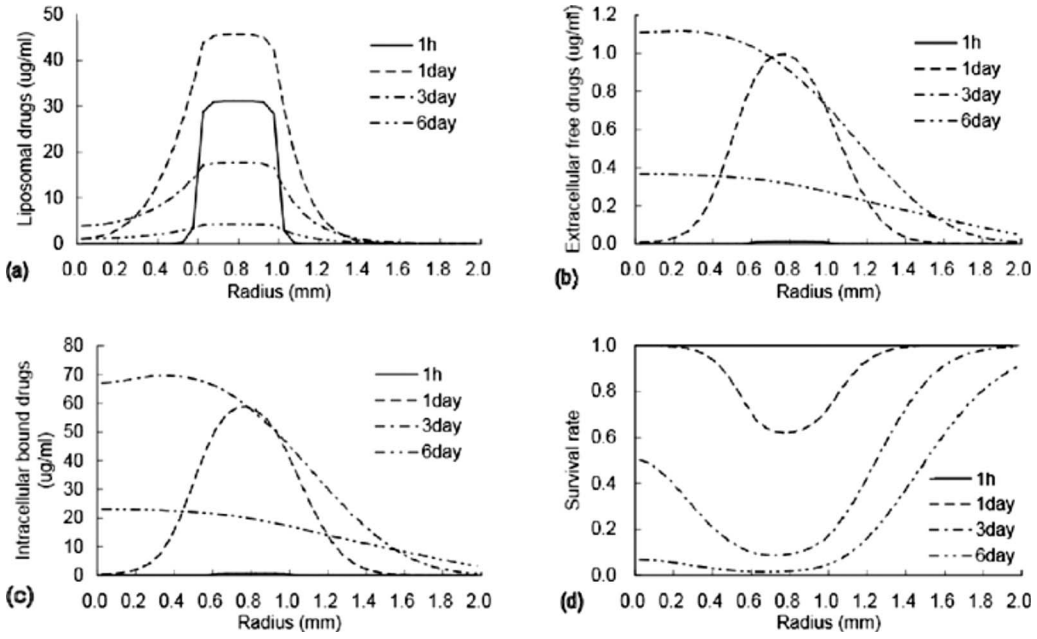

Fig. 4 Simulation results of drug concentration and cell survival rate in the tumor after 1 h liposomal drug delivery aided by hyperthermia at 42°C, where: the central region (0–0.6 mm), the peripheral region (0.6–1.0 mm), and the surrounding normal tissue (1.0–2.0 mm)

$$S_d = \exp\left(-k_d \times \int_0^t C_{D,I} dt\right) \tag{7}$$

where k_d is the pharmacodynamical parameter.

The corresponding boundary and initial conditions are listed as follows.

(1) For infinity,

$$C_{L,E}|_{r=\infty} = 0, \quad C_{D,E}|_{r=\infty} = 0, \quad C_{D,I}|_{r=\infty} = 0 \tag{8}$$

(2) For tumor center,

$$\left.\frac{\partial C_{L,E}}{\partial r}\right|_{r=0} = 0, \qquad \left.\frac{C_{D,E}}{\partial r}\right|_{r=0} = 0 \tag{9}$$

(3) For initial,

$$C_{L,E}|_{t=0} = 0, \quad C_{D,E}|_{t=0} = 0, \quad C_{D,I}|_{t=0} = 0 \tag{10}$$

4 Simulation Results and Discussion

The outcome of the animals treated by the thermally targeted nanoliposome drug delivery has been followed up and reported in Ref. [44]. The histological analysis finds no significant changes in the tumor cells in both the central and peripheral regions right after the heating. But 3 days later, many cells died in the peripheral region, while only a few dead cells were found in the central region. On the sixth day after drug administration, significant tumor cell death is found in both regions. The model developed above is first used to simulate the experimental results. According to the experiments, the tumor is about 1 mm in radius, and the radius of avascular central tumor is about 0.6 mm. With the parameters given in Table 1, Eqs. (1)–(7), the mass transfer of both liposomal and free drugs is numerically solved using MATLAB. Equations (1) and (2) are first solved to obtain $C_{L,E}$, and the results are substituted into Eq. (5). Equations (3)–(7) are solved simultaneously for $C_{D,E}$, $C_{D,i}$, and S. The spatial and temporal concentrations of both liposome and free drugs and the survival rate of the tumor cells are shown in Fig. 4.

As seen in Fig. 4(*a*), there is a great deal of liposomal drugs that accumulated in the peripheral region ($0.6 < r < 1.0$ mm) right after the heating. It decreases with time owing to its breakage and diffusion into the central region and the surrounding normal tissue. While in the central region ($0 < r < 0.6$ mm), the liposomal drug first increases, as the diffusion rate is faster than the rupture rate. But as more and more liposomes break and diffuse, and less come in from blood circulation, its concentration deceases again. The highest concentration in the central region appears 31.5 h after the treatment. The concentrations of free drug released from liposomes in both the peripheral and central regions first increase with time and then decrease (Fig. 4(*b*)). The highest concentration occurs after 42 h in the peripheral region and 70.5 h in the central region. The concentration of the intracellular bound drug changes synchronously with that of the extracellular free drug because of the relatively fast uptake process as compared with drug diffusion (Fig. 4(*c*)).

Numerical results shown in Fig. 4(*d*) indicate that right after the treatment, all the cells are alive. One day later, the drug effect on the tumor cells in the peripheral region appears, and the averaged survival rate decreases to 0.65 in this region. While very little doxorubicin has reached the central region, the average survival rate of the tumor cells is 0.94. On the third day, the survival rate of the tumor cells in the periphery gets even smaller with an average value of 0.10. An obvious decrease in the survival rate in the central tumor also occurs, and the average is 0.30. In 6 days, the survival rate in both regions further decreases, and the average becomes 0.01 and 0.04, respectively, indicating significant cell death. These predictions are in good agreement with the experimental findings reported in Ref. [44].

Furthermore, the model can also be used to predict the treatment effect of a relatively larger tumor (i.e., >1 cm in radius), in which it is more difficult for drug transport to the center. The model presented above has been used to predict drug distribution and the corresponding cell survival rate. With the administered dose (M) of 50 mg/m^2, the drug transport processes in a tumor 1 cm in radius without and with hyperthermia have been simulated, and the results are shown in Figs. 5 and 6, respectively.

As seen in Fig. 5, liposomal and free drugs mainly accumulate in the tumor periphery (6–10 mm). Little drug diffuses into the

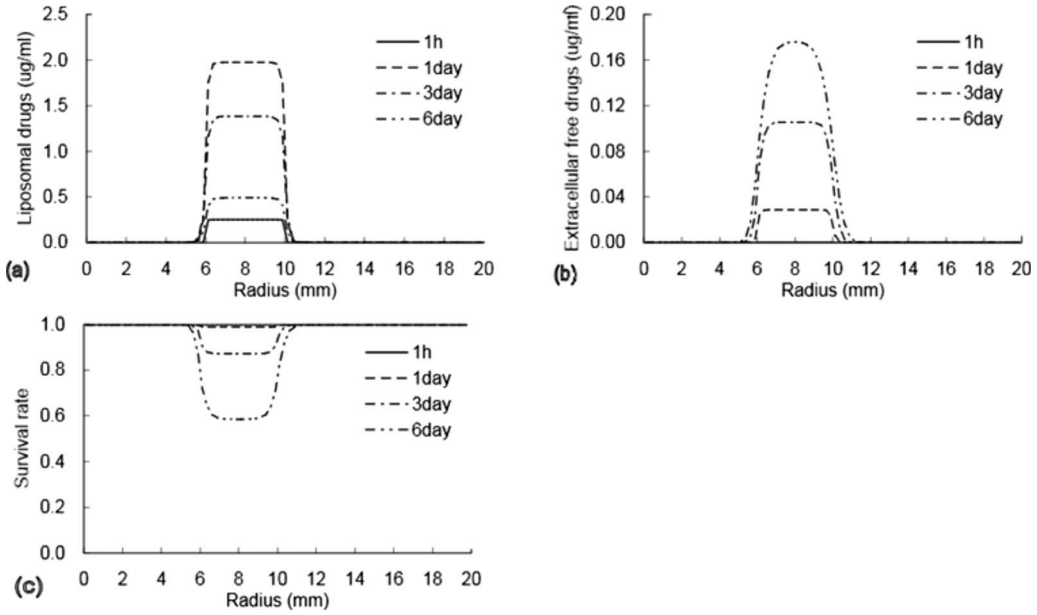

Fig. 5 Simulation results of drug concentrations and cell survival rate in a 1 cm tumor without hyperthermia, where: the central region (0–6 mm), the peripheral region (6–10 mm), and the surrounding normal tissue (10–20 mm)

center even in 6 days after the treatment, thus barely any cells die in the region. Even in the peripheral region, the cell death is insufficient due to the tumor size.

The transport process of liposomal drug after 1 h delivery with hyperthermia at 42°C is simulated, and the corresponding results are shown in Fig. 6. In comparison, the overall trend is quite similar except for the magnitude of the drug concentration and the cell survival rate. The locally imposed hyperthermia has greatly enhanced the accumulation of both the liposomal and free drugs in the peripheral region and resulted in a more serious damage in this region. In 6 days after the treatment, the averaged AUC of the liposomal drug under hyperthermia is about four times of that without hyperthermia, and the survival rate of the tumor cells in the peripheral region is almost 0. However, owing to the impermeability of the tumor mature vessels in the central region and the difficulty of liposomal drug diffusion, as predicted using the model, the drug effect in the tumor center is very limited even with local hyperthermia [31,35].

Encapsulating antitumor drug in liposomes delays the drug release and thus reduces the clearance rate of the drug in vivo. There have been a lot of efforts spent on improving the pharmacokinetics performance of liposomal drugs. Long circulation and ther-

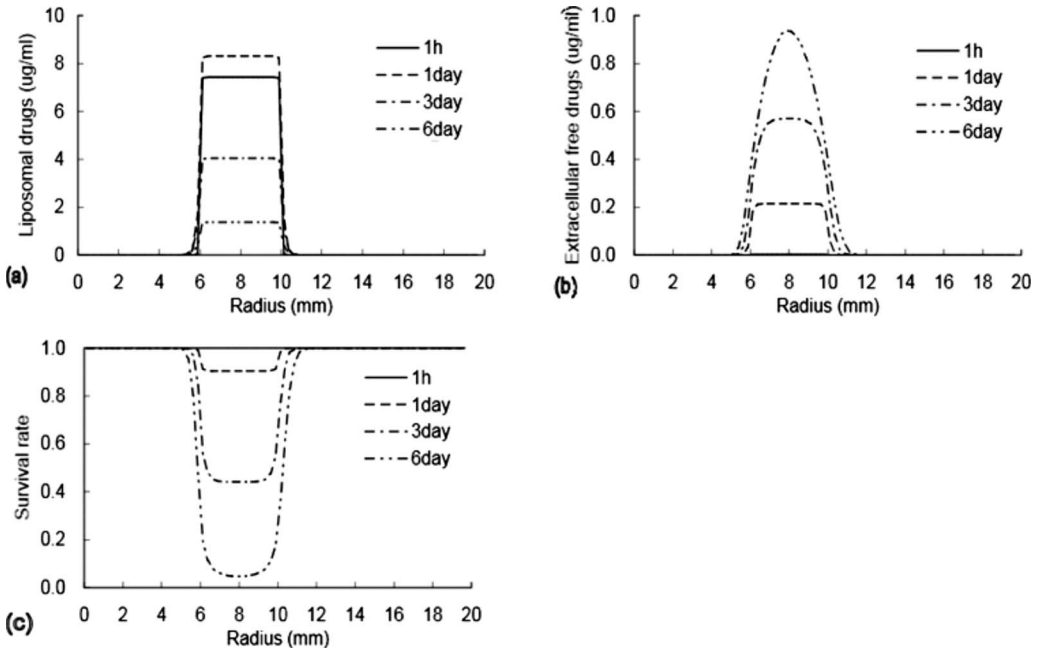

Fig. 6 Simulation results of drug concentrations and cell survival rate in a 1 cm tumor with hyperthermia, where: the central region (0–6 mm), the peripheral region (6–10 mm), and the surrounding normal tissue (10–20 mm)

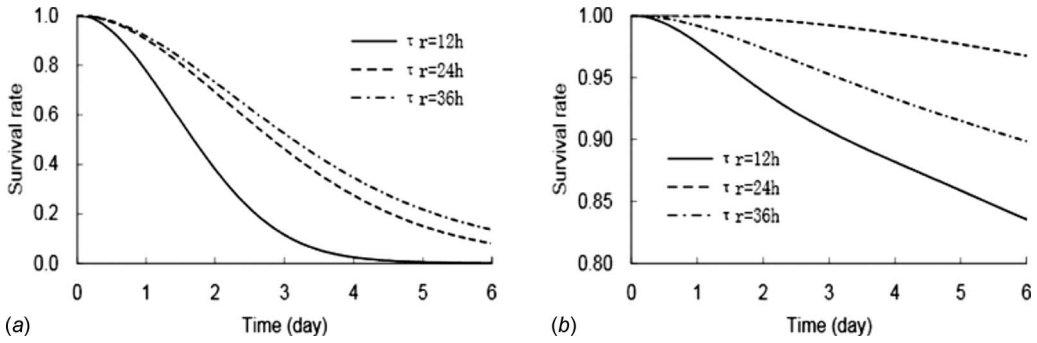

Fig. 7 The effect of liposome rupture time τ_r on drug delivery and tumor therapy: (*a*) average survival rate in the central region of the tumor and (*b*) average survival rate in the peripheral region of the tumor

mosensitive liposome have been developed. The speed of liposomal drug release also influences the treatment. To evaluate the liposome rupture influence, τ_r of 12 h and 36 h are used in the simulation. The numerical results of the average cell survival rate in the peripheral and central regions of tumor are shown in Fig. 7. It is noted that smaller value of τ_r results in better treatment efficacy in both regions. These predictions are in accordance with the experimental findings reported in Ref. [12] where temperature-sensitive liposomal drugs are proven to be more effective.

Different from other models [15,16,18], the present model accounts for the drug induced cell apoptosis or necrosis effect on the drug penetration using a cell survival rate dependent diffusion rate in Eqs. (3) and (4). Figure 8 illustrates the survival rate in the tumor center when the cell necrosis induced diffusivity change (CNIDC) is or is not taken into consideration. Significant difference can be found. As more cells die, the tissue porosity increases and thus the diffusivity. More drugs reach the rest of the tumor cells resulting in more cell death. The results indicate that the influence of the apoptosis or necrosis is an important parameter determining the accuracy of the prediction.

The above study has shown that the thermally targeted drug delivery enhanced the treatment effect of tumor. But, it is still difficult for the drug to diffuse to the central region in a relatively larger tumor and achieve the desired therapeutic effect. This finding is consistent with that reported from previous clinical studies [9,45]. For a complete ablation of large tumors, its central region needs to be treated by other modalities combined, i.e., high temperature or low temperature approaches [46].

5 Study of the Combined RF Ablation With Liposome Drug Treatment of Tumor

Previous clinical studies have shown that the combined RF ablation and liposomal doxorubicin treatment can be used to enhance the delivery of liposomal drugs and to maximize the tumor destruction [46]. To optimize the combined treatment, both the temperature and drug induced cell necrosis need to be considered, thus the coupled temperature and drug distributions after the treatment are of a great importance. The present model is used to simulate the combined RF ablation and liposomal doxorubicin delivery for a tumor 1 cm in diameter. The RF probe, guided by the imaging system, is inserted into the center of the tumor right after intravenous delivery of the liposomal drugs. During the RF treatment, the temperature distribution inside the tumor is analyzed using the Pennes bioheat transfer equation, in which the RF volumetric heating is treated as the source [47]

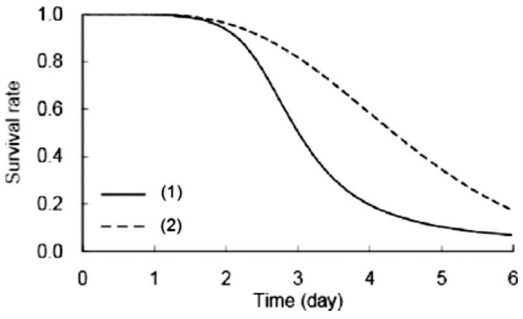

Fig. 8 The effect of cell necrosis induced diffusivity change on tumor therapy: (1) with cell necrosis induced diffusivity change considered; (2) without consideration of cell necrosis induced diffusivity change

$$(\rho c)_t \frac{\partial T_t}{\partial t} = k_t \nabla^2 T_t + \omega_b (\rho c)_b (T_b - T_t) + q_{\mathrm{SAR}} + q_{\mathrm{met}} \tag{11}$$

where T_t is the tissue temperature. k_t is the thermal conductivity, ρ is the density, c thermal capacity, subscript t refers to tissue and b to blood, w_b is the blood perfusion rate, T_b is the blood temperature, and q_{SAR} and q_{met} are the specific absorption rates of the RF heating and the metabolic heat, respectively. k_t, ρ, and c are assumed to be the same in all the regions, while different w_b and q_{met} values are used, as shown in Table 1. Sensitivity of the blood perfusion rate to temperature is considered. From previous experiments, it has been found that blood flow increases to about twofold of w_{b_37} (w_b at 37°C) at 42°C [30] and fourfold of w_{b_37} at 44°C [30]. It stops at temperatures either lower than 8°C [48] or higher than 46°C [30]. The blood perfusion w_b is assumed to change linearly between these temperature points. By considering the RF probe as a finite line source, the specific absorption rate of RF in tissue, q_{SAR}, can be expressed as [37]

$$q_{\mathrm{SAR}} = C_1 p \frac{(2\alpha r + n - 2)e^{-2\alpha r}}{r^n} e^{-z^2/z_c^2} \tag{12a}$$

where z and z_c are the axial distance and the decay distance, respectively, p is the RF power, C_1 is the scaling constant, α is the attenuation constant, n is an exponential constant, and r is the radial distance from the center. Referring to the experimental measurements reported in Ref. [49], the specific adsorption rate of the RF heating is simplified as

$$q_{\mathrm{SAR}} = \begin{cases} C_1 p \dfrac{(0.001058r + 1)e^{-0.001058r}}{r^3} & -z_0 \le x \le z_0 \\ 0 & \text{else} \end{cases} \tag{12b}$$

where z_0 is the active length of the RF probe; it varies with tumor dimensions. The probe diameter is 3 mm. Values of the parameters used are shown in Table 1. To overcome local overheating, the RF probes with internal cooling are normally used [49,50]. In this study, the convective condition between the probe wall and

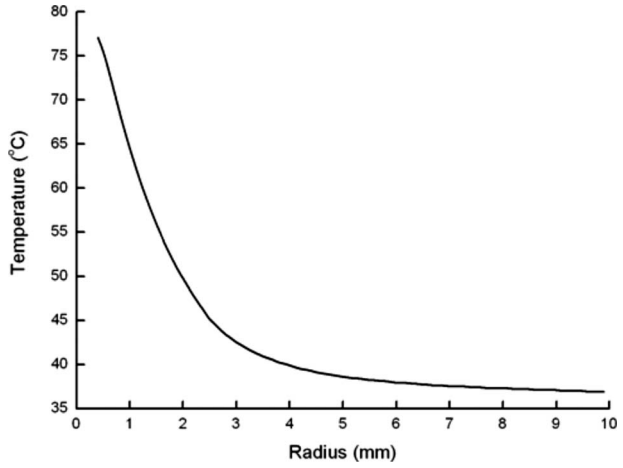

Fig. 9 Temperature distribution in the tumor after 30 min of the RF heating at 10 W; radius represents the distance measured from the RF probe

the flow inside the probe is adopted from Ref. [49], in which low temperature nitrogen is used. The boundary condition for tissue contacting the probe surface is

$$k_t \frac{\partial T_t}{\partial r} = h_g(T_t - T_i) \quad \text{at} \quad r = r_0, z > -z_0 \tag{13}$$

where T_i is the inner-flow temperature, h_g is the internal convection coefficient of the flow, and r_0 is the probe radius.

The apparent vascular permeability, $P_{L,\text{app}}$, is assumed to change linearly with temperature from the initial value P_{L_37} at 37°C to 76-fold P_{L_37} at 42°C [12], and kept until 44°C, when the blood flow starts to drop [51] and decreases linearly to zero at 46°C. During the heating period, the tumor cells are killed through heating, as the drugs are mainly enclosed in liposomes and have not taken into effect. Heating induced survival rate of the tumor cells S_h is

$$S_h = e^{-k_h \int_0^t R^{(43-T)} d\tau} \tag{14}$$

where k_h and R are constants. After heating, the tumor cells that survived are subsequently killed by antitumor drugs. Thus, the total survival rate of cells, S, is expressed as

$$S = S_h \times S_d \tag{15}$$

The partial differential equations (PDEs) governing the unknowns are essentially nonlinear, especially for the RF ablation combined drug delivery process when the apparent permeability, $P_{L,\text{app}}$, and S are also temperature dependent. The distribution of temperature and drug concentration in the tumor and surrounding normal tissue in different time intervals are then numerically obtained using FLUENT.

Temperatures at different distances from the RF probe in the tumor after 30 min of heating are shown in Fig. 9. It can be seen that tissue temperatures in the central region ($0.25 \text{ mm} < r < 2.5 \text{ mm}$) are all above 45°C, and can reach as high as 78°C near the probe in the center, while in the peripheral region ($2.5 \text{ mm} < r < 5 \text{ mm}$) tissue temperatures are between 37°C and 45°C. It is hard to further increase the tissue temperature due to a rapid decay in the RF heating and the much higher local blood perfusion in the periphery.

Distributions of liposomal drug, extracellular free drug, and the survival rate of the tumor cells in different days after the combined RF ablation and liposome drug treatment are shown in Figs. 10(*a*)–10(*c*). Obviously, the liposomal drug mainly concentrates in the peripheral region. Much less liposomal drug extravasates in the central region or in the surrounding normal tissue because of the absence of blood vessels in the tumor center and the low permeability of the vessel wall in normal tissue. The concentration of liposomal drug in the periphery decreases with time due to the decay of liposome concentration in blood and the rupture of liposomes. In 7 days after the treatment, the interstitial liposomal drug concentration decreases to 1.0 μg/ml, and most liposomes rupture. As seen in Fig. 10(*b*), the concentration of the extracellular free drug first increases in the peripheral region, and then decreases as diffusion into the central region. While in the central region, as most of the cells have been killed by the RF heating, only drug diffusion takes place and also decreases later when the source decreases. The cell survival rates with respect to time are shown in Fig. 10(*c*). Most of the tumor cells have been killed right after the RF ablation, while those in the peripheral region are gradually killed by the liposomal drug. The simulation results show that the combined RF ablation and liposomal drug treatment of the tumor could achieve much better treatment effect by overcoming the disadvantages of either one alone, especially for a sizable tumor. The major concern of the RF ablation alone is the increased blood perfusion in the tumor peripheral region during heating, which might result in incomplete killing and increase certain risks of the incidence of tumor metastasis [52,53]. The thermally enhanced extravasation of the nanoliposome drugs could ensure sufficient killing of the surviving tumor cells and vasculature in the peripheral region.

For larger tumors, the heating power of the RF can be increased, and local overheating be prevented by adjusting the flow rate of low temperature nitrogen inside the RF probe. Figure 11 illustrates the extravasation of the liposome drug right after the RF heating of a 3 cm diameter tumor and the survival rate of the tumor cells in 7 days after the combined treatment with different heating powers. Obviously, for the heating powers studied, the higher the power, the more liposome drugs extravasated in the peripheral region, and the more tumor cells that die. In the outer central region of tumor, there is a peak on the curve of the tumor cell survival rate shown in Fig. 11(*b*) for powers that are relatively low. In this region, the temperature increase is not high enough, and the drug fails to have a fatal effect. When the power is increased to 60 W, the highest temperature inside the tumor reaches about 87°C; most of the tumor cells in the central region could be completely killed, but not in the peripheral region, where the cells are mainly killed by the drug. By decreasing the half-life time of the liposome drug τ_r, the survival rate of the tumor cells in this region is significantly decreased, indicating a great potential of the thermally sensitive liposome drug.

The total volume of the tumor cells (3 cm diameter), with the survival rate lower than 0.1%, after the RF ablation alone is compared with that of the combined treatment, as shown in Fig. 12. The treatment region is clearly enlarged through the latter, which accords well with the experimental findings reported in Ref. [46]. On the other hand, it is worthy noting that for the combined treatment, besides the RF heating power and the half-life time of the liposome drug, as studied in this paper, the timing of the liposome drug delivery in relation to the RF ablation is another important factor that would affect the final therapeutic outcome [46].

6 Conclusion

A new mathematical model has been developed to study the thermally targeted drug delivery process in tumor. Both the drug distribution and the treatment efficacy under different treatment protocols have been numerically simulated. The influence of several key parameters on drug delivery and therapeutic efficiency are discussed.

Local hyperthermia enhances the accumulation of liposomal drugs in the tumor region by increasing tumor vessel permeability $P_{L,\text{app}}$ and blood perfusion. Numerical results show higher AUC of liposomal drugs in tumor tissue under the hyperthermic condition. Compared with liposomes, the diffusion of free drug contributes more to drug transport in tumor tissue, since the diffusivity of

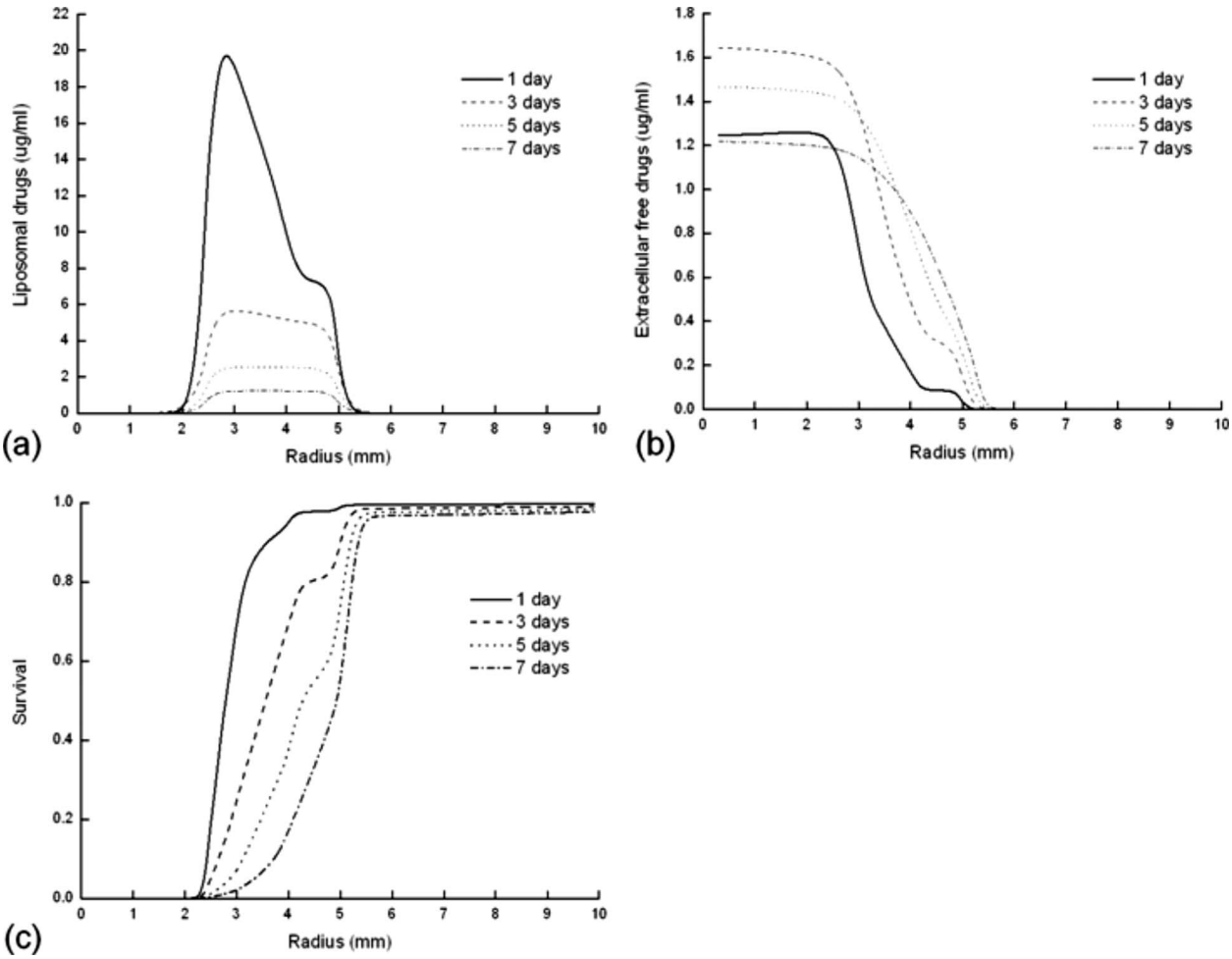

Fig. 10 Simulation results of drug concentrations and cell survival rate distribution in a 1 cm tumor under the combined RF ablation with the liposome drug treatment, where: the central region (0–2.5 mm), the peripheral region (2.5–5 mm), and the normal tissue (5–10 mm). Heating power is 10 W.

free drugs, D_D, is much bigger than the apparent diffusivity of liposome, $D_{L,\mathrm{app}}$. Furthermore, the drug induced cell apoptosis or necrosis improves the diffusivity of free drug so as to improve drug transport in tissue. Such an effect is significant and should be considered for an accurate prediction of the therapeutic effect.

For tumors larger than 1 cm, hyperthermia can only help accu-

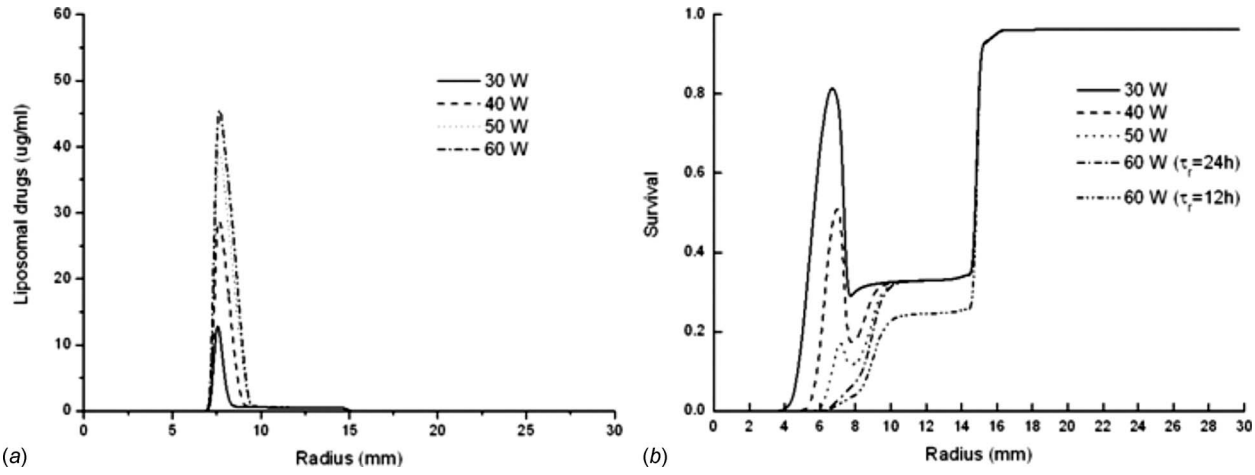

Fig. 11 Simulation results of drug concentrations and cell survival rates in a 3 cm diameter tumor under various powers of the RF heating. (*a*) Concentration of the liposome drug in tumor right after the RF heating, (*b*) tumor cell survival rates in 7 days after the combined treatments for different powers of the RF heating and different half-life times of liposome drug, where: the central region (0–7.5 mm), the peripheral region (7.5–15 mm), and the normal tissue (15–30 mm).

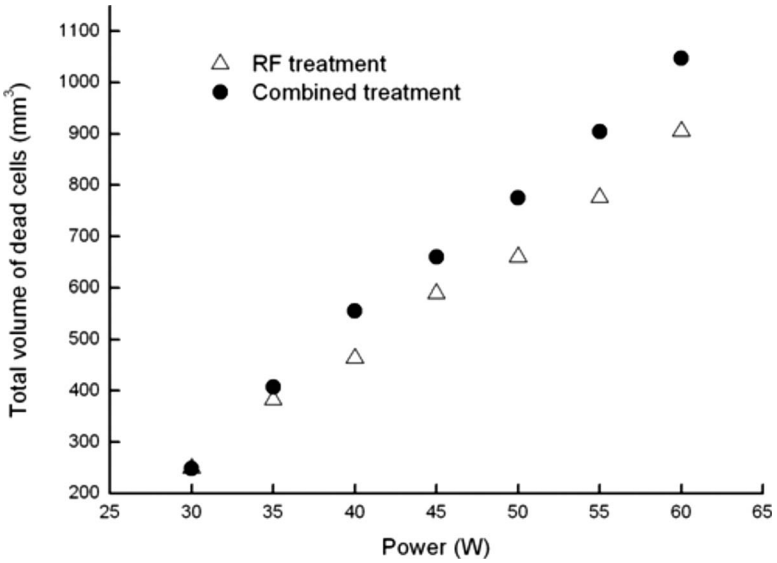

Fig. 12 The total volume of the tumor cells with the survival rate lower than 0.1% after the RF ablation alone and the combined treatment using different heating powers

mulate more antitumor drug in the peripheral region. Insufficient drug in the central region can be overcome through combined RF ablation in the tumor center. But, to reach the complete destruction of the tumor, a detailed treatment planning is needed, especially for tumors with irregular shapes. The present model can be further used to simulate the transport of other nanoparticles or quantum dots in tissue.

Acknowledgment

This work has been supported by the National Natural Science Foundation of China (Contract Nos. 50506016 and 50725622) and Ministry of Science and Technology of China (Contract Nos. 2006CB0D0100 and 2009CB930400).

Nomenclature

C = concentration of the drug
M = drug dose
t = time
D = diffusion coefficient
$P_{L,\mathrm{app}}$ = apparent permeability of the vasculature
A = surface area
S = survival rate
T = temperature
k = thermal conductivity
c = thermal capacity
q_{SAR} = specific absorption rate of the RF heating
q_{met} = metabolic heat
h = convection coefficient
z = axial distance
z_c = axial decay distance
p = RF power

Greek Symbols

ρ = density
φ = volume fraction of interstitial space
ω = blood perfusion rate
$v_{\max}$ = the maximum cellular uptake rate

Subscripts

L = liposome
D = free antitumor drug
E = extracellular
I = intracellular
t = tissue
b = blood
h = heat
d = drug

References

[1] Szoka, F. C., 1991, "Liposomal Drug Delivery: Current Status and Future Prospects," *Membrane Fusion*, J. Wilschut and D. Hoekstra, eds., Marcel Dekker, New York, pp. 845–890.
[2] Gabizon, A., Catane, R., Uziely, B., Kaufman, B., Safra, T., Cohen, R., Martin, F., Huang, A., and Barenholz, Y., 1994, "Prolonged Circulation Time and Enhanced Accumulation in Malignant Exudates of Doxorubicin Encapsulated in Polyethylene-Glycol Coated Liposomes," Cancer Res., **54**(4), pp. 987–992.
[3] Nagayasu, A., Uchiyama, K., and Kiwada, H., 1999, "The Size of Liposomes: A Factor Which Affects Their Targeting Efficiency to Tumors and Therapeutic Activity of Liposomal Antitumor Drugs," Adv. Drug Delivery Rev., **40**(1–2), pp. 75–87.
[4] Kong, G., Braun, R. D., and Dewhirst, M. W., 2000, "Hyperthermia Enables Tumor-Specific Nanoparticle Delivery: Effect of Particle Size," Cancer Res., **60**(16), pp. 4440–4445.
[5] Ning, S., Macleod, K., Abra, R. M., Huang, A. H., and Hahn, G. M., 1994, "Hyperthermia Induces Doxorubicin Release From Long-Circulating Liposomes and Enhances Their Anti-Tumor Efficacy," Int. J. Radiat. Oncol., Biol., Phys., **29**(4), pp. 827–834.
[6] Dvorak, J., Zoul, Z., Melichar, B., Petera, J., Vesely, P., Vosmik, M., and Dolezel, M., 2004, "Liposomal Doxorubicin Combined With Regional Hyperthermia: Reducing Systemic Toxicity and Improving Locoregional Efficacy in the Treatment of Solid Tumors," J. Chemother., **16**, pp. 34–36.
[7] Urano, M., Kuroda, M., and Nishimura, Y., 1999, "For the Clinical Application of Thermochemotherapy Given at Mild Temperatures," Int. J. Hyperthermia, **15**(2), pp. 79–107.
[8] Liu, P., Zhang, A., Xu, Y., and Xu, L. X., 2005, "Study of Non-Uniform Nanoparticle Liposome Extravasation in Tumor," Int. J. Hyperthermia, **21**(3), pp. 259–270.
[9] Kong, G., and Dewhirst, M. W., 1999, "Hyperthermia and Liposomes," Int. J. Hyperthermia, **15**(5), pp. 345–370.
[10] Xu, L. X., Zhu, L., and Holmes, K. R., 1998, "Thermoregulation in the Canine Prostate During Transurethral Microwave Hyperthermia, Part I: Temperature Response," Int. J. Hyperthermia, **14**(1), pp. 29–37.
[11] Maruyama, K., Unezaki, S., Takahashi, N., and Iwatsuru, M., 1993, "Enhanced Delivery of Doxorubicin to Tumor by Long-Circulating Thermosensitive Liposomes and Local Hyperthermia," Biochim. Biophys. Acta, **1149**(2), pp. 209–216.
[12] Gaber, M. H., Wu, N. Z., Hong, K., Huang, S. K., Dewhirst, M. W., and Papahadjopoulos, D., 1996, "Thermosensitive Liposomes: Extravasation and Release of Contents in Tumor Microvascular Networks," Int. J. Radiat. Oncol., Biol., Phys., **36**(5), pp. 1177–1187.
[13] Ribba, B., Marron, K., Agur, Z., Alarcon, T., and Maini, P. K., 2005, "A Mathematical Model of Doxorubicin Treatment Efficacy for Non-Hodgkin's Lymphoma: Investigation of the Current Protocol Through Theoretical Mod-

elling Results," Bull. Math. Biol., **67**(1), pp. 79–99.
[14] Tzafriri, A. R., Lerner, E. I., Flashner-Barak, M., Hinchcliffe, M., Ratner, E., and Parnas, H., 2005, "Mathematical Modeling and Optimization of Drug Delivery From Intratumorally Injected Microspheres," Clin. Cancer Res., **11**, pp. 826–834.
[15] Ward, J. P., and King, J. R., 2003, "Mathematical Modelling of Drug Transport in Tumor Multicell Spheroids and Monolayer Cultures," Math. Biosci., **181**(2), pp. 177–207.
[16] Lankelma, J., Luque, R. F., Dekker, H., Schinkel, W., and Pinedo, H. M., 2000, "A Mathematical Model of Drug Transport in Human Breast Cancer," Microvasc. Res., **59**(1), pp. 149–161.
[17] Lankelma, J., Luque, R. F., Dekker, H., and Pinedo, H. M., 2003, "Simulation Model of Doxorubicin Activity in Islets of Human Breast Cancer Cells," Biochim. Biophys. Acta, **1622**(3), pp. 169–178.
[18] Magni, P., Simeoni, M., Poggesi, I., Rocchetti, M., and De Nicolao, G., 2006, "A Mathematical Model to Study the Effects of Drugs Administration on Tumor Growth Dynamics," Math. Biosci., **200**(2), pp. 127–151.
[19] El-Kareh, A. W., and Secomb, T. W., 2003, "A Mathematical Model for Cisplatin Cellular Pharmacodynamics," Neoplasia, **5**(2), pp. 161–169.
[20] El-Kareh, A. W., and Secomb, T. W., 2005, "Two-Mechanism Peak Concentration Model for Cellular Pharmacodynamics of Doxorubicin," Neoplasia, **7**(7), pp. 705–713.
[21] El-Kareh, A. W., and Secomb, T. W., 2004, "A Theoretical Model for Intraperitoneal Delivery of Cisplatin and the Effect of Hyperthermia on Drug Penetration Distance," Neoplasia, **6**(2), pp. 117–127.
[22] Maruyama, K., Ishida, O., Takizawa, T., and Moribe, K., 1999, "Possibility of Active Targeting to Tumor Tissues With Liposomes," Adv. Drug Delivery Rev., **40**(1–2), pp. 89–102.
[23] El-Kareh, A. W., and Secomb, T. W., 2000, "A Mathematical Model for Comparison of Bolus Injection, Continuous Infusion, and Liposomal Delivery of Doxorubicin to Tumor Cells," Neoplasia, **2**(4), pp. 325–338.
[24] Lankelma, J., Dekker, H., Luque, F. R., Luykx, S., Hoekman, K., van der Valk, P., van Diest, P. J., and Pinedo, H. M., 1999, "Doxorubicin Gradients in Human Breast Cancer," Clin. Cancer Res., **5**(7), pp. 1703–1707.
[25] Jang, S. H., Wientjes, M. G., Lu, D., and Au, J. L., 2003, "Drug Delivery and Transport to Solid Tumors," Pharm. Res., **20**(9), pp. 1337–1350.
[26] Gabizon, A., Shmeeda, H., and Barenholz, Y., 2003, "Pharmacokinetics of Pegylated Liposomal Doxorubicin—Review of Animal and Human Studies," Clin. Pharmacokinet, **42**(5), pp. 419–436.
[27] Elliott, G. D., and McGrath, J. J., 1999, "Freezing Response of Mammary Tissue: A Mathematical Study," Heat Mass Transfer, **44**, pp. 59–64.
[28] Chato, J. C., 1987, "Thermal Properties of Tissues," *Handbook of Bioengineering*, Vols. 9.1–9.13, R. Skalak and S. Chien, eds., McGraw-Hill, New York.
[29] Zhang, A., Xu, L. X., Sandison, G. A., and Zhang, J., 2003, "A Microscale Model for Prediction of Breast Cancer Cell Damage During Cryosurgery," Cryobiology, **47**(2), pp. 143–154.
[30] Xu, L. X., Zhu, L., and Holmes, K. R., 1998, "Thermoregulation in the Canine Prostate During Transurethral Microwave Hyperthermia, Part II: Blood Flow Response," Int. J. Hyperthermia, **14**(1), pp. 65–73.
[31] Siegal, T., Horowitz, A., and Gabizon, A., 1995, "Doxorubicin Encapsulated in Sterically Stabilized Liposomes for the Treatment of a Brain Tumor Model: Biodistribution and Therapeutic Efficacy," J. Neurosurg., **83**(6), pp. 1029–1037.
[32] Nugent, L. J., and Jain, R. K., 1984, "Extravascular Diffusion in Normal and Neoplastic Tissues," Cancer Res., **44**(1), pp. 238–244.
[33] Yuan, F., Leunig, M., Huang, S. K., Berk, D. A., Papahadjopoulos, D., and Jain, R. K., 1994, "Microvascular Permeability and Interstitial Penetration of Sterically Stabilized (Stealth) Liposomes in a Human Tumor Xenograft," Cancer Res., **54**(13), pp. 3352–3356.
[34] Qian, F., Stowe, N., Liu, E. H., Saidel, G. M., and Gao, J., 2003, "Quantification of In Vivo Doxorubicin Transport From PLGA Millirods in Thermoablated Rat Livers," J. Controlled Release, **91**(1–2), pp. 157–166.
[35] El-Kareh, A. W., and Secomb, T. W., 2004, "A Theoretical Model for Intraperitoneal Delivery of Cisplatin and the Effect of Hyperthermia on Drug Penetration Distance," Neoplasia, **6**(2), pp. 117–127.
[36] Tsuchihashi, M., Harashima, H., and Kiwada, H., 1999, "Development of a Pharmacokinetic/Pharmacodynamic (PK/PD)-Simulation System for Doxorubicin in Long Circulating Liposomes in Mice Using Peritoneal P388," J. Controlled Release, **61**(1–2), pp. 9–19.
[37] Zhu, L., Mi, Z., and Xu, L. X., 1998, "Temperature Distribution in Prostate During Transurethral Radio Frequency Thermotherapy Treatment of Benign Prostatic Hyperplasia," *Advances in Heat Mass Transfer in Biotechnology*, HTD-Vol.362/BED-Vol.40, ASME, New York, NY, pp. 117–122.
[38] Jain, R. K., 1987, "Transport of Molecules Across Tumor Vasculature," Cancer Metastasis Rev., **6**(4), pp. 559–593.
[39] Chen, B., and Fu, B. M., 2004, "An Electrodiffusion-Filtration Model for Effects of Endothelial Surface Glycocalyx on Microvessel Permeability to Macromolecules," ASME J. Biomech. Eng., **126**(5), pp. 614–624.
[40] Dreher, M. R., Liu, W., Michelich, C. R., Dewhirst, M. W., Yuan, F., and Chilkoti, A., 2006, "Tumor Vascular Permeability, Accumulation, and Penetration of Macromolecular Drug Carriers," J. Natl. Cancer Inst., **98**(5), pp. 335–344.
[41] El-Kareh, A. W., and Secomb, T. W., 1997, "Theoretical Models for Drug Delivery to Solid Tumors," Crit. Rev. Biomed. Eng., **25**(6), pp. 503–571.
[42] El-Kareh, A. W., Braunstein, S. L., and Secomb, T. W., 1993, "Effect of Cell Arrangement and Interstitial Volume Fraction on the Diffusivity of Monoclonal Antibodies in Tissue," Biophys. J., **64**(5), pp. 1638–1646.
[43] Jang, S. H., Wientjes, M. G., Lu, D., and Au, J. L. S., 2003, "Drug Delivery and Transport to Solid Tumors," Pharm. Res., **20**(9), pp. 1337–1350.
[44] Liu, P., and Xu, L. X., 2006, "Enhanced Efficacy of Anti-Tumor Liposomal Doxorubicin by Hyperthermia," 28th Annual International Conference IEEE Engineering Medicine and Biology Society.
[45] Weinstein, J. N., Magin, R. L., Yatvin, M. B., and Zaharko, D. S., 1979, "Liposomes and Local Hyperthermia: Selective Delivery of Methotrexate to Heated Tumors," Science, **204**, pp. 188–191.
[46] Ahmed, M., and Goldberg, S. N., 2004, "Combination Radiofrequency Thermal Ablation and Adjuvant IV Liposomal Doxorubicin Increases Tissue Coagulation and Intratumoral Drug Accumulation," Int. J. Hyperthermia, **20**(7), pp. 781–802.
[47] Zhu, L., and Xu, L. X., 1999, "Evaluation of the Effectiveness of Transurethral RF Hyperthermia in the Canine Prostate: Temperature Distribution Analysis," ASME J. Biomech. Eng., **121**(6), pp. 584–590.
[48] Schuder, G., Pistorius, G., Fehringer, M., Feifel, G., Menger, M. D., and Vollmar, B., 2000, "Complete Shutdown of Microvascular Perfusion Upon Hepatic Cryothermia Is Critically Dependent on Local Tissue Temperature," Br. J. Cancer, **82**(4), pp. 794–799.
[49] Sun, J. Q., Zhang, A., and Xu, L. X., 2008, "Evaluation of Alternative Cooling and Heating for Tumor Treatment," Int. J. Heat Mass Transfer, **51**(23–24), pp. 5478–5485.
[50] Lee, J. M., Han, J. K., Kim, S. H., Lee, J. Y., Choi, S. H., and Choi, B. I., 2004, "Hepatic Bipolar Radiofrequency Ablation Using Perfused-Cooled Electrodes: A Comparative Study in the Ex Vivo Bovine Liver," Br. J. Radiol., **77**, pp. 944–949.
[51] Eddy, H. A., 1980, "Alterations in Tumor Microvasculature During Hyperthermia," Radiology, **137**(2), pp. 515–21.
[52] Greenstein, A., and Koontz, W. W., Jr., 2002, "Does Local Hyperthermia Affect Metastasis of a Human Prostate Carcinoma Grown in Athymic Nude Mice?," Int. J. Hyperthermia, **18**, pp. 285–291.
[53] Salsbury, A. J., 1975, "The Significance of the Circulating Cancer Cell," Cancer Treat Rev., **2**, pp. 55–72.

Experimental Investigation of Miniature Three-Dimensional Flat-Plate Oscillating Heat Pipe

S. M. Thompson
Graduate Research Assistant

H. B. Ma
Associate Professor
e-mail: mah@missouri.edu

R. A. Winholtz
Associate Professor

C. Wilson
Graduate Research Assistant

Department of Mechanical and Aerospace Engineering,
University of Missouri-Columbia,
Columbia, MO 65211

An experimental investigation on the effects of condenser temperatures, heating modes, and heat inputs on a miniature three-dimensional (3D) flat-plate oscillating heat pipe (FP-OHP) was conducted visually and thermally. The 3D FP-OHP was charged with acetone at a filling ratio of 0.80, had dimensions of 101.60×63.50×2.54 mm^3, possessed 30 total turns, and had square channels on both sides of the device with a hydraulic diameter of 0.762 mm. Unlike traditional flat-plate designs, this new three-dimensional compact design allows for multiple heating arrangements and higher heat fluxes. Transient and steady-state temperature measurements were collected at various heat inputs, and the activation/start-up of the OHP was clearly observed for both bottom and side heating modes during reception of its excitation power for this miniature 3D FP-OHP. The neutron imaging technology was simultaneously employed to observe the internal working fluid flow for all tests directly through the copper wall. The activation was accompanied with a pronounced temperature field relaxation and the onset of chaotic thermal oscillations occurring with the same general oscillatory pattern at locations all around the 3D FP-OHP. Qualitative and quantitative analysis of these thermal oscillations, along with the presentation of the average temperature difference and thermal resistance, for all experimental conditions are provided. The novelty of the three-dimensional OHP design is its ability to still produce the oscillating motions of liquid plugs and vapor bubbles and, more importantly, its ability to remove higher heat fluxes. [DOI: 10.1115/1.3072953]

1 Introduction

Recently, there has been international attention focused on the development and understanding of the oscillating/pulsating heat pipe (OHP) as an innovative solution for efficient heat transport within a variety of electronic/avionic packages. The OHP, first introduced by Akachi [1] in 1990, is a passive heat transfer device capable of possessing lower thermal resistances than that of conventional wicked heat pipes, is less prone to design and performance limitations, and is typically less expensive to manufacture. Conventional OHPs typically exist as a continuous capillary tube arranged in a planar serpentine manner, where one end receives and another end rejects thermal energy. The device is partially filled with a working fluid and is vacuum sealed. The diameter of the tube is made small enough to allow liquid "plug" formation via surface tension. As a consequence of the temperature difference instilled on an OHP, the saturated working fluid will undergo complex displacements of both oscillatory and circulatory characteristics [2,3]. The constant evaporation and condensation of the working fluid will further create an unstable pressure field that adds to the complex motion of this two-phase system. The oscillating heat pipe operates with both sensible and latent heat transfer modes, which has a high potential to provide high heat transfer coefficients, making it a very effective heat transfer device.

There are currently two prominent designs associated with the OHP: a serpentine-arranged tube—a tubular oscillating heat pipe (T-OHP)—and a flat metallic plate with an engraved continuous channel—a flat-plate oscillating heat pipe (FP-OHP). Although open-loop designs have been implemented, it has been found that the closed-loop design for the OHP is superior due to the possibility for bulk circulation [4,5]. Borgmeyer and Ma [3] successfully sealed a copper FP-OHP having square internal channels with a hydraulic diameter of 1.59 mm with Lexan for visualization purposes. A high-speed camera was used to measure the frequency and velocity of the local liquid slug oscillations during heat pipe operation including the effects of heat inputs and orientations. It was found that the oscillations were dependent on both heat input and device orientation. Khandekar et al. [6] measured the effects of gravity and thermal resistance of aluminum 6 turn FP-OHPs, all sealed with transparent glass and charged with ethanol or water. Strong orientation dependence was found, yet it was discovered that the FP-OHP possessing channels with larger rectangular cross sections, with filling ratios below 0.30, had less dependence on orientation, and that rectangular channel designs may be optimal over circular channels for FP-OHPs. Their research indicates that the corners of the rectangular channels may serve as capillary structures at higher filling ratios and may aid circulatory effects as well as promote a two-phase thermosyphon effect. Operating in a bottom heating mode, the lowest thermal resistance achieved for their FP-OHP was 1.1°C/W, and the maximum heat input reached was 75 W. Xu et al. [7] investigated an aluminum FP-OHP having square channels with a hydraulic diameter of 1.9 mm while being charged with HFC-134a or butane. It was found that gravity does have an effect on the thermal performance of the FP-OHP. A side heating mode was formally introduced, and it was found that the FP-OHP optimally performed while in the bottom heating mode. The thermal performance of the FP-OHP in the bottom heating mode was better than those in the top or horizontal heating modes. Thermal resistances of approximately 0.5°C/W and 0.1°C/W were achieved for the FP-OHP while operating in the bottom heating and side heating modes, respectively. Their reported thermal resistances generally increased with heat input. All of these FP-OHPs were contained on one plane. Because the channel density per unit area for those FP-OHPs is low, these FP-OHPs cannot remove heat at a high level of high flux and cannot reach a low thermal resistance.

Contributed by the Heat Transfer Division of ASME for publication in the JOURNAL OF HEAT TRANSFER. Manuscript received November 15, 2008; final manuscript received December 17, 2008; published online February 24, 2009. Review conducted by Robert D. Tzou.

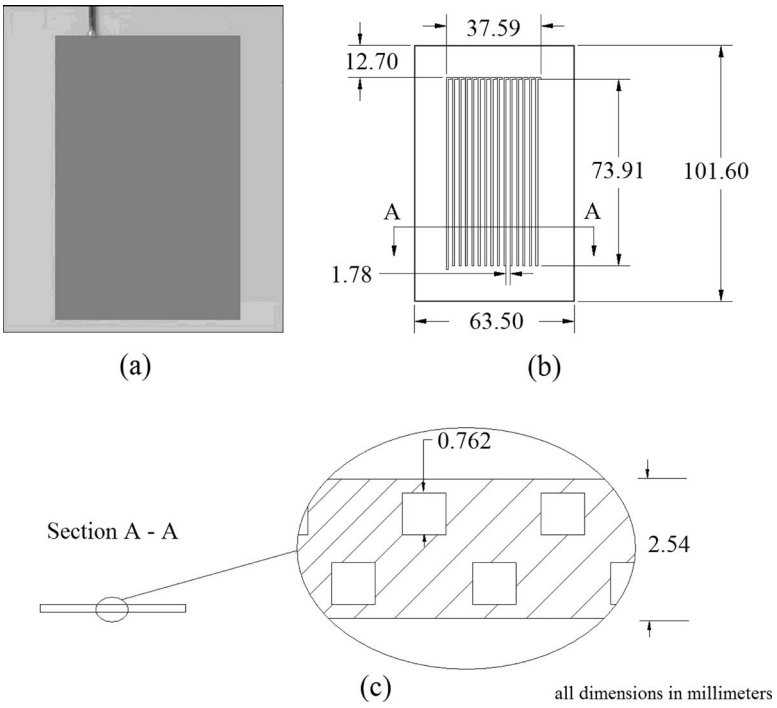

Fig. 1 A three-dimensional oscillating heat pipe (*a*) photo, (*b*) dimensions of base plate, and (*c*) close-up of cross-sectional geometry

In the current investigation, a three-dimensional (3D) flat-plate oscillating heat pipe has been studied. The 3D FP-OHP has two layers of channels. Each layer has 15 turns, giving 30 total turns, when the two layers are interconnected. This new 3D FP-OHP is unique for it focuses on a high-channel density design aimed for high heat flux applications. An extensive experimental investigation on this 3D FP-OHP has been conducted to determine its average temperature difference, thermal resistance, and start-up phenomena during various operating conditions.

2 Design of 3D FP-OHP

The prominent attribute of the OHP is its ability to create liquid plugs and vapor bubbles in the miniature channels. These liquid plugs and vapor bubbles exist due to the OHP being only partially filled with a working fluid and as a result of the internal diameter of the channels. When the internal diameter of the channels is less than a critical diameter, the working fluid will disperse itself into a liquid/vapor train alignment throughout the tube/channel as surface tension forces dominate over gravitational forces. It has been found by Akachi [1] that the critical, or maximum, diameter for surface tension forces to dominate gravitational forces is

$$D_{\text{crit}} = 2\sqrt{\frac{\sigma}{g(\rho_l - \rho_v)}} \tag{1}$$

When the diameter of the channel exceeds this critical value, the working fluid will not form stable liquid plugs and will tend to pool/stratify.

A heat flux level for high heat flux applications was accomplished by maximizing the number of channels per unit area and minimizing the overall dimensions of the device. With this in mind, the diameter of the internal channels, as well as the wall thickness between adjacent channels, was minimized. With the guidance of Eq. (1), the internal hydraulic diameter was chosen to be 0.762 mm. A "dead perimeter" with a width of 12.70 mm was left to surround the channel area to maximize the brazability of the 3D FP-OHP base plate. Figure 1 shows a schematic of this 3D FP-OHP and a photo. As the channel hydraulic diameter becomes smaller, the channel density can be increased, which directly helps increase the capability for the removal of heat with a higher level of heat flux. Of course, the channel shape will have a significant effect on the oscillating motion and heat transfer occurring in an OHP. Considering the fabrication capability, the square cross section shown in Fig. 1 was studied in the current investigation.

The 3D FP-OHP has two layers of channels. The channel on each layer has 15 turns. The channels are approximately 74 mm long, and all channels are interconnected to each other to form a single closed loop. At the end of each channel, the fluid is allowed to transverse a short distance to the beginning of a circular channel that allows the fluid to be perpendicularly transported to the second layer for flow within another channel. The channels on one layer were designed to be offset from the channels on the second layer to enhance visibility of the working fluid during visualization experiments utilizing neutron radiography. A circular charging hole (1.59 mm) connects perpendicularly to the very end of the internal channel for charging purposes. Although Khandekar et al. [6] previously postulated that the thermal resistance between adjacent channels within a FP-OHP must be maximized; the current design actually aims to minimize the thermal resistance by using small walls ($\sim$1.78 mm) and by using copper for the FP-OHP base plate. This was done to challenge the previous hypothesis, since it is believed that the thermal performance of a miniature compact FP-OHP is optimized by enhancing heat transfer between adjacent channels. In accordance with a miniature form factor, the overall thickness of the 3D FP-OHP was minimized. The overall dimensions of the sealed 3D FP-OHP are $101.60 \times 63.50 \times 2.54$ mm^3.

After successfully machining and sealing the 3D FP-OHP by a brazing process, a copper capillary tube (with an outer diameter of 1.59 mm) was positioned and soldered at the charging hole at the end of the device, as shown in Fig. 1(*a*). The 3D FP-OHP was then charged with the working fluid. For the current study, the device was charged with acetone. According to Eq. (1), acetone requires smaller critical hydraulic diameters forming liquid plugs and vapor bubbles in the channel. Acetone contains hydrogen making it favorable for neutron radiography due to its high neutron attenuation [8]. After successfully charging the heat pipe,

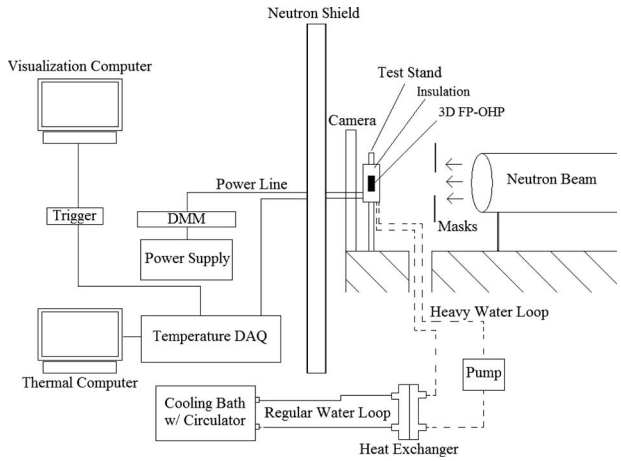

Fig. 2 Schematic of experimental setup

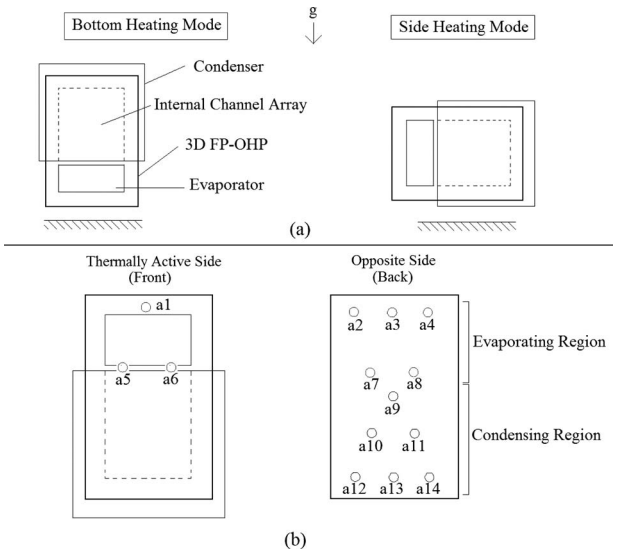

Fig. 3 (*a*) Bottom and side heating modes for 3D FP-OHP oriented with the gravity direction along with (*b*) thermocouple locations (*a*1, *a*2, ..., *a*14 indicate the thermocouple number and location)

pneumatic tube crimpers were used to seal the end of the charging tube. The crimped charging tube was then quickly submerged into liquid solder to further guarantee a proper seal. The liquid filling ratio was 80%.

3 Experimental Setup

In order to effectively test the thermal performance, as well as visualize the internal fluid dynamics, of the 3D FP-OHP while in various heating modes and operating conditions at the neutron imaging facility at NIST [9], a custom testing apparatus was constructed and used within the test setup, as shown in Fig. 2. The testing apparatus consisted of a heating and cooling block, a tilting holding frame, thermocouples, and an insulating case. The heating block was manufactured from electronic-grade copper and had dimensions of $38.1 \times 25.4 \times 6.35$ mm^3. Four holes, each 3.18 mm in diameter, were drilled partially through the thin side of the heating block for the insertion and positioning of four Watlow miniature cartridges heaters. The heating block was firmly attached to the surface of the 3D FP-OHP's evaporator region using aluminum C-clamps. Furthermore, the heating block was placed directly above the channel array width to maximize heat input to the internal working fluid—this allowed for a heated area of approximately 9.67 cm^2. The cooling block was manufactured from aluminum and had dimensions of $76.2 \times 76.2 \times 20.13$ mm^3. Four holes, each 15.88 mm in diameter, were drilled completely through the aluminum block to allow water to flow in series during experiments. The cooling block was firmly attached to the condenser region of one side of the 3D FP-OHP by using a custom-made aluminum clamping mechanism. The clamping mechanism used two aluminum cover plates and threaded rods with nuts to squeeze against the 3D FP-OHP and cooling block. The cooling block was located almost directly under the heating block to restrict the adiabatic section to a negligible length. The cooling block area exceeded the channel array width, allowing for a cooled area of approximately 40.75 cm^2. Omegatherm "201" thermal paste was applied to the heating and cooling block surfaces, and around the circumference of the cartridge heaters, to reduce the thermal contact resistance within these regions.

The 3D FP-OHP was positioned and held in place within a tilting aluminum frame/stand. The heat pipe was held stationary by screwing threaded rods into the side of the aluminum clamping mechanism and into the tilting frame/stand. The tilting nature of the test stand allowed for testing the heat pipe in bottom and side heating modes. Since the neutron beam was fixed horizontally with respect to the ground, the horizontal heating mode could not be investigated at the NIST facilities.

Fourteen type-T thermocouples were applied to the 3D FP-OHP. The majority of the thermocouples were placed on the non-heated side of the 3D FP-OHP to allow for perfect hot plate/cold plate contact. A very small adiabatic section was used for the experiment to allow for placement of thermocouples on the heated side and to minimize thermal interaction between the hot and cold plates. In addition to the 14 thermocouples measuring the temperature distribution of the 3D FP-OHP, another thermocouple (not shown) was used to measure and verify the temperature of the condenser fluid entering the cold plate. Finally, the 3D FP-OHP, along with all clamping mechanisms and the cold and hot plate, were liberally wrapped with fiberglass insulation to reduce heat losses. The insulation shell was then encapsulated with aluminum foil to minimize the release of any irradiated fiberglass during the experiments. Figure 3 illustrates the heating modes investigated along with all the thermocouple locations.

As shown in Fig. 3, four thermocouples are in the evaporator region ($a1-a4$) and six thermocouples in the condenser region ($a9-a14$). The test setup used for all experiments at the NIST neutron imaging facility for the 3D FP-OHP was similar to previous oscillating heat pipe visualization experiments, as conducted by Wilson et al. [8].

Heavy water was used to circulate through the cold plate to allow for better visibility in the neutron camera. Heavy water, as opposed to regular water, is less opaque with regard to neutron imaging due to it having a lower neutron attenuation [8]. Due to the expense of heavy water, a separate pump and hosing line were used to circulate it through the cold plate. The heavy water temperature was held at the condenser fluid temperature by exchanging heat with temperature-controlled regular water in another cooling loop via a heat exchanger. The regular water was circulated and held at a constant temperature via a Julabo F34 circulator/water bath. Temperature data were collected at a sampling rate of 100 Hz using a National Instruments SCXI-1600 data acquisition system (DAQ). All thermocouples had a maximum error, or noise, of ± 0.25°C. Visual data were collected at a rate of 30 frames per second by using a computer workstation at the NIST neutron imaging facility. All visual and thermal data were collected simultaneously with the aid of a communication trigger set up between both the "visualization" computer—used for visual data collection—and the "thermal" computer—used for thermal data collection.

Three experiments, listed in Table 1, were conducted where either the condenser temperature or heating mode was changed for

Table 1 Summary of the three experiments conducted at NIST for the 3D FP-OHP

Experiment No.	Heating mode	Condenser fluid temperature °C	Maximum heat input (W)
1	Bottom	60	100
2	Bottom	20	200
3	Side	60	100

each experiment. Heat input was gradually increased from 0 W for each experiment with multiple step heat inputs with intervals ranging from 5 W to 20 W. Heat input was voltage-controlled using a digital multimeter (DMM) and variable autotransformer. The measured resistance of the parallel-connected cartridge heaters was used with the ideal power input to calculate the input voltage. This "ideal" power input was verified by reading the "true" voltage across the cartridge heaters, as collected from the temperature DAQ. Both transient and steady-state data were collected—each having various data collection periods. Transient temperature measurements were collected immediately after the introduction of the new step heat input. All experiments were stopped when the maximum evaporator temperature neared 100°C, for safety reasons.

4 Experimental Results and Discussion

4.1 Temperature Difference and Thermal Resistance. The average temperature difference across the 3D FP-OHP, ΔT_{avg}, was calculated with

$$\Delta T_{\text{avg}} = \left(\frac{T1 + T2 + T3 + T4}{4}\right) - \left(\frac{T9 + T10 + T11 + T12 + T13 + T14}{6}\right) \quad (2)$$

where temperatures $T1, T2, \ldots, T14$ in Eq. (2) correspond to the respective thermocouple location $(a1, a2, \ldots, a14)$ shown in Fig. 3. All temperatures used in Eq. (2) are average temperatures collected during steady-state tests. In general, the average temperature difference may be found by subtracting the mean condenser temperature from the mean evaporator temperature using the average thermocouple measurements within those prescribed regions. Figure 4 provides the average temperature difference for the 3D FP-OHP at the various heat inputs and operating conditions associated with each experiment.

As shown in Fig. 4, the average temperature difference for the

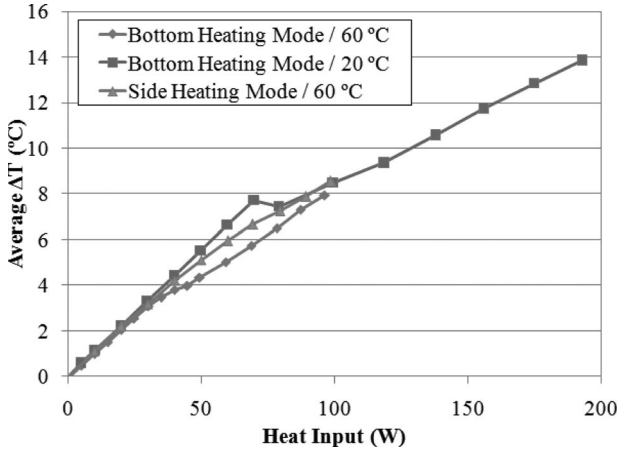

Fig. 4 Average temperature difference versus heat input for all three experiments

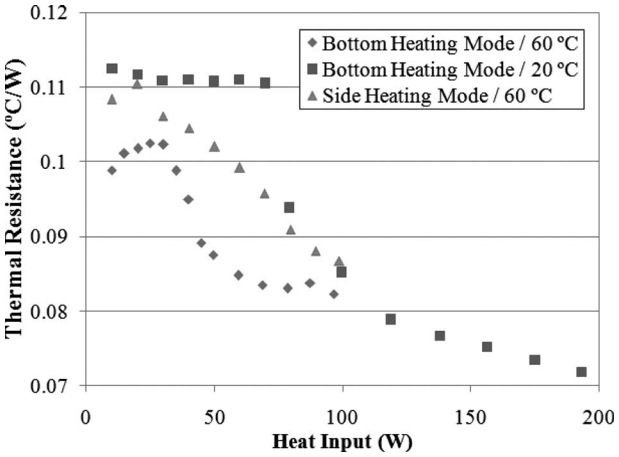

Fig. 5 Thermal resistance versus heat input for all three experiments.

3D FP-OHP has a positive almost-linear dependence on heat input with points of noticeable slope change for both bottom heating experiments. For the side heating mode, the average temperature difference appears to have a higher-ordered dependence on heat input, and no noticeable slope change is observed. The average temperature difference is approximately the same until about 30 W for all three experiments. Beyond 30 W, the 3D FP-OHP operating in a bottom heating mode, with a condenser fluid temperature of 60°C (Experiment No. 1), begins to thermally outperform the other experiments, as indicated by consistently having a smaller average temperature difference at higher heat inputs. However, the highest heat input—without having any evaporator temperature exceeding 100°C—was achieved while having the 3D FP-OHP in a bottom heating mode with a 20°C condenser fluid temperature. At a heat input of 100 W, the average temperature difference was on-the-order of 8°C for all three experiments.

The noticeable slope changes associated with both Experiment Nos. 1 and 2, as shown in Fig. 4, may be attributed to a phenomenon known as the OHP "start-up." This start-up refers to the point in time where temperature and fluid oscillations begin as a result of the heat pipe acquiring sufficient temperature differences and/or a sufficient heat input, or excitation power, necessary for OHP activation. There is no clear point of excitation for the 3D FP-OHP operating in the side heating mode, since its average temperature difference increases continuously with heat input at all times. The most pronounced start-up occurs for Experiment No. 2, wherein the average temperature difference actually decreases when the heat input is increased from 70 W to 80 W.

The nonlinear characteristics associated with the average temperature difference for the 3D FP-OHP may be attributed to its highly nonlinear thermal resistance. The thermal resistance at a specific power input, i, may be approximated as

$$\Psi_{\text{OHP}} = \frac{\Delta T_{\text{avg},i}}{Q_i} \quad (3)$$

The thermal resistance of the 3D FP-OHP for each experiment and each heat input is provided in Fig. 5. Notice that the start-up for the 3D FP-OHP for each experiment is more apparent. It may be observed from Fig. 5 that the 3D FP-OHP thermal resistance is a strong inverse function of heat input for all experiments after start-up. Prior to start-up, only the thermal resistance associated with Experiment No. 2 has a nonpositive dependence on heat input. The inverse relationship of thermal resistance on heat input is higher-ordered for the 3D FP-OHP in both bottom heating modes after start-up, and appears to be almost linear for the side heating mode at all heat inputs. Notice that no minimum was achieved for thermal resistance for any experiment, indicating that

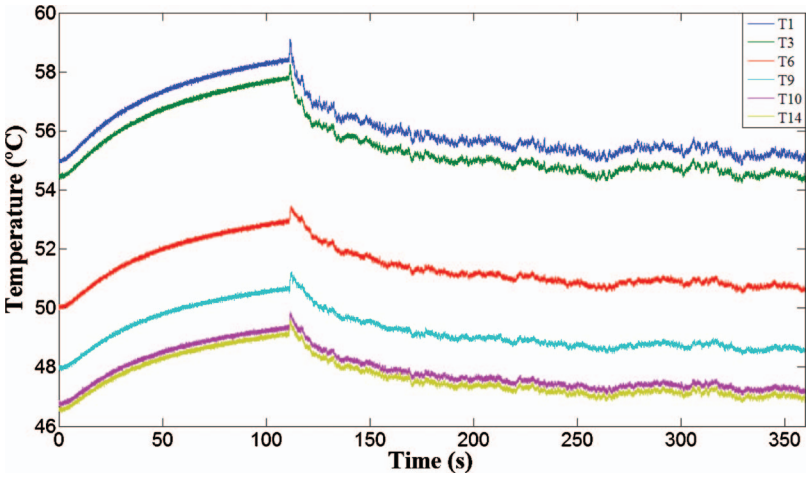

Fig. 6 3D FP-OHP transient temperature response for Experiment No. 2 at 79.3 W

the 3D FP-OHP may be capable of possessing lower thermal resistances at higher heat inputs. At 100 W, the 3D FP-OHP has a thermal resistance on-the-order of 0.085°C/W for all three operating conditions experimented. While operating in the bottom heating mode and having a condenser fluid temperature of 60°C, the lowest thermal resistance is accomplished for the 3D FP-OHP at all heat inputs after start-up and under 100 W. At the same condenser fluid temperature of 60°C, the 3D FP-OHP has a lower thermal resistance operating in a bottom heating mode as opposed to the side heating mode.

The fact that the thermal resistance of the 3D FP-OHP decreases with temperatures below 100 W of heat input is very different from the results obtained by Xu et al. [7]. Their results for their aluminum FP-OHP showed that the thermal resistance increased with all heat inputs under 100 W. Furthermore, their experiments with the side heating mode for the FP-OHP demonstrated a thermal resistance twice as high as the thermal resistance associated with the bottom heating mode, while the current results demonstrate that the side heating mode thermal resistance is comparable in magnitude to that of the bottom heating mode thermal resistances.

4.2 3D FP-OHP Excitation/Start-Up. The excitation of the internal working fluid within the 3D FP-OHP, and hence the start-up of the heat pipe, was clearly observed in both a thermal and visual sense. Thermally, the temperature field began to oscillate pseudochaotically with time. Visually, the internal working fluid began to circulate/oscillate at very high speeds. The pronounced discrete start-ups for the 3D FP-OHP within both bottom heating experiments are verified by observing the temperature data collected during the transient responses at a specific step heat input, as shown in Figs. 6 and 7. It should be noted that although 14 thermocouples were used for all experiments, only six thermocouple readings ($T1$, $T3$, $T6$, $T9$, $T10$, and $T14$) are presented for all temperature plots for better clarity.

The start-up for Experiment No. 2 occurs at approximately 110 s into the transient data collection time for an 80 W heat step input, and the start-up for Experiment No. 1 occurs at approximately 275 s into the transient data collection time for a 35 W heat step input. Each start-up is characterized by the onset of complex temperature field oscillations, or "thermal oscillations," and a uniform temperature field relaxation. The temperature field oscillations appear to oscillate in a superimposed chaotic nature that is not periodic with time. The temperature field relaxation is evidenced by the sharp uniform decline in temperatures across the 3D FP-OHP at the time of start-up where the previous trend of increasing temperature is severely altered. It may be seen that this temperature relaxation is more pronounced for the bottom-heated 3D FP-OHP being cooled with a colder condenser fluid tempera-

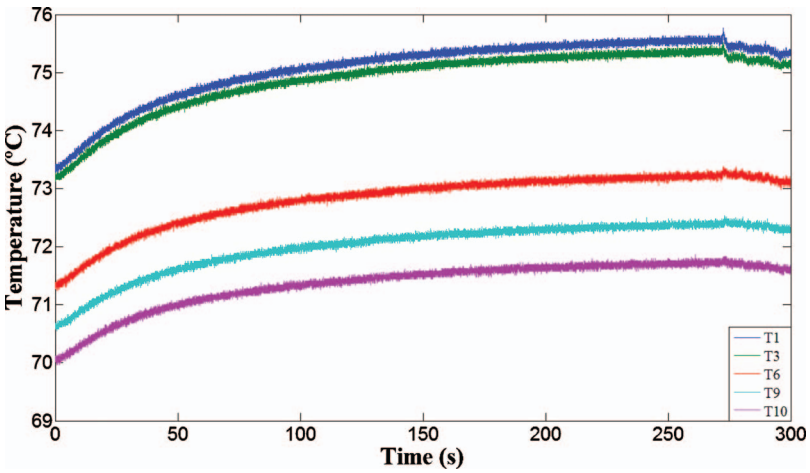

Fig. 7 3D FP-OHP transient temperature response for Experiment No. 1 at 35.1 W

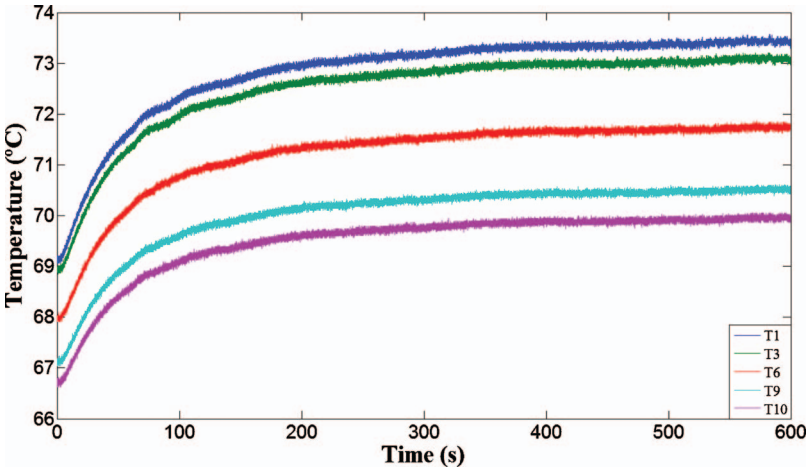

Fig. 8 3D FP-OHP transient temperature response for Experiment No. 3 at 29.9 W

ture of 20°C. The start-up associated with the 3D FP-OHP operating in the side heating mode is less apparent and is more of a gradual phenomenon than both bottom heating experiments, as shown in Fig. 8. In addition, no temperature field relaxation was observed for the side heating mode.

Like the thermal resistance trends, the required excitation powers are confirmed from observing the transient temperature responses that captured the start-ups of the 3D FP-OHP. At this respective step heat input, the minimal required excitation power may be approximated. The exact minimum excitation power is unknown due to adherence to the experimental schedule that enforced step heat inputs. The major observation is that the excitation power has a stronger dependence on the condenser fluid temperature than orientation. This was concluded by seeing that a higher heating power is required for the bottom-heated 3D FP-OHP operating with a colder condenser fluid temperature, and that the excitation power required for the side heating mode is comparable to the excitation power needed for the bottom heating mode at the same condenser temperature. The thermal results from all three experiments have proven that the 3D FP-OHP excitation power is at the very least a function of both heating mode and cooling conditions.

The points of start-up for the 3D FP-OHP may also be observed using Fig. 5, where the start-ups for the bottom heating experiments are clearly visible from the sudden drastic changes in thermal resistance. For a condenser fluid temperature of 60°C, the start-up excitation power is approximately 35 W, and for a condenser fluid temperature of 20°C is approximately 80 W. Figure 5 also provides evidence that the start-up for the side heating mode occurs at around 30 W, as indicated by the maximum. Furthermore, all startups for the oscillating motion were easily observed and confirmed with the neutron imaging results

4.3 Steady-State Temperature Oscillations. Although the transient temperature responses may accurately depict the excitation of the 3D FP-OHP, the essence of the thermal oscillations are better understood by investigating the steady-state temperature measurements. Figures 9–11 show the steady-state temperature distributions at 80 W from each of the experiments. Three interesting observations may be drawn from all experiments. First, the thermal oscillations are chaotic and nonperiodic at all heat inputs succeeding the excitation power; however, the oscillating temperature patterns have similar trends at all heat pipe locations at all times. Second, uniform temperature field disturbances are observed at specific instances in time, where sharp discontinuities exist for all temperature measurements simultaneously. Third, the overall amplitude of the thermal oscillations increases with heat input for both the condenser and evaporator regions, but the amplitudes for thermal oscillations occurring in the evaporator region increase more with heat input than those for the condenser region.

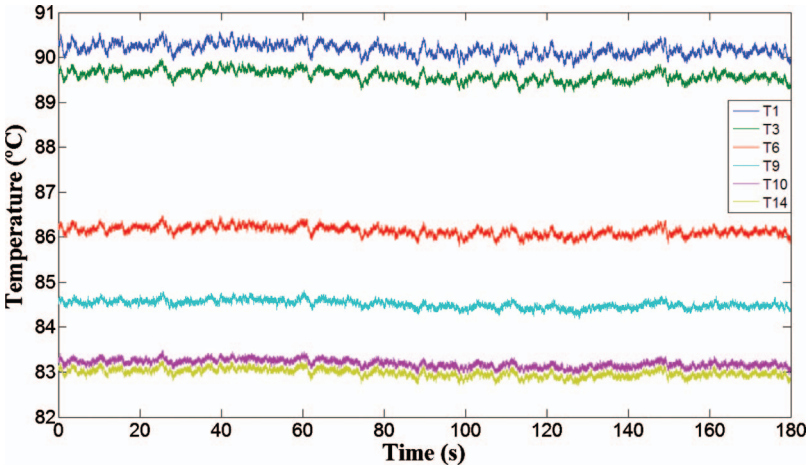

Fig. 9 3D FP-OHP steady-state temperature distribution versus time for Experiment No. 1 at 78.4 W

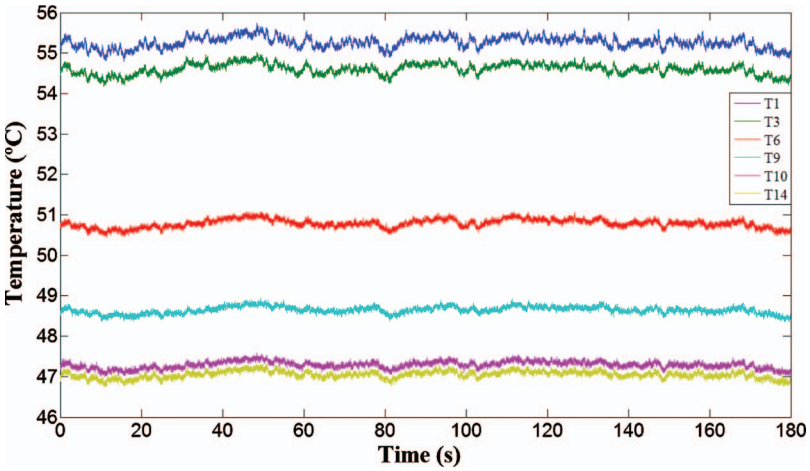

Fig. 10 3D FP-OHP steady-state temperature distribution versus time for Experiment No. 2 at 79.4 W

After excitation of the 3D FP-OHP, thermal oscillations occurred at all thermocouple locations for all three experiments, and the oscillations were sustained until the cessation of each experiment. Visual observation with neutron imaging confirmed that the thermal oscillations began simultaneously with the onset of working fluid oscillations within the 3D FP-OHP. Therefore, the source and behavior of the thermal oscillations is related to the constant phase transition and complex motions associated with the saturated internal working fluid.

There are many qualitative assessments that one may draw from observing the given steady-state thermal oscillations, and these general assessments do hold at multiple heating loads. The prominent feature is that all temperatures, at various locations throughout the 3D FP-OHP, hold similar oscillatory patterns throughout time for a specific heat load, and that the nature of these trends become less eradicated going from the evaporator to the condenser region. This decay of eradicated oscillations is more pronounced for the 3D FP-OHP operating in a side heating mode, where the amplitudes of the thermal oscillations dampen to more smooth lines, as seen in Fig. 11. For the bottom heating mode, the temperature field oscillations are more of a global phenomenon, where general trends are more uniformly shared at all locations around the 3D FP-OHP. Furthermore, the global nature of the thermal oscillations is not planar, as it is evidenced that the similarity in thermal oscillations was shared on both sides of the 3D FP-OHP (i.e., thermocouples $a1$ and $a3$). Hence, the temperature field oscillations are interdependent and the globality, or uniformity, of the oscillations is dependent on the heating mode.

In addition to the thermal oscillations sharing the same overall trend at locations all around the 3D FP-OHP, one may notice that sporadic temperature "troughs" or "spikes" are also globally shared as part of a "temperature field shock" phenomenon. For example, a shared temperature spike may be observed at approximately 25 s in Fig. 9, and a shared temperature trough may be observed at approximately 80 s in Fig. 10. The source for this temperature field shock is still unknown; however, it is believed that this shared temperature disturbance may be attributed to either the internal fluid dynamics of the working fluid or to the complex interdependencies of the temperature field. During the side heating mode, the temperature field shock is less of a global phenomenon and more localized in the evaporator region given to the less global-nature of thermal oscillations.

In an effort to quantify the thermal oscillations, an average-maximum peak-to-peak amplitude, i.e., ΔT_{AMA}, for either the evaporator or condenser region is defined as

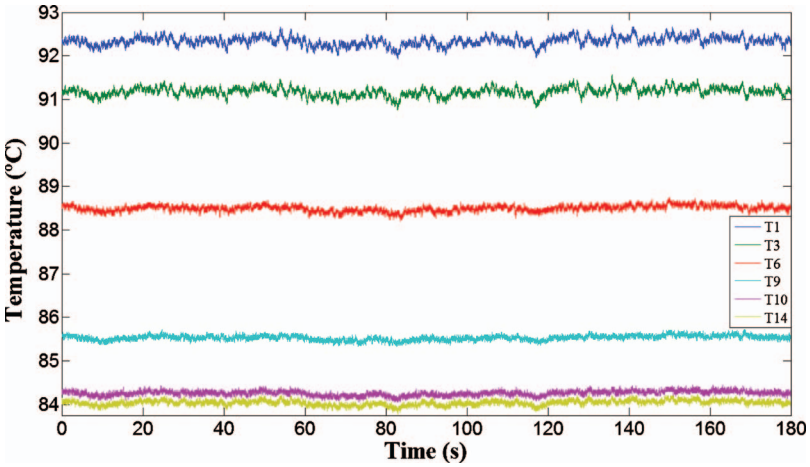

Fig. 11 3D FP-OHP steady-state temperature distribution versus time for Experiment No. 3 at 79.7 W

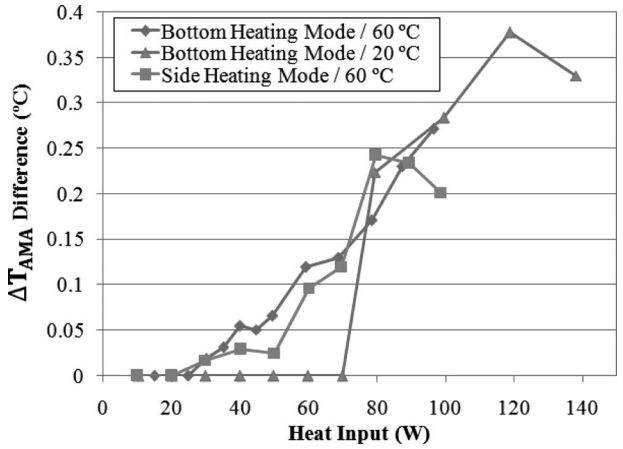

Fig. 12 Average-maximum peak-to-peak amplitude of thermal oscillations at various heat inputs for all experiments

$$\Delta T_{\mathrm{AMA}} = \left| \frac{1}{n} \sum_{i=1}^{n} [\max(T_i) - \min(T_i)] - \Phi_{\mathrm{tc}} \right| \tag{4}$$

where n is the number of thermocouples in the predefined evaporator or condenser region, and the thermocouple noise, Φ_{tc}, is known to be 0.25°C for all experiments. The difference between regional ΔT_{AMA} for thermal oscillations at different heat inputs for all three experiments is shown in Fig. 12.

It may be seen that ΔT_{AMA} for the thermal oscillations increases with heat input after start-up for all heating modes. However, this positive correlation eventually weakens at higher heat fluxes for Experiment Nos. 2 and 3, as evidenced by the local maxima. At this point, ΔT_{AMA} only indicates that the difference in thermal oscillation "strengths" between the evaporator and condenser regions increases with heat input, and that thermal oscillations in the evaporator region consistently remain "stronger" at all heat inputs for all heating modes. The relation between the thermal oscillations and the heat transfer capability of the 3D FP-OHP is unknown at this point, as there appears to be no relation between ΔT_{AMA} and the thermal resistance of the 3D FP-OHP. Note that Fig. 12 confirms that at 80 W, the 3D FP-OHP operating in a side heating mode possesses the highest ΔT_{AMA} in thermal oscillations, as previously illustrated in Fig. 11.

Figure 13 shows the average-maximum peak-to-peak amplitudes, i.e., ΔT_{AMA} of thermal oscillations in the evaporator region and condenser regions. It may be clearly seen that ΔT_{AMA} for thermal oscillations is consistently higher in the evaporator region for all heat inputs and heating modes, indicating that ΔT_{AMA} is a strong function of heat flux. Knowing that Borgmeyer and Ma [3] previously found that the frequency of internal working fluid oscillations has a dependence on heat flux and orientation, and having just observed the clear dependence of the thermal oscillations on both heat flux and orientation, it is apparent that the thermal oscillations are related to internal fluid oscillations. As the heat input increases from 40 W to 60 W for Experiment No. 1 shown in Fig. 13, ΔT_{AMA} has a jump, which means the oscillating motion is not stable. ΔT_{AMA} can be used to indirectly show the instable oscillating motion in an OHP. Also notice that for the 3D FP-OHP operating in a bottom heating mode, with a condenser temperature of 20°C, the most abrupt start-up with highest overall ΔT_{AMA} for thermal oscillations was achieved. This abrupt start-up is evidenced by the large sudden increase in ΔT_{AMA} at a step heat input from 70 W to 80 W. The 3D FP-OHP operating in the side heating mode (Experiment No. 3) had the lowest ΔT_{AMA} for thermal oscillations in both the evaporator and condenser regions at all heat inputs. Also notice that ΔT_{AMA} growth trend within the condenser region for Experiment No. 3 is smooth and gradual. The ΔT_{AMA} quantification provides a means of understanding and picturing the behavior of the thermal oscillations at given heat inputs. It may be seen that as the temperature and/or heat input is increased, ΔT_{AMA} generally increases. However, as alluded to previously, there may be a limit to ΔT_{AMA} of the thermal oscillations. This was observed by the maxima achieved for Experiment Nos. 2 and 3, as shown in Fig. 13. It may be seen that after ΔT_{AMA} reaches a maximum value, it decreases as the heat input continuously increases. In fact, it may be seen that ΔT_{AMA} for thermal oscillations at start-up for Experiment No. 2 is achieved again at almost twice the heat input. It is unclear if ΔT_{AMA} has a limiting maximum value for different experimental conditions, as the maxima observed in Fig. 13 may not be global. However, ΔT_{AMA} reversion/relaxation succeeding the local maxima may indicate limitations associated with the internal working fluid and the overall functionality of the heat pipe.

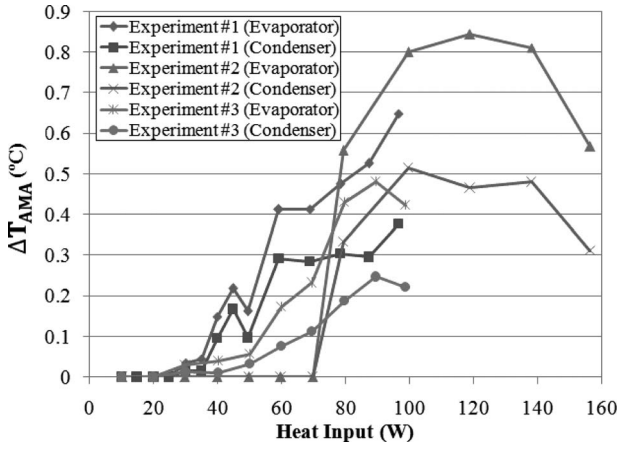

Fig. 13 Average-maximum peak-to-peak amplitude of thermal oscillations at various heat inputs for all three experiments

5 Conclusions

Thermal and visual oscillations were observed for the three-dimensional flat-plate oscillating heat pipe. The results show that for both the side and bottom heating modes, the 3D FP-OHP possessed an average temperature difference of approximately 8°C at a heat input of 100 W. The lowest average temperature difference and thermal resistance were achieved while having the 3D FP-OHP in the bottom heating mode with a condenser fluid temperature of 60°C for heat inputs under 100 W. While operating in a bottom heating mode with a condenser fluid temperature of 20°C, the heat pipe could withstand heat fluxes up to 20 W/cm^2 without any temperatures exceeding 100°C and approached a thermal resistance of almost 0.07°C/W.

Thermal and fluid oscillations were observed after activation/start-up during the transient temperature response to a heat input approximately equal to the excitation power for the respective experimental conditions. In the bottom heating mode, a discrete start-up occurred accompanied by the lowering of thermal resistance and a uniform temperature field relaxation. These observations were more pronounced for the 3D FP-OHP being bottom-heated at a colder condenser fluid temperature. After start-up, the thermal resistance decreased with higher heat inputs for all experimental conditions and no minimum was ever achieved. It was found that the required excitation power is dependent on both orientation and cooling conditions and is higher for the 3D FP-OHP utilizing a lower condenser fluid temperature. For the side heating mode, the start-up was less pronounced and was more of a gradual phenomenon accompanied by no temperature field relaxation.

In general, the average-maximum peak-to-peak amplitude

(ΔT_{AMA}) of thermal oscillations increased with higher heat loads, with amplitudes in the evaporator region growing at a faster rate than those in the condenser region. The overall trends for the thermal oscillations were similar at all thermocouple locations accompanied by sporadic uniform temperature disturbances described as a temperature field shock phenomenon. While the 3D FP-OHP was bottom heated with a condenser fluid temperature of 20°C, thermal oscillations were found to be the strongest at heat inputs over 100 W having a ΔT_{AMA} of around 0.8°C. In addition, there appeared to be a limiting factor associated with the thermal oscillations at higher heat inputs. Thermal oscillations for the side heating mode were more localized in the evaporator region and had the lowest average-maximum peak-to-peak amplitudes from all three experiments.

Since the average temperature difference and thermal resistance of the 3D FP-OHP in a side heating mode were comparable to the bottom heating mode, better gravity independence may be claimed with the three-dimensional design. However, the fact that the temperature oscillations behaved differently for the 3D FP-OHP operating in the side heating mode indicates that the device is still partially influenced by gravity. At this point, the thermal results indicate that minimizing the wall thermal resistance may increase the thermal performance of an FP-OHP, but more research is needed for confirmation. The high-channel density design has proven to be desirable for high heat flux applications, as the 3D FP-OHP performed favorably at heat fluxes up to 20 W/cm^2.

Acknowledgment

The work presented in this article was supported by the Office of Naval Research Grant No. N00014-06-1-1119, under the direction of Dr. Mark Spector, and the DARPA TGP program under the direction of Dr. Tom Kenny. We acknowledge the support of the National Institute of Standards and Technology, U.S. Department of Commerce, in providing the neutron research facilities used in this work.

Nomenclature

a = specified thermocouple/thermocouple location
D = channel diameter, m
g = local acceleration due to gravity, m/s^2
n = No. of thermocouples
Q = power input, W
T = average temperature measurement for specified thermocouple location, °C

Greek Symbols

σ = surface tension, N/m
ρ = density, kg/m^3
Ψ = thermal resistance, °C/W
Φ = peak-to-peak amplitude/noise, °C

Subscripts

AMA = average-maximum peak-peak amplitude
avg = average
crit = critical
l = liquid
OHP = oscillating heat pipe
tc = thermocouple
v = vapor

References

[1] Akachi, H., 1990, "Structure of a Heat Pipe," U.S. Patent No. 4,921,041.
[2] Tong, B. Y., Wong, T. N., and Ooi, K. T., 2001, "Closed-Loop Pulsating Heat Pipe," Appl. Therm. Eng., **21**, pp. 1845–1862.
[3] Borgmeyer, B., and Ma, H. B., 2007, "Experimental Investigation of Oscillating Motions in a Flat-Plate Oscillating Heat Pipe," J. Thermophys. Heat Transfer, **21**(2), pp. 405–409.
[4] Kim, J. S., Bui, N. H., Kim, J. W., Kim, J. H., and Jung, H. S., 2003, "Flow Visualization of Oscillation Characteristics of Liquid and Vapor Flow in the Oscillating Capillary Tube Heat Pipe," KSME Int. J., **17**, pp. 1507–1519.
[5] Zhang, X. M., Xu, J. L., and Zhou, Z. Q., 2004, "Experimental Study of a Pulsating Heat Pipe Using FC-72, Ethanol and Water as Working Fluids," Exp. Heat Transfer, **17**, pp. 47–67.
[6] Khandekar, S., Schneider, M., Schafer, P., Kulenovic, R., and Groll, M., 2002, "Thermofluid Dynamic Study of Flat-Plate Closed-Loop Pulsating Heat Pipes," Microscale Thermophys. Eng., **6**, pp. 303–317.
[7] Xu, G., Liang, S., and Vogel, M., 2006, "Thermal Characterization of Pulsating Heat Pipes," *The Tenth Intersociety Conference on Thermal and Thermomechanical Phenomena in Electronics Systems*, IEEE, San Diego, CA, pp. 552–556.
[8] Wilson, C., Borgmeyer, B., Winholtz, R. A., Ma, H. B., Jacobson, D. L., Hussey, D. S., and Arif, M., 2008, "Visual Observation of Oscillating Heat Pipes Using Neutron Radiography," J. Thermophys. Heat Transfer, **22**(3), pp. 366–372.
[9] Hussey, D. S., Jacobson, D. L., Arif, M., Huffman, P. R., Williams, R. E., and Cook, J. C., 2005, "New Neutron Imaging Facility at the NIST," Nucl. Instrum. Methods Phys. Res. A, **542**(1–3), pp. 9–15.

Recent Work on Boiling and Condensation in Microchannels

Ping Cheng[1]
e-mail: pingcheng@sjtu.edu.cn

Guodong Wang
e-mail: wangguodong@sjtu.edu.cn

Xiaojun Quan
e-mail: quan_xiaojun@sjtu.edu.cn

School of Mechanical and Power Engineering,
Shanghai Jiaotong University,
800 Dong Chuan Road,
Shanghai 200240, P.R. China

Recent work on boiling of water and condensation of steam in single and parallel microchannels is reviewed in this paper. It is found that the amplitude and frequency of fluctuations of temperature and pressure during the unstable flow-boiling mode depend greatly on the inlet/outlet configurations and the exit vapor quality. By fabricating an inlet restriction on each microchannel or the installation of a throttling valve upstream of the test section, reversed flow of vapor bubbles can be suppressed resulting in a stable flow-boiling mode. Boiling heat transfer coefficient and pressure drop in microchannels under stable flow-boiling conditions are obtained. These data at high vapor qualities are found to be substantially different from the correlations obtained for flow-boiling in macrochannels. Microbubble emission boiling phenomena, which can defer the arrival of critical heat flux, exist in a partially heated Pyrex glass microchannel at sufficiently high heat flux and high inlet subcooling conditions. For condensation in a microchannel, transition from annular flow to slug/bubbly flow is investigated. The occurrence of the injection flow is owing to the instability of the liquid/vapor interface. The location, at which the injection flow occurs, depends on the mass flux and the cooling rate of steam. Increase in steam mass flux, decrease in cooling rate, and microchannel diameter tend to enhance the instability of the condensate film on the wall, resulting in the occurrence of injection flow further downstream at increasingly high frequency. The pressure drop in the condensing flow increases with the increase in mass flux and quality or with decreasing microchannel diameter. The existing correlations for pressure drop and heat transfer of condensing flow in macrochannels overestimate the experimental data in microchannels. [DOI: 10.1115/1.3072906]

Keywords: boiling instability, microchannels, inlet restriction, microbubble emission boiling, condensation, injection flow

1 Introduction

Miniaturization of mechanical devices for portability and high efficiency has been the trend of modern engineering, and the rapid advances of microfabrication technology have accelerated such a trend. For reliable designs of many microdevices such as microheat exchangers, inkjet print heads, micropumps, and microactuators [1] in which phase-change heat transfer phenomena often occur in microchannels, it is important to know boiling and condensation heat transfer characteristics at microscale.

Research work on microscale phase-change heat transfer prior to 2004 has been reviewed extensively by Kandlikar [2], Thome [3], and Cheng et al. [1,4]. The Bond number, which is a measure of the relative important of the surface tension to gravitational effect, has been proposed for the classification of microchannels, minichannels, and macrochannels for phase-change heat transfer [1]. Because of the size effect and the predominant of surface tension effect over the gravitational effect, it was found that boiling heat transfer characteristics in microchannels differ in many aspects from those in microchannels. For example, reversed flow of vapor bubbles was observed in flow boiling in microchannels [5]. Measurements showed that unstable and stable flow-boiling modes existed in microchannels depending on heat flux and mass flux [6]. Large-amplitude/long-period fluctuations of temperature and pressure during flow boiling under certain heat and mass flux conditions were recorded [7,8]. The flow-boiling instability was attributed to upstream compressible volume and flow interaction in the headers of parallel microchannels, and the installation of a valve upstream could reduce flow-boiling instability due to the upstream compressible volume substantially [9]. A two-zone model consisting of liquid slug and elongated bubble was used to study evaporation characteristics of elongated bubbles in microchannels [10], and an annular two-phase flow model was developed to predict the saturated flow-boiling heat transfer coefficient [11]. For condensation heat transfer in microchannels, early experimental work showed that condensation heat transfer rate in microchannels was higher than those in macrochannels under similar mass flux and heat flux conditions. It was observed that mist flow existed upstream and intermittent flow downstream in the microchannels [12]. Because the surface tension effect suppresses gravitational effect in microchannels, stratified flow patterns do not exist in condensing flow in microchannels. The occurrence of injection flow during condensation in microchannels was observed [13].

Recent work on flow boiling in microchannels centered on the classification of stable and unstable flow-boiling regimes [14,15], investigations of flow boiling instability [15,16] and measurements of boiling heat transfer coefficient and pressure drop [15,17,18]. The explosive expansion of vapor bubble to upstream in the microchannels was observed [16], and the large amplitude fluctuations of temperature and pressure in flow boiling in microchannels [8] could be attributed to the upstream expansion of vapor bubbles. The fabrication of an inlet restriction in the microchannel was shown to be effective in reducing flow-boiling instability [15,17,18]. Flow-boiling heat transfer characteristics of water [15,19] and refrigerants [20–23] in microchannels were measured under stable boiling conditions. The two-zone model was extended to the three-zone model consisting of liquid slug, elongated bubble, and vapor slug to obtain heat transfer coefficient of elongated bubble flow [24], and comparison with experi-

[1]Corresponding author.

Contributed by the Heat Transfer Division of ASME for publication in the JOURNAL OF HEAT TRANSFER. Manuscript received March 2, 2008; final manuscript received August 3, 2008; published online March 4, 2009. Review conducted by Robert D. Tzou. Paper presented at the 2008 International Conference on Micro/Nanoscale Heat Transfer (MNHT2008), Tainan, Taiwan, January 6–9, 2008.

mental data was made [25]. A flow pattern map in terms of mass flux versus vapor quality for steady bubbly flow and annular flow in microchannels was presented [26]. The saturated critical heat fluxes of R134a and R245fa were determined [27]. Subcooled flow boiling and microbubble emission boiling (MEB) phenomena in microchannels were investigated [28]. For condensation heat transfer in microchannels, recent work focused on the study of the transition from annular to slug/bubbly flow, and the occurrence frequency of the injection flow [29]. Pressure drop and heat transfer coefficient of condensing steam in microchannels were measured and were compared with existing correlations for steam condensing in macrochannels [30,31]. Effects of cross-sectional shape and channel diameter for steam and refrigerants condensing in mini- or microchannels were investigated experimentally and theoretically [32–40]. The above mentioned recent work on boiling and condensation heat transfer in microchannels is the subject of discussion in this review.

2 Recent Work on Flow Boiling in Microchannels

2.1 Unstable Flow Boiling Owing to Upstream Compressible Volume

2.1.1 Classification of Stable and Unstable Flow Boiling in Microchannels. Qu and Mudawar [9] identified two types of flow-boiling instabilities: upstream compressible volume instability and flow interaction instability. Wang et al. [14] found that stable and unstable flow-boiling modes existed in microchannels, depending on four parameters, namely, heat/mass flux ratio, inlet water subcooling, channel geometry (A_w,A_c), and physical properties of the working medium. Subsequently, Wang et al. [15] found that it is more convenient to use the exit vapor quality to classify the flow-boiling regimes, where the exit vapor quality x_e can be calculated from

$$x_e = (h_e - h_f)/h_{fg} \tag{1}$$

with h_f being the saturated liquid enthalpy, h_{fg} the latent heat of evaporation, and h_e the fluid enthalpy at the exit, which can be calculated from

$$h_e = h_{\text{in}} + \frac{q \cdot N \cdot A_w}{G \cdot N \cdot A_c} \tag{2}$$

where h_{in} is the inlet fluid enthalpy, N is the total number of microchannels, A_w is the area of the bottom wall and side walls of each microchannel, and A_c is the cross-sectional area of each microchannel. Substituting Eq. (2) into Eq. (1) gives the exit vapor quality:

$$x_e = \frac{h_e - h_f}{h_{fg}} = \frac{h_{\text{in}} + (A_w/A_c)q/G - h_f}{h_{fg}} = \frac{h_{\text{in}} - h_f}{h_{fg}} + \frac{A_w \text{Bo}}{A_c} \tag{3}$$

where $\text{Bo}=q/Gh_{fg}$ is the boiling number. It is clear from Eq. (3) that the exit vapor quality x_e has included the information of the four parameters: q/G (or Bo), the inlet water temperature (h_{in}), the geometry of the microchannel A_w/A_c, and physical properties of the fluid h_{fg}.

2.1.2 Effects of Inlet/Outlet Configurations on Flow-Boiling Instability. Two types of inlet/outlet connections with the parallel microchannels in the test section are sketched in Fig. 1. Figure 1(*a*) shows the vertical inlet/outlet configurations where subcooled liquid was supplied by one inlet conduit perpendicular to the microchannels, and discharged as vapor through another outlet conduit perpendicular to the microchannels. This type of connections was used by Cheng and co-workers in their flow-boiling experiments [7,8,14], where flow of subcooled liquid at the inlet plenum and vapor at outlet plenums were restricted. Figure 1(*b*) shows the horizontal inlet/outlet connections where the subcooled liquid was flowing freely into the microchannels and vapor is flowing freely out from the microchannels, which was the configuration used by other investigators [9,16].

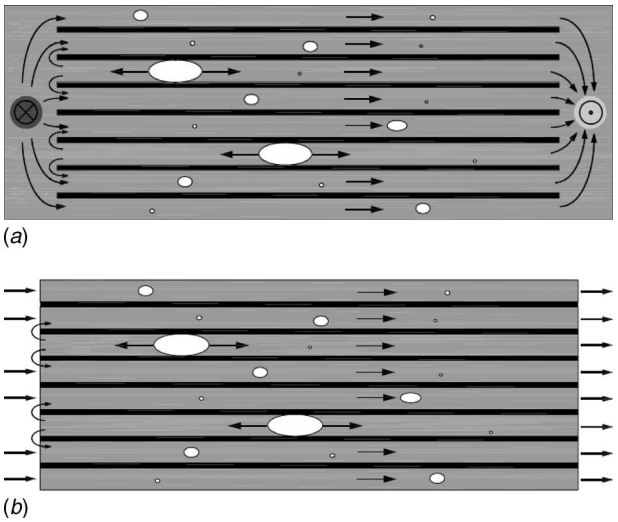

Fig. 1 Parallel microchannels with two different types of inlet/outlet connections [15]

Wang et al. [15] found that the magnitudes of temperature and pressure fluctuations in the unstable flow-boiling mode depend greatly on the configurations of the inlet/outlet connections with the microchannels. Figure 2(*a*) is a flow pattern map in terms of heat flux versus mass flux for flow boiling of water in parallel microchannels (having trapezoidal cross sections with a hydraulic diameter of 186 μm) with vertical inlet/outlet connections at inlet subcooled water of 35°C [13]. It is shown that two inclined straight lines with $q/G=0.96$ kJ/kg ($x_e=0.036$) and $q/G=2.14$ kJ/kg ($x_e=0.228$) dividing the stable and unstable flow-boiling regimes. The steady bubbly/slug flow boiling existed for $q/G<0.96$ kJ/kg ($x_e<0.036$), the bubbly/annular alternating flow-boiling regime existed for $0.96 \text{ kJ/kg} < q/G < 2.14 \text{ kJ/kg}$ ($0.036<x_e<0.228$), and the annular/mist alternating flow boiling existed for $q/G>2.14$ kJ/kg ($x_e>0.228$). Figure 2(*b*) shows the corresponding flow pattern map for flow boiling in the microchannels with horizontal inlet/outlet connections having the same diameter and inlet water temperature. Note that the steady bubble/slug flow-boiling regime in Fig. 2(*a*) with $x_e<0.036$ is smaller than that in Fig. 2(*b*) with $x_e<0.044$. This suggests that instability in parallel microchannels with horizontal inlet/outlet connections was partially reduced compared with those with vertical inlet/outlet connections where the flow could not exit freely because of the vertical outlet conduit, and the vapor bubbles tend to expand upstream because of the confinement of the wall.

Figure 3(*a*) shows the oscillations of wall temperatures, inlet/outlet water temperatures, and inlet/outlet pressures in the parallel microchannels with vertical inlet/outlet connections in the unstable flow-boiling regime at $q=497.8$ kW/m^2, $G=368.9$ kg/m^2 s, and $T_{\text{in}}=35$°C (i.e., $x_e=0.096$) where bubbly/annular alternating flow boiling took place. Figure 3(*b*) shows the same measurements under similar conditions ($q=485.5$ kW/m^2 s, $G=364.9$ kg/m^2 s, and $T_{\text{in}}=35$°C) in parallel microchannels with horizontal inlet/outlet connections. A comparison of Figs. 3(*a*) and 3(*b*) shows that temperature and pressure oscillations in microchannels with vertical inlet/outlet connections were considerably larger than those in horizontal inlet/outlet connections. It can be concluded that microchannels with the vertical inlet/outlet connections are more unstable than those with horizontal inlet/outlet connections because the exit of steam is more restrictive in the former case, which limits the downstream expansion of vapor bubbles. It is interesting to note that the materials used in the inlet connection also affected the amplitude of temperature and pressure oscillations. For example, a flexible inlet tube was used by Wu and Cheng [7,8] in their early experiments

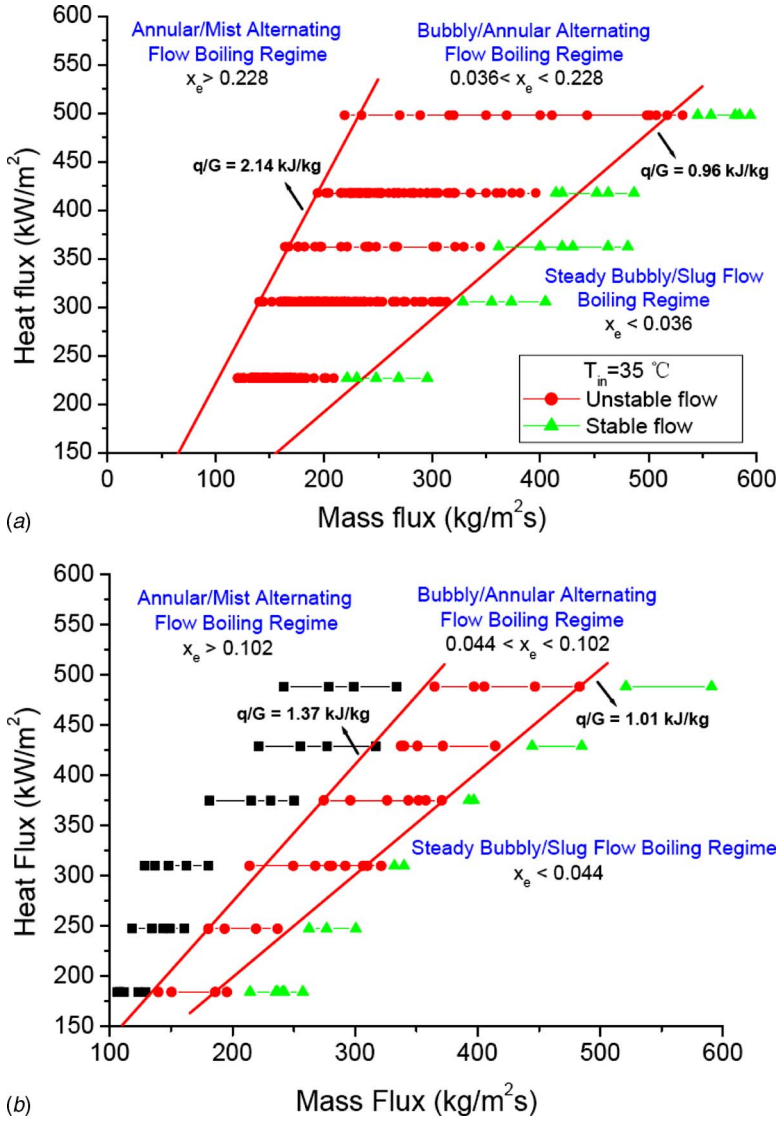

Fig. 2 Different flow-boiling patterns in parallel microchannels (D_h =186 μm) with vertical inlet/outlet connections [14] and with horizontal inlet/outlet connections [15]

while a steel inlet tube was used in their later experiments [14,15]. Consequently, the amplitudes of temperature and pressure oscillations in the former experiments were much larger than those in the latter experiments under similar experimental conditions because the former had a larger upstream compressible volume.

It can be concluded from the work of Cheng and co-workers [7,8,14,15] that the limit of exit quality for which stable flow boiling exits depends on the experimental setup, such as the inlet/outlet configuration and materials used and whether the fluid was driven by a pump of a compressed gas tank. Also, it can be concluded that amplitudes and periods of temperature and pressure oscillations measured by previous investigators did not agree with each other even under similar heat flux, and mass flux conditions can be attributed to the following reasons: (i) different amounts of upstream compressible volumes in different experimental setups, and (ii) the specific time at which measurements of the amplitude and period of oscillations were taken during the unstable flow-boiling conditions [8].

2.2 Stable Flow Boiling in Microchannels. As shown from Fig. 2, stable flow-boiling conditions could be achieved when bubbly/slug flow existed at very low vapor quality (x_e<0.036 for microchannels with vertical inlet/outlet connections and x_e <0.044 for horizontal inlet/outlet connections). To extend the stable flow-boiling regimes in microchannels, methods to increase the stiffness of the upstream volume of the experimental setup must be used. These methods include the fabrication of inlet restrictions on the microchannels [15,17,18] or the installation of throttling/flow-regulating valves upstream of the test section [9,19–23,26,27].

2.2.1 Stable Boiling Flow Patterns. To investigate the stable flow-boiling characteristics at high vapor qualities, Wang et al. [15] fabricated inlet restrictions on each microchannel having a diameter of 186 μm to delay flow-boiling instability occurring in microchannels. Figure 4(*a*) shows that inlet restrictions were fabricated on each of the microchannel with horizontal inlet/outlet connections, while Fig. 4(*b*) shows the detailed dimensions of the cross section of the inlet restriction. Because the inlet restriction on each of the microchannels could prevent vapor bubbles from expanding upstream, reversed flow of vapor was suppressed in these microchannels.

As shown in Figs. 5(*a*) and 5(*b*), temperature and pressure

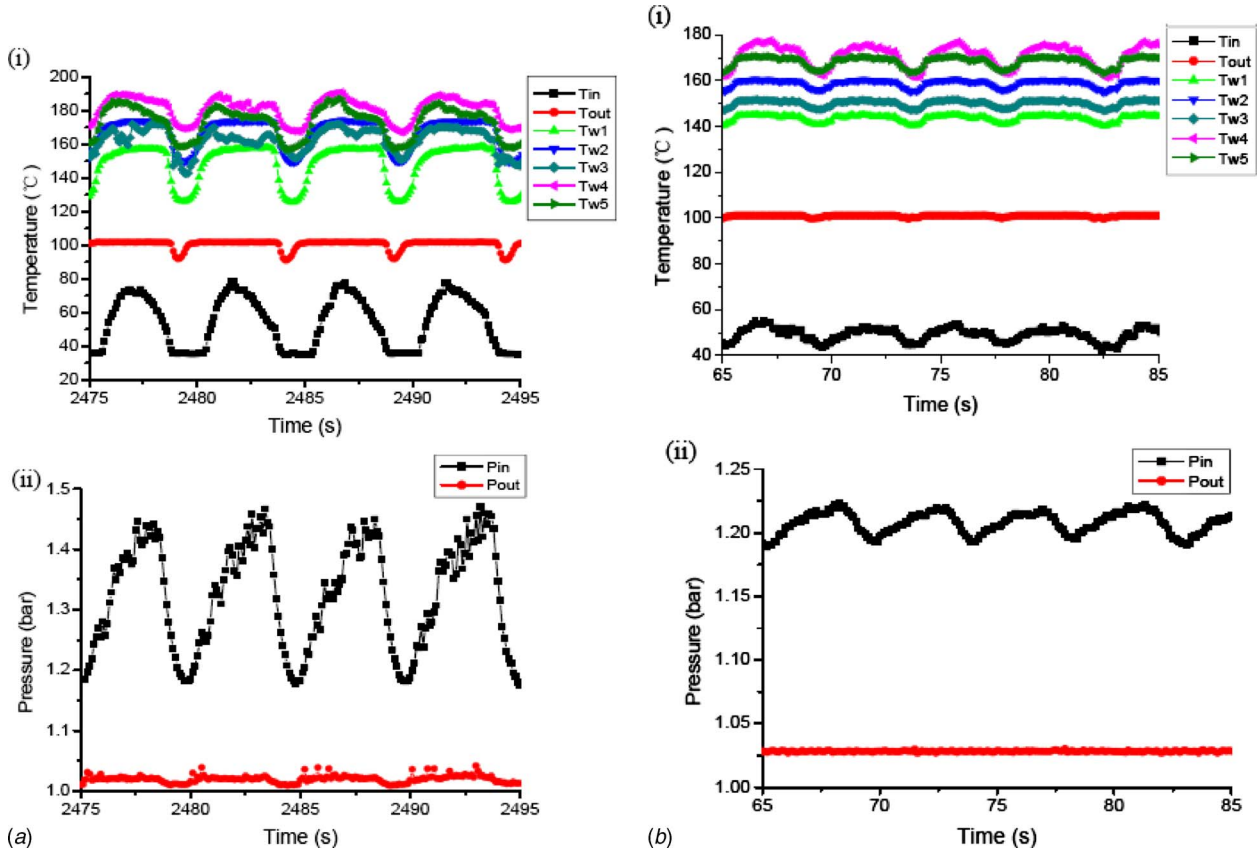

Fig. 3 Measurements of inlet/outlet water and wall temperatures and inlet/outlet pressures in parallel microchannels (D_h =186 μm) in bubby/annular alternating flow-boiling regime: (a) horizontal inlet/outlet connections with q=485.5 kW/m^2, G=364.9 kg/m^2 s, and T_{in}=35°C (x_e=0.096); (b) vertical inlet/outlet connection with q=497.8 kW/m^2, G=368.9 kg/m^2 s, and T_{in}=35°C (x_e=0.099) [15]

variations in the microchannels with inlet restriction were constant with time when the exit vapor quality was as high as x_e=0.359 (at q=364.7 kW/m^2, G=124 kg/m^2 s, and T_{in}=35°C). Thus, stable flow-boiling condition existed at such a high exit vapor quality. Figure 5(*c*) are the photos showing the steady flow-boiling flow patterns at four different locations in the parallel microchannels. It can be seen that isolated bubbles detached near the entrance and moved downstream. As a result of bubble coalescence, vapor plugs were formed further downstream. Annular flow was formed near the outlet with water droplets appearing at the bottom side of the top Pyrex cover. It appears from Fig. 5(*c*) that the nucleation mechanism usually dominates near the onset of boiling at upstream of the microchannels while film vaporization (i.e., convective boiling) becomes predominant in the Taylor bubble and annular flow at downstream.

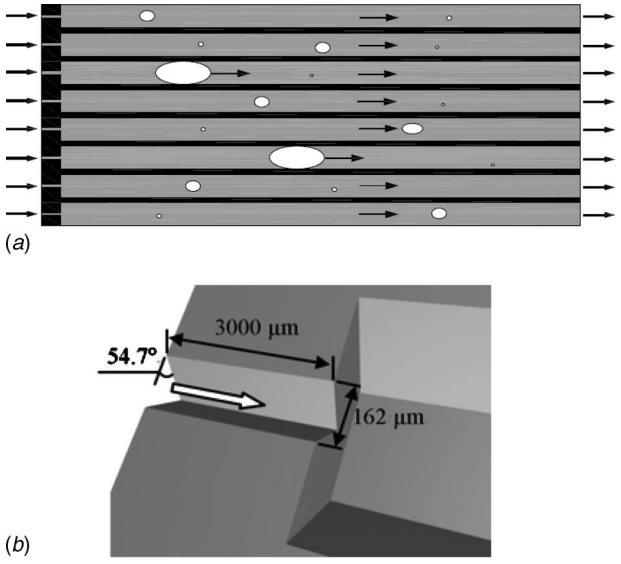

Fig. 4 Microchannels with inlet restrictions [15]

Revellin and Thome [26] installed a valve between upstream reservoir and the test section to delay flow oscillations in their flow-boiling experiments. Figure 6 shows a flow pattern map for stable flow boiling of R134a in the microchannels with D_h =0.5 mm, L=70 mm, at q=50 kW/m^2 in terms of mass velocity versus vapor quality (up to x=0.8). In this figure, isolated bubbly flow, bubbly-slug, slug, slug-semi-annular, semi-annular, annular, and dryout regimes are shown.

2.2.2 Pressure Drop in Stable Flow Boiling. Pressure drop data of water under stable flow-boiling condition in the heated microchannels having D_h=186 μm with inlet restriction were obtained by Wang et al. [15] and the data are presented in Fig. 7 for the exit vapor quality up to 0.4. In the same figure, the data are compared with Mishima and Hibiki's correlation [41] for adiabatic two-phase pressure drop in minitubes with diameters ranging from 1 mm to 4 mm. It can be seen that the average values calculated from the existing correlation predicted the general trend of pressure drop, but underpredicted the pressure drop data at high vapor quality (x_e>0.1). The reasons may be attributed to different flow patterns in microchannels and mini-/macrochannels owing to the following reasons: (i) surface tension effect is more predomi-

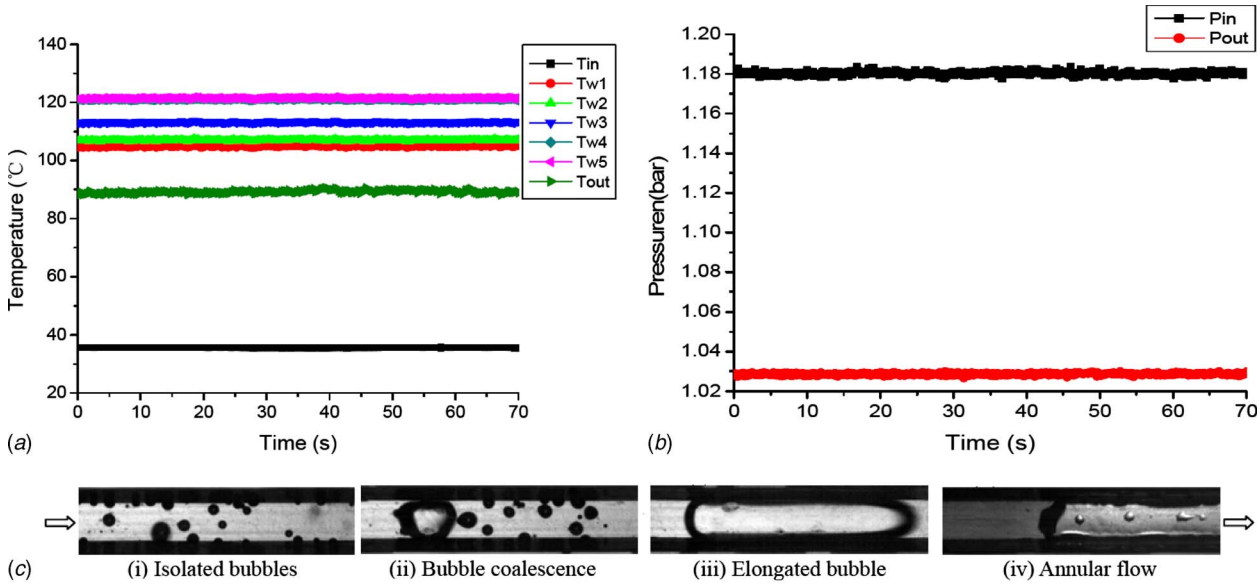

Fig. 5 Temporal pressure and temperature variations during flow boiling of water in microchannels with inlet restrictions (D_h=186 μm) and photos of steady flow-boiling patterns at different locations for q=364.7 kW/m^2, G=124 kg/m^2 s, and T_{in}=35°C (x_e=0.359) [15]

nant than gravitational effect in microchannels, (ii) smooth surface conditions of silicon microchannel compared with the relatively rough surface condition of metal tubes, and (iii) the corner effect of the trapezoidal cross section of the silicon microchannels compared with the round tubes. As shown in Fig. 5(*c*), the coalesced bubbles in the microchannel were confined, elongated and finally formed annular flow downstream. On the other hand, many bubbles grew and flowed freely along the mini-/macrochannel without restriction. Also, confined bubbles formed at high vapor quality, blocking the free flow of vapor bubbles in microchannels. Thus, the greater pressure drop in microchannels is due to the additional friction related to the elongated bubbles, as well as due to local dryout.

2.2.3 Heat Transfer in Stable Flow Boiling

2.2.3.1 Boiling Heat Transfer Coefficient of Water. Boiling heat transfer coefficient of water for a vapor quality up to x_e <0.28 was measured by Sobierska et al. [19] using a copper-based minichannel having a rectangular cross section with a hydraulic diameter of 480 μm and with a valve installed upstream of the test section. Figure 8 presents the local boiling heat transfer coefficient of water versus vapor quality at a mass flux of 200 kg/m^2 s for different heat fluxes. The bubbly flow, slug flow (confined bubble), and annular flow regimes are divided by two inclined straight lines. It is seen that the subcooled liquid began at a negative vapor quality at inlet and the local boiling heat transfer coefficient increased as the vapor quality increased in downstream. The local boiling heat transfer coefficient reached a maximum value at low vapor quality ($x<0.05$) where slug flow (confined bubble) existed. The boiling heat transfer coefficient in this regime depended greatly on heat flux. With increasing vapor quality downstream, the local boiling heat transfer coefficient decreased continuously. The decrease in the boiling heat transfer coefficient is small in the annular flow regime ($x>0.1$) and becomes relatively independent of heat flux at high vapor quality.

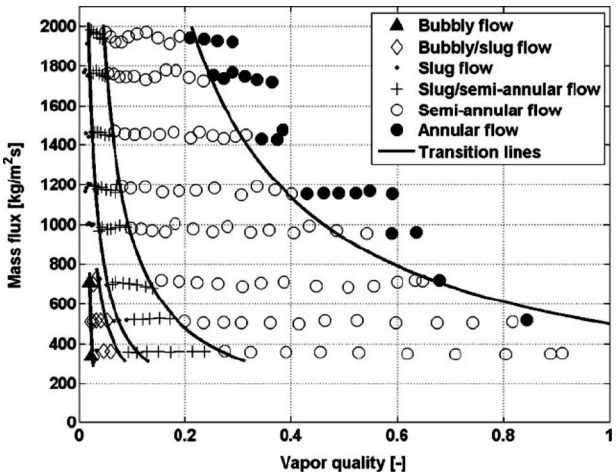

Fig. 6 Flow pattern map for stable flow boiling of R134a in microchannel (D_h=509 μm) at different mass fluxes [26]

Figure 9 shows the data for boiling heat transfer coefficient of water in silicon microchannels with D_h=186 μm obtained by Wang et al. [15]. It can be seen from the data that the local boiling heat transfer coefficient reached a peak value at low vapor quality ($x_e<0.05$) and then decreased with the increase in vapor quality. At low vapor quality of $x_e<0.1$, the heat transfer coefficient depended greatly on heat flux suggesting nucleate boiling mechanism controlled. In the annular flow regime ($x_e>0.1$), the boiling heat transfer coefficient is relatively independent of heat flux and vapor quality. The solid lines are the boiling heat transfer coefficient predicted from Kandlikar correlation [42], which was based on over 10,000 data points for flow boiling in mini-/macrotubes having diameters ranging from 3 mm to 25 mm. It is shown that although the Kandlikar correlation predicted the general trend of the boiling heat transfer coefficient data in the microchannels, it overpredicted the data in high flux and high vapor quality regimes. It is interested to note that the peak in heat transfer coefficient data occurred at low vapor quality between 0 and 0.2 in microchannels as compared with that at high vapor quality between 0.7 and 0.9 in large channels [43]. This difference in heat transfer behavior results from the confinement effect on bubbles in microchannels. Confined bubbles in microchannels grow in length rather than in diameter and form elongated slug flow. The elongated slug could suppress bubble nucleation at low vapor quality

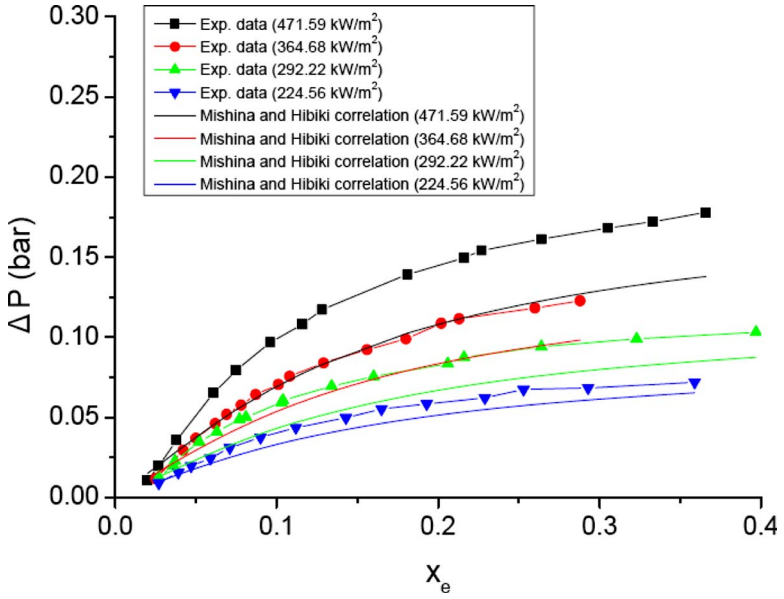

Fig. 7 Pressure drop data for steady flow boiling of water in microchannels (D_h=186 μm) and its comparison with Mishima and Hibiki correlation for flow boiling in mini/microchannels at different heat fluxes [15]

and caused local dryout at high vapor quality, both of which decrease the boiling heat transfer coefficient in the microchannel.

2.2.3.2 Boiling Heat Transfer Coefficient of Refrigerants. Agostini et al. [20,21] investigated the flow-boiling characteristics of R236fa and R245fa in a silicon-based multimicrochannels heat sink with D_h=336 μm with a valve upstream of the test section. They also found that the heat transfer coefficient versus vapor quality reached a maximum heat flux in low vapor quality region ($0<x_e<0.2$) and then decreased with further increase in heat flux. The influence of mass flux on the boiling heat transfer coefficient was more pronounced for R245fa than that for R236fa, especially at very high heat flux conditions.

Harirchian and Garimella [22] performed an experiment to investigate the effect of microchannel size on flow-boiling heat transfer coefficient of FC-77. Seven different sets of silicon parallel micro- and minichannels of rectangular cross sections with width ranging from 100 μm to 5850 μm at a fixed depth of 400 μm (i.e., D_h=160–749 μm) were used in their experiments and a throttling valve was placed upstream of the test section. The length of the microchannels was 12.7 mm, which was much shorter than other channel lengths ranging from 30 mm to 330 mm [14,15,19–21,26,27]. Figure 10(*a*) shows the effects of microchannel width on boiling curves of FC-77 at a constant mass flux of 700 kg/m^2 s. It can be seen that nucleation started earlier in a smaller microchannel. Figure 10(*b*) shows the influence of the microchannel width on the boiling heat transfer coefficient at the same mass flux of 700 kg/m^2 s. At this mass flux and at a heat flux $q<150$ kW/m^2, the heat transfer coefficient of the smallest microchannel (with 100 μm width) was higher than larger microchannels. This is because of lower wall superheat that is required for nucleation in the 100 μm wide microchannels, as shown in Fig. 10(*a*), leading to an early arrival of confined bubble flow in the smallest microchannel. This led to higher boiling heat transfer coefficients of the 100 μm wide microchannel at low heat fluxes.

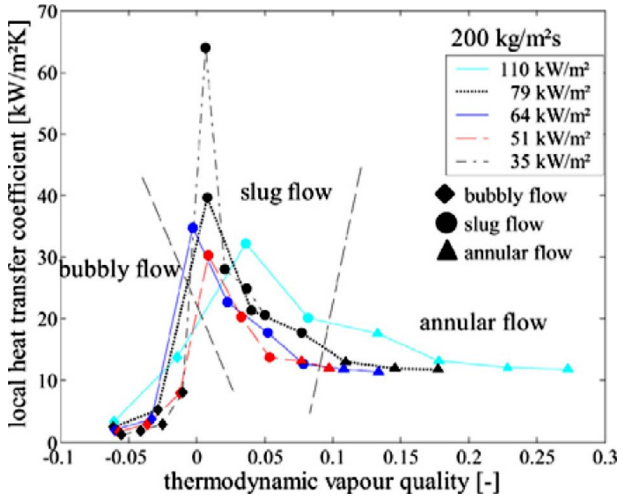

Fig. 8 Local boiling heat transfer coefficient of water in microchannel (D_h=480 μm) at mass flux of 200 kg/m^2 s [19]

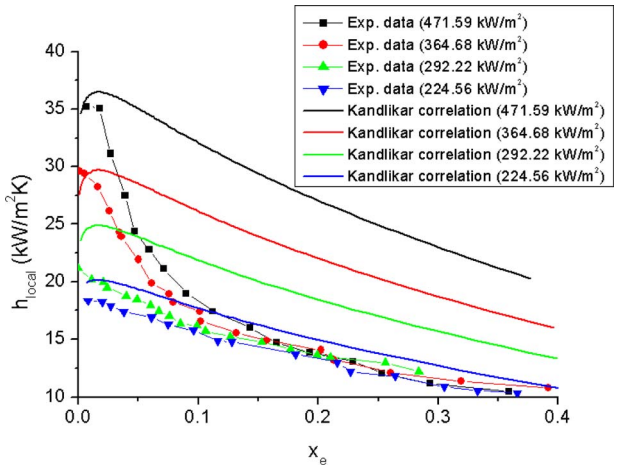

Fig. 9 Comparison of boiling heat transfer coefficient data of water in microchannels (D_h=186 μm) with Kandlikar correlation at different heat fluxes [15]

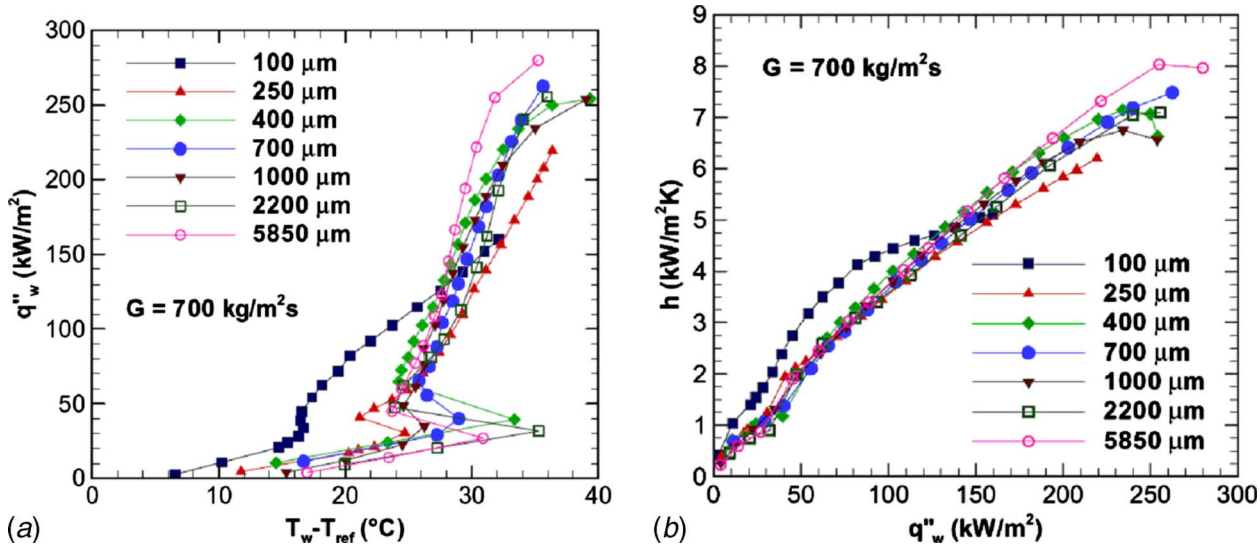

Fig. 10 Effects of microchannels width on boiling curves of FC-77 and boiling heat transfer coefficient versus wall heat flux at G=700 kg/m² s [22]

Because the microchannels used in Harirchian and Garimella's experiment [22] was short, the confined bubble might appear to be an annular flow in their experiment.

Bertsch et al. [23] investigated flow boiling of R134a in a copper plate evaporator having *multiminichannels* (with D_h =1090 μm) using a regulator valve to adjust flow rate in upstream. Figure 11(*a*) shows the effect of mass flux on the local boiling heat transfer coefficient of HFC-134a versus the vapor quality at a fixed saturation pressure of 550 kPa. It can be seen that the heat transfer coefficient increased with increasing mass flux and reached a maximum heat transfer coefficient at a low vapor quality of 0.2, which is in agreement with the general trend of flow boiling of water in minichannels [15,19]. Figure 11(*b*) shows the effect of saturation pressure (ranging from 400 kPa to 750 kPa) on the local heat transfer coefficient at a constant mass flux of G=40.5 kg/m² s. It is seen that the effect of saturation pressure on heat transfer coefficient is negligibly small in the range of saturation pressure under consideration.

2.2.3.3 Model of Evaporation of Elongated Bubble Flow. Thome et al. [24] extended their two-zone (liquid slug/elongated bubble) model to a three-zone (liquid slug/elongated bubble/vapor slug) model without bubble coalesce to study the evaporation of elongated bubbles in microchannels, which is sketched in Fig. 12(*a*). The model was used to calculate the heat transfer coefficient in this flow-boiling pattern during the cyclic passage of liquid slug, elongated bubble, and vapor slug, assuming that the bubble frequency, the minimum liquid film thickness at dryout, and the liquid film formation thickness were known a priori. The temporal variations in the heat transfer coefficient in the three zones during a cycle are presented in Fig. 12(*b*). Based on Fig. 12(*b*), the local time-average heat transfer coefficient in a cycle could be computed. Compared with 1591 data points taken from seven independent studies, Dupont et al. [25] found that this new model predicted 67% of the database within ±30%. The model also successfully predicted the trend of the heat transfer data (e.g., the peak of boiling heat transfer coefficient occurs at low vapor

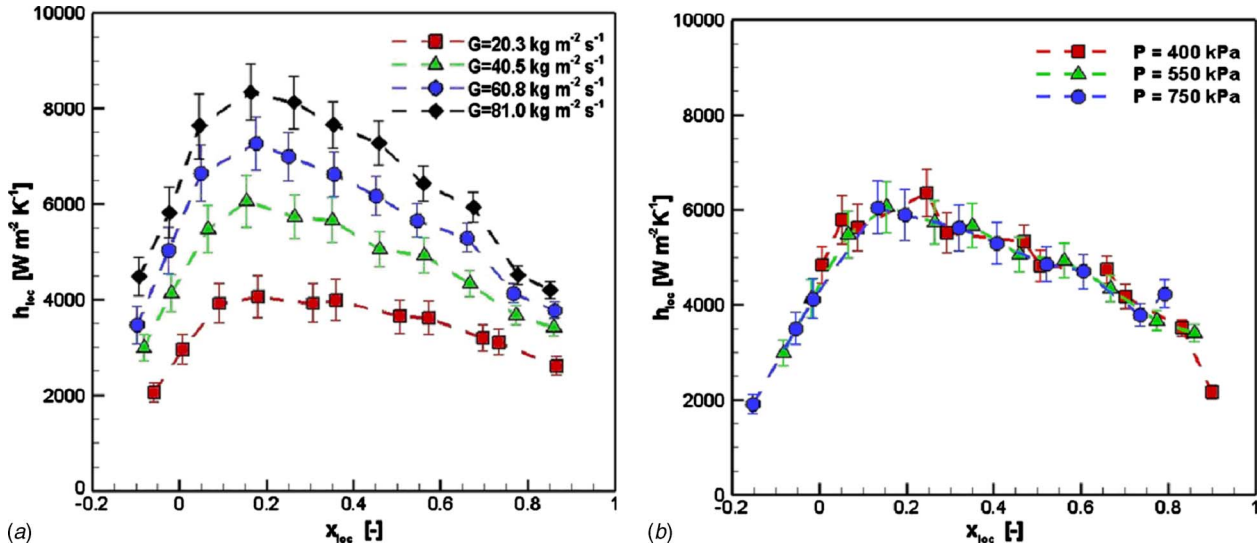

Fig. 11 Boiling heat transfer coefficient of R134a versus vapor quality at different mass fluxes and saturation pressures in a minichannel with D_h=1090 μm [23]

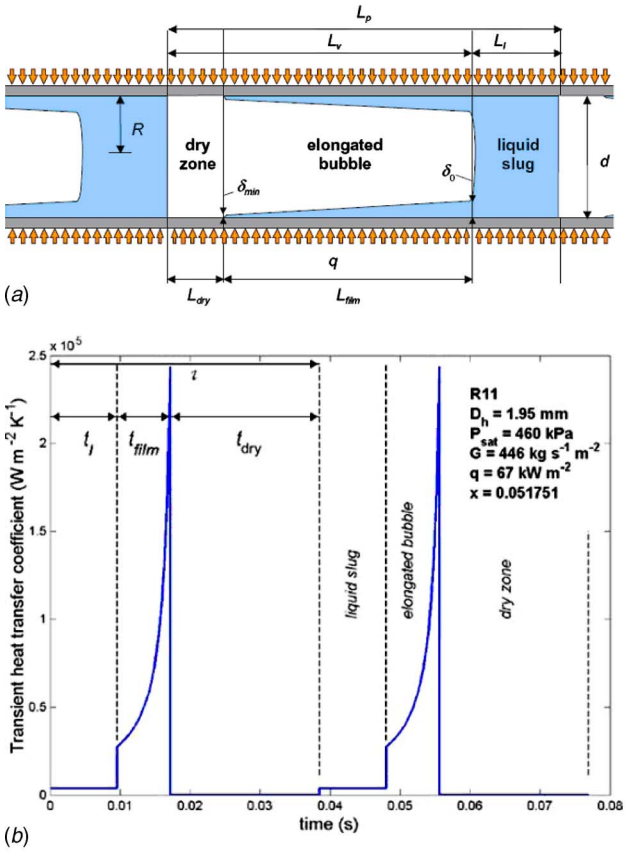

Fig. 12 Three-zone model for elongated bubble flow and cyclic variation in boiling heat transfer coefficient [24]

quality). Figure 13 depicts the comparison of this model with experimental data of R134a provided by Agostini [44], where the model results based on global parameters (solid line) and optimum parameters (dotted lines) are also presented. The global parameters referred to the three key parameters (bubble frequency, minimum liquid film thickness at dryout, and liquid film formation thickness), which were calculated from three empirical equations, while optimum parameters referred to the three key parameters, which were obtained using least-squares fit with specific experimental data. Therefore, the three optimum parameters in one experiment were different from the other. For this reason, it can be seen that the model results based on optimum parameters are in good agreement with experimental data. Although the model predictions based on global parameters show large differences from experimental data, the model was capable to predict the trend of the data correctly.

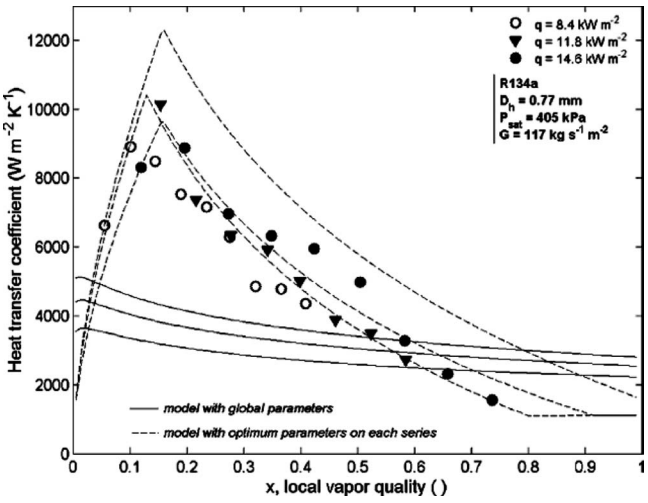

Fig. 13 Comparison of three-zone model with Agostini's flow-boiling data of R134a in a 0.77 mm tube [25]

2.2.3.4 Saturated Critical Heat Flux. Wojtan et al. [27] performed a series of tests to determine the effects of mass flux, heated length, and inlet subcooling on saturated critical heat flux (CHF) of R134a and R245fa in single stainless steel microtubes of 0.5 mm and 0.8 mm in diameter, which were uniformly heated. Figure 14 shows the determination of CHF of R134a at $G=1000$ kg/m^2 s, $T_{sat}=30°$C in a microtube having $D_h=0.5$ mm and $L_h=70$ mm. It can be seen that the heat flux increased almost linearly with wall temperature until it reached a maximum heat flux at $q=163$ kW/m^2, which is the critical heat flux of R134a at $G=1000$ kg/m^2 s. The effects of mass velocity and heated length on saturated CHF in two microchannels with different hydraulic diameters are presented in Figs. 15(*a*) and 15(*b*), respectively. It is shown that CHF is higher in a microchannel with a larger hydraulic diameter. For a microchannel with a specific diameter, the CHF increases with the mass velocity (Fig. 15(*a*)) but decreases with the heated length (Fig. 15(*b*)). The saturated critical heat flux data of R134a and R245fa can be correlated as

$$q_c = 0.437\left(\frac{\rho_v}{\rho_L}\right)^{0.073} \mathrm{We}^{-0.24}\left(\frac{L_h}{D}\right)^{-0.72} Gh_{fg} \tag{4}$$

where $\mathrm{We}=G^2L_h/(\rho_L\sigma)$ is the liquid Weber number with L_h being the heated length of the channel.

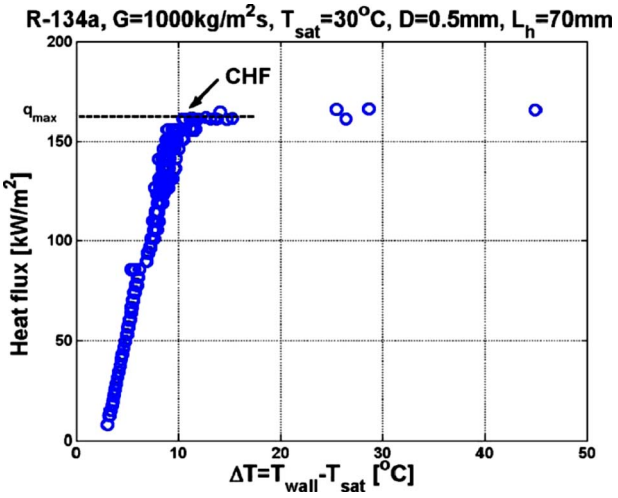

Fig. 14 Determination of saturated CHF of R134a at G =1000 kg/m^2 s, T_{sat}=30°C, in a microtube having D=0.5 mm, L_h=70 mm [27]

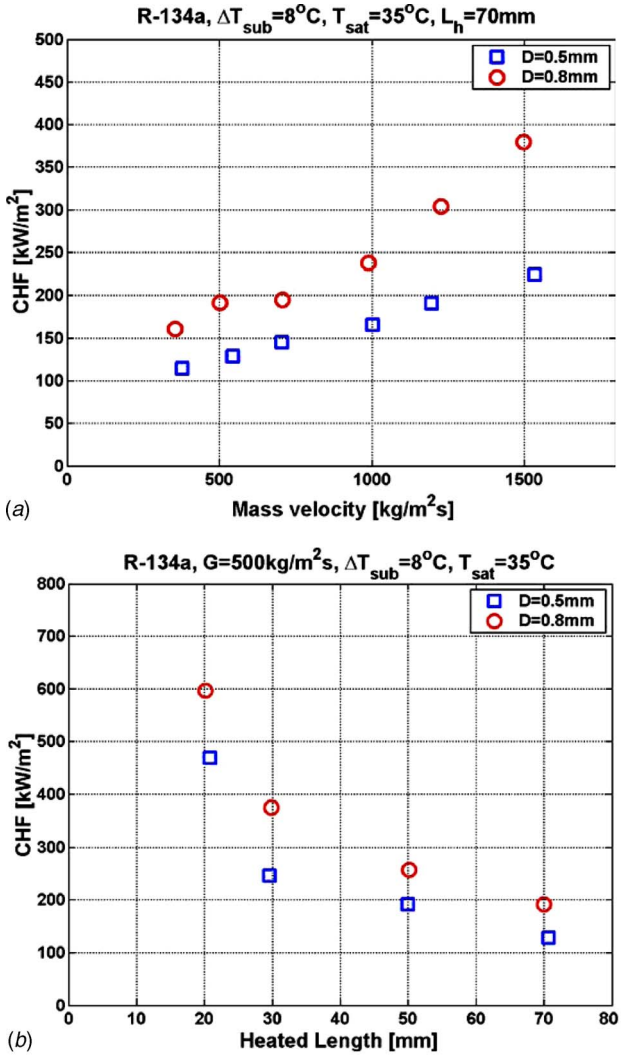

Fig. 15 Effects of mass flux and heated length on saturated CHF of R134a in two microtubes of 0.5 mm and 0.8 mm in diameters [27]

2.2.4 Subcooled Flow Boiling and Microbubble Emission Boiling Phenomena. In 1981, Inada et al. [45] discovered the MEB phenomena in pool boiling using a heated vertical copper cylinder of 10 mm in diameter submerged in water at 30 K. Since that time, many authors have investigated microbubble emission pool boiling [46] and flow boiling in minichannels [47,48]. Most recently, Wang and Cheng [28] investigated subcooled flow boiling in a partially heated microchannel with D_h=155 μm. Figure 16(*a*) is a sketch of a microchannel integrated with a microheater used in their experiment. The microheater, 200 μm in width and 2000 μm in length, was located between 6.5 mm and 8.5 mm from the entrance at the bottom Pyrex glass wall of the microchannel having 280 μm in width and 15 mm in length. Figure 16(*b*) is a photo showing the serpentine Pt microheater used in the experiment. As shown from this figure, the Pt wire occupied an area of 0.28 mm^2, covering approximately 70% of the Pyrex glass area.

Figure 17 shows the effects of mass fluxes (G =294.6 kg/m^2 s, 589.2 kg/m^2 s, and 883.8 kg/m^2 s) on boiling curves (in terms of heat flux versus temperature) with T_{in}=20°C. It is shown that (i) at high degree of subcooling of 80°C, MEB occurred at mass fluxes from 294.6 kg/m^2 s to 883.8 kg/m^2 s at sufficiently high heat flux; (ii) a higher heat flux was required to

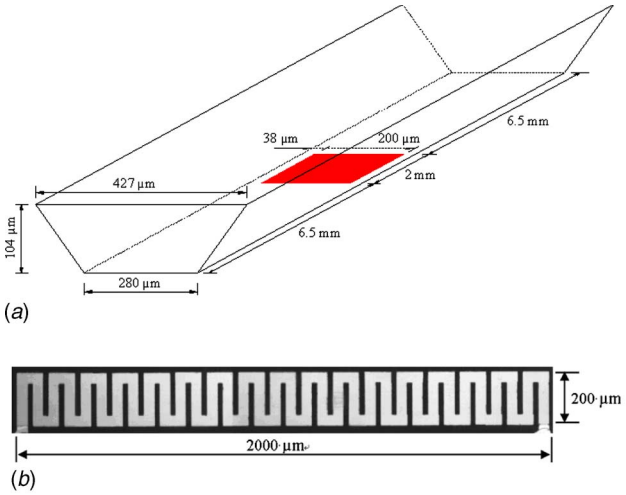

Fig. 16 A microchannel integrated with a serpentine microheater [28]

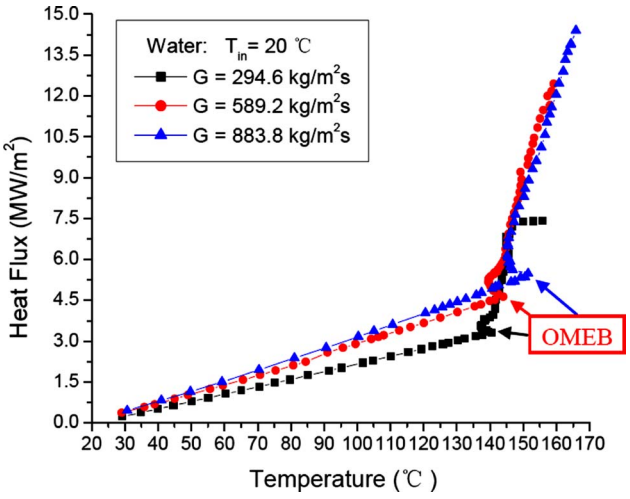

Fig. 17 Effects of mass flux on subcooled flow boiling of water in a single microchannel (D_h=155 μm) with T_{in}=20°C [28]

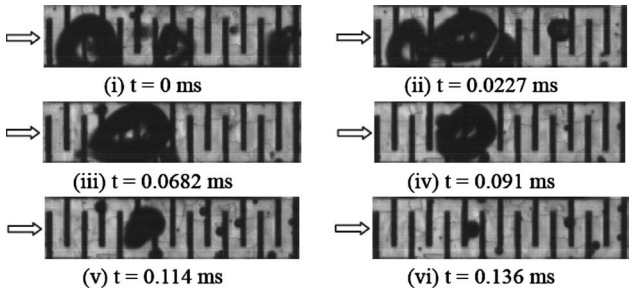

Fig. 18 Photos of bubble behavior in a single microchannel (D_h=155 μm) in fully developed MEB of water at q =6.21 MW/m^2, G=294.6 kg/m^2 s, and T_{in}=20°C [28]

initiate the onset of microbubble emission boiling (OMEB) at higher mass flux; (iii) the superheat of the microheater in OMEB was larger at a higher mass flux; (iv) the mass flux had little effects on the boiling curves in the fully developed MEB regime; and (v) the maximum heat flux without burnout increased as the mass flux increased. For example, the maximum heat flux was 7.3 MW/m^2 at G=294.6 kg/m^2 s, while a heat flux as high as 14.41 MW/m^2 at G=883.8 kg/m^2 s was observed without reaching the critical heat flux. Figure 18 are the photos showing fully developed MEB occurred on the microheater at q =6.21 MW/m^2 with G=294.6 kg/m^2 s and T_{in}=20°C. It can be seen that three bubbles formed into a large bubble as a result of coalesce in 0.0682 ms on the microheater. Due to the condensation and instability of bubble interface between vapor and subcooled water, many micobubbles were emitted during the collapse of the bubble.

3 Recent Work on Condensation in Microchannels

Early work by Wu and Cheng [13] found that mist flow, annular flow, injection flow, and slug/plug flow (confined bubbles) and bubbly flow (isolated bubbles) existed in condensing flow of steam in microchannels. Recently, Quan et al. [29–31] conducted a series of experiments on condensation of steam in microchannels (60 mm long and trapezoidal cross sections) to study flow patterns, pressure drop, and heat transfer in microchannels. A heater was added in the experimental loop before the inlet of the microchannel to ensure that no water droplet was formed and entered into the microchannel periodically, causing temperature fluctuations as in the previous condensation experiment by Wu and Cheng [13]. Parallel microchannels were used in order to reduce the errors of estimating condensation heat transfer to the fluid, while single channel was used for the determination of the occurrence frequency of injection flow to avoid flow interaction from neighboring channels.

The fluid flow and heat transfer characteristics in condensation in microchannels depend on the mass flux G and the condensation heat transfer Q, and the latter can be expressed in dimensionless form in terms of the condensation number, Co, which is defined as

$$\mathrm{Co} = \frac{Q}{m_v h_{fg}} = \frac{Q}{GAh_{fg}} \tag{5}$$

where m_v is the mass flow rate of steam, h_{fg} is the latent heat of vapor, and A is the cross-sectional area of the microchannel. Thus, Co is a measure of effectiveness of condensation process: The higher is the Co, the larger is the cooling rate. If steam is completely condensed at the exit, Q can be calculated from

$$Q = m_v(h_{vi} - h_{vo}) \tag{6a}$$

where h_{vi} and h_{vo} are the inlet enthalpy of steam and the outlet enthalpy of condensate, respectively. If the stream is not completely condensed at the exit, then the following expression can be used to calculate Q:

$$Q = m_c c_p(T_{co} - T_{cin}) + Q_{env} \tag{6b}$$

where Q_{env} is heat transfer to the environment, m_c is the mass flow rate of cooling water, c_p is the specific heat of cooling water, and (T_{co}-T_{cin}) is the temperature difference of the inlet and outlet of cooling water.

3.1 Condensation Flow Regimes. Wang et al. [49] studied experimentally the flow regimes for condensation of R134a in parallel aluminum minichannels of 1.46 mm hydraulic diameter. Figure 19(a) is their experimental results showing the mist flow, annular flow, and wavy/slug flow in condensation flow in microchannels, which is similar in trend to the boiling flow pattern map of R134a in a microchannel, as shown in Fig. 6. The data obtained by Quan and Cheng [31] for transition from annular to slug/bubbly flow for steam condensing in parallel microchannels having a hydraulic diameter of 151 μm are also presented in Fig. 19(b). It can be seen that the quality (x) at the transition point is higher at the lower value of mass flux (G), meaning that the size of intermittent regime increases with the decrease in mass flux (G) in a given microchannel. The dashed line in the figure represents the correlation given by Garimella et al. [50] for transition from annular to slug/bubbly flow in condensation of R134a in minitubes with $0.424 < D_h < 0.839$ mm, and $150 < G < 750$ kg/m^2 s which is given by

$$x \le \frac{a}{G + b} \tag{7}$$

where a=69.5763+22.595 exp(0.2586D_h) and b=−59.9899 +176.8137 exp(0.3826D_h).

It is rather surprising to see that the data obtained by Quan and Cheng [31] for condensation of steam in a trapezoidal microchannel is in excellent agreement with the extrapolated values predicted from Eq. (7) obtained by Garimella et al. [50] in minutes for condensation of R134a for mass flux greater than 50 kg/m^2 s.

3.1.1 Location of Transition From Annular to Plug/Slug Flow. The location at which transition between annular and slug flows took place in condensation of steam in parallel mirochannels having 136 μm in diameter was investigated [29]. Figure 20 shows the effects of mass flux of steam on the variation in the dimensionless distance Z/L (with L being the length of the microchannel and Z the location at which injection flow occurred) as a function of the condensation number, Co. Note that Z/L=0 means that the injection flow occurred at the entrance (Z=0), and the microchannel was fully occupied by plug/slug flow and single-phase liquid. On the other hand, Z/L=1 means that the injection flow occurred at the end of the microchannel (Z=L), i.e., the microchannel was fully occupied by the annular flow. It can be seen from Fig. 20 that (i) at a constant Co, Z/L increases with the increase in G, meaning that the annular flow regime in microchannels is expanded and the slug/bubbly flow regime shrank as the value of G is increased; (ii) at a constant G, Z/L increases with the decrease in the condensation number, meaning that injection flow occurs further downstream, and the annular flow regime is expanded.

3.1.2 Occurrence Frequency of Injection Flow. A single microchannel having D_h=128 μm was used to determine the occurrence frequency of injection flow. Figure 21 depicts the effects of mass flux and cooling rate of steam on the occurrence frequency of the injection flow in the microchannel. It is shown that the occurrence frequency of the injection flow increases as the steam mass flux is increased. This is because higher mass flux induced instability, leading to a higher occurrence frequency of the injection flow. At a given mass flux of steam, higher cooling rate leads to lower occurrence frequency because interfacial condensation tends to reduce the interface instability [51].

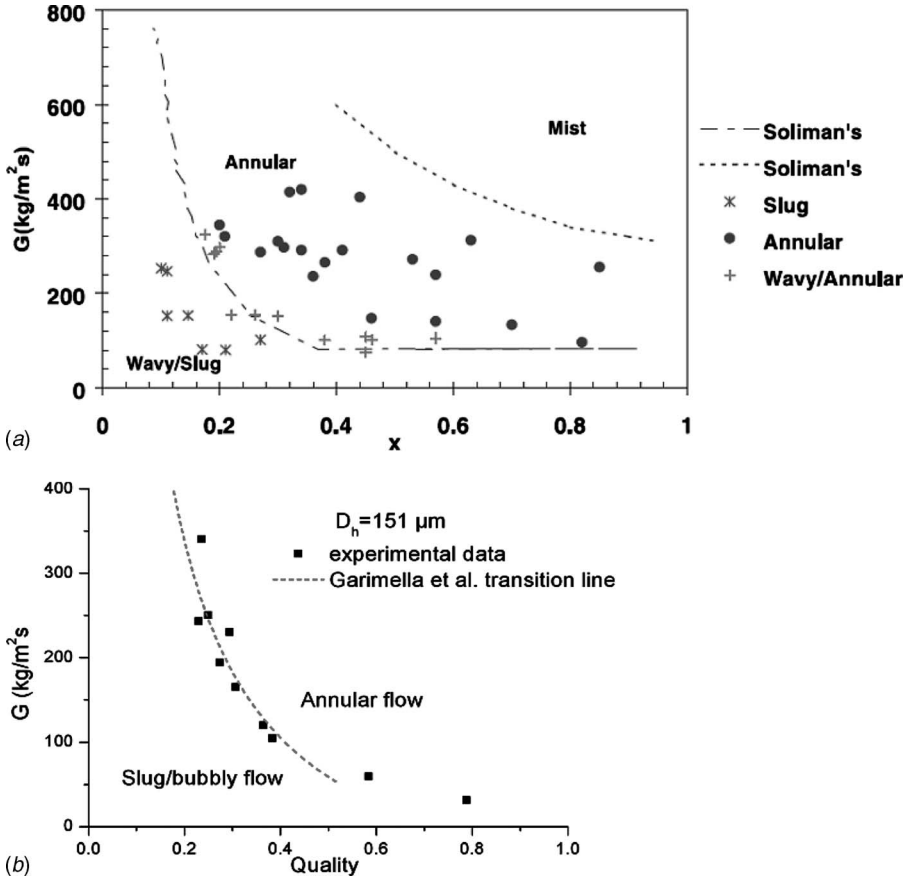

Fig. 19 Condensation flow regimes in minichannels [49] and microchannels [31]

3.2 Pressure Drop in Condensation Flow. Cavallini et al. [40] measured the condensation two-phase pressure gradient of R134a and R410A inside a multiport minichannel with a hydraulic diameter of 1.4 mm. It was found that several models available in the literature for pressure drop such as Friedel correlation [53] could predict the experimental data of R134a fairly well. However, these correlations tend to overestimate the pressure drop data of R410A. Shin et al. [52] obtained the pressure drop measurements for condensation flow of R134a in a microchannel having a hydraulic diameter of 691 μm. They found that at low mass flux ($G<200$ kg/m^2 s), the pressure drop in condensation flow in a microchannel is lower than that predicted by Friedel's correlation [53] for macrotubes. At higher mass fluxes ($G>200$ kg/m^2 s), however, the pressure drop in condensation flow in a microchannel can be predicted well by Friedel's correlation. The above two studies show that applicability of Friedel's correlation for two-phase pressure drop in microchannels depended on the type of

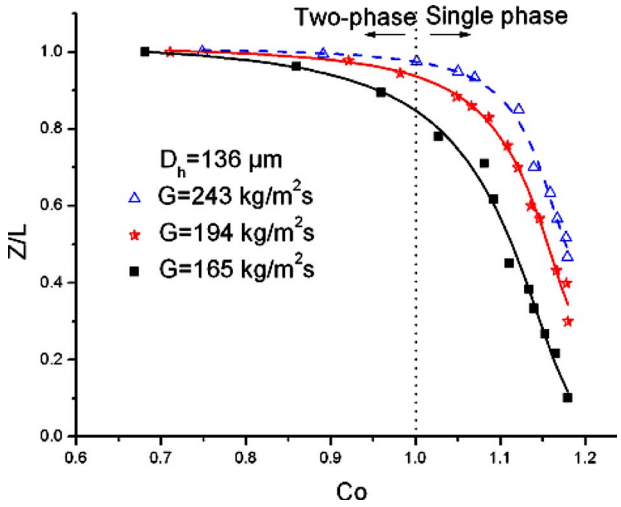

Fig. 20 Effects of mass flux of steam on location of injection flow Z/L versus Co in parallel microchannels of 136 μm in diameter [29]

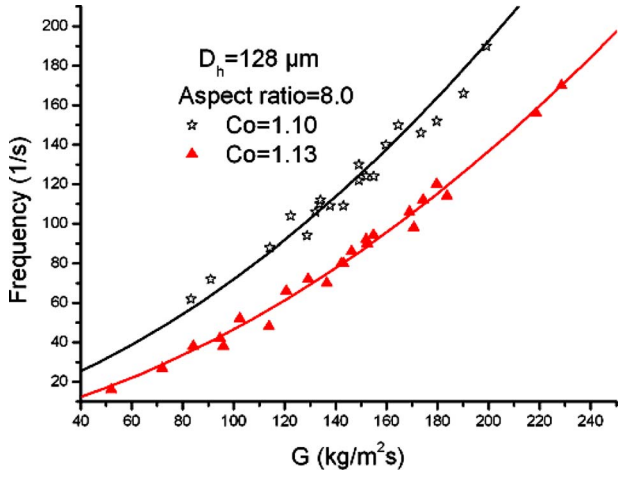

Fig. 21 Effects of steam mass fluxes on occurrence frequency of injection flow at different Co numbers in a single microchannel of 128 μm in diameter [29]

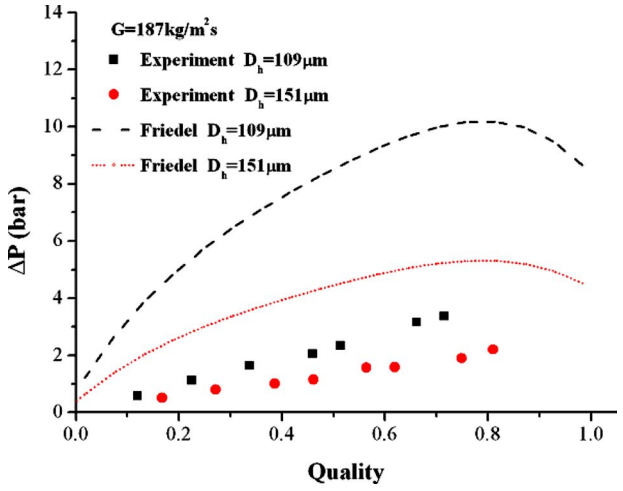

Fig. 22 Two-phase pressure drops in condensation of steam in two set of parallel microchannels of 109 μm and 151 μm in diameters [30]

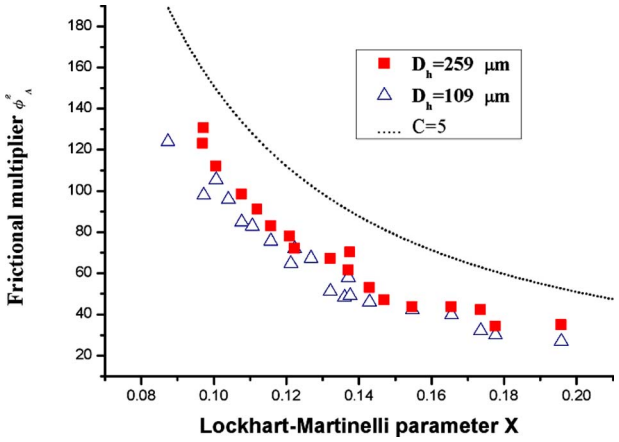

Fig. 23 Variation in Φ_L^2 versus X in two sets of parallel microchannels having 109 μm and 259 μm in diameters [30]

working fluid [40] and the magnitude of mass flux [52]. Thus, in order to predict condensation pressure drop in microchannel well, several parameters such as the channel diameter, mass flux, and properties of working fluids should be included in the correlation equation. For this reason, Hwang and Kim [32] modified the Matinelli–Chisholm constant C by including confinement number (N_{conf}) and the Reynolds number (Re) to account for the effects of surface tension and mass flux to correlate pressure drop data for condensation of R134a in microtubes. A flow-regime-based pressure drop model was developed by Nino et al. [33]. For the intermittent flow, an alternative method using average kinetic energy of two-phase mixtures was presented based on the homogenous flow model. For the annular flow regime, the two-phase multiplier was proposed as a function of the Lockhart–Martinelli parameter, the Weber number, and the liquid to vapor density ratio. It is noted that the above pressure drop correlation for two-phase flow cannot be reduced to single phase at limiting vapor qualities of 0 and 1, respectively.

Recently, Quan et al. [30] carried out an experiment on two-phase pressure drop of steam condensing inside smooth trapezoidal silicon microchannels with D_h=109, 142, 151, 259 μm, respectively. The condensation pressure drop data of steam in two set of parallel microchannels with D_h=109 and 151 μm are presented in Fig. 22, which shows that the pressure drop is smaller for the microchannel with a larger diameter. Friedel's correlation [53] for adiabatic two-phase pressure drops computed for D_h =109 and 151 μm are plotted as dashed lines and a dotted line in the same graph for comparison purposes. It is shown that Friedel's correlation for two-phase flow in macrochannels overestimates the condensation pressure drop in the microchannels. The two-phase frictional multiplier Φ_L^2 versus the Martinelli parameter X (the pressure drop ratio of the liquid phase to vapor phase), determined from their experimental data, is presented in Fig. 23, which shows that frictional multiplier is smaller in a microchannel with smaller diameter. The values of the two-phase frictional multiplier predicted by the Lockhart–Martinelli correlation with C =5 (the smallest value of C for macrochannels) are plotted as dotted lines in Fig. 23. It is shown that the values of Φ_L^2 computed based on the pressure drop data in microchannels are below the baseline of C=5. The pressure drop data in the microchannels were used to correlate the modified Matinelli–Chisholm constant C to give $C=0.168\ \text{Bo}^{0.265}\ R_{\text{Lo}}^{0.337}\ \text{Su}^{-0.041}$, where Bo is the Bond number; Re_{Lo} is the Reynolds number based on the liquid only, and $\text{Su}=\mu_\ell^2/(\rho_\ell D_h \sigma)$ is the Suratman number.

3.3 Heat Transfer in Condensation Flow. Recently, a great deal of theoretical [34,35,54] and experimental work [36–38] has been devoted to study the effects of cross-sectional shape on condensation heat transfer in microchannels. Wang and Rose [34] developed an analytical solution for annular condensation in microchannels of square and triangular cross sections, taking into account of surface tension, shear force and gravity in the condensation process. Their numerical results showed that surface tension effect is important at upstream, whereas it is relatively unimportant downstream because the channel is flooded there [34]. The heat transfer enhancement in the upstream of the microchannels is explained by the surface-tension-generated transverse pressure gradient in the condensate film. The effects of cross-sectional shape on the local heat transfer coefficients is analyzed for condensation of R134a at G=500 kg/m^2 s in minichannels having different cross-sectional shapes [35]. The numerical results showed that the film along the sides of the noncircular channel becomes thinner compared with those in a circular channel due to the condensate flowing toward the corners. Figure 24 shows the effects of cross-sectional shapes of the microchannels on the variation in circumferential mean condensation heat transfer coefficients along the distance in microchannels [35]. It is shown that the circumferential mean condensation heat transfer coefficients of noncircular channels are higher than those of the circular channels at the upstream of the channels because of the thinning of the liquid film. This also leads to an increased condensate loading along the noncircular channels, meaning that the liquid film is thicker along the wall of noncircular minichannel than that of the

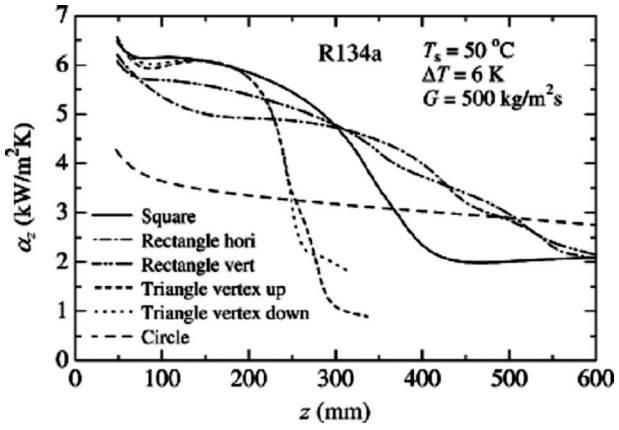

Fig. 24 Variation in mean heat transfer coefficients along the microchannels with different cross-sectional geometry [35]

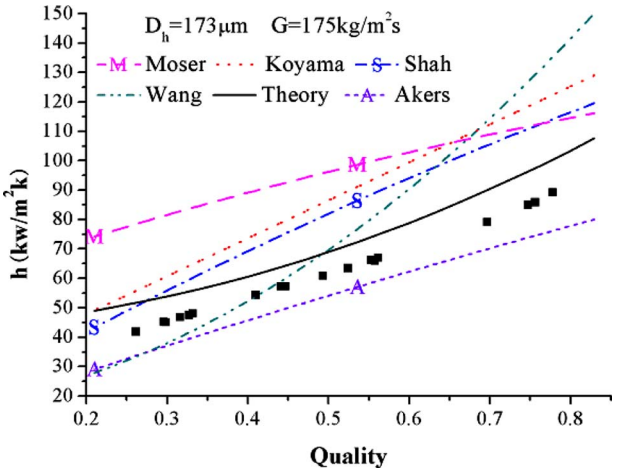

Fig. 25 Heat transfer coefficient for annular flow of steam condensing in single microchannel of 173 μm in diameter [31]

circular minichannel downstream. For this reason, the annular condensation heat transfer coefficient of a noncircular minichannel is lower than that of a circular minichannel at the same location downstream. This suggests that length-averaged condensation heat transfer coefficient of a noncircular microchannel may be higher or lower than that of a circular microchannel with the same hydraulic diameter, depending not only on mass flux but also on the length of the microchannel.

Shin and Kim [36] performed an experiment to investigate effects of cross-sectional shape on the average heat transfer coefficient of condensing flow of R134a in multiport extruded aluminum minichannels, having a diameter of less than 1 mm with an effective length of 171 mm. They found that heat transfer coefficients had a greater dependency on mass flux and quality in the circular microchannels than those in rectangular microchannels. Their experimental data also show that the average-over-length condensation heat transfer coefficient in a rectangular microchannel is higher than that in a circular microchannel (having the same hydraulic diameter) at low mass flux, but the reverse was true at higher mass flux. However, no satisfactory reasons were given to explain these trends.

Bandhauer et al. [37] measured the condensation heat transfer coefficients of R134a in circular microchannels by developing a novel thermal amplification technique. They noted that the available shear-driven models led to poor predictions because of the inadequate calculation of shear stresses using pressure drop models that were not applicable to microchannels. A heat transfer model for annular flow was developed based on the boundary layer analyses, using the pressure drop correlation for microchannels to calculate the shear force. They pointed out that the heat transfer model based on annular flow mechanism appears to be applicable to the mist and mist-annular overlap regions in the high mass flux and high quality case. Subsequently, Agarwal et al. [38] measured the condensation of refrigerant R134a in six horizontal noncircular microchannels ($0.424 < D_h < 0.839$ mm) of different shapes in the mass flux range of $150 < G < 750$ kg/m^2 s. They found that the modified version of the above annular flow heat transfer model for circular microchannels was also suitable for noncircular microchannels, with the corresponding shear stress obtained from the noncircular microchannel pressure drop model. The heat transfer coefficients were found to be highest for the rectangular channel, followed by the square and circular channels (having the same cross-sectional area).

Quan and Cheng [31] measured the condensation heat transfer coefficient of steam in a single microchannel of 173 μm in diameter with integrated Pt temperature sensors fabricated on the bottom wall. Figure 25 is a comparison of their heat transfer coefficient data for annular condensation flow in microchannels with existing correlations for condensation in macro- and minichannels [49,55–58]. The data show that the condensation heat transfer coefficient in microchannels increases with the vapor quality, which is in agreement with the existing correlations. It can be seen that the two-phase multiplier approaches for predicting condensation heat transfer of annular flow given by Moser et al. [55], Shah [57] for macrochannels, and Koyama et al. [56] and Wang et al. [49] for minichannels overestimate the heat transfer coefficient data in microchannels. This is because the existing condensation heat transfer correlations used condensation pressure drop correlations for macrochannels, which overestimate the condensation pressure drop data in microchannels. On the other hand, the correlation by Akers et al. [58], based on the homogenous model, underestimates the condensation heat transfer coefficient in microchannels probably because the value of viscosity computed from their viscosity model was too high, leading to a low value of "equivalent Reynolds number." The solid line in Fig. 25 represents the analytical solution obtained by Quan and Cheng [31] for condensation heat transfer versus vapor quality in microchannels. This analytical solution was based on the boundary layer approach and using the pressure drop [30] and void fraction correlations [39] for microchannel flows. It is shown that the analytical solution is in satisfactory agreement with the experimental data. This analytical solution indirectly accounts for surface tension through the pressure drop correlation for the shear stress calculation to yield accurate heat transfer predictions for the annular condensing flow in microchannels.

4 Concluding Remarks

Recent work on boiling and condensation heat transfer in microchannels since 2004 has been reviewed in this paper. The following conclusions can be drawn from the recent work.

For flow boiling in microchannels:

1. Upstream compressible volume has been identified as the sources of flow-boiling instability in microchannels. The amount of upstream compressible volume depends on the experimental setup (such as the configuration/materials used for inlet/outlet connections and the apparatus for driving the fluid such as a pump or a pressurized tank). However, it is not clear how to quantify the amount of upstream compressible volume for an experimental setup.
2. Stable flow boiling exists at low exit vapor quality of the microchannels where bubbly and bubbly/slug flows exist. The fabrication of inlet restriction or the installation of throttling valves at upstream of the test section can suppress flow-boiling instability so that stable flow-boiling conditions can be achieved at high exit vapor quality.
3. Nucleate boiling predominates near the outset of nucleation at upstream of the microchannels while annular two-phase flow prevails at downstream.
4. The local boiling heat transfer coefficient peaks in the bubbly flow regimes at low vapor quality in microchannels, whereas the local boiling heat transfer peaks at high vapor quality in macrochannels. This is because confined bubble occurs earlier in flow boiling in channels with a smaller diameter.
5. Existing correlations of local boiling heat transfer coefficient in minichannels overestimate local boiling heat transfer coefficient in microchannels because of suppression of bubble nucleation by elongated bubbles at low vapor quality and local dryout phenomenon at high vapor quality.
6. MEB occurs in partially heated microchannels at sufficiently high heat flux and high inlet subcooling conditions. The occurrence of MEB carries away a large amount of heat and delays the appearance of the critical heat flux.

For flow condensation in microchannels:

1. Injection flow is a transition from annular flow to slug/bubbly flow in condensation flow in microchannels, owing to liquid/vapor interface instability.
2. The location at which injection flow occurs depending on the mass flux of steam, the condensation heat flux, and the vapor quality.
3. The annular flow regime in microchannel will be expanded and slug/bubbly flow regime will be shrunk with decreasing condensation heat flux or increasing mass flux.
4. The occurrence frequency of the injection flow increases with the increase in mass flux, the decrease in condensation heat flux, or the decrease in microchannel diameter.
5. Correlations for pressure drop and heat transfer coefficient of condensation flow in macro- and minichannels overestimate the pressure drop and heat transfer of condensation flow in microchannels.
6. Theoretical investigations on flow condensation in microchannels confirm that surface tension effects are more important at upstream of the microchannels in which annular flow pattern prevails, and the surface tension effect is less important downstream where the microchannel is flooded and isolated bubbles appear. The heat transfer coefficient of *annular* condensation flow in a noncircular microchannel is higher than that of a circular microchannel with the same hydraulic diameter because of the thinning of the liquid film owing to the surface tension effect.

Acknowledgment

This work was supported by the National Natural Science Foundation of China through Grant No. 50536010.

Nomenclature

A = total cross section area of channel (m^2)
A_c = cross-sectional flow area of each microchannel (m^2)
A_w = area of microchannel bottom wall and side walls of each channel (m^2)
Bo = boiling number
C = Matinelli–Chisholm constant
Co = condensation number
D_h = hydraulic diameter (m)
f = frequency
G = mass flux (kg/m^2 s)
H = gap between bottom and top of channel (m)
h_e = exit fluid enthalpy (J/kg)
h_{in} = inlet fluid enthalpy (J/kg)
h_f = saturated liquid enthalpy (J/kg)
h_{fg} = latent heat of evaporation (J/kg)
L = total length of channel (m)
m = mass flow rate (kg/m)
N = total number of microchannels
N_{conf} = confinement number
Q = heat transfer rate (W)
q = heat flux (W/m^2)
q_c = critical heat flux (W/m^2)
ΔP = pressure drop (bar)
Re = Reynolds number
Su = Suratman number
t = time (s)
T = temperature (°C)
W_b = bottom width of channel (m)
We = Weber number
W_t = top width of channel (m)
W_t/H = aspect ratio
x = vapor quality
x_e = vapor quality near exit
Z = transition location

Greek Symbols

ρ = density (kg/m^3)
μ = viscosity (N s/m^2)
σ = surface tension (N/m)
ϕ_L^2 = two-phase frictional multiplier

Subscripts

b = bottom of microchannel substrate
c = cooling water
e = expansion
h = heating
in = inlet
l = liquid
out = outlet
w = wall
v = vapor

References

[1] Cheng, P., and Wu, H. Y., 2006, "Mesoscale and Microscale Phase-Change Heat Transfer," Adv. Heat Transfer, **39**, pp. 461–563.
[2] Kandlikar, S. G., 2002, "Fundamental Issues Related to Flow Boiling in Minichannels and Microchannels," Exp. Therm. Fluid Sci., **26**, pp. 389–407.
[3] Thome, J. R., 2004, "Boiling in Microchannels: A Review of Experiment and Theory," Int. J. Heat Fluid Flow, **25**, pp. 128–139.
[4] Cheng, P., Wu, H. Y., and Hong, F. J., 2007, "Phase-Change Heat Transfer in Microsystems," ASME J. Heat Transfer, **129**, pp. 101–107.
[5] Kandlikar, S. G., Steinke, M. E., Tian, S., and Campbell, L. A., 2001, "High Speed Photographic Observation of Flow Boiling of Water in Parallel Minichannels," ASME National Heat Transfer Conference, Los Angeles, CA, Jun. 10–12.
[6] Brutin, D., Topin, F., and Tadrist, L., 2003, "Experimental Study of Unsteady Convective Boiling in Heated Minichannels," Int. J. Heat Mass Transfer, **46**, pp. 2957–2965.
[7] Wu, H. Y., and Cheng, P., 2003, "Visualization and Measurements of Periodic Boiling in Silicon Microchannels," Int. J. Heat Mass Transfer, **46**, pp. 2603–2614.
[8] Wu, H. Y., and Cheng, P., 2004, "Boiling Instability in Parallel Silicon Microchannels at Different Heat flux," Int. J. Heat Mass Transfer, **47**, pp. 3631–3641.
[9] Qu, W. L., and Mudawar, I., 2003, "Measurement and Prediction of Pressure Drop in Two-Phase Micro-Channel Heat Sinks," Int. J. Heat Mass Transfer, **46**, pp. 2737–2753.
[10] Jacobi, A. M., and Thome, J. R., 2002, "Heat Transfer Model for Evaporation of Elongated Bubble Flow in Microchannels," ASME J. Heat Transfer, **124**(6), pp. 1131–1136.
[11] Qu, W. L., and Mudawar, I., 2003, "Flow Boiling Heat Transfer in Two-Phase Micro-Channel Heat Sinks—II. Annular to-Phase Flow Model," Int. J. Heat Mass Transfer, **46**(15), pp. 2773–2784.
[12] Chen, Y. P., and Cheng, P., 2005, "Condensation of Steam in a Silicon Microchannels," Int. Commun. Heat Mass Transfer, **32**, pp. 175–183.
[13] Wu, H. Y., and Cheng, P., 2005, "Condensation Flow Patterns in Silicon Microchannels," Int. J. Heat Mass Transfer, **48**, pp. 2186–2197.
[14] Wang, G. D., Cheng, P., and Wu, H. Y., 2007, "Unstable and Stable Flow Boiling in Parallel Microchannels and in a Single Microchannel," Int. J. Heat Mass Transfer, **50**, pp. 4297–4310.
[15] Wang, G. D., Cheng, P., and Bergles, A. E., 2008, "Effects of Inlet/Outlet Configurations on Flow Boiling Instability in Parallel Microchannels," Int. J. Heat Mass Transfer, **51**, pp. 2267–2281.
[16] Hetsroni, G., Mosyak, A., Pogrebnyak, E., and Segal, Z., 2005, "Explosive Boiling of Water in Parallel Micro-Channels," Int. J. Multiphase Flow, **31**, pp. 371–392.
[17] Kandlikar, S. G., Willistern, D. A., and Borrelli, J., 2005 "Experimental Evaluation of Pressure Drop Elements and Fabricated Nucleation Sites for Stabilizing Flow Boiling in Minichannels and Microchannels," ASME Paper No. ICMM2005–75197.
[18] Kosar, A., Kuo, C. J., and Peles, Y., 2006, "Suppression of Boiling Flow Oscillations in Parallel Microchannels by Inlet Restrictors," ASME J. Heat Transfer, **128**, pp. 251–260.
[19] Sobierska, E., Kulenovic, R., and Mertz, R., 2007, "Heat Transfer Mechanism and Flow Pattern During Flow Boiling of Water in a Vertical Narrow Channel—Experimental Results," Int. J. Therm. Sci., **46**, pp. 1172–1181.
[20] Agostini B., Thome J. R., Fabbri M., Michel B., Calmi D., Kloter U., 2008, "High Heat Flux Flow Boiling in Silicon Multi-Microchannels—Part I: Heat Transfer Characteristics of Refrigerant R236fa," Int. J. Heat Mass Transfer, **51**, pp. 5400–5414.
[21] Agostini B., Thome J. R., Fabbri M., Michel B., Calmi D., Kloter U., 2008, "High Heat Flux Flow Boiling in Silicon Multi-Microchannels–Part II: Heat Transfer Characteristics of Refrigerant R245fa," Int. J. Heat Mass Transfer, **51**, pp. 5415–5425.

[22] Harirchian, T., and Garimella, S. V., 2008, "Microchannel Size Effects on Local Flow Boiling Heat Transfer to a Dielectric Fluid," Int. J. Heat Mass Transfer, **51**, pp. 3724–3735.
[23] Bertsch, S. S., Groll, E. A., and Garimella, S. V., 2008, "Refrigerant Flow Boiling Heat Transfer in Parallel Microchannels as a Function of Local Vapor Quality," Int. J. Heat Mass Transfer, **51**, pp. 4775–4787.
[24] Thome, J. R., Dupont, V., and Jacobi, A. M., 2004, "Heat Transfer Model for Evaporation in Microchannels. Part I: Presentation of the Model," Int. J. Heat Mass Transfer, **47**(14–16), pp. 3375–3385.
[25] Dupont, V., Thome, J. R., and Jacobi, A. M., 2004, "Heat Transfer Model for Evaporation in Microchannels. Part II: Comparison With the Database," Int. J. Heat Mass Transfer, **47**(14–16), pp. 3387–3401.
[26] Revellin, R., and Thome, J. R., 2007, "A New Type of Diabatic Flow Pattern Map for Boiling Heat Transfer in Microchannels," J. Micromech. Microeng., **17**(4), pp. 788–796.
[27] Wojtan, L., Revellin, R., and Thome, J. R., 2006, "Investigation of Saturated Critical Heat Flux in a Single, Uniformly Heated Microchannel," Exp. Therm. Fluid Sci., **30**, pp. 765–774.
[28] Wang, G. D., and Cheng, P., 2009, "Subcooled Flow Boiling and Microbubble Emission Boiling Phenomena in a Partially Heated Microchannel," Int. J. Heat Mass Transfer, **52**, pp. 79–91.
[29] Quan, X. J., Cheng, P., and Wu, H. Y., 2008, "Transition from Annular Flow to Plug/Slug Flow in Condensation of Steam in Microchannels," Int. J. Heat Mass Transfer, **51**(3–4), pp. 707–716.
[30] Quan, X. J., Cheng, P., 2008, "An Experimental Investigation on Pressure Drop of Steam Condensing in Silicon Microchannels," Int. J. Heat Mass Transfer, **52**, pp. 54–58.
[31] Quan, X. J., Cheng, P., 2008, "Condensation Heat Transfer Coefficients in Trapezoidal Silicon Microchannels," unpublished.
[32] Hwang, Y. W., and Kim, M. S., 2006, "The Pressure Drop in Microtubes and the Correlation Development," Int. J. Heat Mass Transfer, **49**, pp. 1804–1812.
[33] Nino, V. G., and Jassim, E. W., 2006, "Flow-Regime-Based Model for Pressure Drop Predictions in Microchannels," HVAC&R Res., **12**(1), pp. 17–33.
[34] Wang, H. S., and Rose, J. W., 2005, "A Theory of Film Condensation in Horizontal Noncircular Section Microchannels," ASME J. Heat Transfer, **127**, pp. 1096–1105.
[35] Wang, H. S., and Rose, J. W., 2006, "Film Condensation in Horizontal Microchannels: Effect of Channel Shape," Int. J. Therm. Sci., **45**, pp. 1205–1212.
[36] Shin, J. S., and Kim, M. H., 2005, "An Experimental Study of Flow Condensation Heat Transfer Inside Circular and Rectangular Mini-Channels," Heat Transfer Eng., **26**(3), pp. 36–44.
[37] Bandhauer, T. M., Agarwal, A., and Garimella, S., 2006, "Measurement and Modeling of Condensation Heat Transfer Coefficients in Circular Microchannels," ASME J. Heat Transfer, **128**(10), pp. 1050–1059.
[38] Agarwal, A., Bandhauer, T. A., and Garimella, S., 2007, "Heat Transfer Model for Condensation in Non-Circular Microchannels," ASME Paper No. ICNMM2007-30223.
[39] Jassim, E. W., and Newell, T. A., 2006, "Prediction of Two-Phase Pressure Drop and Void Fraction in Microchannels Using Probabilistic Flow Regime Mapping," Int. J. Heat Mass Transfer, **49**, pp. 2446–2457.
[40] Cavallini, A., Del Col, D., Doretti, L., Matkovic, M., Rossetto, L., and Zilio, C., 2005, "Condensation Heat Transfer and Pressure Gradient Inside Multiport Minichannels," Heat Transfer Eng., **26**(3), pp. 45–55.
[41] Mishima, K., and Hibiki, T., 1996, "Some Characteristics of Air-Water Two-Phase Flow in Small Diameter Vertical Tubes," Int. J. Multiphase Flow, **22**(4), pp. 703–712.
[42] Kandlikar, S. G., 1990, "A General Correlation for Saturated Two-Phase Boiling Heat Transfer Inside Horizontal and Vertical Tubes," ASME J. Heat Transfer, **112**(1), pp. 219–228.
[43] Wojtan, L., Ursenbacher, T. U., and Thome, J. R., 2005, "Investigation of Flow Boiling in Horizontal Tubes: Part II—Development of a New Heat Transfer Model for Stratified-Wavy, Dryout and Mist Flow Regimes," Int. J. Heat Mass Transfer, **48**, pp. 2970–2985.
[44] Agostini, B., 2002, "Etude expérimentale de l'ébullition de fluide refrigerant en convection force dans des mini-canaux," Ph.D. thesis, Université Joseph Fourier, Grenoble.
[45] Inada, S., Miyasaka, Y., Izumi, Y., and Owase, Y., 1981, "Study on Subcooled Pool Boiling: 1st Rep. Effect of Liquid Subcooling on Local Heat Transfer Characteristics," Transaction of JSME, **47**, pp. 852–861.
[46] Shoji, M., and Yoshihara, M., 1991, "Burnout Heat Flux of Water on a Thin Wire," *Proceedings of 28th National Heat Transfer Symposium of Japan*, Vol. 27, pp. 121–123.
[47] Suzuki, K., and Kawada, R., 2004, "On Subcooled Flow Boiling With Microbubble Emission in a Horizontal Circular Channel," The First International Symposium on Micro & Nano Technology, Honolulu, HI, Mar. 14–17.
[48] Suzuki, K., Kokubu, T., Nakano, M., Kawamura, H., Ueno, I., Shida, H., and Ogawa, O., 2005, "Enchancement of Heat Transfer in Subcooled Flow Boiling With Microbubble Emission," Exp. Therm. Fluid Sci., **29**, pp. 827–832.
[49] Wang, W. W. W., Radcliff, T. D., and Christensen, R. N., 2002, "A Condensation Heat Transfer Correlation for Millimeter-Scale Tubing With Flow Regime Transition," Exp. Therm. Fluid Sci., **26**, pp. 473–485.
[50] Garimella, S., Killion, J. D., and Coleman, J. W., 2002, "An Experimentally Validated Model for Two-Phase Pressure Drop in the Intermittent Flow Regime for Circular Microchannels," ASME J. Fluids Eng., **124**, pp. 205–213.
[51] Chan, S. H., Wang, Y. S., and Tan, C. C., 1994, "The Effect of Mass Transfer on Kelvin–Helmholtz Instability at the Gas-Liquid Interface of a Sonic Reacting and Non-Reacting Gas Jet Submerged in a Liquid," Int. J. Heat Mass Transfer, **37**, pp. 1123–1132.
[52] Shin, J. S., and Kim, M. H., 2004, "An Experimental Study of Condensation Heat Transfer Inside a Mini-Channel With a New Measurement Technique," Int. J. Multiphase Flow, **30**, pp. 311–325.
[53] Friedel, L., 1979, "Improved Friction Pressure Drop Correlation for Horizontal and Vertical Two-Phase Pipe Flow," European Two-Phase Flow Group Meeting, Ispra, Italy, Paper No. 2.
[54] Zhao, T. S., and Liao, Q., 2002, "Theoretical Analysis of Film Condensation Heat Transfer Inside Vertical Mini Triangular Channels," Int. J. Heat Mass Transfer, **45**, pp. 2829–284.
[55] Moser, K. W., Webb, R. L., and Na, B., 1998, "A New Equivalent Reynolds Number Model for Condensation in Smooth Tubes," ASME J. Heat Transfer, **120**(2), pp. 410–417.
[56] Koyama, S., Kuwahara, K., Nakashita, K., and Yamamoto, K., 2003, "An Experiment Study on Condensation of Refrigerant R134a in a Multi-Port Extruded Tube," Int. J. Refrig., **26**(4), pp. 425–432.
[57] Shah, M. M., 1979, "A General Correlation for Heat Transfer During Film Condensation in Tubes," Int. J. Heat Mass Transfer, **22**(4), pp. 547–556.
[58] Akers, W. W., Deans, H. A., and Crosser, O. K., 1959, "Condensation Heat Transfer Within Horizontal Tubes," Chem. Eng. Prog., Symp. Ser., **55**(29), pp. 171–176.

Solution of Thermally Developing Zone in Short Micro-/Nanoscale Channels

Masoud Darbandi[1]
Professor
e-mail: darbandi@sharif.edu

Shidvash Vakilipour
Ph.D.
Research Fellow
e-mail: svakilipour@alum.sharif.edu

Department of Aerospace Engineering,
Sharif University of Technology,
P. O. Box 11365-8639, Tehran, Iran

We numerically solve the Navier–Stokes equations to study the rarefied gas flow in short micro- and nanoscale channels. The inlet boundary conditions play a critical role in the structure of flow in short channels. Contrary to the classical inlet boundary conditions, which apply uniform velocity and temperature profiles right at the real channel inlet, we apply the same inlet boundary conditions, but at a fictitious position far upstream of the real channel inlet. A constant wall temperature incorporated with suitable temperature jump is applied at the channel walls. Our solutions for both the classical and extended inlet boundary conditions are compared with the results of other available Navier–Stokes and lattice Boltzmann solvers. It is shown that the current extended inlet boundary conditions can effectively improve the thermofluid flow solutions in short micro- and nanoscale channels. [DOI: 10.1115/1.3072908]

Keywords: microscale flow, nanoscale flow, inlet boundary conditions, slip velocity, temperature jump, heat transfer

1 Introduction

Demand in design and fabrication of micro-/nanoelectromechanical systems (MEMS/NEMS) has promoted the researchers to work on better understanding of flow and heat behaviors in micro- and nanoscales. Many numerical efforts have been devoted to predict the fluid flow and heat transfer in long micro- and nanochannels. Contrary to long channels, the developing zones in short channels play a critical role in calculating important flow and heat parameters such as the mean friction factor and the Nusselt number. However, the boundary conditions imposed around a channel effectively affect the magnitudes of such parameters. Among them, the solid wall and inlet boundary conditions seem to be the most sensitive ones and need to be applied correctly. In this work, we mainly focus on improving these boundary condition implementations.

Kavehpour et al. [1] utilized a control volume method to solve flow in a long microchannel. They specified a uniform axial velocity and a zero transverse velocity at the inlet section. Their velocity profiles showed overshoots in the region close to the inlet section. Guo and Wu [2] also carried out numerical studies in a microtube with large L/D ratio and specified a fully developed no-slip profile at the inlet. Beskok and Karniadakis [3,4] simulated flow and heat in a microchannel with $L/H=8$ using a spectral element approach. They applied inlet boundary conditions right at the channel inlet using a uniform velocity profile. They also reported overshoots in the velocity profiles close to the channel inlet. Asako and Toriyama [5] used the arbitrary-Lagrangian–Eulerian method and numerically solved flow in microchannels with $L/H \geq 100$. They started their computations assuming uniform inlet velocity, while the inlet pressure was extrapolated from the interior of computational domain. They corrected the inlet velocity using an expression for stagnation pressure in terms of the inlet pressure, velocity, and specific internal energy variables. Gamrat et al. [6] performed a numerical study to evaluate the entrance effect on flow and heat behaviors in microchannels with $L/H=82$, 273, and 820 using two types of inlet boundary conditions. First, they considered a uniform inlet condition right at the channel inlet. Second, they simulated the real inlet condition considering the complete geometry constructed in their experiment as the solution domain. They showed that the Nusselt numbers for the case with specifying uniform inlet boundary conditions right at the channel inlet were higher than those of the complete geometry simulation. Hung and Ru [7] studied heat and fluid flow in a microchannel with $L/H=5$ using the lattice Boltzmann method. They specified uniform axial velocity and temperature profiles at the channel inlet. Niu et al. [8] also used the lattice Boltzmann method to simulate flow in a channel with $L/H=20$. They applied diffuse scattering boundary conditions at the solid walls and a uniform inlet velocity at the inlet.

Past investigations in macroscale channels have shown that the numerical solution of the Navier–Stokes equations with no-slip wall boundary conditions would face with two singularities right at the solid walls. They result in two overshoots in the velocity profile beside the walls and close to the inlet region [9,10]. Darbandi and Schneider [9] presented a detailed investigation in the entrance region and quantified the overshoot magnitudes for a wide range of Reynolds numbers. Later, we studied the entrance flow problem in the inlet of microchannels using an improved hydrodynamic boundary condition [11]. The main idea was to employ the inlet condition somewhere upstream and far from the real channel inlet. We solved microflow fields and evaluated our results against available analytical solutions. In this work, we extend our work to thermally developing zones in micro- and nanoscale channels. However, to show the significance of this work, we use two types of inlet boundary conditions. The first type is consistent with the classical inlet boundary conditions, i.e., it implements uniform velocity and temperature profiles right at the real channel inlet. The second or extended inlet boundary condition permits suitable flow condition to be caught automatically at the channel inlet. In this work, the results of latter boundary conditions are compared with those of former ones and other available numerical solutions.

2 Boundary Condition Treatments

We solve the steady-state Navier–Stokes equations to simulate rarefied micro- and nanogas flows. The detail of numerical modeling is very long and it is addressed in Refs. [11–14]. In this paper, we briefly describe the ways that the required boundary conditions are applied at the channel boundaries. We first describe the solid wall boundary condition treatments. The flow regime in micro- and nanochannels can be categorized using the Knudsen number definition $\mathrm{Kn}=\lambda/H$, where λ and H are the mean-free path of gas molecules and the channel height, respectively. As the Knudsen layer thickness beside the wall increases to more than 10% of the bulk flow size, the flow regime becomes transition. As is known, the first-order slip velocity and temperature jump conditions produce erroneous results in simulating the transition regime. To avoid inaccuracies of the first-order boundary conditions, the slip velocity and temperature jump can be predicted in

[1]Corresponding author.

Contributed by the Heat Transfer Division of ASME for publication in the JOURNAL OF HEAT TRANSFER. Manuscript received March 16, 2008; final manuscript received October 19, 2008; published online February 11, 2009. Review conducted by Robert D. Tzou. Paper presented at the 2008 International Conference on Micro/Nanoscale Heat Transfer (MNHT2008), Tainan, Taiwan, January 6–9, 2008.

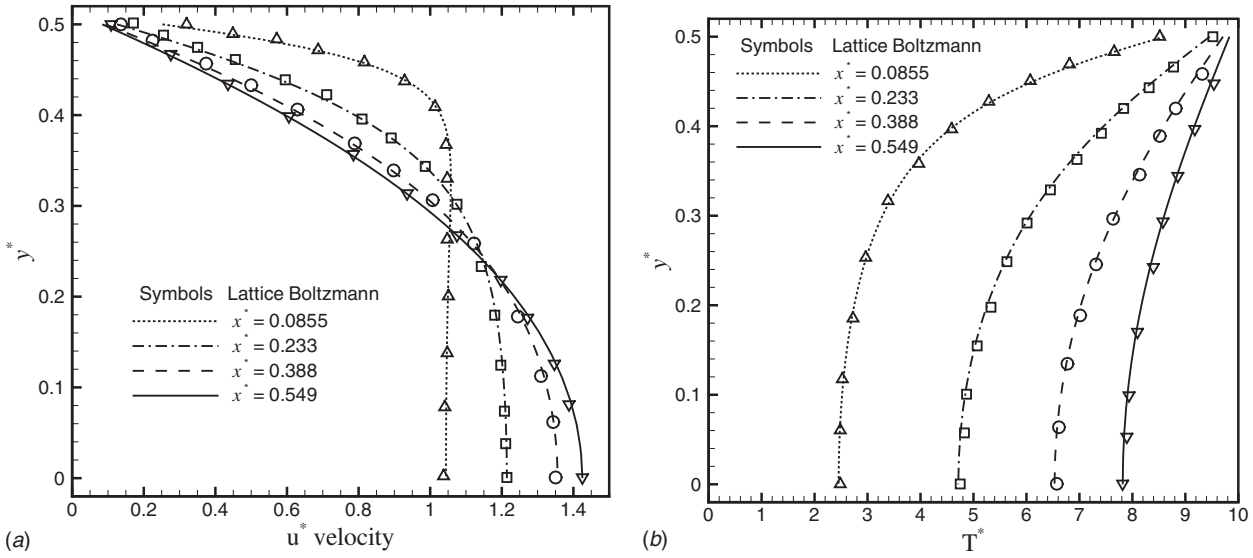

Fig. 1 The current (*a*) axial velocity and (*b*) temperature profiles at four locations in a channel and comparison with the lattice Boltzmann solutions [8], Re=0.01 and Kn=0.015

the vicinity of the solid wall based on the kinetic theory assumptions. Considering the momentum and energy flux exchanges at one mean-free path away from the solid wall, the slip velocity u_s and temperature jump T_s can be calculated from the second-order boundary conditions, which are given by [4]

$$u_s = \frac{u_\lambda + (1-\sigma_v)u_\lambda + \sigma_v u_w}{2} \tag{1}$$

$$T_s = \frac{CT_\lambda + T_w}{1+C} \tag{2}$$

where $C=[(2-\sigma_T)/\sigma_T][2\gamma/((\gamma+1)\mathrm{Pr})]$. The subscripts s, w, and λ denote the magnitudes at the boundary of slip layer, wall, and one mean-free path away from wall, respectively. The tangential momentum σ_v and energy accommodation σ_T coefficients denote the exchange ratio of momentum and energy fluxes between the wall and fluid particles. The ratio of specific heat coefficients and the Prandtl number are represented by γ and Pr, respectively.

The friction coefficient can be expressed in terms of Reynolds number and the nondimensional velocity gradient at the wall. It yields

$$C_f\ \mathrm{Re} = 2\frac{(\partial u^*/\partial y^*)_w}{u_b^*} \tag{3}$$

where $\mathrm{Re}=(\rho u_{\mathrm{in}}H)/\mu$, $u^*=u/u_{\mathrm{in}}$, and $y^*=y/H$. The subscripts in and b refer to the inlet and bulk magnitudes, respectively. Using nondimensional temperature definition $T^*=T/T_{\mathrm{in}}$, the Nusselt number, in a channel with uniform wall temperature, is calculated from

$$\mathrm{Nu} = 2\frac{(\partial T^*/\partial y^*)_w}{(T_w^* - T_b^*)} \tag{4}$$

of which the wall temperature is specified as $T_w^*=10$. It should be noted that the slip velocity boundary condition is applied via using Eq. (1), while Eq. (2) is utilized to calculate the temperature jump as the isothermal boundary condition adjacent to the solid wall.

Second, we describe the inlet boundary conditions. Following Ref. [11], there are two choices to treat the axial velocity and temperature at the inlet boundary. One choice is to locate the inlet at $x^*=x/H=0$. We refer to this location as the real inlet. Another choice is to locate the inlet at a fictitious section, which is in upstream and sufficiently far from the real inlet. For example, it is at $x^*=-5$ in the current test case. However, the influence of the implemented freestream condition is suitably transformed into the real inlet section via applying the symmetric boundary conditions at the fictitious horizontal walls extended in upstream of the real channel inlet. This is described in the following paragraph. The imposed boundary conditions at the inlets are $u_{\mathrm{in}}^*=1$, $v_{\mathrm{in}}^*=0$, and $T_{\mathrm{in}}^*=1$.

Since the geometry and boundary conditions are symmetric, we solve the flow field for one-half of the channel only. We apply $\partial u^*/\partial y^*=0$, $v^*=0$, and $\partial T^*/\partial y^*=0$ at the channel centerline. These boundary conditions are also applied on the extended walls in case of using a fictitious inlet. At the outlet, we specify a uniform pressure distribution $P=P_{\mathrm{out}}$. The current authors have already shown that their basic Navier–Stokes solver is robust enough to solve long macrochannels accurately despite applying the outlet boundary conditions at positions very close to the inlet section, where the flow is not certainly developed [15]. Therefore, we can similarly solve short micro-/nanoscale channels, where the slip flow regimes may not reach a fully developed condition at their outlets.

3 Results and Discussion

To compare our results with other solutions, we choose the test case presented in Ref. [8]. It is a short channel with $L/H=20$, $\mathrm{Re}=0.01$, and $\mathrm{Kn}=0.015$. At the first step, we specify the inlet boundary conditions at $x^*=0$. Figure 1 illustrates the axial velocity and temperature profiles at four stations in the channel. The results are compared with those of the lattice Boltzmann simulation [8]. There are excellent agreements between them. As it is seen in Fig. 1(*a*), the velocity slip is higher at lower distances from the inlet section. This is due to high normal gradients of axial velocity close to the inlet section. As was described before, the singularities located on the corners of the channel inlet cause overshoots in the velocity profiles. This phenomenon is more pronounced at higher Reynolds numbers. As is seen in this figure, the velocity profile very close to the inlet section performs slight overshoot, which is justifiable [9–11]. Moreover, the temperature profiles in Fig. 1(*b*) show the influence of thermal developing zone near the inlet section. The figure shows that the temperature of gas reaches the temperature of the wall at very short distances from the inlet. It is because of the chosen low Reynolds number. Since the temperature jump magnitudes are directly affected by the normal ve-

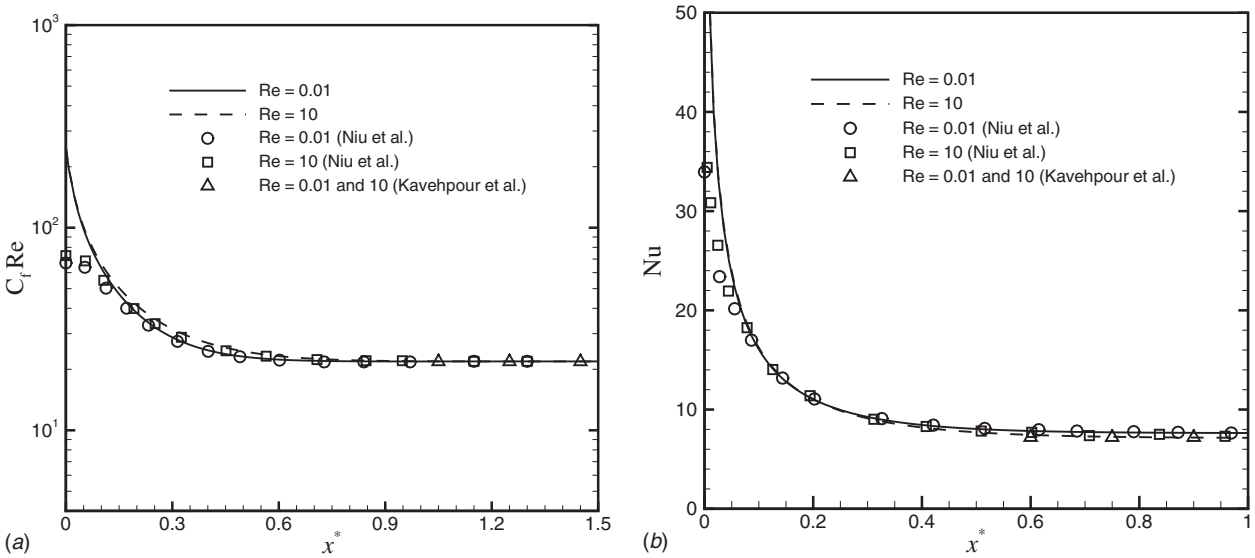

Fig. 2 The (*a*) friction factor and (*b*) Nusselt number distributions in a short channel and comparing them with the results of Niu et al. [8] and Kavehpour et al. [1], Re=0.01 and 10 and $Kn_{in}=0.015$

locity gradients at the entrance zone, the temperature jumps grow as the velocity gradients increase at the wall close to the inlet section.

Figure 2 illustrates the variations in friction factor and Nusselt number along the channel with $Kn_{in}=0.015$ and Re=0.01 and 10. The results are compared with the results of the lattice Boltzmann method [8] and finite-volume simulation [1]. Since Kavehpour et al. [1] studied long microchannels, their results are limited to the fully developed region. Therefore, we show their results close to the outlet, where the fully developed conditions are expected to be reached. As it is observed, the present rarefied flow solutions are in excellent agreement with those of Kavehpour et al. [1] and Niu et al. [8] except for $x^* \leq 0.1$. The main reason for the differences nearby the inlet section returns to different treatments of the two singularities, appeared at the two corners of the channel inlet. As it was mentioned in Sec. 1, these singularities are highly grid dependent and their magnitudes change with refining the grid [9,10]. Normally, a higher grid resolution would result in a more accurate solution in the region close to the inlet. The figure shows that both the friction factor and Nusselt number are not sensitive to Reynolds number in this range of work. This point is confirmed by the fully developed results presented in Ref. [1].

At the second step, we need to locate the fictitious section somewhere upstream of the inlet section. This location mainly returns to the strengths of the convection and conduction heat transfers in the domain and especially close to the inlet section. Logically, the fictitious section should be far enough to be free from the conduction influence close to the real inlet section. As is known, the weight of conduction to convection heat transfers can be evaluated by $(Re\ Pr)^{-1}$ if the energy equation is properly nondimensionalized [16]. This suggests that the conduction heat transfer is the dominant physics in the flow fields with $Re < 1$. In other words, the choice of $T^*_{in}=1$ at the fictitious inlet section should be correct. Our experience showed that the choice of $x^*=-5$ would satisfy this requirement and would create more reliable and more realistic boundary conditions at the real inlet.

Figure 3 shows the friction factor and Nusselt number distributions along the channel for various Knudsen numbers from no-slip to transition regimes. Comparing the results at Kn=0.015 with those in Fig. 2(*a*), the current results predict less friction factor magnitude at $x^*=0$. The maximum friction factor at each Knudsen number appears right at the real channel inlet, where the highest normal gradient velocity exists. Additionally, the current developed friction factor decreases in the early transition regime, i.e., at $Kn_{in}=0.2$ and 0.4. This is because the velocity profile becomes more flattened as the Knudsen number increases. Figure 3(*b*) shows the Nusselt distributions in the developing zone. To magnify the variation close to the channel entrance, the horizontal axis is presented in a logarithmic scale. Comparing with the results presented in Fig. 2(*b*), the Nusselt number magnitude right at the real inlet is less than what it was predicted via using the classical inlet boundary conditions. It should be noted that the Nusselt magnitude in the fully developed region only depends on the Knudsen number and is not affected by the type of inlet boundary condition at all. Figure 3 also shows that the no-slip boundary condition is not suitable to treat heat and flow as the Knudsen number increases.

Figures 4 illustrates the variations in friction factor and Nusselt number along the channel using Re=1 and 10 and $Kn_{in}=0.015$. Despite a close agreement between the current solution and that of the lattice Boltzmann method in the fully developed region, the friction factor and Nusselt number are predicted less than those of the lattice Boltzmann method in the entrance region. There is a question of which solution is more accurate. As mentioned in Sec. 1, Gamrat et al. [6] experienced a higher friction factor and Nusselt number in their developing zone, when they specified uniform velocity and temperature at the real inlet of the channel. In other words, their classical type of boundary conditions overpredicted their measurement. Our results in Fig. 4 perform similar conclusions. Therefore, it is concluded that the implementation of the inlet boundary conditions at a fictitious inlet section and at upstream of the real inlet section would result in more realistic solutions than those of applying a uniform inlet boundary condition right at the real inlet. The figure shows that the current flow and heat transfer solutions approach those of other researchers in the fully developed zone. In other words, the solutions in the fully developed zone are independent of the developing zone solution.

4 Conclusions

The flow and heat behaviors were investigated in short micro- and nanoscale channels applying the second-order slip velocity and temperature jump boundary conditions at the solid walls and two types of inlet boundary conditions. First, we implemented the classical inlet boundary condition and evaluated the achieved results against other reliable numerical and lattice Boltzmann solutions. Our calculated velocity and temperature profiles and the

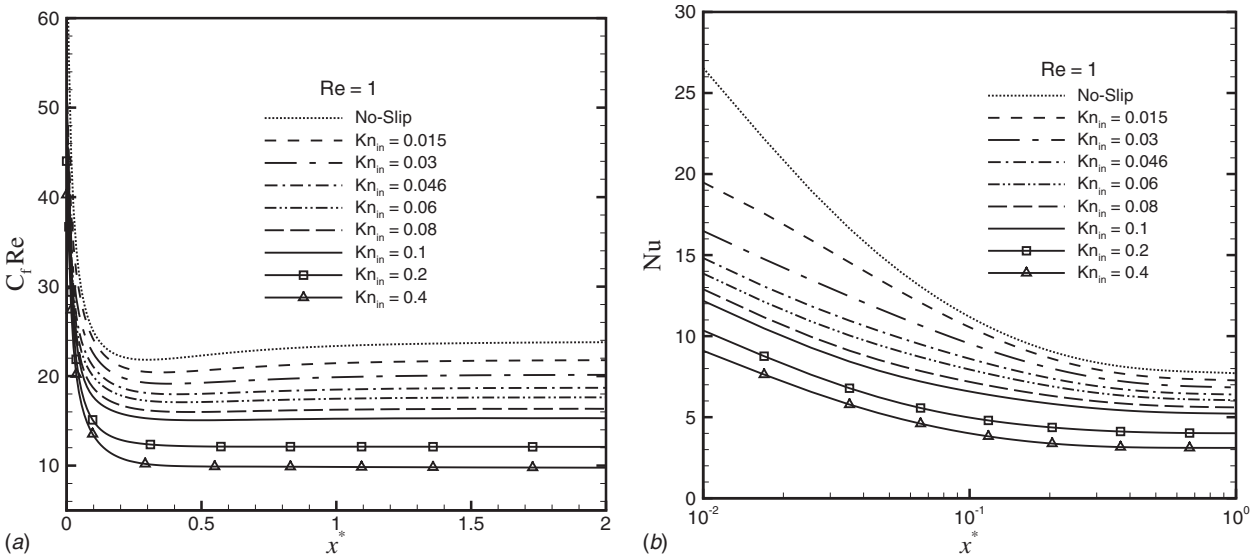

Fig. 3 The (*a*) friction factor and (*b*) Nusselt number distributions in a short channel applying various inlet Knudsen numbers, Re=1

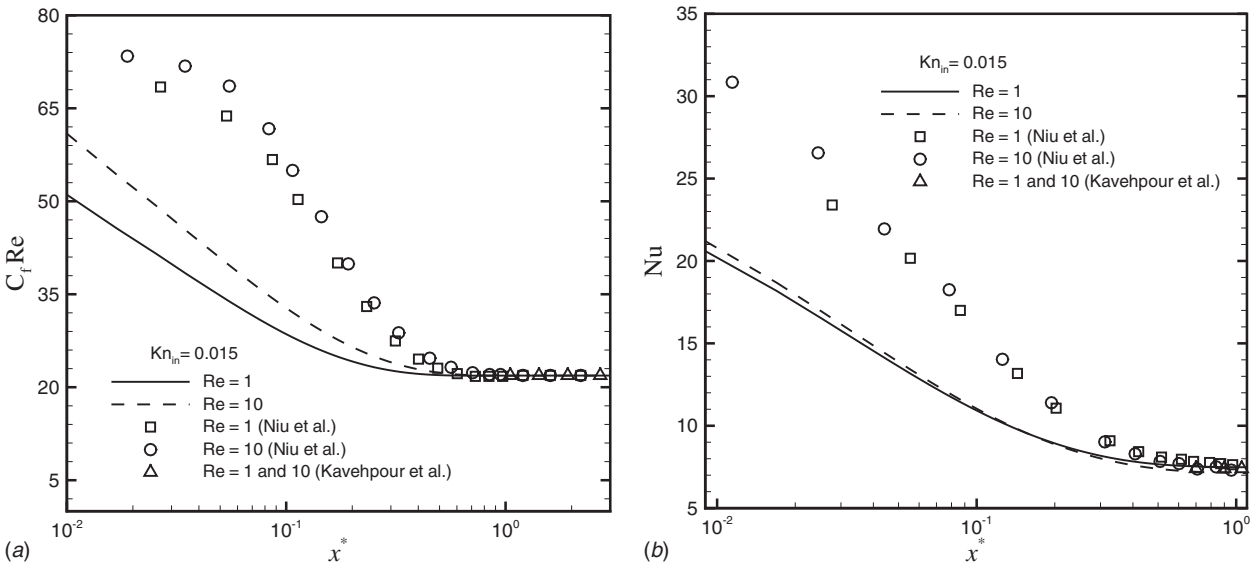

Fig. 4 The (*a*) friction factor and (*b*) Nusselt number distributions in a short channel with Re=1 and 10 and Kn_{in}=0.015

distributions of friction factor and Nusselt number along the channel were in excellent agreement with those of the lattice Boltzmann solution except in the vicinity of the channel inlet. Second, we simulated the fluid flow and heat transfer in micro- and nanochannels benefiting from more realistic inlet boundary conditions applied far upstream of the inlet section. Employing the symmetric boundary conditions at the extended fictitious horizontal walls, more realistic boundary conditions were simulated at the real inlet. We provided evidence that applying the inlet boundary conditions at the fictitious section would result in more realistic solutions, and can be reliably used in design and fabrication of microelectromechanical systems.

Acknowledgment

The support of the Research and Technology Center in Sharif University of Technology is gratefully acknowledged.

References

[1] Kavehpour, H. P., Faghri, M., and Asako, Y., 1997, "Effects of Compressibility and Rarefaction on Gaseous Flows in Microchannels," Numer. Heat Transfer, Part A, **32**, pp. 677–696.
[2] Guo, Z. Y., and Wu, X. B., 1998, "Further Study on Compressibility Effects on the Gas Flow and Heat Transfer in a Microtube," Microscale Thermophys. Eng., **2**, pp. 111–120.
[3] Beskok, A., and Karniadakis, G. E., 1994, "Simulation of Heat and Momentum Transfer in Complex Microgeometries," J. Thermophys. Heat Transfer, **8**, pp. 647–655.
[4] Beskok, A., and Karniadakis, G. E., 1999, "A Model for Flows in Channels, Pipes, and Ducts at Micro and Nano Scales," Microscale Thermophys. Eng., **3**, pp. 43–77.
[5] Asako, Y., and Toriyama, H., 2005, "Heat Transfer Characteristics of Gaseous Flows in Microchannels," Microscale Thermophys. Eng., **9**, pp. 15–31.
[6] Gamrat, G., Favre-Marinet, M., and Asendrych, D., 2005, "Conduction and Entrance Effects on Laminar Liquid Flow and Heat Transfer in Rectangular Microchannels," Int. J. Heat Mass Transfer, **48**, pp. 2943–2954.
[7] Hung, W. C., and Ru, Y., 2005, "A Numerical Study for Slip Flow Heat Transfer," Appl. Math. Comput., **173**(2), pp. 1246–1264.
[8] Niu, X. D., Shu, C., and Chew, Y. T., 2007, "A Thermal Lattice Boltzmann Model With Diffuse Scattering Boundary Conditions for Micro Thermal

Flows," Comput. Fluids, **36**, pp. 273–281.
[9] Darbandi, M., and Schneider, G. E., 1998, "Numerical Study of the Flow Behavior in the Uniform Velocity Entry Flow Problem," Numer. Heat Transfer, Part A, **34**, pp. 479–494.
[10] Darbandi, M., and Hosseinizadeh, S. F., 2004, "Remarks on Numerical Prediction of Wall Shear Stress in Entry Flow Problems," Commun. Numer. Methods Eng., **20**, pp. 619–625.
[11] Darbandi, M., and Vakilipour, S., 2007, "Developing Consistent Inlet Boundary Conditions to Study the Entrance Zone in Microchannels," J. Thermophys. Heat Transfer, **21**(3), pp. 596–607.
[12] Darbandi, M., and Schneider, G. E., 1998, "Analogy-Based Method for Solving Compressible and Incompressible Flows," J. Thermophys. Heat Transfer, **12**(2), pp. 239–247.
[13] Darbandi, M., Roohi, E., and Mokarizadeh, V., 2008, "Conceptual Linearization of Euler Governing Equations to Solve High Speed Compressible Flow Using a Pressure-Based Method," Numer. Methods Partial Differ. Equ., **24**(2), pp. 583–604.
[14] Darbandi, M., and Vakilipour, S., 2008, "Developing Implicit Pressure-Weighted Upwinding Scheme to Calculate Steady and Unsteady Flows on Unstructured Grids," Int. J. Numer. Methods Fluids, **56**(2), pp. 115–141.
[15] Darbandi, M., and Vakilipour, S., 2007, "Using Fully Implicit Conservative Statements to Close Open Boundaries Passing Through Recirculations," Int. J. Numer. Methods Fluids, **53**(3), pp. 371–389.
[16] Darbandi, M., and Hosseinizadeh, S. F., 2006, "Numerical Simulation of Thermobuoyant Flow With Large Temperature Variation," J. Thermophys. Heat Transfer, **20**(2), pp. 285–296.